Novel Techniques for Liquid Xenon Time Projection Chambers:

A ^{37}Ar Calibration Source for Dark Matter Searches and Characterization of Silicon Photomultipliers

Dissertation zur Erlangung des Grades
Doktor der Naturwissenschaften

vorgelegt dem

Fachbereich 08 - Physik, Mathematik und Informatik
der Johannes Gutenberg-Universität Mainz

von

Christopher Hils

geb. am 10.04.1984 in Worms

31. Oktober 2024

1. Berichterstatter:
2. Berichterstatter:

Datum der mündlichen Prüfung: 12.03.2025
D77: Dissertation Johannes Gutenberg-Universität Mainz

Erklärung

Hiermit versichere ich gemäß, § 12 Absatz 3 e) der Promotionsordnung des Fachbereichs 08 Physik, Mathematik und Informatik vom 2. Dezember 2013

- dass ich die vorgelegte Arbeit selbständig verfasst habe und ausschließlich die angegebenen Quellen und Hilfsmittel verwendet wurden. Von der Ordnung zur Sicherung guter wissenschaftlicher Praxis in Forschung und Lehre und vom Verfahren zum Umgang mit wissenschaftlichem Fehlverhalten habe ich Kenntnis genommen.
- dass die vorgelegte Arbeit nicht als Prüfungsarbeit für eine andere Prüfung eingereicht wurde.
- dass ich die vorgelegte Abhandlung oder Teile davon noch nicht als Dissertation bei einer anderen Fakultät oder einem anderen Fachbereich eingereicht habe.

Mainz, den 31. Oktober 2024:

_____

Christopher Hils

Abstract

Astronomical observations of the dynamics of galaxies and galaxy clusters suggest they have to contain substantially more mass than is directly observed, the so-called dark matter (DM). This finding is supported by measurements of the cosmic microwave background (CMB), which requires five times more inert mass than regular, 'baryonic' matter participating in acoustic oscillations of the primordial plasma. Furthermore, the observed structures in the universe constrain the DM to be non-relativistic at the epoch of matter-radiation equality. The combined observations exclude every known particle in the standard model of particle physics, leaving the explanation of the phenomenon to new physics.

The XENON detectors utilize dual-phase time projection chambers (TPCs), dedicated to the search for DM, focused in particular on one suitable candidate, the weakly interacting massive particles (WIMPs). The last two detectors of the series contain 2 t and 5.9 t as an active liquid xenon target for XENON1T and XENONnT, respectively. Although no DM has been detected yet, new exclusion limits were set.

To produce reliable results, the detector characteristics need to be well known. This is achieved with calibrations, where the detector is exposed to radiation with well-known properties. These can be external sources, but also radioactive isotopes mixed directly into the xenon can be used to verify detection efficiency and uniformity throughout the detector volume.

This work focuses on the introduction of a new internal low-energy source, the radioactive isotope ^{37}Ar. Two transitions at energies of 2.82 keV and 0.27 keV, respectively, are used for calibration. The source can be produced on-site at the University of Mainz at the TRIGA research reactor located on campus. On the hardware side, a dosing system was developed to fine-dose the amount of activity injected into the TPC. Also, the procedure to remove the source from the xenon was successfully performed, by the cryogenic distillation column of the XENON1T/nT recirculation system.

A complete calibration run was performed at the end of data taking of XENON1T and after the first science run of XENONnT. The high statistics and uniformity of ^{37}Ar data stressed the impact of field non-uniformity on charge carrier and photon production in xenon and therefore on the applied event corrections. Based on this calibration, we found an event-reconstruction anomaly in the top part of the TPC for low energies and developed a correction. With the calibration data, the photon and electron yields of xenon for the 2.82 keV decay were measured at 32.27 ± 0.52 ph/keV and 41.02 ± 1.06 e$^-$/keV, respectively. For the lower value of 0.27 keV an electron yield of $68.0^{+6.3}_{-3.7}$ e$^-$/keV was found.

Planned improvements of liquid xenon TPCs include a possible replacement of current photo multiplier tubess (PMTs) with modern, compact silicon photomultipliers (SiPMs). To evaluate the feasibility and performance of SiPMs in xenon detectors, a test setup was developed to characterize the sensors under detector conditions. This setup and first steps in data analysis are presented in this work, with a possible future upgrade of the local 'MainzTPC' in mind.

Zusammenfassung

Die Bewegungen von Galaxien und Galaxiehaufen legen Nahe, dass sie deutlich mehr Materie anthalten müssen als direkt beobachtet wird, die sogenannte dunkle Materie (DM). Dies wird durch Messungen der kosmischen Hintergrundstrahlung bestätigt, welche fünfmal mehr DM als sichtbare, 'baryonische' Materie erfordert, welche an den akustischen Schwingungen des Urplasmas beteiligt ist. Desweiteren kann durch die beobachtete Struktur des Univerums eine relativistische Natur der DM zur Zeit des Materie-Srahlungs Gleichgewichts ausgeschlossen werden. Alle Teilchen des Standardmodells sind durch Beobachtungen ausgeschlossen, was nur 'Neue Physik' als Erklärung lässt.

Das XENON-Experiment verwendet zwei-phasen Zeitprojektionskammern zur Suche nach DM, im Speziellen nach den schwach wechselwirkenden WIMPs (eng. weakly interacting massive particles). XENON1T enthielt 1.3 t, XENONnT enthält 5.9 t flüssiges Xenon als aktive Detektormasse. Obwohl bisher keine DM nachgewiesen wurde, konnte der theoretisch erlaubte Parameterraum eingegrenzt werden.

Um verlässliche Ergebnisse zu erzielen, muss der Detektor möglichst gut verstanden werden. Dies geschieht mit Hilfe von Kalibrationen, oft basierend auf Strahlung bekannter Energie, die sowohl von außen, als auch ins Innere des Detektors eingebracht werden. Damit kann sowohl die Nachweiseffizienz als auch die Detektorhomogenität verifiziert werden.

Der Fokus dieser Arbeit liegt auf der Einführung einer neuen, niederenergetischen Kalibrationsquelle, dem radioktiven Isotop ^{37}Ar, welches mit dem TRIGA-Reaktor der Universität Mainz direkt auf dem Kampus hergestellt werden kann. Zwei Zerfallskanäle mit jeweils 2.82 keV und 0.27 keV Zerfallsenergie werden zur Kalibration verwendet. Zur Dosierung der in den Detektor eingebrachten Aktivität wurde eine Dosiervorrichtung entwickelt. Ebenso wurde die Entfernung des ^{37}Ar aus dem Xenon mit Hilfe der kryogenen Destillationssäulen des Rezikulationssystems von XENON1T/nT erfolgreich durchgeführt.

Am Ende der Laufzeit von XENON1T, sowie nach der ersten Messkampagne von XENONnT, wurde jeweils eine ^{37}Ar Kalibration durchgeführt. Durch die ^{37}Ar Daten wurde der Einfluss von Feldinhomogenitäten auf die Erzeugung von Elektronen und Photonen in Xenon deutlich. Für niederenergetische Ereignisse, ähnlich der von ^{37}Ar, wurde eine Rekonstruktionsanomalie im oberen Bereich der TPC gefunden und eine entsprechende Korrektur entwickelt. Mit diesen Daten wurde die Photonen- und Elektronenausbeute für den 2.82 keV Zerfall zu jeweils 32.27 ± 0.52 ph/keV und 41.02 ± 1.06 e$^-$/keV bestimmt, für den 0.27 keV Zerfall wurde ein Wert von $68.0^{+6.3}_{-3.7}$ e$^-$ keV für die Elektronenausbeute gefunden.

Geplante Verbesserungen für flüssig-Xenon TPCs schließen auch ein Ersetzen der herkömmlichen PMTs mit modernen, kompakten SiPMs ein. Zum Einschätzen der Machbarkeit und Leistungsfähigkeit von SiPMs wurde eine Teststation zur Charakterisierung der SiPM Eigenschaften entworfen. Eine erste Messung und Analyse, insbesondere bezüglich einer Aufrüstung der MainzTPC, wird in dieser Arbeit dargelegt.

Contents

Introduction **13**

1. Dark Matter Introduction **15**
1.1. Hints for the existence of Dark Matter . . . 15
1.2. ΛCDM model . . . 16
1.3. Cosmic Microwave Background . . . 17
1.3.1. Weakly Interacting Massive Particles as dark matter candidates 18
1.4. Alternative Dark Matter Candidates . . . 19
1.5. Alternative theories . . . 20
1.6. Dark Matter detection . . . 21
1.7. Experimental realisation of Dark Matter searches . . . 25

2. The XENON1T detector **29**
2.1. Xenon as detection medium . . . 29
2.2. Working principle of the XENON1T TPC . . . 35
2.3. Determination of detector specific photon and electron gain factors utilizing the Doke plot . . . 37
2.4. Photo multiplier tube properties . . . 39
2.5. Gas recirculation and purification system . . . 40
2.6. Detector shielding and background reduction . . . 42
2.7. Data acquisistion: event building . . . 43
2.8. Signal corrections . . . 44

3. First ^{37}Ar Calibration of a Dark Matter detector - XENON1T **49**
3.1. Introduction . . . 49
3.2. ^{37}Ar as calibration source . . . 49
3.3. Measurement Run Preparations and Setup . . . 51
3.3.1. Ampule production and source irradiation . . . 51
3.3.2. ^{37}Ar dosage and injection system . . . 54
3.3.3. Dosing procedure . . . 56
3.4. ^{37}Ar Calibration of XENON1T . . . 57
3.4.1. Live activity monitoring . . . 57
3.4.2. Argon injection . . . 58
3.4.3. Argon outgassing test . . . 60
3.4.4. Argon distillation phase - preliminary analysis . . . 60
3.5. Summary . . . 63

4. Low-energy Electronic Recoil Calibration of XENON1T with ^{37}Ar 65
4.1. Science Run 1 cut selection . . . 66
4.2. Distillation analysis after event selection . . . 70
4.3. Measurement of the electron lifetime with ^{37}Ar and comparison with other calibration sources . . . 73
4.4. Fitting the signal distribution in S1-S2 . . . 101
4.5. Modeling the S1-S2 signal distribution . . . 102
4.6. Signal threshold in S1 . . . 106
4.7. Improved fitting of the signal distributions . . . 108
4.8. Determination of photon and electron gain factors for XENON1T . . . 113
4.9. Combined energy fit for the ^{37}Ar peak . . . 114
4.10. Energy resolution for ^{37}Ar . . . 115
4.11. Single electron gain measurement . . . 116
4.12. Alternative charge yield calculation . . . 121
4.13. S2-only analysis . . . 123
4.14. Electron and photon yield in liquid xenon from the ^{37}Ar calibration . . . 127
4.15. Impact of ^{37}Ar calibration on the XENON1T low-energy electronic-recoil excess . . . 128
4.16. Summary and conclusion . . . 132

5. ^{37}Ar Calibration of the XENONnT detector 135
5.1. Calibration system upgrade in XENONnT . . . 135
5.2. First ^{37}Ar calibration in-between science runs in XENONnT . . . 138
5.3. First look at XENONnT data . . . 140
5.4. Summary and Outlook . . . 144

6. Semiconductor photon detectors 147
6.1. Introduction . . . 147
6.2. Working principle of SiPMs . . . 147
6.3. Characteristic properties of SiPMs . . . 152

7. Design and construction of a test setup for SiPM characterization 159
7.1. Introduction . . . 159
7.2. SiPM Samples . . . 159
7.3. Test setup design for measurements in liquid xenon . . . 161
7.4. Gaseous xenon infrastructure . . . 168
7.5. Sensor power supply . . . 170
7.6. Low temperature amplifier for SiPM measurements . . . 170
7.7. Signal readout . . . 173
7.8. First Measurements of SiPM samples . . . 175
7.8.1. Signal shapes for the SiPM samples . . . 175
7.8.2. Determination of breakdown voltage . . . 177
7.8.3. Gain . . . 179
7.8.4. Correlated noise measurement . . . 180

7.8.5. Dark count rate . . . 182
7.9. Measurements with xenon scintillation light . . . 184
7.10. Summary, conclusion and outlook . . . 185

A. Appendix: Applying a global fit to voxelized data to extract the S1 detection threshold 187
A.1. Motivation . . . 187
A.2. Fit performance . . . 188

B. Appendix 193
B.1. XENON1T working principle . . . 193
B.2. XENON1T ^{37}Ar Distillation . . . 195
B.3. XENON1T Electron lifetime estimation . . . 198
B.4. XENON1T Afterpulse correction . . . 204
B.5. XENON1T 2D-Fit plots . . . 206
B.6. Additional plots: SiPM Introduction . . . 207
B.7. Additional plots: SiPM Setup . . . 208
B.8. Code snippets for 2D fits . . . 215
B.8.1. Likelihood class for voxel fits . . . 215
B.8.2. Update of Likelihood class to allow global fitting . . . 216
B.9. ^{37}Ar S1-cS2 voxel-fit results . . . 217
B.10. XENONnT data analysis . . . 225

Acronyms 227

List of Figures 229

List of Tables 233

Bibliography 235

Introduction

Astronomical observations have shown that only a small fraction of the observable universe is made from baryonic matter. Observations of the cosmic microwave background have shown that the universe primarily consists of dark energy and dark matter. This assumption is based on the ΛCDM model, the current standard model for cosmology. Part of the name, CDM, standing for **C**old **D**ark **M**atter, already infers an important property for possible DM candidates, namely being cold, which in this context refers to be non-relativistic.

One prominent candidate for a DM particle is the so-called WIMP. Detection efforts are made via indirect detection with a search for WIMP annihilation products such as γ-rays, neutrinos or cosmic rays, as well as with production attempts in colliders, such as the Large Hadron Collider. The third channel is direct detection, where the measurement of collisions between WIMPs and baryonic matter is attempted. Several experimental techniques are suited for direct detection measurements, at which the most applied ones are cryogenic crystal and noble gas detectors.

Noble gas detectors are often realized in the form of dual-phase TPC. This kind of detectors typically consist of a large volume of liquid noble gas with a thin vapour layer on top, which is observed by two arrays of photosensors on top and the bottom of the detector. Signals are created in the liquid phase, creating a primary scintillation signal and electrons, which are drifted by an applied electric field to the gas phase, where they create a secondary scintillation signal. Several properties of the interaction can be derived from these two scintillation signals, for example, the deposited energy, or if it is interacting with the shell or the nucleus of the xenon atom. This allows the identification of possible WIMP candidates and also allows to conclude on possible mass and cross-section of the WIMP.

One prominent experiment utilizing the noble gas xenon is the XENON experiment. It consists of a series of experiments, in which XENON100 with an active detector mass around 100 kg of xenon was the first to look for DM. The advancement of the series over XENON1T (with 1.3 t of active mass), the current XENONnT (5.9 t), and the possible future projects of DARWIN (40 t) or XLZD (60 t) highlight an advantage of this technology: easy scalability to improve sensitivity.

Increasing the size of the detector also entails challenges that need to be solved. Larger dimensions mean longer drift times. This requires higher purity of the xenon and a better understanding of the electrical field. To understand the detector behavior, calibrations are performed. The excellent self-shielding property of xenon, for instance, is beneficial for background suppression but also renders the usage of external calibration sources unfeasible. Therefore internal calibration sources, directly

mixed into the xenon, are utilized. In this work a new internal source is introduced, the isotope ^{37}Ar with a half-life of 35 days.

^{37}Ar works similar to the already used ^{83m}Kr , distributing homogeneously throughout the detector volume, albeit it decays with much lower line energies of 2.82 keV and 0.27 keV. Due to its long half-life, it needs to be removed actively after the calibration, utilizing already existing distillation facilities. This work describes the production of the source, the injection into and removal from the experiment, as well as a series of analyses. These include the measurement of the light and charge yield of xenon at the ^{37}Ar energies and the finding of other detector effects, like field effects and signal afterpulse separation, that influence energy reconstruction, especially at these low energies.

The scintillation signals in a TPCs are usually read out with a PMT. In the last years, a new type of photosensor emerged, the SiPM. A test setup was built to characterize the properties of various vacuum ultraviolet (VUV) sensitive SiPM models and test their suitability for use in a liquid xenon TPC.

This work describes the setup and presents a first analysis of the data gained in a run with the SiPMs under liquid xenon conditions. Currently, upgrades are implemented to characterize a set of the newest generation of SiPMs, which are ultimately used in the future version of the local 'MainzTPC'.

1. Dark Matter Introduction

In this chapter a general overview is given in Section 1.1 for the evidence observed that led to the introduction of the concept of DM. Section 1.2 introduces the ΛCDM model, which describes the observed effects. The WIMP is a DM candidate, which is the primary detection target of the XENON DM detector series, on which large parts of this work are based. These particles are, however, not the only DM candidates that provide the expected properties. Some further candidates are shortly mentioned in section 1.4, as well as some mechanisms and explanations that try to avoid the introduction of new particles altogether are mentioned in section 1.5. Only very short explanations are given for these alternatives, which are far from being complete or from providing a satisfactory explanation. They are mentioned to clarify the vastness of possibilities to explain the observed phenomena, but providing more details is beyond the scope of this work.

In the following section 1.6, a coarse overview of the direct detection approach is given, as well as a brief overview of how these concepts are realized in experimental setups in section 1.7.

1.1. Hints for the existence of Dark Matter

Galaxy cluster observations

The first observations teasing a large amount of invisible matter in the universe were conducted in the 1930s by Fritz Zwicky. He measured the velocity distribution in the Coma galaxy cluster and found a far larger spread of velocities for its constituents than expected. Based on optical observations, the cluster consists of 800 individual nebulae within a radius of approximately 1 million light years. Utilizing the Virial theorem:

$$E_{Kin} = -\frac{1}{2} E_{Pot} \tag{1.1}$$

one can calculate the mean velocity of its constituents and find a value of 80 km/s. This is in strong tension with the measured velocity distribution, based on the redshifts of the nebulae, which shows far larger differences in speed of up to 2000 km/s. To be consistent with observations, the mass of invisible 'dark matter' must be much larger than that of the visible one (although Fritz Zwickys calculation resulted in a mass-to-light ratio of 400, which is far too large, caused by using the Hubble constant known at that time [1]) [2].

Rotation curves

In the late 1960s, Vera Rubin determined the rotation speeds of stars around the center of their galaxy by measuring the redshift of these stars caused by the motion. It became obvious, that especially the stars more distant from the galaxy center moved faster than expected [3]. Following Newton the relation between rotation speed and distance to the galactic center should follow the relation

$$v \propto \sqrt{\frac{1}{r}}$$

as it was also observed for the planetary movement in our solar system. In the observed galaxies, the speed of the outer stars is nearly constant as shown in Fig. 1.1.

This hints at the existence of additional mass, invisible in the EM-spectrum, which is needed to explain the observed movement. In modern cosmological models a halo of this invisible mass, called Dark Matter, encompasses the galaxies. These halos are assumed to extend to a radius several times larger than the visible components of the observed galaxy [4].

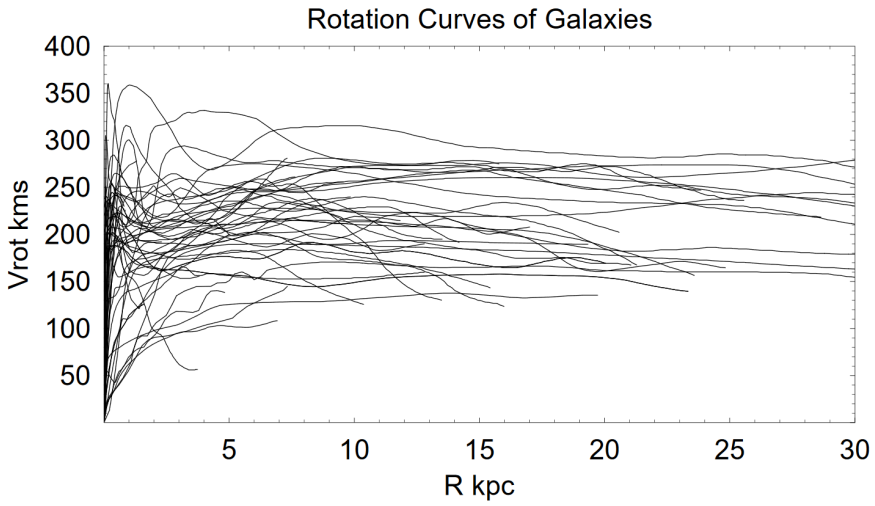

Figure 1.1.: *Various rotation curves of different galaxies. [3].*

1.2. ΛCDM model

The ΛCDM model is the current standard model describing cosmology, as it is the simplest model providing reasonably good explanations for the observed properties of the cosmos. These include the CMB observed and mapped by multiple satellite and ground-based instruments, the observed structure (distribution of matter) of the universe, the abundance of the light elements and their isotopes (hydrogen and helium) created in the Big-Bang nucleosynthesis (BBN), and the observed expansion of the universe.

In the ΛCDM model the universe consists of three major constituents: dark energy, dark matter, and baryonic matter. The latter is the *ordinary* matter, which participated in BBN, interacted via electromagnetism with the photons in the primordial plasma (the source of the CMB), and eventually form the stars and gas we observe today.

The Λ is the cosmological constant, representing the vacuum energy of space, and is the simplest model for of dark energy. This constant is present in Einsteins field equations and has the same properties as an energy density. It also provides a 'pressure', which is, however, negative and responsible for the observed accelerated expansion of the universe.

The CDM stands for Cold Dark Matter, already implying additional properties of the unknown particles first proposed by Fritz Zwicky. Besides having to be non-baryonic (also including electrons) in nature, it must be *cold*. This refers to the kinetic energies of the dark matter particles, meaning their speed has to be already non-relativistic at the time of matter-radiation equality. This requirement results from observations of the cosmological structure, the distribution of the galaxies and galaxy clusters in the universe. Resulting structures from simulations were only comparable with observations if the assumed velocity distribution of the DM particles were non-relativistic.

As dark matter cannot be directly observed, electromagnetic interaction can be excluded. Thus, within the standard model (SM), dark matter can only interact via gravity or the weak force. This only leaves one particle of the standard model as a candidate for DM: the neutrino. The neutrino, however, is very light and therefore was moving at relativistic velocities in the early universe (and well beyond decoupling of the CMB), and hence can be ruled out as a major DM-contribution by early simulations of its impact on structure formation. Due to its relativistic (*hot*) nature, the structure of the universe would be much more smeared out than actually observed [5].

1.3. Cosmic Microwave Background

Predicted in 1948 by Ralph Alpher and Robert Herman [6], the CMB was discovered in 1964 by Arno Penzias and Robert Wilson [7]. The CMB is a remnant of the Big Bang, showing the state of the universe at an age of approximately 380000 years. At this point, it reached a temperature of 3000 K, where atoms were able to form and photons were able to move freely through space for the first time. Today the CMB can be described with a black-body spectrum at a temperature of 2.726 K. Several satellite missions were launched to perform precise measurements of this background radiation. These missions, starting with COBE (Cosmic Background Explorer), followed by WMAP (Wilkinson Microwave Anisotropy Probe), and Planck discovered small anisotropies in the CMB which are shown in Fig. 1.2.

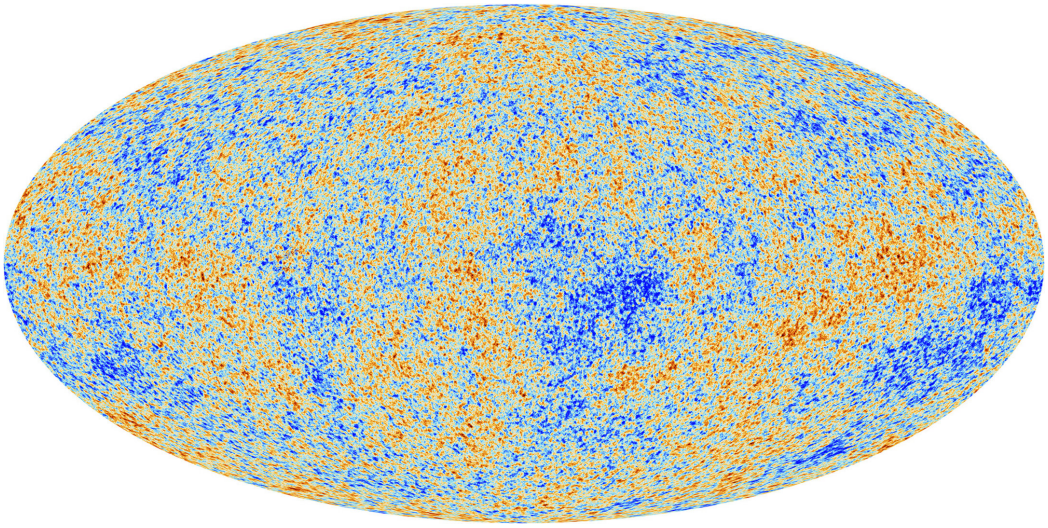

Figure 1.2.: *Cosmic Microwave Background measured by the Planck satellite. It shows the temperature fluctuations (with a variation of* $\pm\, 300\,\mu K$ *) in the microwave background with a mean temperature of 2.726 K. [8].*

After the removal of foreground radiation emitted mainly from the galaxy, the measured temperature map can be decomposed into spherical harmonics with a Fourier transformation. The resulting power spectrum can be fitted with the standard model of cosmology, the Λ-Cold Dark Matter (Λ-CDM) model. It is currently the simplest model, using only 6 parameters to describe age, shape, and composition of the universe. The power spectrum and the Λ-CDM fit can be seen in Fig. 1.3. Also shown in the figure are the shapes of the model for a different value of the Ω_{CDM} parameter, which represents the DM content in the universe. The position of the higher acoustic peaks, especially the third, clearly depends strongly on the amount of DM. This is in agreement with the assumption that a different amount of DM would result in a different structure size. In all variations the first acoustic peak stays at the same position, validating a flat geometry of the universe. Resulting from the Λ-CDM fit to the Planck data, the universe is composed of 4.9% baryonic matter, 26.8 % dark matter, and 68.3% dark energy [9].

1.3.1. Weakly Interacting Massive Particles as dark matter candidates

Based on the presented observations and on the derived properties determined for DM, baryons can be excluded to be the constituents of DM. Additionally, their contribution to the energy content of the Universe is constraint to $\sim 5\,\%$. As neutrinos are also ruled out based on structure observations, the Standard Model of Particle Physics does not provide any suitable DM candidate.

Therefore, to solve the DM mystery, many *new physics* particles are suggested. One class of particles that provide particles with suitable properties are the WIMPs. They

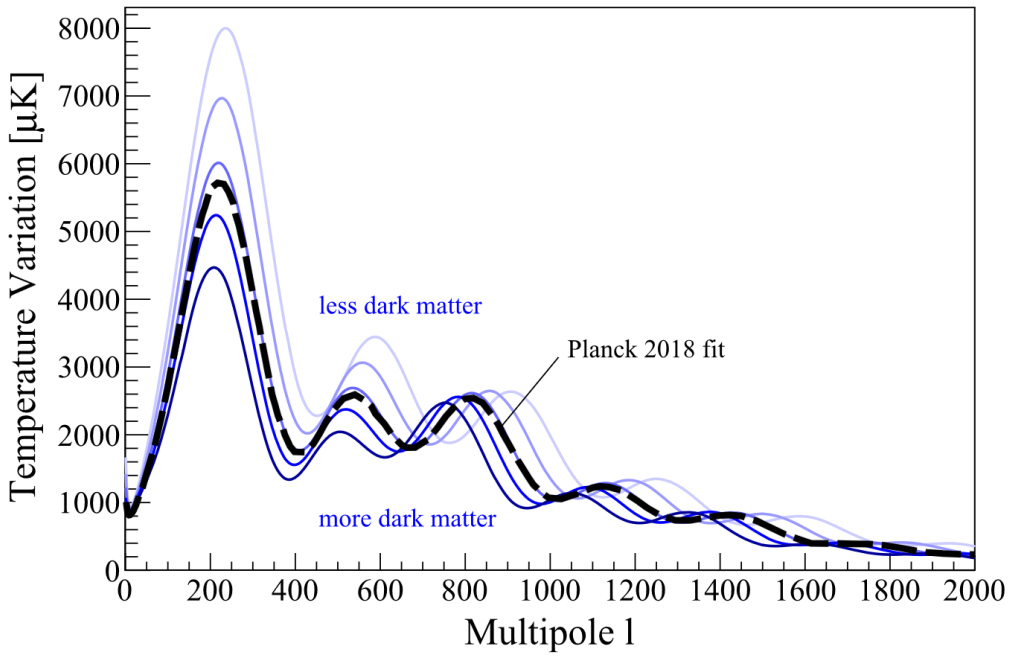

Figure 1.3.: *Temperature power spectrum (2018) measured by the Planck satellite. The figure shows the shape of the Λ-CDM model for variations of the parameter Ω_{CDM} representing the DM content of the universe, between values of 0.11 and 0.43. The multipoles l correspond to a certain angular size, with the main peak at $l \sim 200$ corresponding to $\sim 1°$ and $l \sim 1800$ to $\sim 0.1°$. The figure is taken from [10].*

are provided as the lightest particles in several theories, including supersymmetric particles, Kaluza-Klein particles from theories including extra dimensions and the lightest particles in Little Higgs models [10]. The WIMPs are expected within a mass range of $1 - 10^5\,\mathrm{GeV/c^2}$, whereby the typical mass predicted by the supersymmetric theories is around $100\,\mathrm{GeV/c^2}$ [10]. The expected interaction cross sections for such particles range from $10^{-41}\mathrm{cm}^2$ to $10^{-48}\mathrm{cm}^2$ [11, 12].

A requirement for these particles to count as suitable DM candidates is that they have to be stable to be able to explain the current amount of DM observed in the universe.

1.4. Alternative Dark Matter Candidates

Axions

Axions are well-motivated DM candidates, originally introduced to solve the *strong CP problem* [13, 14]. The mass of axions is well constrained by various experimental and astrophysical observations. Masses above 50 keV are ruled out by beam dump experiments, as no observations were made in this field. This value is further lowered by astrophysics based on observations of red dwarves and supernovas. Axions would

provide an efficient way for a star to lose energy as they could leave the star unhindered from anywhere inside the star while photons can only be emitted from the surface. Therefore axions would shorten the expected lifespan of stars. Similarly, light axions would provide an alternative to neutrinos as an energy loss mechanism in case of a supernova. As the number of neutrinos observed in various experiments during supernova SN1987a followed the theoretical expectations, this further limits the mass range for axions and places an upper limit in the order of 10^{-3} eV [15].

Axion like particle (ALP) arise from similar symmetry breakings in various other theories and as such they have similar properties but are not as confined in their mass range as the axion and also allow for masses in the keV-range. The axion mass is well below the detection threshold of detectors like for instance XENON1T/XENONnT, ALPs, however, are massive enough, but have not been observed so far.

Sterile Neutrinos

Sterile neutrinos are theoretically well-motivated hypothetical particles that interact solely via gravity. They are introduced to understand the low mass of the three active neutrinos (e, μ, τ) and are mixed with all three active neutrino states. As the sterile neutrino disappears/appears every time an active neutrino interacts (absorbed/created), it has to be unstable. To be a valid DM candidate it has to have an adequate lifetime, at best in the order of the age of the universe. DM containing sterile neutrinos are expected to be not completely dark and emissions in the X-ray regime are expected. Observations of dwarf spheroidals have not yet yielded a result and as such provide a lower bound for the sterile neutrino mass in the order of keV [15].

1.5. Alternative theories

There are several attempts to explain the observed effects without adding a hidden mass in the form of DM. In the following, the most prominent theories are mentioned, but this list is far from complete.

MACHOS

Before the era of precision cosmology, the observed effects were tried to be explained with objects made of normal, baryonic matter. These objects were deemed to be hard to observe due to lack of illumination or emission of light. As such these objects consist of brown dwarfs (failed stars), rogue planets, ejected from their solar systems, and black holes without an accretion disc. These objects are collectively called Massive Compact Halo Objects (MACHOs) [16]. Utilizing microlensing, it was found, that the amount of observed objects is insufficient to account for the amount of dark matter needed [17]. Primordial Black Hole (PBH) are formed in the very early stages of development of the universe before the Big Bang nucleosynthesis. Therefore they do not account for the 5 % contribution of baryonic matter derived from the CMB [10].

Observations of gravitational waves, emanated from mergers of PBHs with masses of 20 - 30 $M_\odot$, revealed that PBHs only contribute about 1 % of the DM [18].

MOND and TeVeS

In 1983, Mordehai Milgrom presented an idea to avoid introducing DM by modifying the long-range behavior of gravity, called Modified Newtonian dynamics (MOND). More precisely he introduced a constant a_0 with the dimension of acceleration and a numerical value of approximately $2 \cdot 10^{-8} m\,s^{-2}$. For objects experiencing a gravitational acceleration $a \gg a_0$, the classical Newtonian dynamic is reproduced. For a in the order of a_0 or smaller, the modified dynamics deviates from the classic by having a much weaker drop-off of the gravitational force compared to the Newtonian dynamic: MOND predicts a drop-off proportional to the inverse of the distance, while Newton predicts a reduction by the inverse of the square of the distance [19].

MOND was initially developed to explain the flat velocity distribution at the outer regions of spiral galaxies. It also explains well other observations, one, for example, is the Tully-Fisher relation between the luminosity of a spiral galaxy and its rotation velocity [20].

It however struggles to provide a proper explanation for other observations, including the shape of the CMB power-spectrum or the effect of gravitational lensing observed in galaxy clusters.

A summary of which observations can be explained with MOND and which are not can be found in [21].

The tensor-vector-scalar (TeVeS) gravity is an attempt of a relativistic generalization of MOND. Although with TeVeS the power spectrum of the microwave background can be modeled, it still cannot explain the effects of weak lensing when it comes to (irregular) galaxy clusters. It was possible to model galaxy clusters without the use of DM, but still a collisionless particle was needed. Therefore a large abundance of neutrinos had to be introduced, with an assumed neutrino mass in the order of 2 eV, which in the meanwhile was excluded by the KATRIN experiment [15, 22].

1.6. Dark Matter detection

Besides the observations that hint at the existence of DM, there are three more approaches to detect DM. One is the production of DM in accelerators such as the Large Hadron Collider, where it can be indirectly detected via the missing transverse momentum of the DM particle [23]. The second approach tries to identify the decay products that follow an annihilation process of DM particles into SM-particles like $e^- e^+$ and $P\bar{P}$ matter-antimatter pairs, as well as γ-rays and neutrinos. As the charged particles can be deflected by interstellar magnetic fields and as a result lose the directional information, the search is focused on the γ-rays and neutrinos. The search with γ-ray telescopes like HESS and MAGIC, or neutrino observatories like IceCube and

Super-Kamiokande, is focused on regions of space where an increased density of DM particles is expected, e.g. the galactic center or spheroidal dwarf galaxies [24, 25].

The third approach tries to directly detect DM particles via interaction with baryonic matter. As DM carries no electric charge, it will not interact with the shell electrons of atoms but will scatter off elastically from its nucleus via a weak interaction.

A measured signal strongly depends on the distribution of DM particles in the galaxy, as well as their kinematics. These properties can be derived from astrophysical observations. DM can assumed to be a collisionless gas, forming an isotropic halo around the galaxy with its particles bound by gravity. The density profile can be calculated to be:

$$\rho(r) = \frac{\sigma^2}{2\pi G r^2} \tag{1.2}$$

The r^{-2}-dependence in Eq. 1.2 also explains the velocity distribution observed in galactic rotation curves. To be able to compare the measurement results of different experiments, usually a common value for the DM density ρ_0=0.3 GeV c^{-2} cm^{-3} is used, albeit newer measurements suggests a value of ρ_0=$0.46^{+0.07}_{-0.08}$ GeV c^{-2} cm^{-3} [10, 26].

The velocity of the particles in this isotropic halo are assumed to follow a Maxwellian distribution [10]:

$$f(\vec{v}) = N \cdot exp\left(-\frac{3|\vec{v}|^2}{2\sigma(R)^2}\right) \tag{1.3}$$

Formally, the velocities in the distribution can reach infinite values. In reality, there is a threshold velocity where the particles are no longer bound by the gravitational field. For the Milky Way galaxy this velocity is found to be $v_{esc} \simeq 544\,\mathrm{km\,s^{-1}}$, based on measurements of the fastest observed stars [27].

$\sigma(R)$ is the velocity distribution around a mean velocity v_M at a certain distance R from the center of the galaxy. For the position of earth at a distance of approximately 8 kpc from the center, this results in a radial velocity v_M=220 km s^{-1}. The significantly larger value of the escape velocity v_{esc} when compared to the orbital velocity of the Sun suggests a large amount of mass outside the solar orbit which agrees with the assumption of a DM halo.

In the case of an interaction between a WIMP and a nucleus, the energy is transferred via elastic scattering. From kinematics one can derive the nuclear recoil (NR) energy E_R transferred to the target nucleus:

$$E_R = \frac{\mu^2 v_\chi^2}{m_N}(1 - cos\,\theta_R) \tag{1.4}$$

where $\mu = \frac{m_\chi m_N}{m_\chi + m_N}$ is the reduced mass (with m_χ is the WIMP mass and m_N the mass of the nucleus) and θ_R the recoil angle.

From this the minimal velocity v_{min} necessary for a recoil energy E_R can be calculated:

$$v_{min} = \sqrt{\frac{E_R m_N}{2\mu^2}} \tag{1.5}$$

The expected interaction rate of WIMPs scatter of target nuclei is given by:

$$\frac{dR}{dE_{nr}} = \frac{M}{m_N} \cdot \frac{\rho_0}{m_\chi} \int_{v_{min}}^{v_{esc}} v f(v) \frac{d\sigma}{dE_R} dv \tag{1.6}$$

where M is the total target (detector) mass, ρ_0 the local DM density of $0.3\,\mathrm{GeV\,c^{-2}\,cm^{-3}}$ (see Eq. 1.2), and $f(v)$ the velocity distribution (see Eq. 1.3). Based on Eq. 1.7 the event rates for different detector materials can be calculated. The result for some example materials are shown in Fig. 1.4.

Another effect that needs to be considered is the size and the substructure of the target nucleus. For small momentum transfers of a WIMP interaction, the deBroglie wavelength can be calculated to be in the order of pm. This is much larger than the diameter of even heavy target nuclei like, for example, xenon, which can be approximated with $d \approx (2.5\,fm)A^{1/3}$, where A is the atomic number. In this case, the internal structure of the nucleus is not resolved and the WIMP scatters coherently of the nucleus.

With an increasing momentum transfer, the deBroglie wavelength decreases until parts of the nucleus are resolved, and as such the coherence is lost. To account for this the form factors of the nucleus have to be taken into account. The (recoil-)energy and velocity dependent WIMP-nucleus cross section is then given by:

$$\frac{d\sigma}{dE_{nr}} = \frac{m_N}{2v^2\mu^2} \left(\sigma_{SI} F_{SI}^2(E_{NR}) + \sigma_{SD} F_{SD}^2(E_{NR})\right) \tag{1.7}$$

where σ_{SI} and σ_{DI} are the basic cross-sections for spin-independent (SI) and spin-dependent (SD) interactions and F_{SI}^2 and F_{DI}^2 are the corresponding form factors to account for the structure of the nucleus [28]. This is also especially relevant for heavy and large nuclei. The SI cross section is given by:

$$\sigma_{SI} = \frac{4\mu^2}{\pi} \left[Z \cdot f_p + (A - Z) \cdot f_n\right]^2 \propto A^2 \tag{1.8}$$

where μ is the reduced mass of the WIMP-nucleus system and f_p and f_n are the WIMP-proton and WIMP-neutron coupling factors [28]. If the SI is fundamentally at the quark/gluon level, protons and neutrons might be similar and $f_p \sim f_n$ can be assumed. Therefore the cross-section scales with A^2, indicating that with the use of heavier target nuclei as a detection medium, the interaction rates can be expected to be higher. This however comes at the cost of a higher detection threshold, as the expected recoil energy is also smaller for heavier nuclei, see Fig. 1.4.

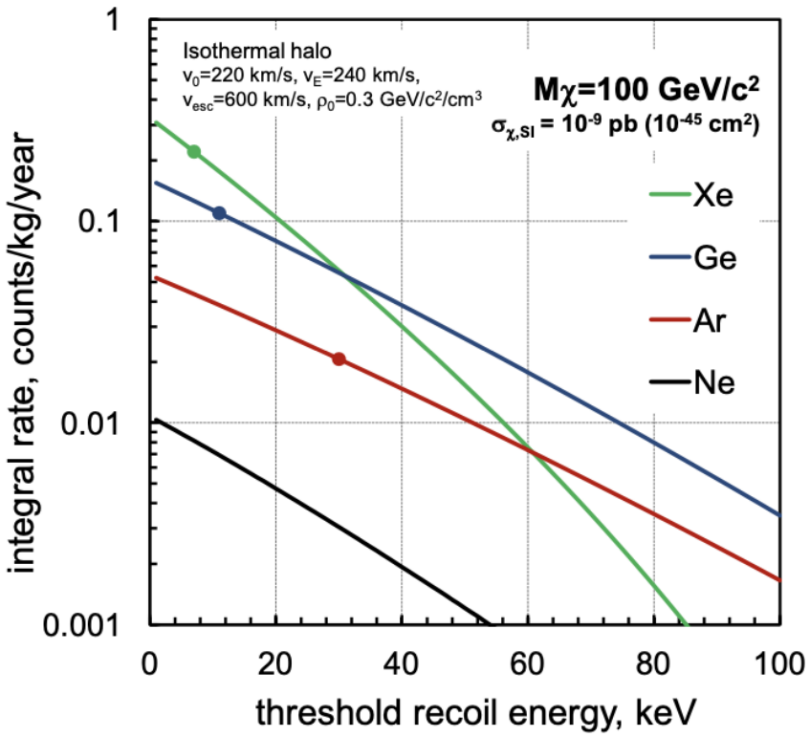

Figure 1.4.: *Event rates for different detector materials in events per kg per year in dependence of the energy. Xenon achieves the highest rates for low energy interactions. Figure taken from [29].*

In case of a SD interaction, where the WIMP couples to unpaired nuclear spins, the cross section is given by:

$$\sigma_{SD} = \frac{32 G_F^2 \mu^2}{\pi} \frac{J+1}{J} \left[a_p \langle S_p \rangle + a_n \langle S_n \rangle \right]^2 \tag{1.9}$$

where J is the nuclear angular momentum, a_p/a_n the proton/neutron couplings, and $\langle S_p \rangle / \langle S_n \rangle$ the expectation values of the resulting proton/neutron spins, respectively [28]. This can lead to very different cross-sections of nuclei with different compositions of protons and neutrons, but similar atomic numbers, compared to the simple relation of a SI interaction given in Eq. 1.8.

No WIMPs have been detected so far, so current experiments can only exclude certain parameter ranges. These are based on a fixed DM density and the measurement time of the experiment. XENON1T for instance can exclude SI WIMP-nucleon cross-sections larger $\sigma_n > 4 \cdot 10^{-47}\,\mathrm{cm}^2$ for particles with a mass of approximately $30\,\mathrm{GeV}/c^2$ [30]. Generally DM search results are presented in exclusion plots, which show the lowest sensitivity limit of an experiment. An example including the exclusion limits from various experiments is given in Fig. 1.5.

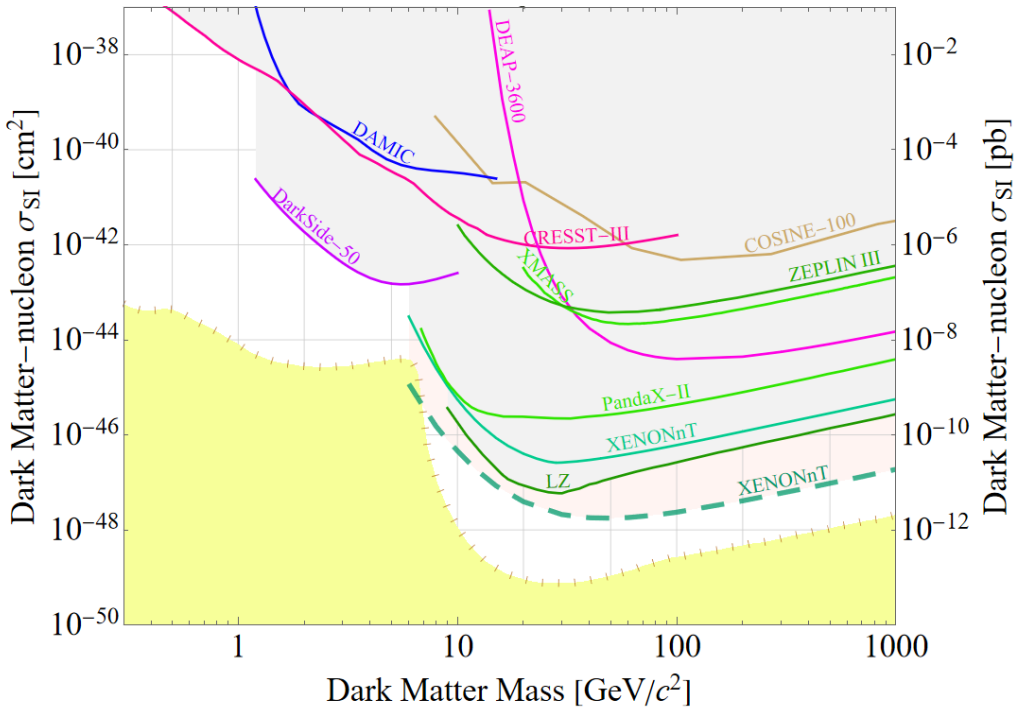

Figure 1.5.: *Exclusion limits for spin-independent nuclear recoils achieved for multiple experiments. The results are scaled to a local DM density of 0.3 GeV/c^2. The solid lines are exclusion limits, the dashed line for XENONnT is a projection for the expected sensitivity for a 20 ty exposure. Plot created with [31] v5.18.*

Direct detection experiments can be realized with various methods, utilizing a variety of detection materials. Possible detection channels are shown in Fig. 1.6. These include light detection of scintillation light, ionization, and heat. Depending on the detector type, one or two of these three detection channels are used for particle detection.

1.7. Experimental realisation of Dark Matter searches

This chapter gives an overview of the most facilitated experimental setups used in the hunt for DM, but it should not be considered a complete list. A more thorough list with more detailed explanations for the various experiments is given in [24].

Direct detection experiments can be realized with various methods, utilizing a variety of detection materials. Possible detection channels are shown in Fig. 1.6. These include the detection of scintillation light, ionization, and phonons/heat. Depending on the detector type, one or two of these three detection channels are used for particle detection.

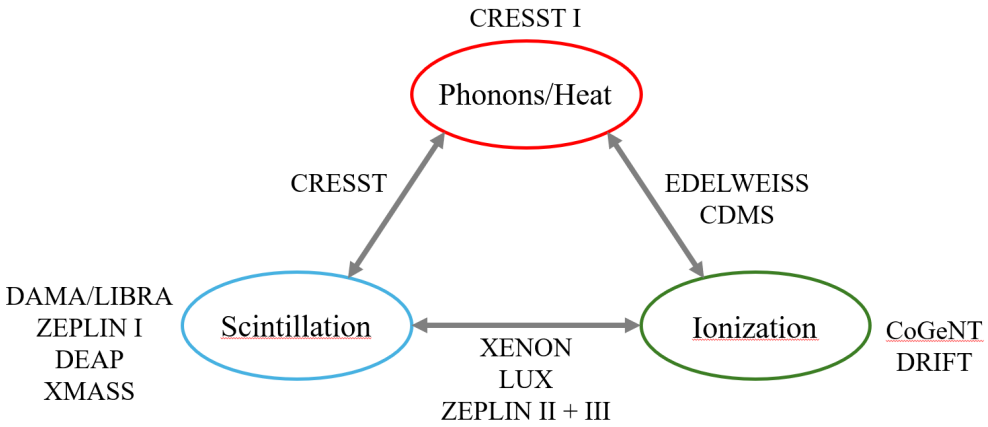

Figure 1.6.: *Possible detection channels used by various direct DM detection experiments.*

Typical detection devices used in DM search are inorganic scintillator crystals made of thallium doped NaI or CsI. The high density of these materials provides a high stopping power and therefore detection efficiency. The thallium-doping adds luminescence centers, increasing the light emission and additionally shifting it to higher wavelengths, which allows for more efficient detection. This is particularly important as only the scintillation signal is acquired from this type of detector [24]. One experiment facilitating NaI(Tl) is the DAMA/LIBRA experiment, which claims an annual-modulated single-hit detection [32]. Similar experiments like SABRE, COSINUS (both in preparation) [33, 34] and ANAIS-112 are using the same type of highly pure NaI(Tl) crystals, trying to reproduce the findings of DAMA/LIBRA, with first ANAIS-112 results already being inconsistent with DAMA/LIBRA [35].

Cryogenic bolometers are crystalline detectors that collect the phonon signals caused by an energy deposition of a collision with a particle and provide excellent energy resolution. The crystals, usually made of germanium or silicone, are usually cooled down to temperatures in the order of 10 mK. An energy deposit results in a temperature rise in the order of μK, which can be detected with an attached transition edge sensor, that is usually operated in the transition between conducting and superconducting state. In this state a small change in temperature results in a large change in resistivity, which can easily be measured. This phonon signal is proportional to the deposited energy. Additionally, the scintillation or charge signal can be collected, allowing also to discriminate between nuclear and electronic recoil. The germanium/silicon crystal-based CDMS series of experiments as well as the germaniumcrystal-based CoGeNT are examples of experiments that utilize this type of detector [24].

Another very important class of DM detector utilizes liquefied noble gases. Typically these detectors are based on xenon or argon, as they are excellent scintillators. A particular de-excitation mechanism after an energy deposit, which includes the formation of an excimer state ensures a high transparency of these gases for their own scintillation light. The light is emitted at wavelength 128 nm and 178 nm for argon and

xenon respectively. As the argon scintillation wavelength is deep in the UV regime, so usually wavelength shifting is required for efficient detection, while for xenon sensitive photocathod-materials for PMTs are available. As both elements are used in a gaseous/liquid state, detectors can relatively easily scaled up to larger volumes/masses to increase sensitivity, while this is much harder to achieve for semiconductor-based detectors, as the achievable crystal size is usually limited. These properties also apply to krypton, but compared to argon and xenon krypton contains several unstable isotopes which result in a high material-internal background.

Liquid argon is used in the DEAP-series of experiments [36], and more recently the DarkSide experiments facilitating dual-phase TPCs [37, 38]. Xenon in the liquid and gaseous phase is used in the dual-phase TPCs of the XENON- and LUX/ZEPLIN collaborations. More details on the scintillation processes and the working principles of dual-phase TPCs, focused on the use of xenon, are explained in the following chapter.

2. The XENON1T detector

In this chapter, the XENON1T experiment is presented. It is the largest underground laboratory and is located in Italy, at the Laboratori Nazionali del Gran Sasso (LNGS) below the Gran Sasso mountain. The experimental halls are covered by 1400 m of rocks, providing shielding equivalent to about 3600 m of water [39]. This location provides sufficient shielding to run low-background experiments. Besides the series of XENON experiments also other experiments searching for DM are located in the experimental halls, including NiI(Tl) scintillator-based detectors like DAMA/LIBRA or SABRE and COSINUS, which both try to verify the DAMA/LIBRA results [40, 41, 42]. Contrary to other underground laboratories it was built beside a highway tunnel and as such can easily be reached by car.

As the name suggests, XENON1T utilizes the noble gas xenon as a detection medium. Section 2.1 summarizes its physical properties. Also, the interaction mechanisms which convert the energy deposited in an interaction into a detectable signal are explained. The Doke plot, which allows the determination of the photon and electron gain of the detector from different sources, is introduced in section 2.3. Section 2.2 explains the working principle of the XENON1T TPC. The PMTs and their properties are briefly discussed in section 2.4, as it was found that the afterpulses that can occur after the initial signal play an important role later in the analysis of the ^{37}Ar data. Section 2.5 shortly explains the purification system with a focus on the cryogenic distillation, a critical component in background reduction and in the removal of ^{37}Ar after calibration. Additional methods and measures to further reduce background are summarized in 2.6. The following section 2.7 gives a short summary of how the individual PMT signals are combined into the events later used in the analysis. The signals combined into events need to be processed further to correct them for spatial and field effects, which can alter signal position and size. This process is explained in 2.8.

2.1. Xenon as detection medium

Physical properties

The XENON1T detector utilizes liquefied xenon in its natural abundance as the detection medium. Natural xenon consists of 9 different isotopes, of which 7 are stable and 2 are unstable, but with extremely long half-life times larger than 10^{21} years. Due to these properties, xenon is a detector medium with very low intrinsic radioactivity, making it well suited for the use in a low event-rate detector. It should be mentioned

that the presence of different isotopes, and also with different spin configurations, offer additional measurement channels [43, 44]. This will, however, not be further followed up in this work. An overview of the isotopic composition is shown in Table 2.1.

Xenon has a relatively high boiling temperature compared to other noble gases. At a pressure of one standard atmosphere, xenon is liquid in a very narrow temperature window between 162 K and 165 K. Xenon liquefaction, however, can be achieved much easier than, for instance, argon, which is operated in detectors with a similar purpose, but requires cooling to much deeper temperatures. A phase diagram of xenon can be found in Fig. B.1 in the appendix on page 193.

Isotope	Abundance	$T_{1/2}$
^{124}Xe	0.09 %	$1.8 \cdot 10^{22}$ y
^{126}Xe	0.09 %	stable
^{128}Xe	1.92 %	stable
^{129}Xe	26.44 %	stable
^{130}Xe	4.08 %	stable
^{131}Xe	21.18 %	stable
^{132}Xe	26.89 %	stable
^{134}Xe	10.44 %	stable
^{136}Xe	8.87 %	$2.165 \cdot 10^{21}$ y

Table 2.1.: *Composition of natural xenon as it is used in the XENON1T experiment [45].*

Interaction properties

In the case of an interaction, energy is deposited in the liquid xenon, leading to the excitation or ionization of xenon atoms at the interaction site. Some energy is also lost in the form of heat to secondary recoils and so-called sub-excitation electrons. The energy is considered lost as these effects can not be detected with a TPC, the type of detector this work focuses on.

The relaxation/recombination of the excited/ionized atoms does not happen directly from atomic xenon. Instead, the excited atoms form so-called excimers (short for excited dimers), excited pseudo molecules, with nearby neutral atoms. These excimers then decay back into 2 neutral xenon atoms under the emission of a photon:

$$\begin{aligned} Xe^* + Xe + Xe &\longrightarrow Xe_2^* + Xe \\ Xe_2^* &\longrightarrow 2Xe + h\nu \end{aligned}$$

In the case of ionization, a charged excimer is formed, recapturing an electron into a higher excited state. In the first de-excitation process, heat is emitted. Thereafter it follows the same process chain as in the excited case:

$$\begin{aligned} Xe^+Xe &\longrightarrow Xe_2^+ \\ Xe^+e^- &\longrightarrow Xe^{**} + Xe \\ Xe^{**} &\longrightarrow Xe^* + heat \\ Xe^* + Xe + Xe &\longrightarrow Xe_2^* + Xe \\ Xe_2^* &\longrightarrow 2Xe + h\nu \end{aligned}$$

The photons emitted from the excimers are in the VUV regime at a wavelength of 177.6 nm. The fact that the photon is emitted from an excited state of the excimer and not from the atomic shell is essential, as this intermediate step is the reason for the high transparency of xenon for its own scintillation light.

The light curve from this excimer de-excitation is composed of two different components. A fast component from the decay of an excited singlet state and a slow one from an excited triplet state of the excimer, with decay times of around 4 ns and 22 ns, respectively. These two components are present for interactions with for instance an α-particle, while a relativistic electron only has one decay time component, which is around 45 ns (see also Fig. B.2 in the appendix on page 194). In theory, this allows particle discrimination via pulse shape analysis, it is however hard to realize for xenon due to the very short decay times [45].

The distribution of the energy between the three mentioned channels is primarily dependent on the incident particle [46]. The incident energy E_0 is distributed between the different channels, which can be described with the Platzman equation [47, 48]:

$$E_0 = N_i E_i + N_{ex} E_{ex} + N_\epsilon \epsilon \tag{2.1}$$

The energy is distributed between N_i ionized atoms with an average energy deposit of E_i, N_{ex} excited atoms with an average energy deposit of E_{ex} and N_ϵ sub-excitations electrons (electrons which fail to produce S1 signals), which cannot be detected.

The number of photons gained from an interaction is given by:

$$N_{ph} = N_{ex} + r \cdot N_i \tag{2.2}$$

while the number of freed electrons is given by:

$$N_e = (1 - r) \cdot N_i \tag{2.3}$$

With r being the recombination probability for the ionized atoms. In case of no recombination, the mean energy needed to create an electron-ion pair is given by:

$$W_q = \frac{E}{N_i} \tag{2.4}$$

In case of full recombination the mean energy to create a photon is given by:

$$W_{ph} = \frac{E}{N_i + N_{ex}} \tag{2.5}$$

With Eq. 2.4, this can also expressed as:

$$W_{ph} = \frac{W_q}{1 + N_{ex}/N_i} \tag{2.6}$$

W_{ph}, in the following only W, is the working function that represents the mean energy to create either a photon or to free an electron. When measured, this value also incorporates the energy lost to sub-excitations and heat, which are still present in Eq. 2.1. Therefore the measured value for W is generally larger than the actual mean energy needed to create an excited stated or ion-pair, as defined in Eq. 2.6. The conventional value of the work function is $W = 13.7 \pm 0.2\,eV$ [46]. This value is generally used in the publications of the XENON collaboration as well as in other liquid xenon TPC based experiments like PandaX-4T and LZ [49, 50]. Newer measurements found a lower value at $W = 11.5^{+0.2}_{-0.3}\,eV$ [51, 52]. To keep the results comparable with XENON publications, $W = 13.7\,eV$ is used in this work.

The total number of quanta generated is $N_q = N_{ex} + N_i$. The Platzman equation can be rewritten as:

$$E_0 = W \cdot N_q \cdot \frac{1}{L} \tag{2.7}$$

The factor $L \in [0, 1]$ is a quenching factor which depends on the type of the incoming particle, which in turn defines the interaction type. Incoming photons can interact via photoeffect, Compton scattering, or pair production (depending on the energy of the incoming photon). These interactions happen with the electrons in the xenon electron shell and therefore are called electronic recoil (ER). The same accounts for interacting electrons (from a β-decay, for example). If the incoming particle interacts with the nucleus instead, which is the case, for example, for neutrons, the interaction is called a NR. For dark matter candidates WIMPs are expected to be detected in the NR channel, while axions are expected to interact via ER.

A NR is usually accompanied by a lot of secondary interaction between neighboring atoms in the liquid. These are, however, so low in energy that they cannot be detected and as such, similar to the heat channel, this energy is lost for the measurement. Therefore, for a NR, the energy measured is significantly lower than for an equal ER deposit, which is described by the Lindhard effect and incorporated into the quenching factor L [47, 53]. In the case of an ER this factor can be considered to be $L = 1$.

When an electric field is applied, the freed electrons from ionization are drawn away from the interaction sites and can be measured separately, but at the cost of reducing the number of recombination photons.

This effect, called scintillation quenching [45], is described by a change in the recombination probability r (used in equations 2.2 and 2.3) as follows:

$$r = 1 - \frac{ln(1 + N_i\xi)}{N_i\xi} \tag{2.8}$$

r can be calculated using the Thomas-Imel box model, which assumes an uniform distribution of electron-ion pairs in a certain volume (the 'box') alongside the interaction track, and that they are isolated from each other (assuming the range of the Coulomb force between the electron and ion is smaller than their spacing) [54]. The field dependent parameter ξ can be written as a power law:

$$\xi = \gamma\mathcal{E}^{-\delta}, \tag{2.9}$$

where γ and δ are empirical parameters [55].

Besides the field, the linear energy transfer (LET) influences the ratio between produced photons and electron-ion pairs. The LET is equivalent to the stopping power and is effectively the loss of energy per unit length dE/dx. Particles undergoing a NR like neutrons or WIMPs leave a track with a higher ionization density, e.g., a higher LET, than electrons or photons interacting via an ER. Intuitively the ionization density affects also the recombination probability, as a higher density increases the probability of recombination of electron ion pairs. This directly opens a discrimination channel, as for a NR signal a smaller charge signal is to be expected than for an ER interaction of the same energy.

The LET is expected to increase with decreasing energy of the incident particle, for instance, for electrons below 1 MeV [56]. Therefore an increase of the photon yield is expected for decreasing particle energies. Instead, for xenon it is observed, that the photon yield becomes independent for energies below O(100 keV) or even decreases for energies below O(10 keV). This is shown in Fig. 2.1 for different applied drift fields and NR and ER interactions.

Fig. 2.1 also shows the charge yields, the number of electrons created. The total number of quanta $N_q = N_e + N_{ph}$ is only dependent on the energy deposit of the incident particle, the type of interaction [ER, NR], and the mean energy W. As this total number of quanta needs to be constant, but the ratio of created photons and electrons is field-dependent, the photon and charge yield are highly anti-correlated. Therefore an increase of field strength to enhance the charge signal would decrease the light signal and vice versa.

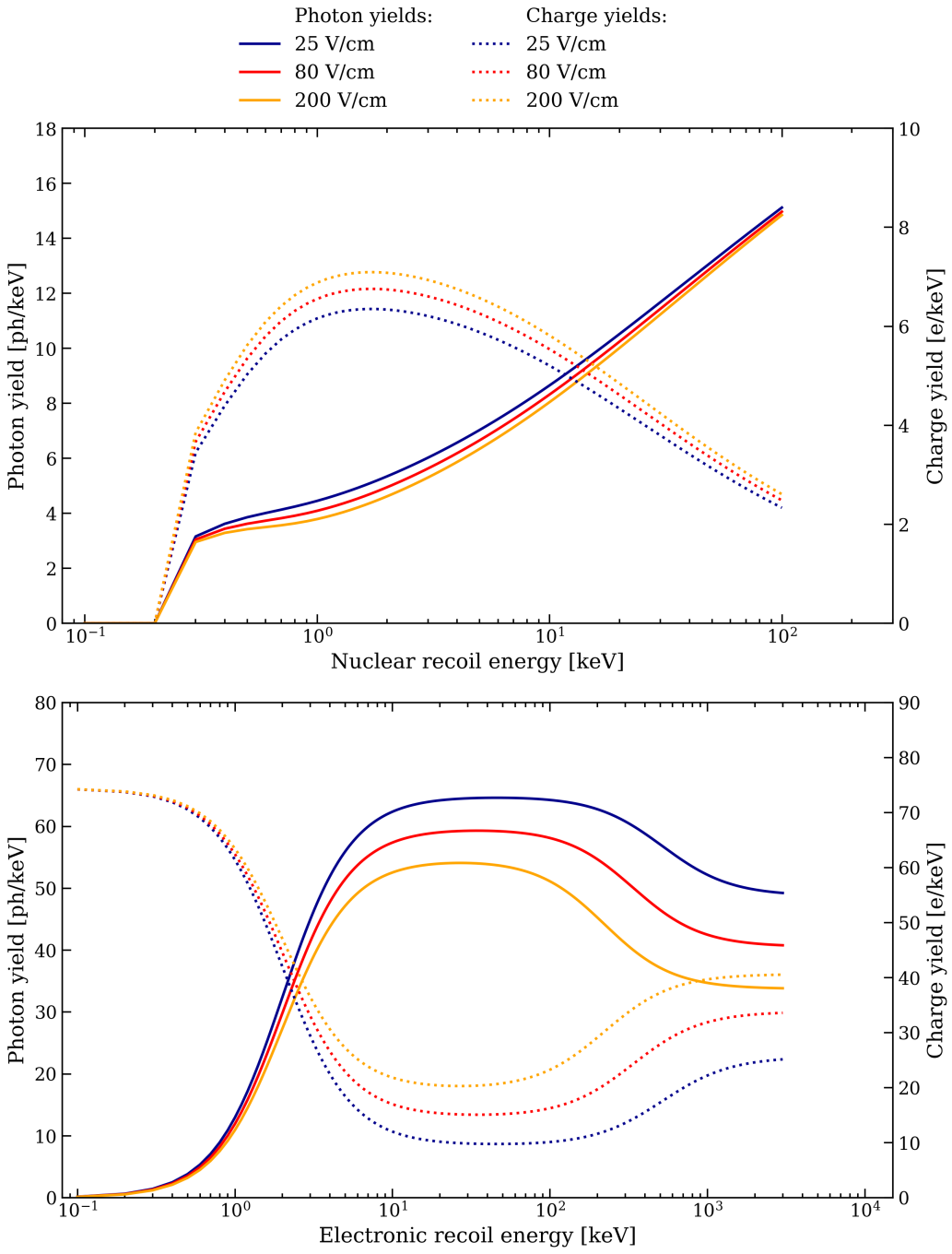

Figure 2.1.: *Charge and light yields in xenon in dependence on the interaction energy for nuclear and electronic recoils in the top and bottom plot, respectively. The different colors show the behaviours for different applied drift fields. The red line shows the yields at a field of 80 V/cm, which represents the field applied in XENON1T data used for this work. The yields were obtained using Nestpy version 2.0.0.*

2.2. Working principle of the XENON1T TPC

The XENON1T detector is a so-called dual phase liquid xenon (LXe) TPC. The dual-phase designation refers to the fact that the detection medium xenon is present in its liquid and gaseous state. As shown in Fig. 2.2, the detector has a cylindrical shape with a diameter of 96 cm and a height of 97 cm. Two arrays of PMTs, facing the lower and upper end of the cylinder, are used for light detection.

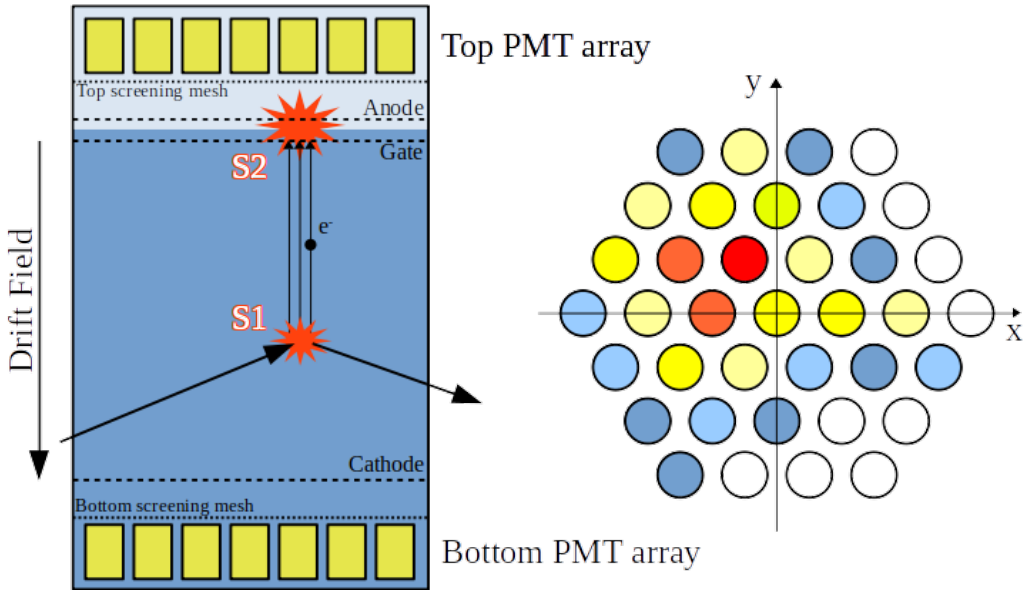

Figure 2.2.: *The working principle of a time projection chamber is shown on the left. An incoming particle interacts with the xenon and creates excited and/or ionized atoms. Recombination of electrons with ions and relaxation of excited states creates the prompt scintillation signal S1. Part of the freed electrons are drifted by the applied drift field to the gate and subsequently extracted into the gas phase by the applied extraction field, creating the secondary scintillation signal S2. The z-component of the interaction point can be derived from the time difference between the S1 and S2 signals (drift time of the electrons). The right scheme shows a simplified example pattern on a PMT array which can be used to extract the x-y-position of the interaction to achieve full 3D-position reconstruction.*

In total 248 PMTs in two arrays are used for signal readout. The PMT-array at the top is instrumented with 127 PMTs, the one at the bottom with 121 [39, 57]. At the bottom of the detector and with a distance of 5 mm to each other just below and above the liquid-gas interface three meshes are used to apply an electrical field throughout the detector. The drift field with a strength of 82 V/cm is applied between the cathode mesh at the bottom of the TPC and the gate mesh just below the liquid-gas interface. Above, between the gate mesh and the anode mesh, an even higher voltage is applied to create the extraction field with a field strength of 8.1 kV/cm [58]. Additional meshes are placed in front of both PMT arrays, acting as shielding to protect the photo

sensors. Between the gate and anode mesh, the sensitive volume of the detector is surrounded by copper rings, forming a field cage to ensure a homogeneous drift field. To increase the light collection efficiency, all surfaces not equipped with light sensors are covered with PTFE (polytetrafluoroethylene, Teflon™), which features a very high reflectivity in the VUV wavelength regime.

The detection process of an interaction is sketched in Fig. 2.2, based on the interaction properties of xenon described in Section 2.1. After an energy deposit, recombination and relaxation of the xenon leads to the emission of a prompt scintillation signal, called *S1*. Due to the applied drift field, freed electrons are drifted upwards, where they are extracted into the gas field and accelerated by the extraction field. The energy gained by the extraction field allows every electron to excite a certain number of xenon atoms in the gas phase, leading to a direct proportionality between the number of extracted electrons and produced photons. These photons are detected as the secondary scintillation signal *S2*.

The S2 signal creates a light pattern on the top PMT array which allows for a position reconstruction in the x-y-plane. Additionally, the drift velocity in xenon is known for the applied drift field. With this velocity and the time difference measured between the S1 and the S2 signals, the depth of the interaction can be calculated.

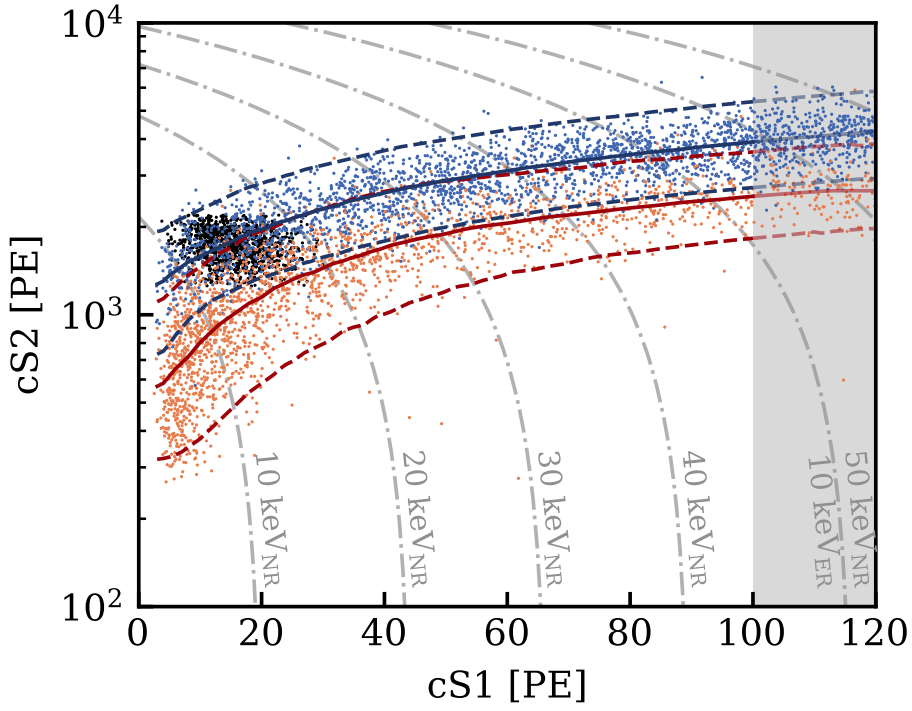

Figure 2.3.: *Separation of ER (blue) and NR (orange) events due to different S1-S2 ratios, shown on data from XENONnT. The separation gets stronger for a stronger applied drift field. Also the ^{37}Ar data (black) from the first calibration in XENONnT is shown, being in the ER-band as expected. Figure taken from [59].*

This allows a completed 3D reconstruction of the position where the interaction took place. This powerful advantage of the TPC type of detector helps in background reduction, as it is explained later in Section 2.8.

Another powerful feature of the TPC is the power to distinguish between interaction types. As explained previously in section 2.1, the different interaction types, ER and NR produce signals with a different S1-S2 ratio for a given field. Fig. 2.3 shows the different S1-S2 ratios for the different interaction types, allowing the discrimination between ER and NR.

Neutrons, since electrically neutral, also interact with the nucleus producing a NR signature, similar to the one expected from a WIMP. A part of their interactions can be filtered by identifying multi-scatter events, as this can occur for neutrons, but this is most unlikely for WIMPs due to their expected low interaction cross-section.

2.3. Determination of detector specific photon and electron gain factors utilizing the Doke plot

As explained in 2.1, the interaction energy of an incoming particle with the xenon is distributed between scintillation photons n_{ph} and ionization electrons n_e, depending on the applied drift field. For the XENON1T detector, a linear response in energy is expected. This is given by the detector-specific photon and electron gains g_1 and g_2, respectively. The detector signals are designated as S1 and S2 for the light and charge signal, respectively. The relation between the number of photons/electrons and the detector signals S1/S2 is then given by:

$$E = W \cdot (N_{ph} + N_e) = W \cdot \left(\frac{cS1}{g_1} + \frac{cS2}{g_2} \right) \tag{2.10}$$

The 'c' in front of the detector signals S1/S2 indicate that the signals are already corrected for certain effects induced by the detector. This is discussed in more detail in Section 2.8.

With the expressions for light and charge yield, L_y and Q_y:

$$L_y = \frac{cS1}{E} \tag{2.11}$$

and

$$Q_y = \frac{cS2}{E}, \tag{2.12}$$

equation 2.10 can be rewritten as:

$$Q_y = \left(-\frac{g_2}{g_1} \cdot L_y + \frac{g_2}{W} \right). \tag{2.13}$$

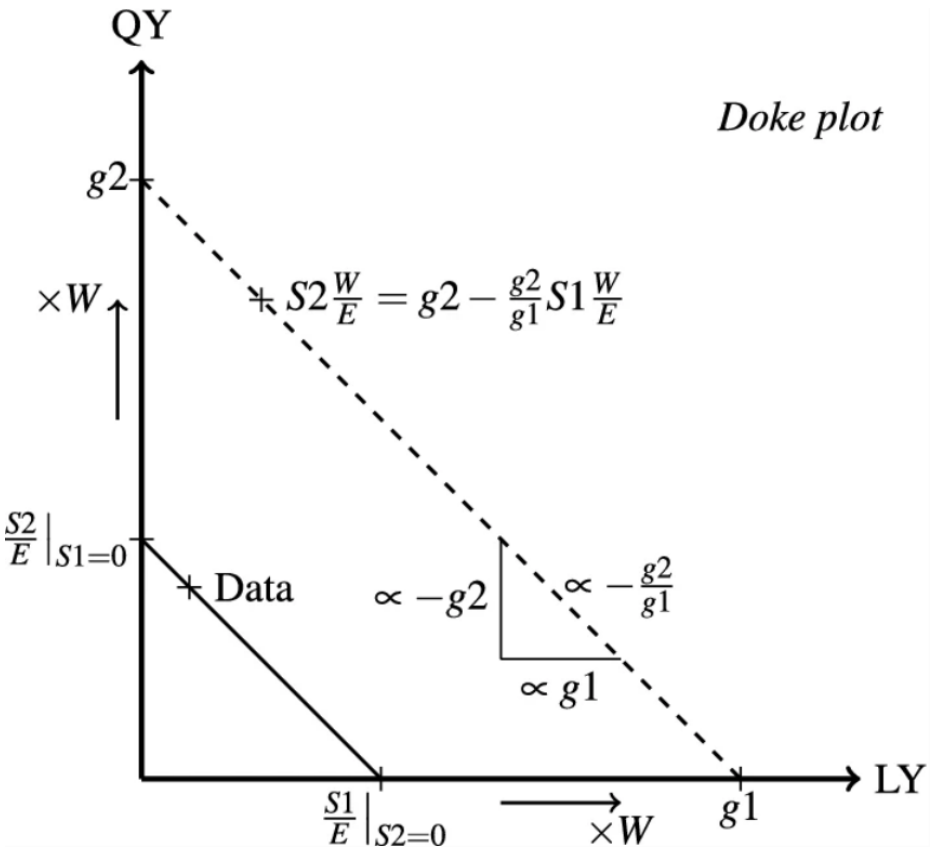

Figure 2.4.: *Schematic of a so-called Doke plot. The charge yield is plotted versus the light yield. Due to the anti-correlation between the two parameters, a negative slope is expected. In the case of XENON1T, a linear relation is expected for sources with different line energies (at the same field). The solid and the dashed line show the same light and charge yield values, but scaled with a different value for W, which can also be determined with this plot. Figure taken from [51].*

In the so-called *Doke* plot, the charge yields Q_y are plotted against the light yields L_y. From this plot, the detector-dependent gain properties g1 and g2 can be obtained as shown in Fig. 2.4. This can be achieved in two ways: the same source can be used at different field settings or various sources with different line energies can be used at the same field. This type of plot can also be used to extract the value of the working function W, as it is done in [51].

In the analysis, additionally to the designated calibration sources, even some sources that are designated as background in DM search are used. This allows for a wider energy range to be probed and thus for a wider energy range in which linearity can be verified.

2.4. Photo multiplier tube properties

The light signals in the TPC are detected using 248 PMTs distributed in two arrays at the top and at the bottom of the TPC. XENON1T used circular R11410-21 PMTs from Hamamatsu with a diameter of 3 inches. These PMTs are of the so-called head-on type: the entry quartz window is followed by the photocathode, the dynode arrangement, and the anode, which collects the electrons. A scheme of a typical PMT is shown in Fig. 2.5. PMTs of the same type are also operated in similar other experiments using liquid and gaseous xenon, including PandaX [50] and NEXT [60].

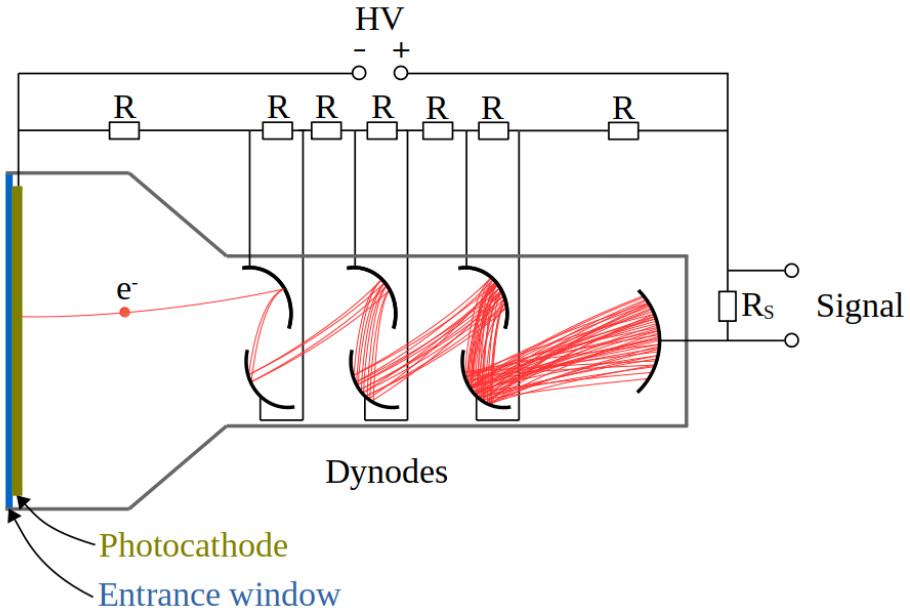

Figure 2.5.: *Schematic of a PMT, showing the working principle. The supply voltage is applied between the photocathode and anode. A voltage divider chain supplies intermediate voltage steps to the dynodes. If a photon hits the photocathode, photoelectrons are emitted and accelerated towards the first dynode. There secondary electrons are produced which are accelerated towards the next dynode, producing even more electrons and so on. In the last step the electron cloud is collected by the anode, and the voltage drop over the resistor R_s can be read out as a signal. The gain of the PMT is given by the total electron multiplication factor between the photocathode and anode. Depending on requirements, they can be operated with positive or negative HV.*

The R11410 PMTs are specifically designed for low-background applications as the search for DM. Besides a high radio purity, a high quantum efficiency (QE) at the xenon scintillation wavelength of 178 nm, and a stable operation at liquid xenon temperatures are required. All PMTs used in XENON1T were tested and characterized thoroughly before they were used in the experiment [61]. In these tests the most important quantities to evaluate PMT performance like QE, gain, dark count rate, and afterpulse rate are determined.

In the analysis later presented, it was found that the PMT afterpulses (APs) have a significant impact on the analysis of the ^{37}Ar events and therefore on all low energy events in general. APs occur when residual gas atoms in the vacuum are hit by electrons that drift from the photocathode to the first dynode. When they are ionized they drift towards the photocathode where they can produce secondary electrons creating a second signal after the initial one. The time difference between the primary signal and AP even allows identification of the contaminations. These contaminants primarily originate from tiny leaks, allowing the surrounding gases, in our case xenon, to slowly leak into the vacuum of the PMT. This was also analyzed in more detail in [61], resulting in Fig. 2.6, which shows the AP timings for different contaminants in a PMT after operation in liquid xenon.

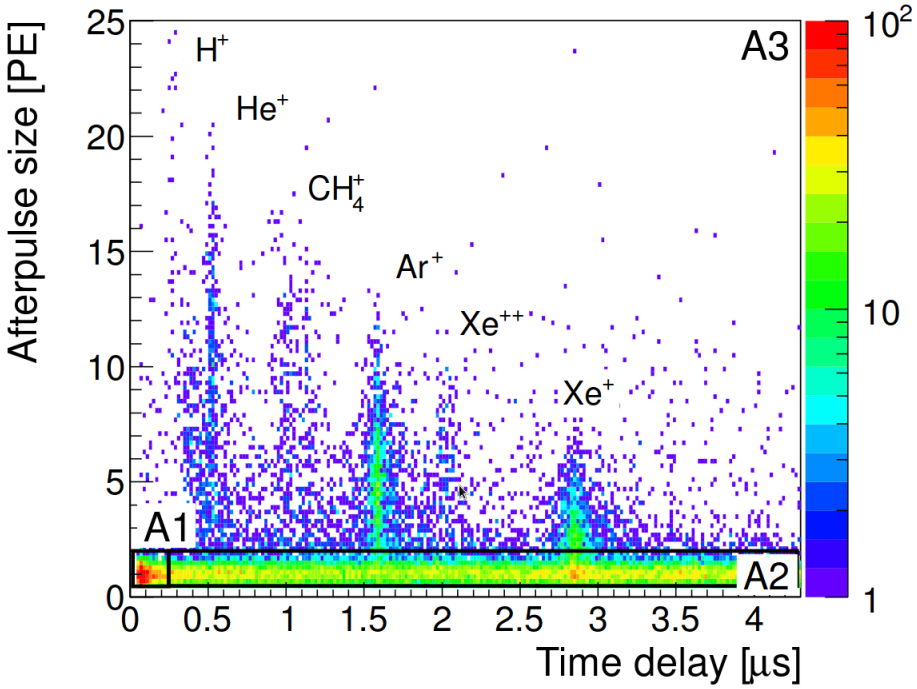

Figure 2.6.: *Afterpulse timing for different contaminants in the tested PMT. These contaminants can enter the PMT through tiny leaks and therefore depend highly on the environment the PMT is operated in. As expected for the PMTs used in XENON1T, xenon is responsible for a significant amount of the recorded afterpulses. The figure is taken from [61].*

2.5. Gas recirculation and purification system

General overview

The operation of the XENON1T detector requires a complex infrastructure to keep stable temperature and purity levels. The system used in the XENON1T experiment, the gas recirculation and purification system, is housed in a 3-story building next to

the detector. Fig. 2.7 shows a (very) simplified schematic with the most important components of the system.

When the detector is not in operation the xenon is stored in ReStoX (short for **Re**covery and **Sto**rage of **X**enon). It is a spherical storage facility, using liquid nitrogen to cool down, condense, and freeze xenon. It is capable to store up to 7.6 tons of xenon at room temperature at a pressure of 72 bar [62]. The storage capability was slightly too low for the next phase of the XENON experiments, XENONnT, which contains in total about 8 tons of xenon. Therefore a second storage device ReStoX II was added to the system.

The source box contains the intrinsic calibration sources used in XENON1T. It contains the ^{83m}Kr and the ^{220}Rn source used in the calibration of the XENON1T-TPC. The ^{37}Ar calibration hardware needed will also be connected in this place to the recirculation system. This is described in more detail in chapter 3.3.2.

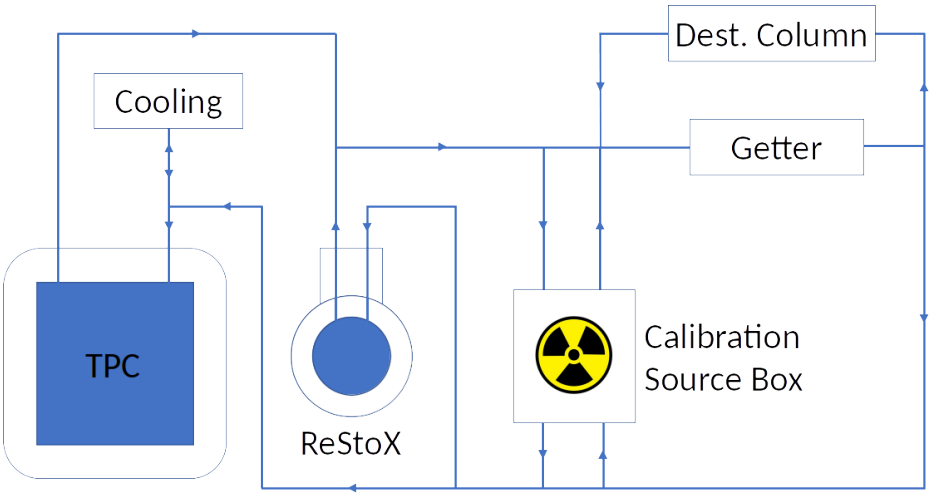

Figure 2.7.: *Very simplified schematic of the XENON1T gas system showing the most important subsystems and the interconnections. The most important components for this work, besides the TPC, are the calibration source box, where the ^{37}Ar will be added to the system, and the distillation column, which is needed to remove the ^{37}Ar after the calibration.*

Krypton distillation column

One subsystem is of particular interest for this work: the krypton distillation column, initially designed to remove the long-living, background-producing isotope ^{85}Kr. The distillation column takes advantage of different vapor pressures of the components of a mixture to separate them.

Simplified, the column consists of a condenser at the top to liquefy the gas mixture and a boiler at the bottom to evaporate it. The more volatile components are enriched in the gas phase at the top of the column, while the less volatile are accumulated in the liquid phase at the bottom. In XENON1T, the column is operated at liquid xenon

temperatures, with the different parts of the column ranging in temperature between -92.5 °C and -97.7 °C at pressures between 2.6 bar and 1.9 bar, respectively.

The polluted xenon gas is injected in between the condenser and re-boiler, the clean xenon is taken at the bottom from the liquid, while the contaminants (with higher volatility) are enriched in the gas phase at the top. The pollution-enriched gas, called the off-gas, is then taken from the top and removed from the system. The system is designed in a way, that only about 1 % of the input is lost as off-gas, which is recuperated as Kr-enriched Xe-gas in a bottle.

A measure of the effectiveness of depletion/enrichment in the gas phase is given by the relative volatility α, derived from Raoult's law:

$$\alpha = \frac{P_{contaminant}}{P_{Xe}} \tag{2.14}$$

Table 2.2 provides the vapor pressures of relevant noble gases and their relative volatilities with respect to xenon. The column has proven to effectively remove ^{85}Kr from the xenon. As the relative volatility of argon is even higher, it was expected to be removed with even higher efficiency. This was tested in the first calibration of XENON1T with ^{37}Ar at the end of XENON1T operation. The analysis of the ^{37}Ar distillation is shown in Chapters 3.4.4 and 4.2.

The information summarized in this section is presented in greater detail in [63, 64, 65].

Noble Gas	Vapour pressure [bar]	Relative volatility α
Argon	≈100	≈50
Krypton	20.9	10.4
Xenon	2.0	1
Radon	0.2	0.1

Table 2.2.: *Table of relevant noble gases, their vapour pressures and the resulting relative volatilities (with respect to xenon, at a temperature of -98 °C). Values taken from [63].*

2.6. Detector shielding and background reduction

XENON1T is a low background experiment. Due to the low expected cross section of a WIMP-nucleon interaction, the expected number of events for the detector is in the $O(1)$ evt/kg/year. In order to be able to distinguish these events from backgrounds, the latter must be reduced as much as possible. One major background contribution comes from cosmic radiation. This component is mainly shielded by placing the XENON1T detector underground at the LNGS, below 1400 m of rock. However, muons created by cosmic ray interactions with the atmosphere can reach these depths

at a still considerable flux of $(3.31 \pm 0.03) \cdot 10^{-4}\,(m^2 s)^{-1}$ [39]. These events are removed by using an active veto system. It consists of a cylindrical tank, 10 m in diameter and 10 m in height, filled with ultrapure water. On the inside, it is equipped with 84 PMTs and a highly reflective foil on the walls. A passing muon will interact with the water by emission of Cherenkov light which will be detected by the PMTs. In case of a signal in the TPC and a coincident signal in the active muon veto, the event will be discarded as background.

Besides the cosmic radiation, the radioactivity of the rock surrounding the detector and intrinsic to the construction materials of the detectors must be taken into account. Due to the high atomic number, xenon has a high self-shielding for γ-rays. This results in a high γ-ray induced event rate on the outer regions of the detector, while the core of the detector is very quiet. This feature can be exploited by the 3D-reconstruction capability of the TPC: It allows for a fiducialisation of the detector volume, the definition of a virtual inner detector used for scientific data gathering, while surface events can be rejected as background. This selection is done on the software analysis level.

Additionally, the detector's ability to distinguish between different interaction types allows discrimination between nuclear and electronic recoils.

Further reduction of background and unwanted events is done on the level of data analysis. After the event building data cuts are applied. They allow for data selection to take signal properties like pulse width into account.

2.7. Data acquisistion: event building

The fundamental signal, recorded by a single PMT and afterwards digitized, is called a *pulse*. A pulse consists of roughly 100 samples and covers a time window of $\sim 1\,\mu$s. Pulses are recorded whenever an amplitude threshold is exceeded. As this is done on an individual channel/PMT basis, each channel is 'self-triggering' and no global, all-channel controlling trigger signal is needed. All pulse information is stored in a MongoDB database [66].

The higher tiers of analysis are performed on *events*. Events consist of grouped pulses and are created on a single computer, called the event-builder, which reads all the pulse data from the MongoDB. Here the pulses are combined into *signals* or *peaks* and also the signal/peak type is determined. The signal type is dependent on the grouping and distribution of pulses in time. A tight time coincidence window of the pulse-time (time-stamp of the recorded pulses, usually the start time) of 100 ns is used to identify S1 signals. Additionally, to reduce the impact by noisy PMTs, a 3-fold coincidence is required for a signal to be identified as S1. S2 signals are generally much larger, such that pulses within $1\,\mu$s are grouped into a S2.

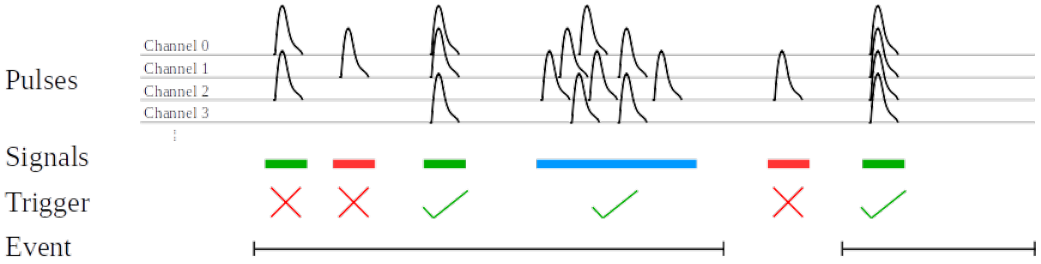

Figure 2.8.: *Working principle of the event builder. Pulses are combined into signals: signals classified as S1 are marked with green, signals classified as S2 are marked in blue, and lone hits in red. Signals reaching a certain amount of contributing pulses can generate trigger signals (S1: more than 50 contributing pulses; S2: more than 60 contributing pulses), which are used to build an event.*

A schematic of how pulses are merged into signals and how events are created from signals is shown in Fig. 2.8. Events are usually triggered (defining an event time stamp) by an S2, it is however also possible to trigger on an S1. These trigger signals are dependent on the amount of pulses contributing to a signal. For an S1 trigger at least 50 pulses have to contribute, for an S2 trigger at least 60. Finally an event is built by grouping all signals that are recorded within a 1 ms time window before and after the trigger signal. This basic time window length is chosen to cover the complete electron drift-time range of XENON1T, which is about 750 μs long. Overlapping time windows of different trigger signals are combined into a single event. As a result, longer events with a duration of up to 10 ms are possible. This allows for a more detailed data selection in the higher analysis steps later.

More detailed information about the XENON1T DAQ system can be found in [66].

2.8. Signal corrections

The raw data needs to be corrected for diverse detector effects. Both the S1 and S2 signal are strongly affected by spatial effects, but also by properties of the used PMTs. The S1 is mainly influenced by the light collection efficiency (LCE) ϵ_L of the detector. This correction factor measures the relative variations of the LCE throughout the TPC. It is estimated using ^{83m}Kr , which is assumed to distribute homogeneously throughout the TPC. Therefore the measured variations in the spatial event distribution can directly be used to create a 3D spatial map of correction values.

The PMTs performance also significantly affect the signals. The important parameters to describe the PMT performance are the quantum efficiency ϵ_{QE} and collection efficiency ϵ_{CE}. ϵ_{QE} is the efficiency that one incident photon creates an electron on the photocathode, ϵ_{CE} is the efficiency that this electron is collected by the first dynode in the PMT and thus starts the detection process. Additionally, there is also a chance that two photoelectrons are created by one photon, which is given as double-photon emission probability p_{dpe}. This results from the high ($\approx 7\,eV$) energy of the 178 nm

scintillation photon compared to the work function of the photocathode [67]. For the S1 signal, these factors combine into the correction parameter:

$$g_1'(x,y,z) = (1 + p_{dpe}) \cdot \epsilon_L(x,y,z) \cdot \epsilon_{QE} \cdot \epsilon_{CE} \tag{2.15}$$

To create the S2 signal, electrons need to be extracted from the liquid to the gas phase. The efficiency of this process is given by ϵ_{ext} and is strongly field-dependent. After extraction the electrons are dragged through the xenon vapor to the anode, exciting the gas atoms and creating the secondary scintillation signal S2. The amplification factor G is field-dependent and as such position-dependent, as small spatial variations of the field can impact G. This effect is visible in G of the XENON1T ^{37}Ar calibration data, as shown in the analysis in chapter 4.11. For the S2 the correction parameter is given by:

$$g_2'(x,y) = \epsilon_{ext}(x,y) \cdot G(x,y) \tag{2.16}$$

The S2 signal needs to be corrected for the electron drift loss. As this process is similar to an absorption process it can be modeled accordingly by an exponential attenuation. This is used to correct the S2 signal size based on the drift time of the electrons, given by the time difference between S1 and S2. The corrected S1 and S2 can then be written as:

$$cS1 = S1(x,y,z)\frac{g_1}{g_1'(x,y,z)}, \tag{2.17}$$

where $g_1 = \langle g_1'(x,y,z)\rangle$,

$$cS2 = S2(x,y,z)\frac{g_2}{g_2'(x,y)}e^{z/(\tau_e \cdot \nu_d)}, \tag{2.18}$$

where $g_2 = \langle g_2'(x,y)\rangle$, τ_e is the electron lifetime and ν_d is the electron drift velocity [68]. With these values of cS1 and cS2 the total energy can be estimated, as shown in Section 2.3:

$$E = W \cdot \left(\frac{cS1}{g_1} + \frac{cS2}{g_2}\right) \tag{2.19}$$

The S2 signal's x-y-positions are reconstructed using a neural network that is trained on simulated S2 hit patterns on the top PMT array. Inhomogeneities in the drift field due to wall charge-up effects cause a radially inward drift of electrons, especially of events taking place near the outer edge and at deeper positions of the TPC. Spatial correction is again estimated using ^{83m}Kr calibration data [30]. Fig. 2.9 summarizes the steps from an energy deposit, over the application of corrections, towards the corrected signals cS1 and cS2, which are used in the later analysis.

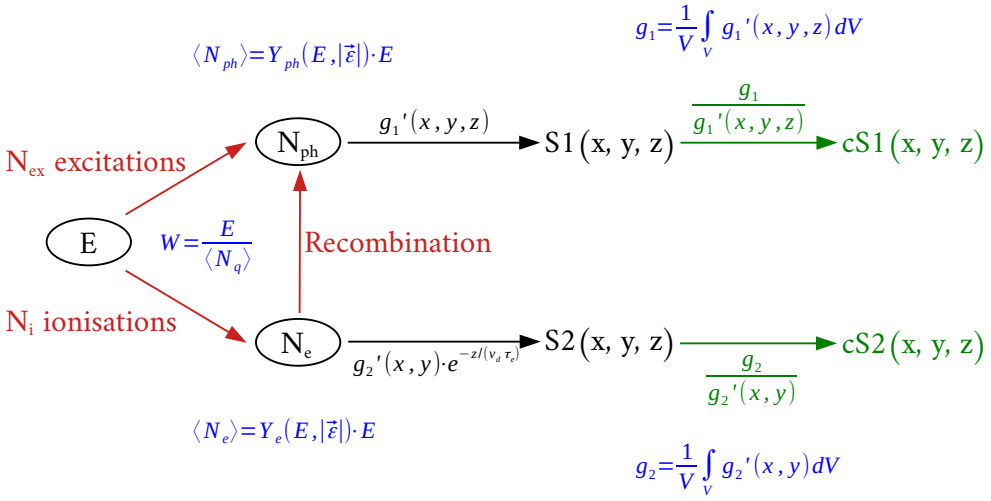

Figure 2.9.: *Sketch summarizing the steps from energy deposit in the detector to the corrected signals cS1(x, y, z) and cS2(x, y, z). The mean number of produced photons and electrons can be calculated from Y_{ph} and Y_e, the photon and electron yield of xenon for a given energy deposit E and applied field $\vec{\epsilon}$. An estimation of the number of produced photons and electrons for an interaction and the deposited Energy can also be computed from the corrected cS1 and cS2 as shown in Equations 2.20, 2.21, and 2.19.*

cS1 and cS2 can directly be used to estimate the number of photons and electrons created in the interaction, as well as the deposited energy (see Eq. 2.19):

$$\hat{N}_{ph} := \frac{cS1}{g_1} \tag{2.20}$$

$$\hat{N}_e := \frac{cS2}{g_2} \tag{2.21}$$

The effect of this correction is shown in Fig. 2.10, showing the difference between the observed and corrected positions of ^{37}Ar events, with a correction based on ^{83m}Kr data.

The field correction is used for position correction only. As it was found during the analysis of the data collected during ^{37}Ar calibration, the field variation also significantly impacts the scintillation process. The field variations introduce an interaction-energy dependent variation in photon and electron gain, which is shown in more detail in chapter 4.3. Correction for this effect however is difficult to realize, as the corrections applied in chapter 4.3 are based on simulation data and require knowledge of the interaction energy. This is given for calibration sources, but certainly not for background/dark matter interactions. For this reason, the data corrections are consistently based on ^{83m}Kr data.

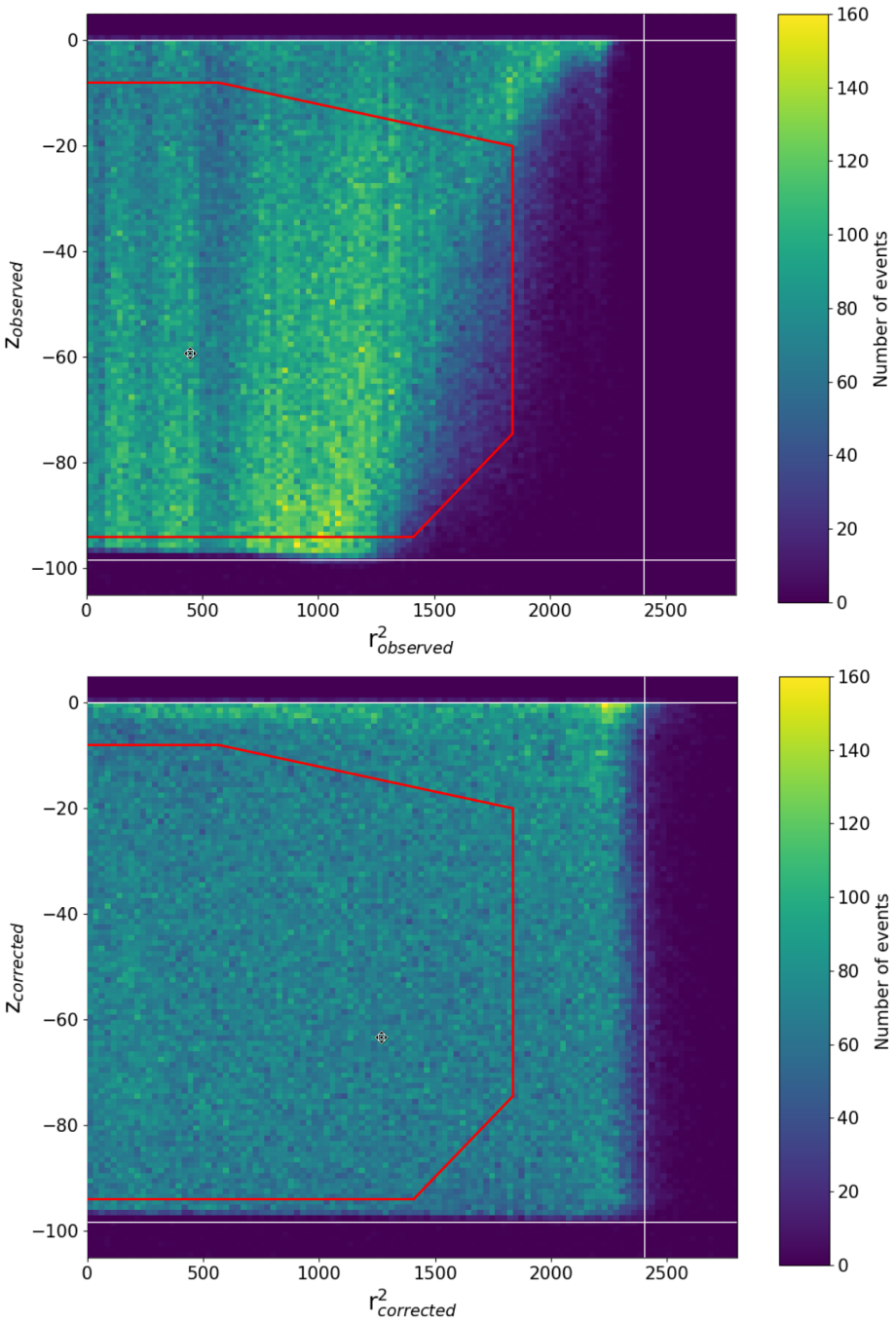

Figure 2.10.: *Example of the position correction. The top plot shows the uncorrected data, where no interactions are located in the lower outer edge of the TPC. This is caused by field inhomogeneities due to wall charge-up effects, which cause the electrons to drift inwards. This is corrected with the help of correction maps based on* ^{83m}Kr *(and later* ^{37}Ar *) calibration data. The red lines mark the fiducial volume used later in the analysis.*

3. First ^{37}Ar Calibration of a Dark Matter detector - XENON1T

3.1. Introduction

In this chapter a newly introduced, internal calibration source for liquid noble gas detectors is presented: ^{37}Ar. The properties of ^{37}Ar, which make this a suitable source to examine the lower detection threshold of the current state-of-the-art liquid noble gas TPCs like XENON1T (and XENONnT) are discussed in section 3.2. Section 3.3 describes the production of this new source and its injection system for XENON1T. The injection of ^{37}Ar and the calibration process are presented in section 3.4. Due to its half-life, active removal after calibration is necessary, with a preliminary analysis during the calibration described in section 3.4.4 and a more detailed analysis performed in section 4.2.

3.2. ^{37}Ar as calibration source

^{37}Ar is a radioactive isotope of the noble gas argon with a half-life of 35.011 days. It purely decays via electron capture into ^{37}Cl . The energy difference between the ground-states of ^{37}Ar and ^{37}Cl (Q-value) is 813.87 keV [69]. This energy is mainly released in the form of a neutrino when the electron is captured. To fill the gap in the electron shell caused by the capture, electrons from higher shells descend into the freed position under the emission of characteristic x-rays or an Auger electron. The energy of the emitted Auger electron is determined by the binding energy of the electrons of the newly formed ^{37}Cl atom. The electrons from the innermost shell, the K-shell, have the highest probability of being captured. For the ^{37}Ar decay, this capture has a branching ratio of 90.2 %. From the binding energy for this shell of a ^{37}Cl atom, this results in an energy of 2.82 keV for the released Auger electron. Also captures from higher shells are possible, but with much lower probabilities of 8.7 % for L1-shell captures and 1.1 % for M1-shell captures. These transitions also take place with an even lower energy emission of 0.27 keV and 0.02 keV for the L- and M-shell transitions, respectively [70].

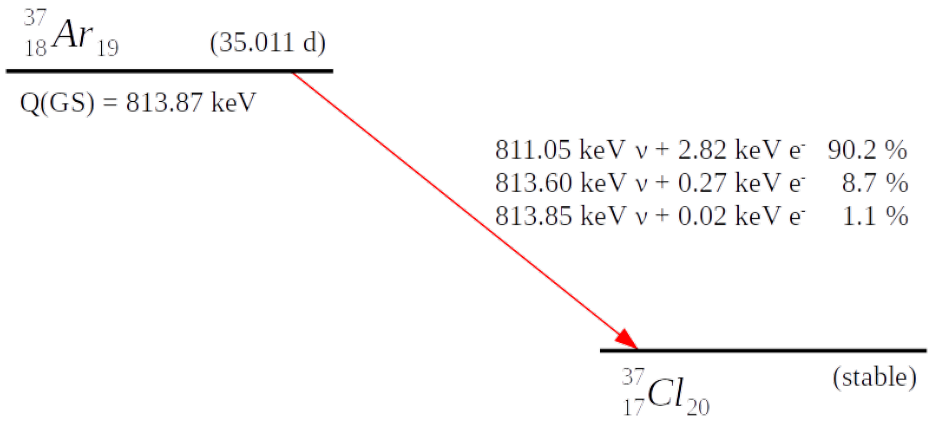

Figure 3.1.: *Decay scheme of ^{37}Ar into ^{37}Cl, where the major component of the decay energy is carried away by a neutrino. The most probable decay with an energy of 2.82 kev has a branching ratio of 90.2 % for an electron capture from the K-shell, with lower energetic transitions happening with a ratio of 8.7 % and 1.1 % for L1- and M1-shell captures, respectively [70].*

This places it in the energy region of the lower detection threshold of the XENON1T detector. As it emits x-rays/electrons, it is detected via the ER channel of the TPC, providing a better understanding of the ER background of the detector and thus might lead to an improved background reduction in the data.

The only source in the same energy range used in XENON1T so far was ^{220}Rn, which decays via the emission of β-particles, covering a wide range of energies with a continuous spectrum. Conversely, ^{37}Ar offers multiple mono-energetic lines as shown in Fig. 3.1, which offers complementary calibration options compared to a continuous energy spectrum.

Similar to ^{83m}Kr, ^{37}Ar is a noble gas and as such can be mixed directly into the detection medium xenon. This provides a homogeneous distribution throughout the detector. Exploiting this feature, ^{37}Ar can also be used, to calibrate the spatial response of the detector using its line emissions.

The higher shell captures, which happen with much lower probabilities have decay energies below the detection limit of XENON1T. A simple calculation with a light yield of $L_y \approx 1 - 2\,\mathrm{pe/keV}$, based on Noble Element Simulation Technique (NEST) [71], shows that the number of photons expected for an S1 is

$$S1 = L_y \cdot E = 2\,\mathrm{pe} \cdot 0.27\,\mathrm{keV} < 1\,pe \tag{3.1}$$

As for an L-shell capture, the expected number of photons in an S1 signal is smaller than one, we don't expect to see a signal, especially when taking the light collection efficiency into account and the requirement of a 3-fold coincidence for the PMTs. However, due to the amplification of the charge signal the secondary scintillation signal should still be detectable. This is realized with the so-called *S2-only* analysis. In this

specialized analysis only the S2 signals are used, which makes some modifications to the analysis process necessary. More about this analysis can be found in Chapter 4.13.

3.3. Measurement Run Preparations and Setup

This section describes the production of the ^{37}Ar sources, the dosing system used in the calibration, and the calibration procedure.

3.3.1. Ampule production and source irradiation

There are multiple ways to produce a ^{37}Ar source, with the main three being:

- Proton capture on ^{37}Cl: $^{37}\mathbf{Cl}(p,n)^{37}\mathbf{Ar}$
  This reaction requires a proton accelerator [69].

- Neutron capture on ^{40}Ca: $^{40}\mathbf{Ca}(n,\alpha)^{37}\mathbf{Ar}$
  For this reaction fast neutrons with energies of 5 to 6 MeV are necessary, which can be provided by an AmBe-source. After irradiation, the ^{37}Ar needs to be separated from the ^{40}Ca in a complex procedure. A description of the procedure and all steps necessary can be found in [69, 72]

- Neutron capture on ^{36}Ar: $^{36}\mathbf{Ar}(n,\gamma)^{37}\mathbf{Ar}$
  This reaction can be achieved with thermal neutrons in a nuclear reactor. As the University of Mainz operates a TRIGA Mark II reactor [69], we decided to use this reaction to produce the calibration source.

Ampule production and filling

To allow for irradiation with neutrons, a containment material with only limited neutron interaction and also a very low activation rate has to be chosen. A material typically used for the irradiation of gas samples is fused quartz. It consists only of silica (SiO_2, plus impurities below the maximum allowed limits set by industry standards) and thus produces no long-lived isotopes during irradiation. A list of the isotopes produced during irradiation and their half-lifes are shown in Table 3.1.

Isotope	Half-life
^{28}Al	2,24 min
^{29}Al	6,56 min
^{31}Si	157,3 min

Table 3.1.: *Half-life times of isotopes created during irradiation of a fused quartz ampule.*

Isotope	Natural abundance	Enriched abundance	Half-life	Decay mode	Daughter nucleus
^{36}Ar	0.336 %	99.935 %	stable	-	-
^{37}Ar	-	-	35.01 d	electron capture	^{37}Cl
^{38}Ar	0.063 %	0.064 %	stable	-	-
^{39}Ar	-	-	269 a	β^-	^{39}K
^{40}Ar	99.6 %	0.001 %	stable	-	-
^{41}Ar	-	-	109.34 min	β^-	^{41}K

Table 3.2.: *Table of all relevant argon isotopes with natural abundance [73]. The enriched abundance column gives the values of the enriched argon sample irradiated in the reactor.*

As a further advantage, the material is also easy to clean, making it easy to avoid impurities in the gas samples, which might later contaminate the detector during calibration.

The ampules are filled with enriched ^{36}Ar with an enrichment grade of 99.935%. The exact composition is shown in Table 3.2. Using enriched ^{36}Ar has multiple advantages. The contribution of ^{36}Ar to the natural abundance is only 0.336%, as is shown in Table 3.2. By increasing the abundance by about a factor of 300, the production rate of ^{37}Ar is increased by the same factor. Additionally, the production of ^{41}Ar from neutron capture on ^{40}Ar present in the natural argon is reduced by a factor $\approx 10^5$.

The ^{36}Ar is stored in a 0.5 l gas cylinder containing 50 mg of gas, which results in a filling pressure of only 0.110 mbar (which is further reduced with each successive filling process). A simple setup was built, using only this low pressure to fill the ampule. This setup was volume-optimized to reduce the amount of gas wasted after the filling procedure. The setup, a sketch is shown in Fig. 3.2, includes a pressure sensor used for measuring the filling pressure of the ampule. For the whole setup, a volume estimation was done, allowing, together with the pressure, for an estimation of the amount of gas in the ampule. To further reduce the amount of waste gas (all gas inside the cross, the sensor, and the valve is lost after a filling), multiple ampules are filled simultaneously during one procedure.

A blanket for the ampules was prepared with pre-shaped ampules, only connected with a thin glass tube to allow an easy separation after filling in the argon.

Before filling, all components were cleaned in an ultrasonic bath, afterward cleaned with isopropyl alcohol, and finally flushed with distilled water. For further cleaning after mounting the setup was leak tested and pumped down to 10^{-7} mbar for several days.

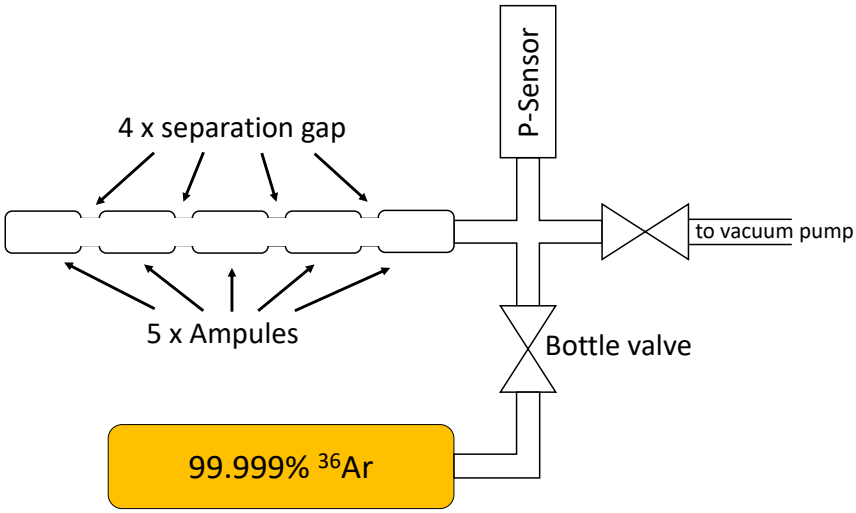

Figure 3.2.: *The system used to fill the ampules. The system was pumped at the pumping port. The measured pressure was used to calculate the amount of gas in the ampules. After filling, the ampules were separated one after another by a glassblower.*

For the filling procedure of the ampules the valve to the pump was closed and the bottle valve opened. The pressure value was noted and used to calculate the amount of gas in the ampules. After closing the connection to the bottle, a glassblower separated the single ampules one after another from the pre-shaped glass.

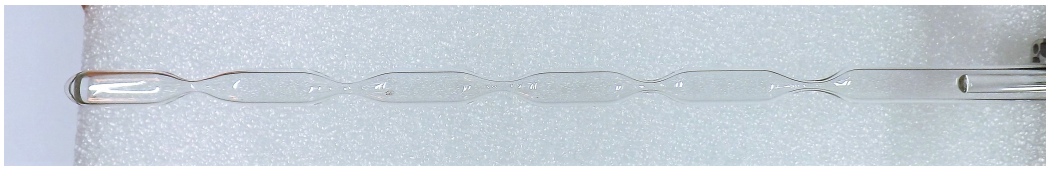

Figure 3.3.: *Prepared ampule blanket before filling and separation.*

Ampule irradiation

^{36}Ar irradiation took place at the TRIGA reactor situated on the campus of the University of Mainz. This reactor is a TRIGA Mark II pool-type reactor with a continuous thermal power output of 100 kW. Additionally, the reactor can also be used in a pulsed mode with a power output of 250 MW within a 30 ms pulse. However, the pulsed mode is not needed for the irradiation [74]. For the irradiation, a position in the center of the reactor was chosen, making use of the highest possible neutron flux of $4.2 \cdot 10^{12}\,\mathrm{n\,cm^{-2}\,s^{-1}}$. The activity aimed for, also to stay within the agreed limits with the LNGS, was 100 kBq.

3.3.2. ^{37}Ar dosage and injection system

After irradiation, the ampule contains ^{37}Ar with an activity of approx. 100 kBq. The amount to be injected in the detector for one calibration is on the order of Bq. Therefore a system is necessary that opens the sealed ampule and dilutes the source into the xenon, allowing for precise dosing of activity into the detector. This so-called dosimetry branch was designed and built in Mainz and first tested with the small Mainz TPC during the master thesis of Daniel Wenz [75, 76]. The system is shown in Fig. 3.4, both as a computer aided design (CAD) drawing and photo. It consists of two sub-systems, the ampule container and the activity monitor, as well as several small volumes and valves crucial to the dosing procedure.

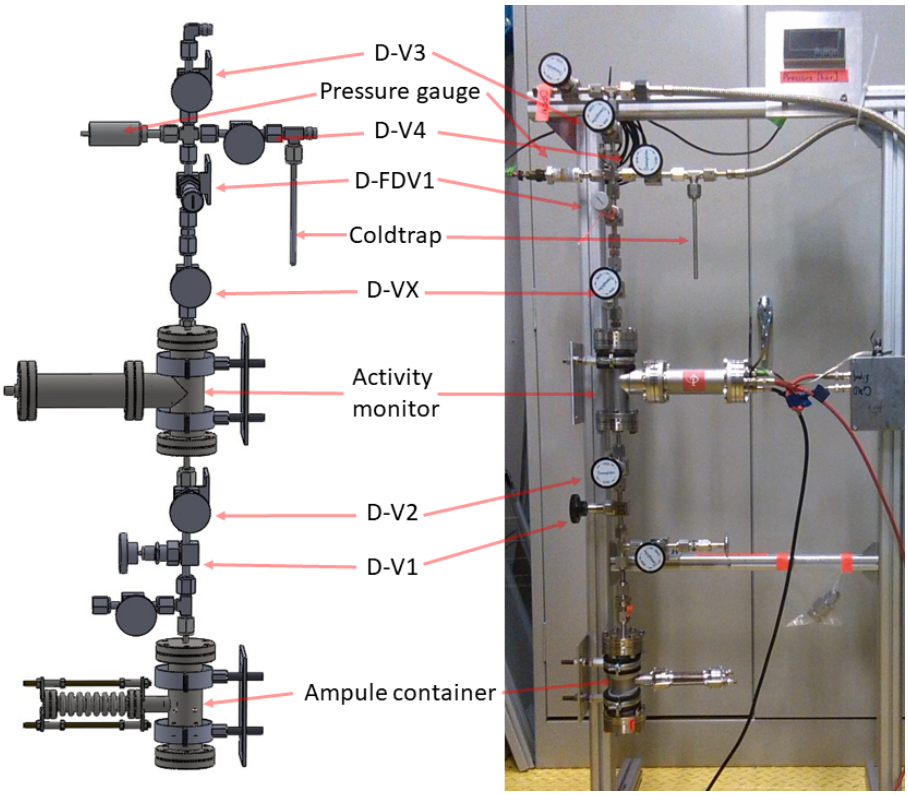

Figure 3.4.: *Side-by-side view of a CAD drawing of the dosing branch and the realized system connected to the XENON1T gas recirculation system. Some part orientations were adapted to better fit the available space, but the features remained unchanged.*

The **ampule container** stores the ^{37}Ar calibration gas and includes a guillotine mechanism to open the ampule. A CAD-drawing is shown in Fig. 3.5. Before opening the ampule, the volume is filled with xenon at a pressure of approximately 2 bar. This is necessary for the later dosing procedure, as the ampule has a filling pressure of only 110 mbar, which would be further reduced to the order of mbar when the gas expands into the evacuated volume. As the dosing is based on volume ratios only, xenon can be used as a carrier gas to ease the dosing. To open the ampule, the guillotine is

lowered, guided by threaded rods to avoid damage to the bellow.

The second system is a simple **activity monitor** to measure the argon activity in a well-defined volume of xenon gas to verify the overall activity in the ampule after irradiation. Due to the energy of the ^{37}Ar decay of only 2.82 keV, the electrons and X-rays cannot penetrate the glass walls of the ampule. Thus no external measurement can be performed to confirm the activity after irradiation. The camera consists of 1" Hamamatsu R5820 PMT facing a well-defined volume milled into a PTFE cylinder. Teflon was used for its high reflectance in the UV regime to maximize the light collection efficiency of the setup.

The third part is the actual dosing volume, a small pipe-cross, connected to the camera. A second connection is occupied by a pressure sensor. The other attachments are connected to the source box of XENON1T and allow for a part of the recirculation flow to be redirected through the dosing volume to flush the calibration gas into the detector.

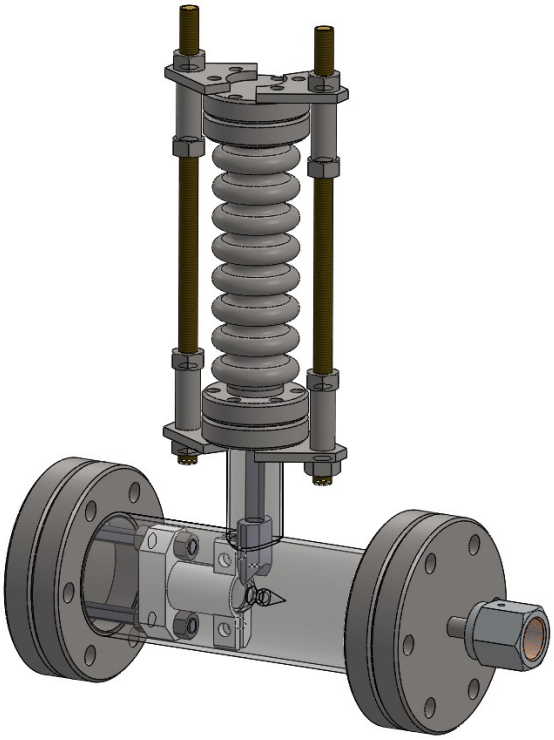

Figure 3.5.: *CAD drawing of the source container with ampule and guillotine mechanism to open the ampule and release the ^{37}Ar.*

Activity camera subsystem issues

Initially, there was a major problem of sparking during PMT high voltage ramp-up, with the sparking voltage strongly dependent on the xenon pressure. The first actions

were based on the assumption that the sparks occur between the PMT housing and the steel pipe used as a vessel. The PMT was operated with a base designed for negative high voltage. In this mode, the metallic hull of the PMT was on the same potential as the applied operating voltage of -900 V. As the distance between the vessel and PMT shell was only between 1 to 2 mm, a flashover at this point seemed most probable. An additional PTFE layer was wrapped around the PMT to prevent the sparks, but additional tests did not show any improvement. Also switching to a positive operated PMT base did not solve the problem. As in this mode the PMT hull is on the same potential as the vessel, sparking can only occur between the PMT pins and the base. A test in a glass vessel filled with argon revealed the sparking to happen indeed between the pins and the hull of the PMT. This was rather surprising as this PMT model was already operated in the XENON100 experiment without encountering this issue.

The problem was solved by applying a layer of a liquid high vacuum sealant on the back of the PMT, covering the complete metallic backside. Initially, as a material to close small leaks in connections, the electrically isolating sealant worked well as an additional isolation layer. Tests with the MainzTPC also showed no contamination of the xenon with respect to signal reduction.

The setup as a hole in its current state, however, proved to be insufficient to detect the ^{37}Ar decays in gaseous xenon. It is still part of the dosing branch as its volume is needed to achieve sufficient dilution of ^{37}Ar, but it cannot be used to determine the ^{37}Ar activity before injection into XENON1T.

One possible upgrade is the implementation of electrodes to apply an electric field and thus achieve proportional scintillation to improve the sensitivity of the device. This upgrade, however, has yet to be implemented.

3.3.3. Dosing procedure

Diluting the activity takes place in several steps, of which each is based on the volume ratios of the different parts of the setup. The volumes of the different sections are estimated by measuring the dimensions, using the CAD drawings of the parts or using volume values provided by the manufacturer, in the case of the valves. The values for the volumes and the corresponding activities are given in Table 3.3, the designations for the parts can be found in Fig. 3.4.

Volume location	Volume [cm^3]
Ampule container	181.3 ± 1.7
D-V1 to D-V2	2.0
Activity camera	318.3 ± 0.3
D-VX to D-FDV1	3.1
Dosing volume with pressure gauge	8.9 ± 0.3

Table 3.3.: *Volumes of the dosing branch with estimated volumes that are used to calculate the dose of ^{37}Ar injected into the detector.*

Before opening the ampule, the storage volume is filled with xenon at 1.97 bar, acting as a carrier gas for the dosing procedure. The first dilution step takes place from the ampule volume to the small volume between valves D-V1 and D-V2. These two have volumes of $181.3 \pm 1.7\,\mathrm{cm}^3$ for the ampule volume and $2\,\mathrm{cm}^3$ for the inter-valve volume (no uncertainty given by the manufacturer). This results in a separation ratio of 1:90.6. As both volumes are filled with xenon, the argon transport is based on diffusion only.

In the next step, the content of the small volume is diluted into the big camera section with a volume of $318.3 \pm 0.3\,\mathrm{cm}^3$. Argon transport is again based on diffusion. The dilution ratio of this step is 1:159.

Initially, the next step was filling the volume between D-VX and D-FDV1 was filled again by letting the argon diffuse into the volume. Shortly before argon injection, the cross was evacuated with the cold trap. After this, the valve D-FDV1 was opened carefully, allowing a to achieve a pressure precision in the cross of the order of 10 mbar, corresponding to an activity in the sub-Bq range.

This last step was later modified on-site in the way that the section between valves D-VX, D-V3, and D-V4 was evacuated with the cold trap, after that the volume between D-VX and D-FDV1 was filled from the camera section with a gas flow and no longer by a diffusion process. This greatly enhanced the speed at which the dosing can be performed. Additionally, the last gas transport step based on diffusion was removed, a process taking much more time (in the order of hours) than anticipated in the beginning.

3.4. ^{37}Ar Calibration of XENON1T

3.4.1. Live activity monitoring

We monitored the injected activity by observing the trigger rate of each run. As data transfer and processing added a delay of around 8 h between actions on the TPC and the possibility of taking a detailed look into the processed data, the monitoring of the trigger rate was a much faster method to see the impact of each new argon dose immediately. Given that at the beginning of the measurement argon-specific event selections were not defined yet, the observed trigger rate of the TPC consisted of the base rate plus the rate added by the ^{37}Ar source.

The base rate was a composition of the real background rate and the rate added by the ^{83m}Kr source, which was also open at the beginning of the measurement. This had the advantage that data from both sources with identical detector conditions was taken at the same time. This allows for a direct comparison of both sources in later analysis.

3.4.2. Argon injection

The goal of the first argon calibration was to reach a measurable ^{37}Ar activity comparable to at least the background rate of the detector, which was taken directly from the trigger monitor of XENON1T to be 4.8 Hz. The background rate was also determined based on 20 runs directly before the calibrations where a mean event rate of 15880 events/run are observed. The runs used for background estimation can be found in Appendix B.2 in Fig. B.3. This number is equal to an event rate of 4.4 Hz, based on a run duration of one hour, and is used as the background rate in the following analysis. Based on this estimation, to reach an event rate well above the background, an injection of at least 5 Bq into the detector was the target.

As the ^{37}Ar data can also be used to perform a spatial calibration (test for spatial uniformity of the event distribution, determination of spatial dependencies of the response) or to determine the electron drift time, a sufficient number of events is required. For a rough division of the detector volume in 1000 voxels (of arbitrary shape) requiring approximately 1000 events in each voxel to reach a passable statistical error and given a limited time window of only two weeks for the measurement, a minimal event rate of 5 Hz is required, in agreement with the previous assessment.

In addition to the ^{37}Ar, the ^{83m}Kr source was open in parallel during the first days of the measurement. Based on the event numbers shown in Fig. 3.6 before the first ^{37}Ar injection (timestamp A), a mean number of 21298 events/run was observed, corresponding to an event rate of 5.92 Hz, determining an ^{83m}Kr rate of approx 1.5 Hz. As the ^{83m}Kr decay deposits more energy in the TPC, these events are distinguishable from each other in the S1-S2 space and no interference with the ^{37}Ar was expected.

After the first injection, performed with the initial method, a continuous rate increase was observed, although much slower and with a much smaller magnitude than expected, only increasing the event numbers per run from 21298 to 24861, which corresponds to a rate increase from 5.92 Hz to 6.91 Hz. The observed rate increase was only one-quarter of the expected one based on the injected amount of 4 Bq. It was assumed that the majority of the injected gas was distributed in the gas volume of the detector and only a small fraction was kept in the liquid. Also, the delivery speed of the ^{37}Ar was very slow and the activity transfer into the detector was not yet fully completed, even after one day of waiting, as it is visible in Fig. 3.6 between timestamps A and B.

To reach a higher activity in the TPC, a second injection was carried out, introducing approximately four times the amount of ^{37}Ar into XENON1T. To shorten the mixing time, the cold trap was used for a faster transfer into the recirculation cycle. The size of the injection was intended to be 18 Bq, resulting in a rate increase from 6.91 Hz to 9.60 Hz as shown in Fig. 3.6 between timestamps B and C.

After the rate stabilized, it still was below 10 Hz, so a third injection was performed, introducing an activity comparable to the first injection, but using the refined injection method. This resulted in the peak rate of 10.26 Hz, which was the minimal goal to reach sufficient statistics. The rate increase is visible in Fig. 3.6 between timestamps

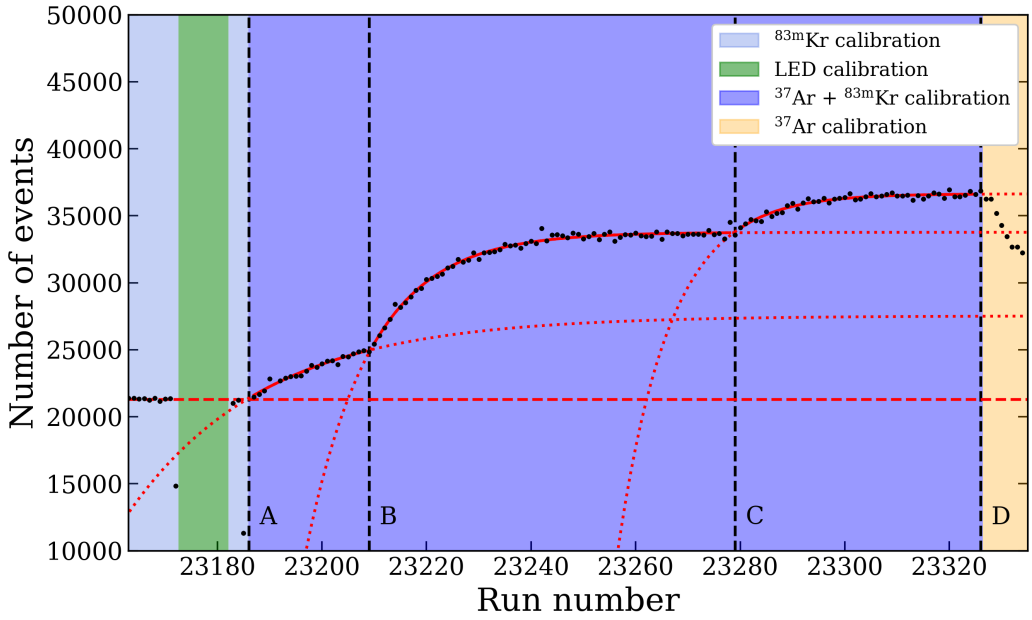

Figure 3.6.: *The injection steps of ^{37}Ar into the TPC. The first injection of argon with an estimated activity of 4 Bq (timestamp A). The second injection with 18 Bq (timestamp B) and the third one with 4 Bq (at timestamp C). Timestamp D marks the closure of the ^{83m}Kr source, which was open in parallel. The dashed line shows the combined mean number of events for the background and ^{83m}Kr calibration. The solid lines show the fit results (and the used data range) with the function given in Eq. 3.2, while the dotted lines show the complete shape.*

C and *D*.

These rate estimations are mostly based on rates of single runs and especially the first injection can not be quantified this way as it never settled. Therefore each injection was fitted with a saturation function of the shape:

$$R(t) = R_{off} + R_{inj} \cdot (1 - e^{\frac{x-x_0}{\tau_i nj}}) \tag{3.2}$$

where R_{off} is the offset caused by background and ^{83m}Kr, R_{inj} the injected ^{37}Ar rate and τ_{inj} the time constant for reaching the plateau.

Each injection was fitted with this function individually, the resulting functions are shown in Fig. 3.6 and the parameters are given in Table 3.4.

After the three calibration gas injections it was decided to close the krypton source to record datasets containing only argon data. Argon-only data taking in this way was done for 8 days. During this period the decay of ^{83m}Kr and ^{37}Ar was observed. On these rates, a function consisting of two decay terms, one for each of the isotopes, and a constant offset for the detector background, was fitted using the function:

$$R_{Decay}(t) = R_{off} + A_{Ar} \cdot e^{-(t/(\tau_{Ar}))} + A_{Kr} \cdot e^{-(t/(\tau_{Kr}))} \text{ with } \tau_i = t_{i,1/2}/ln\,2 \tag{3.3}$$

Injection	Activity [Bq]	R_{inj} accumulative	R_{inj} individual	R_{inj} [Hz]	τ [h]
1	4	6234	6234	1.73	26.38
2	18	12468	6234	1.73	12.38
3	4	15341	2873	0.80	9.68

Table 3.4.: *Results of a simple analysis on the event numbers for the ^{37}Ar injections. The large decrease of effective rate increase per additional injected Bq of ^{37}Ar activity suggests a large uncertainty in the dosing procedure and/or a pile-up effect. The strong reduced τ for the second and third injection confirm a faster mixing by the adapted injection procedure. As this rough analysis is based on the event numbers only without any data selection with the sole purpose to monitor the injection process, no uncertainties are given.*

The offset R_{off} was extracted as a mean value of 20 runs from the beginning of October, where no calibration data was taken or no other tests were performed. The runs used for background estimation can be found in Appendix B.2 in Fig. B.3. From these runs a mean background of 15879.80 events/run was extracted and given to the fit-function as a fixed parameter.

One uncertainty not taken into account in this analysis is the fact that we are using the run number as a sort of time measure. This introduced a small error as one run does not cover exactly one hour of data taking but in most cases 2 to 3 seconds more. To use the actual event times for this first analysis, processed data would have been necessary again.

3.4.3. Argon outgassing test

After the initial argon data taking, a test was performed to measure the mixing properties of argon and xenon. This test was also intended to help understand the discrepancy between the assumed amount of activity introduced in the detector and the actually measured increase in the trigger rate. For this test, the gas recirculation system was put into a setting in which no gas from the gas volume above the detector was fed back into the recirculation and cleaning circle. This resulted in a *dead end* for the gas on top of the detector. Fig. 3.8 shows the response of the trigger rate to this new setting, a steep decrease, which points to a fast outgassing of argon from the liquid xenon. This also shows that constant recirculation is needed to keep the ^{37}Ar in the liquid phase of xenon.

3.4.4. Argon distillation phase - preliminary analysis

The second question addressed by this first calibration with ^{37}Ar was the one of the removability of the calibration gas. The property making argon so interesting for calibration, namely having a low emission energy of 2.82 keV, makes it also dangerous for

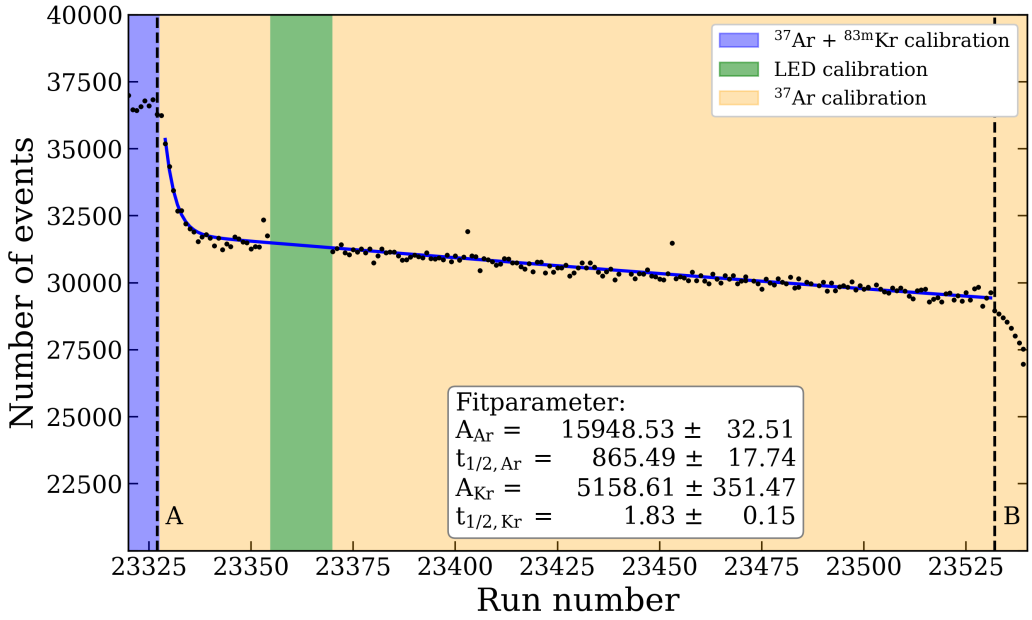

Figure 3.7.: *After the last ^{37}Ar injection and the closure of the ^{83m}Kr source (at time A), the decay of both isotopes was observed. The fast decay component of Krypton, in the beginning, is clearly visible, a result of the short half-life of 1.83 h. Also the slow component of ^{37}Ar with a half-life of 35 days can be seen by a steady decrease of the number of events in the datasets.*

the actual dark matter search. If not properly removed, ^{37}Ar can produce background signals in the energy region of interest where WIMP interactions are expected. The XENON1T detector uses a distillation column for krypton removal. As argon has an even higher vapor pressure, an even higher removal factor is expected for argon than for krypton.

A simple exponential fit is used to determine some basic properties of the argon distillation:

$$R_{Distillation} = R_{offDist} + A_{Ar} \cdot exp^{(-(x-x_{0,dist}/\tau_{dist}))} \tag{3.4}$$

The free parameters used in the fit are the background level B, the number of argon events per run A, and the time constant of the distillation τ_{dist}. The fit is shown in Fig. 3.8. Table 3.5 shows the fit results. The number of events from the fit can be converted into an event rate with the given run duration of one hour. This results in an argon activity of 3.395 ± 0.014 Bq, sitting on top of a background rate of 4.452 ± 0.005 Hz which is in agreement with a background rate measured before the start of the calibration of 4.4 Hz. The rate reduction half-life time is 40.86 ± 0.31 h. This can be converted into a *decade distillation* time of 3.92 ± 0.03 d, the time needed to reduce the activity by a factor of 10. This time addresses the total reduction of activity and is a combination of reduction by distillation and the natural decay of the

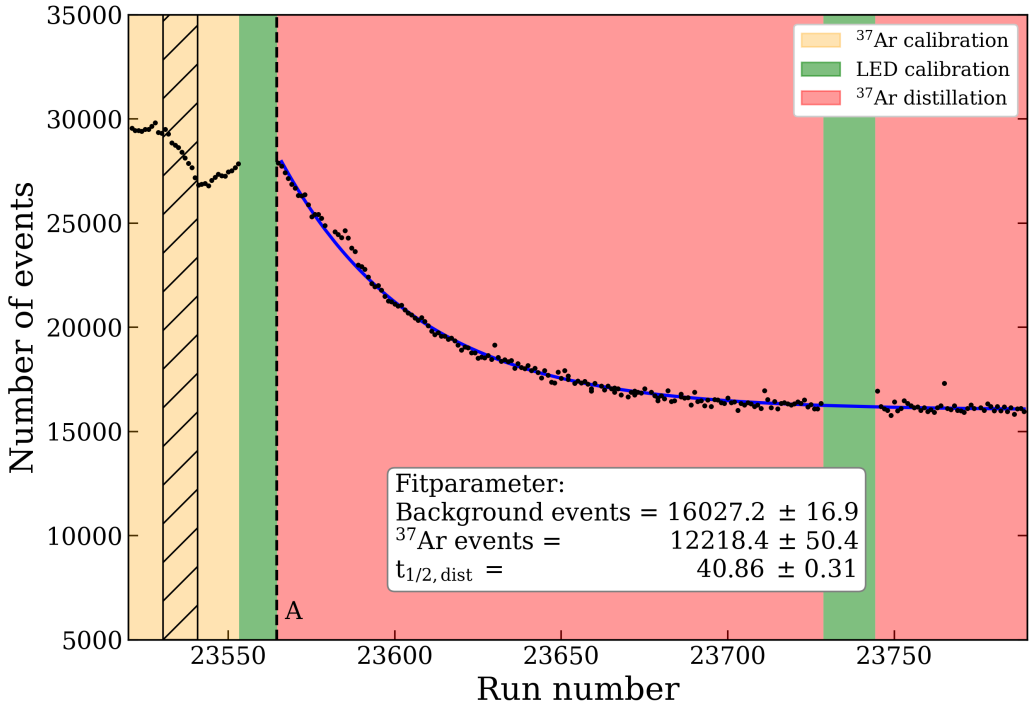

Figure 3.8.: *Distillation phase of the ^{37}Ar calibration sequence, starting at timestamp A. The red marked data is taken during active distillation. From an exponential fit with Eq. 3.4 the time constant of the distillation can be extracted, resulting in a half-life time for the activity of (40.86 ± 0.31) h. This results in a decade reduction time of (3.92 ± 0.03) days. The average number of background events per run based on the fit is (16027.2 ± 16.9). The hatched area marks the time window of the outgassing test.*

isotope.

These parameters are for the initial distillation phase and are based on the event rate only. They give an indication of what to expect for a more refined analysis. For this, a proper data selection is necessary, which is presented in the next chapter.

Parameter	Value	Error
Background rate [Hz]	4.452	±0.005
Ar activity [Bq]	3.395	±0.014
τ [h]	40.86	±0.31
Decade distillation time [d]	3.920	±0.030

Table 3.5.: *Results of the exponential fit on the distillation runs, converted to event rates. The main result of this preliminary analysis is the time needed to reduce the event rate by one order of magnitude:* 3.92 ± 0.03 *days.*

3.5. Summary

After initial testing with the small TPC setup in Mainz, the dosing branch was shipped to LNGS and successfully connected to the calibration system of XENON1T. At the end of the last science run of XENON1T, the first calibration of a dark matter detector with ^{37}Ar was performed.

The calibration was started with small doses to verify ^{37}Ar activity. During multiple injections to reach the target activity, the dosing procedure was improved and shortened. After several days of data taking, the ^{37}Ar was removed successfully during a 3-week distillation campaign, utilizing the krypton distillation column.

The activity was monitored live with a preliminary analysis based only on the event trigger rates of the detector.

The experience gathered during the calibration led to a redesign of the dosing branch and an improved, less time-consuming dosing procedure. This updated setup is now permanently installed inside the calibration box of the XENONnT gas system.

4. Low-energy Electronic Recoil Calibration of XENON1T with ^{37}Ar

The calibration of XENON1T took place over two weeks, providing several hundred hours of ^{37}Ar data at full rate, partially taken in parallel with ^{83m}Kr to facilitate direct comparison of both sources. This period was followed by a four-week distillation campaign to prove the removability of ^{37}Ar. Monitoring of the calibration and preliminary analysis of the distillation, as shown in chapter 3.4, was based on the detected event rate only. In this chapter, the analysis with selected ^{37}Ar data is repeated to confirm the preliminary results. Section 4.1 therefore introduces the data cuts used, to ensure a clean data selection. In section 4.2 the rate analysis is redone, this time with the properly selected ^{37}Ar rate only, resulting in the time constant for the distillation process.

The following sections use the ^{37}Ar data in its function as a calibration source. In section 4.3 the electron lifetime, a value essential for S2 signal correction, is calculated based on ^{37}Ar data. The result reveals a discrepancy and an anomaly compared to the standard value used in the XENON1T data analysis previously. A further comparison of the different electron lifetimes for multiple sources and the correction based on an electric-field simulation are shown, as well as an observed anomaly in the ^{37}Ar lifetime calculation, that results in a new correction for low energy signals. The development of the fit model for the 2.82 keV ^{37}Ar energy peak in S1-S2 data space is shown in sections 4.4, 4.5, 4.6, 4.7, followed by the calculation of the final results of the photon and electron yields for ^{37}Ar in section 4.8 (A simultaneous fitting method of the different regions, to simultaneously extract the S1 threshold of the TPC, is explored in the appendix A.1).

An alternative way to calculate the electron yield is started in section 4.11 with the estimation of the single electron yield. This value can then be used to directly compute the electron yield, as it is done in section 4.12.

An analysis of the data for the even lower energy peak at 0.27 keV, based solely on small S2 signals, is shown in section 4.13. Finally, the impact of this new analysis on already published XENON1T results, which especially include an observed excess of signals in the same energy regime as the ^{37}Ar decay, is analyzed in section 4.15 [77].

4.1. Science Run 1 cut selection

The first step in data selection is to select the relevant data by a coarse energy selection in the cS1-cS2_*bottom* space. Here cS1 stands for the *corrected*-S1, which refers to a correction for the (x,y,z)-position-dependend light collection efficiency of the S1 signal. Similarly, the S2 signal is corrected for (x-y)-dependent effects in electron extraction efficiency and proportional scintillation, and a depth correction based on drift time. The "*bottom*" indicates, that from the S2 signal only the light detected by the bottom PMT-array is used. This selection is done as the bottom part of the S2 is much more uniformly distributed and as such much less affected by, for instance, a defective PMT in the light pattern [39].

In XENON1T simulations were done with the Bayesian Band Fitting (BBF) framework. BBF utilizes a Marcov Chain Monte Carlo (MCMC) algorithm to provide an accurate description of the data. A simple simulation for a 2.82 keV interaction gave a prediction of the expected ^{37}Ar peak position and distribution in the cS1-cS2_*bottom* space. From the result of this simple simulation, some pre-selection borders were chosen: cS1 $>$ 0 pe, cS1 $<$ 50 pe and cS2_bottom $<$ 2500 pe.

Further data refinement is done by applying a set of cuts, designed to remove unwanted events. First, the official Science Run 1 (SR1) fiducial volume cut is applied. The cut removes events based on their position too close to the edges of the TPC, which are most likely caused by radioactive decays on the detector walls or from outside of the detector. Of all the applied cuts, this has by far the largest impact, removing approximately 40 % of the events. Other cuts are designed to remove events that might negatively impact the analysis due to an irregularity in peak-pairing, peak shape, etc. The cuts applied to the ^{37}Ar data, with a short explanation and selection criteria, are listed in the following, the survival fraction is listed in Table 4.1:

- **InteractionPeaksBiggest:**
  This cut is used to check for a correct pairing of the *s1* and *s2* signals. It is tested that the largest *s1* and the largest *s2* of a waveform are paired into an event. The condition implemented is:

  $$(s1 > largest\_other\_s1)\&(s2 > largest\_other\_s2)$$

- **S2TailCut:**
  This cut is designed to remove events containing an *s2* sitting on the tail of a *s2* signal from a previous event. This should help to remove accidental coincidence events before analysis. The cut introduces a new parameter which is designed as:

  $$s2\_over\_tdiff = s2\_area/(time\ difference\ to\ next\ event\ S2)$$

  For the current event, the maximum value of the last 50 values is taken and compared to a threshold value. This threshold value is chosen in a way, to keep the cuts acceptance at $\approx$ 95 %.

- **S2Width:**
  This cut is designed to remove gas events, accidental coincidences and events with unphysical drift times. To achieve this, the *s2_width* parameter is compared to a value obtained by applying a diffusion model to describe the evolution of the electron clouds during the drift in the liquid xenon and thus the expected time distribution of the *s2* signal. If the difference between the model measured *s2_width* is too large, the event is removed.

- **S2SingleScatter(Simple):**
  A cut to remove double scatter events, often caused by neutrons, although none are expected during ^{37}Ar calibration. For WIMPs, just a single interaction is to be expected, due to the very low cross section. For this kind of double scatter, only a single *s1* signal is expected, but at least two *s2* signals. Therefore the size of the *largest_other_s2* is compared to a threshold. This threshold (for the "'S2SingleScatterSimple"' version) is given by the empirical expression:

  $$largest\_other\_s2 < 0.00832 \cdot s2 + 72.3$$

  The more general version of the cut pays more attention to larger *s2* signals, adapting the threshold to higher values. For the range of interest for argon the *s2* signals are below 4000 pe. In this range, the thresholds given by both versions of the cut are nearly identical, with deviation starting in the third digit.

- **PreS2Junk:**
  A noise cut to remove waveforms with a noisy or shifted baseline. The major noise contribution originates from single electron signals, which follow a large S2 signal or originate from photoionization of the meshes.

  $$CutSignalOverPreS2Junk = (area\_before\_main\_s2 - s1) < 300$$

- **S1MaxPMT:**
  Removes an event when the contribution of a single PMT is dominant in the signal composition. This can happen if afterpulses or light emissions occur after large *s2* signals or scintillation in the photocathode occurs, producing an accidental coincidence. The condition to pass this cut is given by:

  $$s1\_largest\_hit\_area < 0.052 \cdot s1 + 4.15$$

- **S1PatternLikelihood:**
  Removes noise from events caused by the accidental coincidence of lone hit signals wrongly paired to a valid event. These events however differ from real events by a different PMT hit pattern for the S1 signals. Comparison with acceptable hit patterns derived from simulations allows the removal of most of these events.

- **CS2AreaFractionTop:**
  Another cut to remove gas events. This cut addresses a group of events that can pass the S2Width cut by applying a cut on the s2_area_fraction_top.

- **S2PatternLikelihood:**
  This cut is designed to remove events with an S2 pattern containing more than one maximum, which can occur in the case of a multi-scatter event or just an anomalous PMT hit pattern. This results in a pass condition based on the *S2_pattern_fit* value, a measure for the goodness of fit for the position reconstruction:

$$s2\_pattern\_fit < 0.0404 \cdot s2 + 594 \cdot s2^{0.0737} - 686$$

- **S1SingleScatter:**
  A cut to ensure a correct S1-S2 pairing by testing alternative pairings. If additional S1 signals can be paired with the main S2 (the time difference between the two signals is smaller than the maximum drift time in the TPC) and also the *S2_width* of the new pairing fits with the new drift-time (a comparison between the *S2_width* and the expected value derived from a diffusion model is made), the event is rejected.

- **KryptonMisIdS1:**
  Removes events originating from ^{83m}Kr decays, where large S1 signals are misidentified by PAX as S2 signals and thus are not recognized by other cuts like S1SingleScatter. To remove these events conditions for the *largest_other_s2* and the *largest_other_s2_delay_main_s1* parameter are set:

$$largest\_other\_s2 < 100\,|$$

$$largest\_other\_s2\_delay\_main\_s1 < -3000\,|$$

$$largest\_other\_s2\_delay\_main\_s1 > 0$$

- **PosDiff:**
  A cut to remove events with a larger difference in the reconstructed positions provided by the two different used reconstruction methods, the neural net (NN) and the Top Pattern Fit (TPF). The difference D is given by:

$$D = \sqrt{(x^{NN}_{observed} - x^{TPF}_{observed})^2 + (y^{NN}_{observed} - y^{TPF}_{observed})^2}$$

  The cut condition for the parameter D are given by:

$$D < 2429.322 \cdot exp(-\frac{log_{10}(s2)}{0.362}) + 1.587$$

- **SingleElectronS2s:**
  Optimizing for efficiency at the event building phase, the event classification of Processor for Analyzing XENON (PAX) allows a quite high number of single electron signals to be misclassified as S1 signals. These signals can be falsely paired with an S2, creating single electron background in the data. This cut is utilizing machine learning to reduce this background.

Cut	Effects	Fraction passed [%]
Fiducial Cut	Remove background events at detector edges	59.4
InteractionPeaksBiggest	Tests for correct pairing of largest S1/S2	96.2
CS2AreaFractionTop	Gas event removal	88.0
S2SingleScatter	Removes double scatter events	98.2
S2Width	Remove gas events/wrong drift-time combinations	95.6
DAQVeto	Remove possibly corrupted events due to busy DAQ	95.6
S1SingleScatter	Avoid Pile-up events	98.2
S2PatternLikelihood	Remove events with strange S2 hit pattern	85.5
KryptonMisIdS1	Remove events wrongly identified as krypton events	100
PosDiff	Remove events with different positions reconstructed by diff. reconstruction algorithms	94.1
SingleElectronS2s	Remove S2 due to single electron emission	99.1
S1PatternLikelihood	Remove events with strange S1 hit pattern	98.4
S1MaxPMT	Remove events based mostly on a single PMT	99.6
PreS2Junk	Noisy waveforms	99.9
S2TailCut	Remove events with overlapping S2	97.0
MuonVeto	Remove events with coincidence in the Muon Veto	99.5

Table 4.1.: *List of data cuts used in the analysis of ^{37}Ar data, based on already existing cuts of SR1. The fraction passed value should give an idea of the impact of certain cuts on the data. Due to a possible correlation between cuts that address similar events, these numbers might change slightly, when the cuts are applied in a different order.*

Table 4.1 gives a summary of the cuts used in this analysis and additionally the fraction of events that survive the cuts (individually for each cut). The numbers given are dependent on the order in which the cuts are applied, as some cuts address similar events (for example 'CS2AreaFractionTop' and 'S2Width' both address gas events) and as such are partially correlated.

For the distillation analysis an energy selection and a series of cuts were applied to the processed data to achieve a better result for the distillation time constant. The basic data quality cuts were applied first, including 'DAQVeto', 'MuonVeto', 'Flash' and 'S2Tails' cut. For further analysis an energy selection in the cS1/cS2 space was done, only considering events with $0 < \text{cS1} < 50$ and $0 < \text{cS2} < 2500$.

After this selection the rest of the cuts listed in Table 4.1 are applied. One additional cut, 'S1PMT3fold', was also included to ensure a 3-fold coincidence for the selected events (3-fold coincidence = at least 3 PMTs contribute to the event). To lower the sensitivity threshold, SR2 data was recorded partially with a 2-fold coincidence. As most of the used cuts were never adapted to 2-fold data, which might affect some of the cuts targeting low energy events, the 'S1PMT3fold' cut ensures proper functionality of the applied cuts.

4.2. Distillation analysis after event selection

The preliminary analysis of the xenon distillation after the ^{37}Ar calibration shown in Chapter 3.4.4 was based on a simple study of the detector event rates in the taken data sets. This worked fine for an initial result, but also includes some drawbacks including uncertainties in the result. For instance, the time steps were taken in one-hour steps, but the duration of one run is usually a few seconds longer than an hour, resulting in an accumulated time error, which can have an impact on the time constant of the applied exponential fit.

Additionally, the preliminary fit was done on the data rates only and as such is sensitive to a change in running conditions. Under normal conditions, the background should be stable and as such provide only a constant offset in the rate. Any irregularities, however, would affect the analysis and the fit results. This might be, for instance, an additional calibration source like ^{83m}Kr , so that the rates of both sources are affecting the analysis. With a proper event selection this can be avoided.

Fig. 4.1 shows the effects of the cuts on the data. Many of the events cut have either a very small S1 or S2 peak. These events are usually the result of a faulty pairing by PAX, where a valid S1/S2 is paired with a random small peak, classified as S2/S1 because no other valid peak was found in the allowed time window. This can, for instance, happen for gas events, where a large S2-like signal is produced in the gas phase, but there actually is no valid S1 produced.

The same procedure was applied to nearly all SR1 data to extract a value for the background in the same energy region. In this work the background is estimated from 'science' data, i.e., the data primarily used in dark matter search, as, during normal

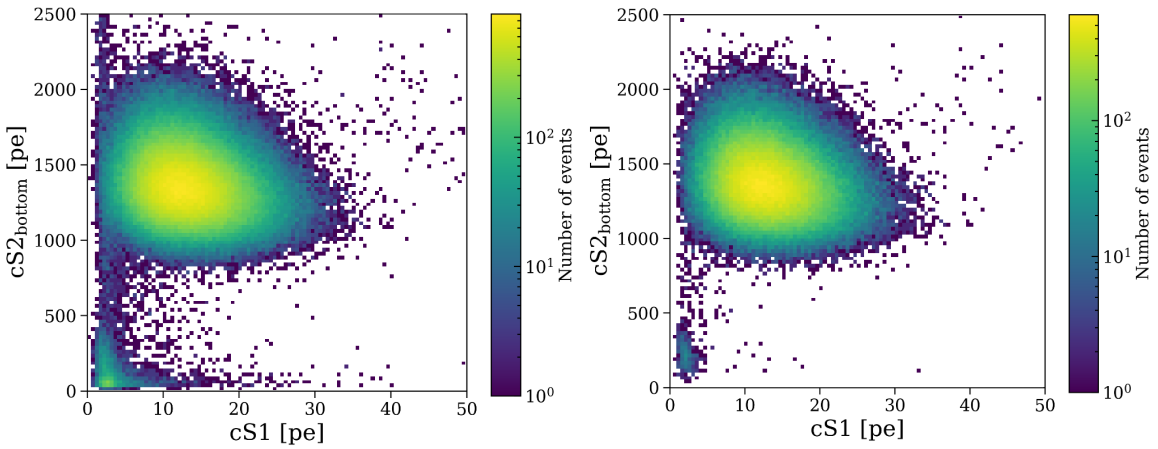

(a) ^{37}Ar *peak before cuts.* (b) ^{37}Ar *peak after cuts.*

Figure 4.1.: *Effects of the cuts on the selected* ^{37}Ar *events. The cuts mainly remove events with very small S1 or S2 signals. These are usually wrongly paired events, where either the valid S1 or S2 peaks are paired with a random small peak. In the corner with very low S1 and S2 values, besides some background events, some S2s from the 0.27 keV transition can be found, where they are paired with a random small peak classified as S1 (a detailed plot showing the 0.27 keV transition is shown in Fig. B.4 in the appendix on page 196). The plots for the cut effects are based on 50 runs of* ^{37}Ar *data, representing roughly 2 days of data taking.*

operations background events are expected to dominate in this energy regime. This evaluation of the background is necessary to accurately calculate the ^{37}Ar removal. The results of the cuts on the background events are shown in Fig. 4.2.

The Figures 4.1 and 4.2 illustrate the cut effects in the box energy selection for $0 < \text{cS1} < 50$ and $0 < \text{cS2} < 2500$. For the actual rate calculation used for the distillation analysis, an even finer selection was done: an ellipsoid selection region in cS1-cS2 space, containing 99,6 % of all argon events was chosen. This selection was applied to the ^{37}Ar data, as well as the background data to provide clean data samples. The ellipsoid selection is shown in Fig. B.5 in the appendix on page 197. With this selection and corrected for the lifetime, the background rate found is:

$$R_{Bkg} = (0.719 \pm 0.054)\,/t/d$$

A background correction is not necessary during the calibration data taking due to the amount of the injected ^{37}Ar , which achieves event rates in the order of 10 Hz. The value becomes important in the later stages of the distillation, when the number of events per run reduces drastically, partially with no valid ^{37}Ar events at all after applying the cuts. In the further analysis, the runs were grouped for each day. Even with these large time intervals, there are two days with no detected ^{37}Ar event, while for the last days at most one event was found. To extract the time constant of the distillation, the rate development was fitted with two exponential decays combined

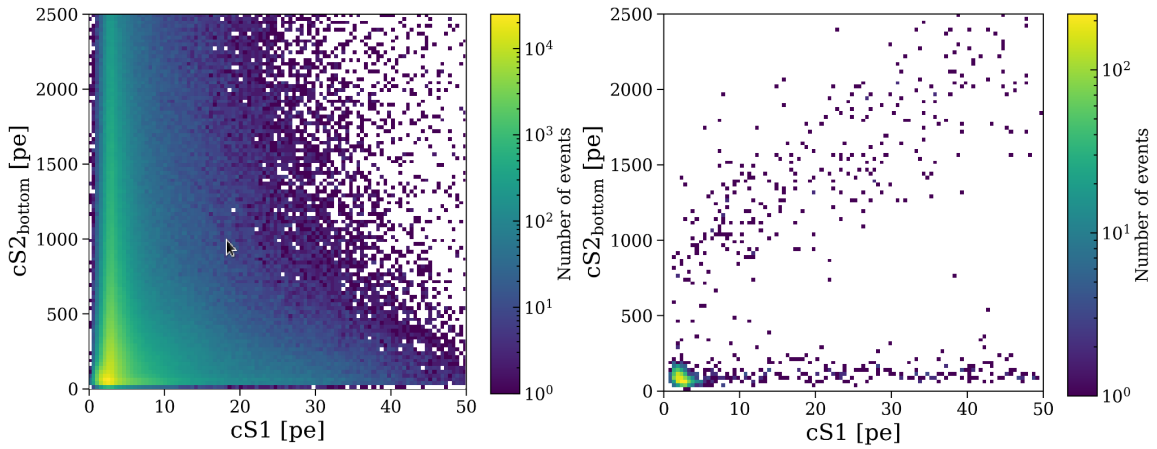

(a) *Background before cuts.*

(b) *Background after cuts.*

Figure 4.2.: *Effects of the cuts on the background in the same energy selection range as for the ^{37}Ar data. The plots effectively remove the bulk of the events, just leaving a few events on the ER-band and in the corner with very small S1 and S2. These events are easily removed with an S2 cut, leaving the ^{37}Ar peak region untouched. The background analysis is based on all of SR1 data (excluding calibrations or otherwise faulty marked runs) and represents roughly 184 days of data.*

with a linear offset for the background component. A binned likelihood fit is used to also take the days without any ^{37}Ar event into account. The function minimized is shown in Eq. 4.1.

$$R_{Ar,tot} = R_{Bkg} + H(t) \cdot R_{Ar} \cdot e^{-\frac{t}{\tau_{Dist}}} \cdot e^{-\frac{t}{\tau_{Dec}}} \tag{4.1}$$

The total rate $R_{Ar,tot}$ is composed of the background rate R_{Bkg} and the ^{37}Ar rate, which is reduced over time by two effects following an exponential decay: the distillation with a time constant of τ_{Dist} and the natural decay with a time constant of τ_{Dec}, which is fixed to $\tau_{Dec} = 50.55\,\mathrm{d}$ ($t_{1/2,Ar} \,/\, log(2)$). A Heavyside step function $H(t)$ is used to 'switch on' the argon at the start of the distillation period at time t = 0. The result of the fit is shown in Fig. 4.3.

The fit results in a decay time constant $\tau = 1.972 \pm 0.013$ days. With this value a rate reduction by a factor of ten every 4.543 ± 0.030 days can be computed.

Based on this analysis, we conclude that the ^{37}Ar can be removed efficiently within a reasonable time frame of 24 days. This qualifies this calibration source to be used not only after the experimental run at the end of an experiment's lifetime, as it was done for XENON1T, but also as an intermediate source for calibrations in between science runs.

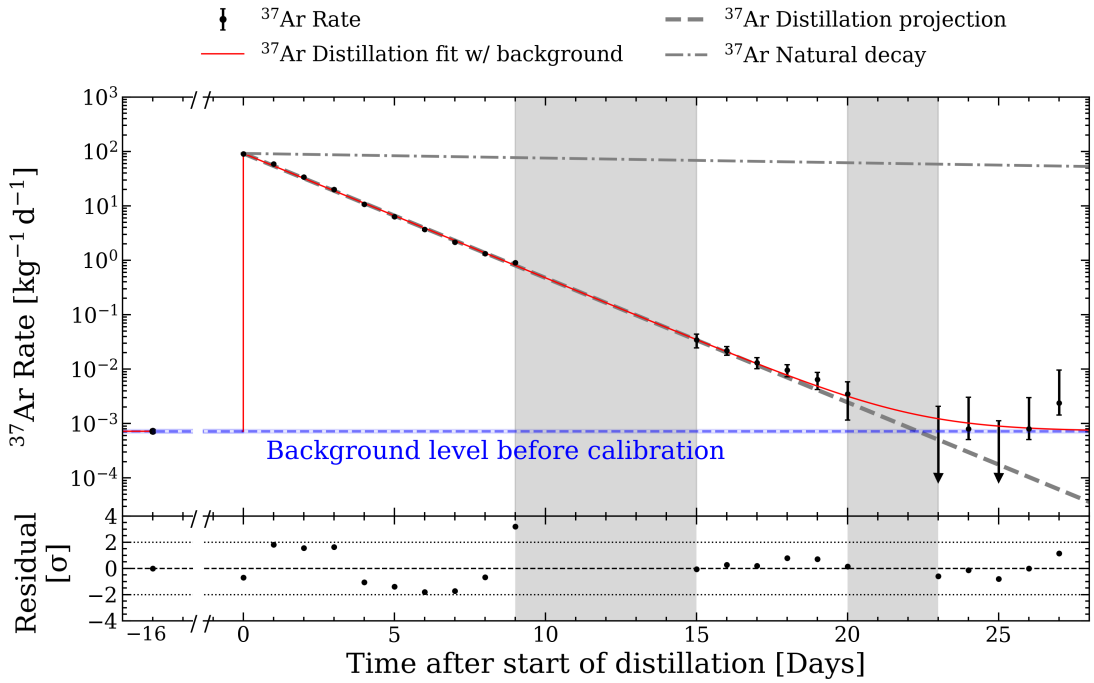

Figure 4.3.: *Distillation phase after the first ^{37}Ar calibration of XENON1T. The rate reduction is caused by a combination of distillation and natural decay. The background level from before calibration is reached after approximately 24 days. For comparison, the dashed-dotted grey line shows the rate reduction by natural decay only. With only this process present, it would take about 570 days to reach the background level again. For the last days, the measured rate was very low, with two days where no events were found at all, represented by the arrows. The uncertainties for the low rates in the last days were calculated using Feldman-Cousins intervals [78]. The fit accurately describes the rate, as can be seen in the residuals. The residuals are calculated by computing the difference between the data and the model and dividing it by the σ of the data. The grey regions show time windows during which other calibrations and tests were done, so no clean ^{37}Ar data is available from these days.*

4.3. Measurement of the electron lifetime with ^{37}Ar and comparison with other calibration sources

The XENON1T TPC is about 1 m in height, which is therefore the maximum distance the electrons created in an interaction have to drift to the liquid-gas interface before being extracted to create the S2 signal. During this drift, the electrons can be caught by electro-negative impurities in the liquid xenon. This behavior is similar to an absorption effect and thus, like in the case of photons absorbed in a transparent

medium, the 'absorption' of electrons during drift through the liquid xenon can be described by an exponential function.

Due to this, the electron lifetime is strongly correlated with the amount of impurities in the xenon, which is why the xenon needs to be constantly purified during the measurement.

To correct for the loss during electron drift, measurement and monitoring of the electron lifetime is necessary. In XENON1T, this is achieved with the help of regular calibrations using ^{83m}Kr. The ^{83m}Kr data can be plotted in a 2D-histogram, where the parameter 'S2_bottom' is plotted vs. 'drift_time'. As mentioned before, the parameter 'S2_bottom' indicates that only the part of the signal recorded by the bottom PMT array is used. To achieve a tighter band in the event distribution, the events are x-y-position corrected. This correction becomes even more important for sources with similar energies, as they might not be able to be distinguished without the correction.

The drift time is closely related to the z-position of the event in the detector. It reaches from 0 from an interaction on top of the liquid volume to a maximum of 750 μs for an interaction taking place at the position of the anode of the TPC. The maximum drift time is dependent on the applied drift field, which was set at 82 V/cm during data taking.

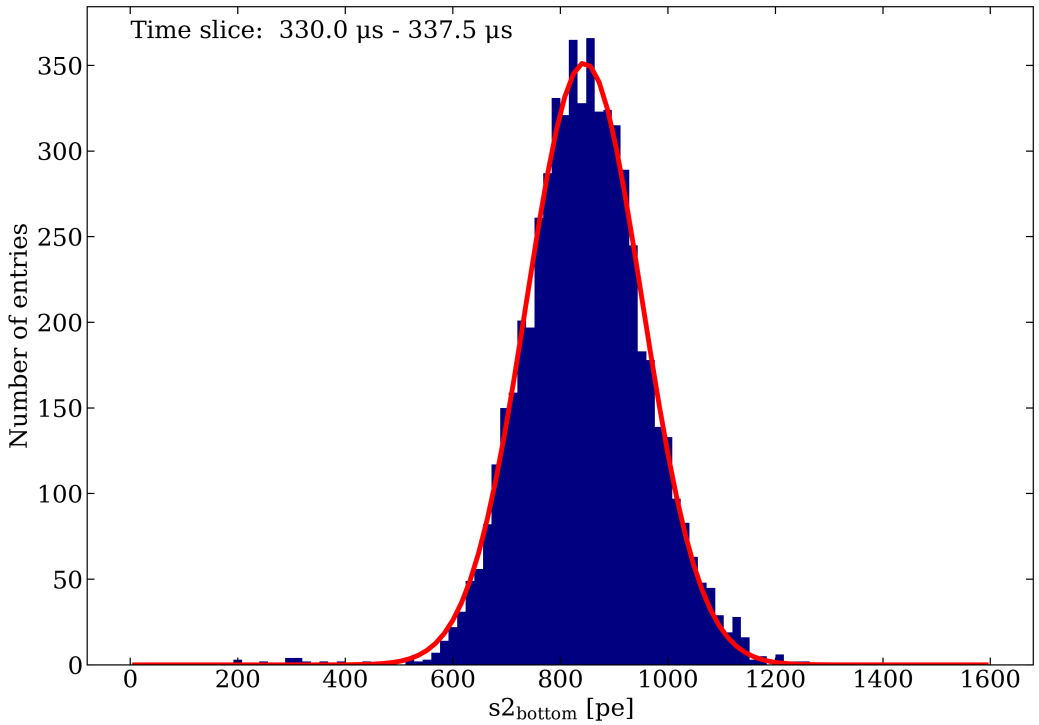

Figure 4.5.: *Example of a Gaussian fit on one of the $s2_{bottom}$ distributions, here randomly selected for the time slice of 330.0 to 337.5 µs drift-time. The mean values resulting from these fits are then fitted with the exponential function describing the electron lifetime.*

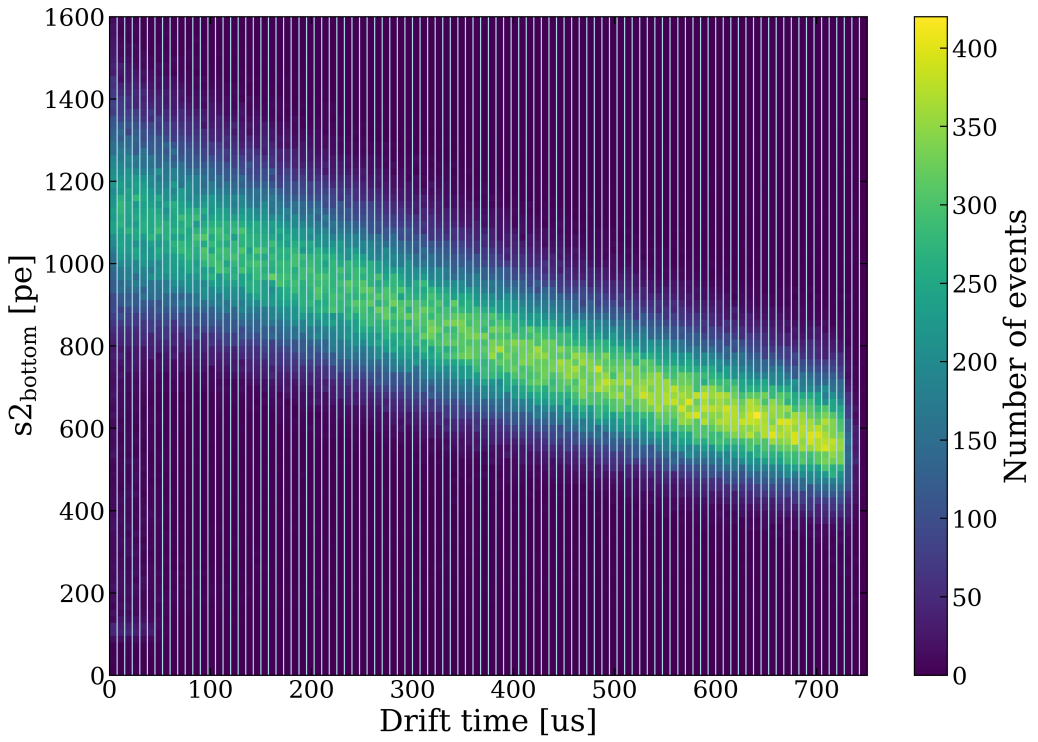

Figure 4.4.: *Exponential distribution of the $s2_{bottom}$ size in dependence of the drift time. The vertical lines show the division into drift-time slices that are later individually fitted with a Gaussian function.*

For a proper fit, the data is cut into drift-time slices of equal duration. The events of each time slice are filled into a histogram and the resulting 's2_bottom' distribution is fitted with a Gaussian to determine the mean value and the corresponding error. An example of such a fit applied to ^{37}Ar data is shown in Fig. 4.5. On the resulting mean values of all slices the exponential function of shape

$$s2 = s2_0 \cdot e^{-\frac{t}{\tau}} \tag{4.2}$$

is fitted, with the parameter τ giving the electron life time.

With ^{37}Ar an additional internal source is now available to be compared to ^{83m}Kr. As both sources were active in the TPC at the same time during the first week of the ^{37}Ar calibration run, both sources can be analyzed and compared directly, because data taking happened under the same exact detector conditions for both sources. The numbers of events for both sources were high enough to allow a fine time binning. Thus the drift time range was divided into 100 time slices for the analysis. The electron lifetime extracted with ^{37}Ar data has a value of $(947.00 \pm 0.18)\,\mu$s.

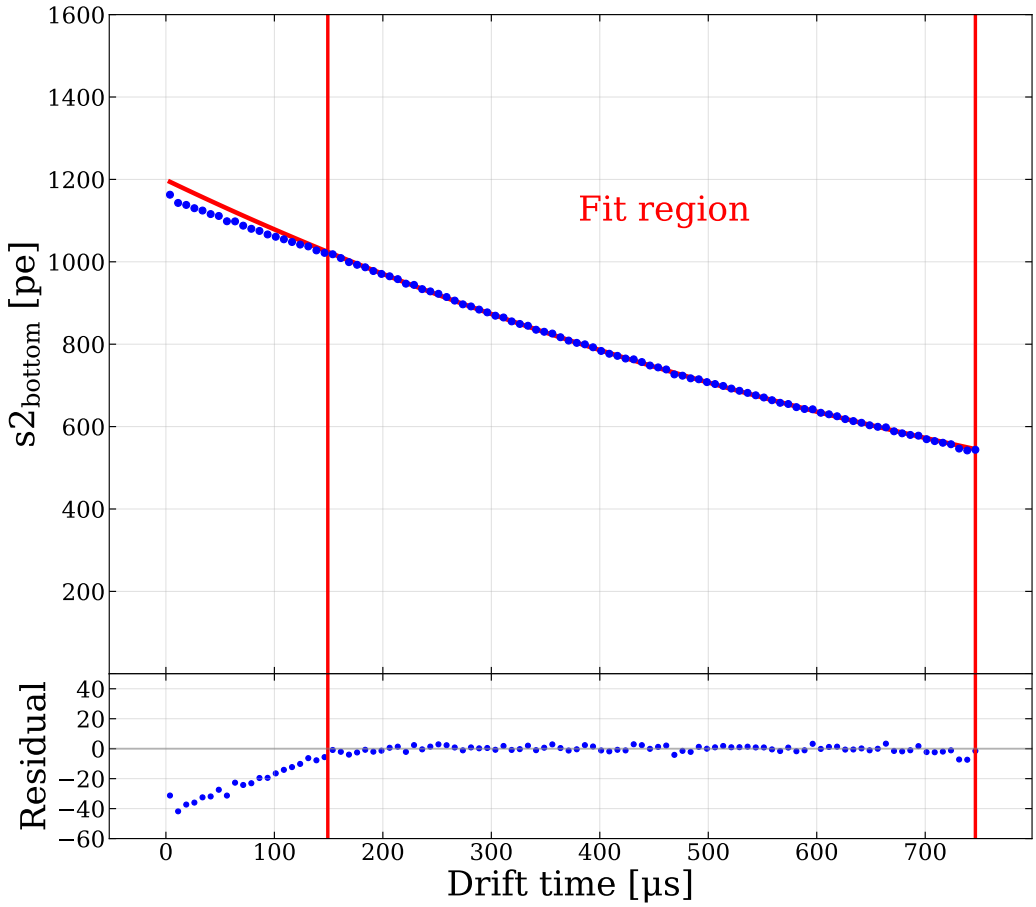

Figure 4.6.: *Exponential fit to the mean $s2_{bottom}$ values obtained from the Gaussian fits in each time slice. As can be seen, there is a significant discrepancy between the expected exponential behavior for drift times lower than 150 µs which roughly refers to the top 20 cm of the TPC. This anomaly is only observed for ^{37}Ar. From this fit an electron lifetime of (947.00 ± 0.18) µs is obtained.*

As can be observed in Fig. 4.6, ^{37}Ar shows a deviation from the expected exponential distribution for the top 20 cm of the detector. When compared with other calibration sources, as can be seen later in this and the following chapter, this is a feature unique to ^{37}Ar. It was found that this feature hints at so far unknown detector properties, which are discussed in more detail in Section 4.3.

Comparison with the electron lifetimes of other calibration sources

The value of the electron lifetime found for ^{37}Ar in the previous section is significantly higher than the value determined for ^{83m}Kr, with a value of $(832.62 \pm 0.43)\,\mu$s.

Besides this discrepancy between the measured electron lifetimes of ^{37}Ar and ^{83m}Kr, another one was already known for some time. The electron lifetime value obtained from ^{220}Rn, a calibration source used in irregular intervals, is much shorter than the value found for ^{83m}Kr. When comparing the decay energies of the three calibration isotopes, ranging from 2.82 keV (for ^{37}Ar) over 41.5 keV (^{83m}Kr) to 6.3 MeV (^{220}Rn, α-decay), this indicates an energy dependency of the electron lifetime.

To confirm this hypothesis, the electron lifetimes of the meta-stable xenon isotopes ^{129m}Xe and ^{131m}Xe are also determined. These excited states are formed as a side effect during neutron calibrations in the TPC when the energy transferred to the xenon isotopes is high enough to excite meta-stable states. The half-life times of these states are considerably long, 8.88 d for ^{129m}Xe and 11.93 d for ^{131m}Xe. The decay energies are 236.1 keV and 163.9 keV, respectively, thus placing these sources higher than krypton but much lower in energy than the radon source. During normal detector operation, these isotopes are considered low-rate background and runs recorded directly after neutron calibrations are therefore not used for dark matter searches. Due to the low rate, only a few thousand events are available for this analysis. To account for this, not 100, but only 30 time slices to extract the electron lifetimes are used.

The values found are $(747.93 \pm 2.65)\,\mu$s and $(825.78 \pm 4.90)\,\mu$s for ^{129m}Xe and ^{131m}Xe, respectively.

The extracted lifetimes confirm the assumption of an energy dependence for the lifetimes, as they result in lower values than the ^{83m}Kr, but higher values than the ^{220}Rn-fit.

To extend this analysis to higher energies, the same procedure was also applied to the persistent ^{222}Rn background. This isotope is part of the ^{238}U decay chain and therefore it is present in nearly every material, even in the construction materials of the detector, despite a reduction by screening and selection. Radon emanates into the liquid xenon from all surfaces which are in contact with xenon.

One main contributor to the radon content in the first science runs of XENON1T were the QDrive pumps used for gas recirculation. These pumps use pistons driven by a linear motor to move the gas. As they are free of lubricant, they are suited for ultra-pure experiments, but they are constructed from common materials without treatment or selection to reduce radioactive emanations [79].

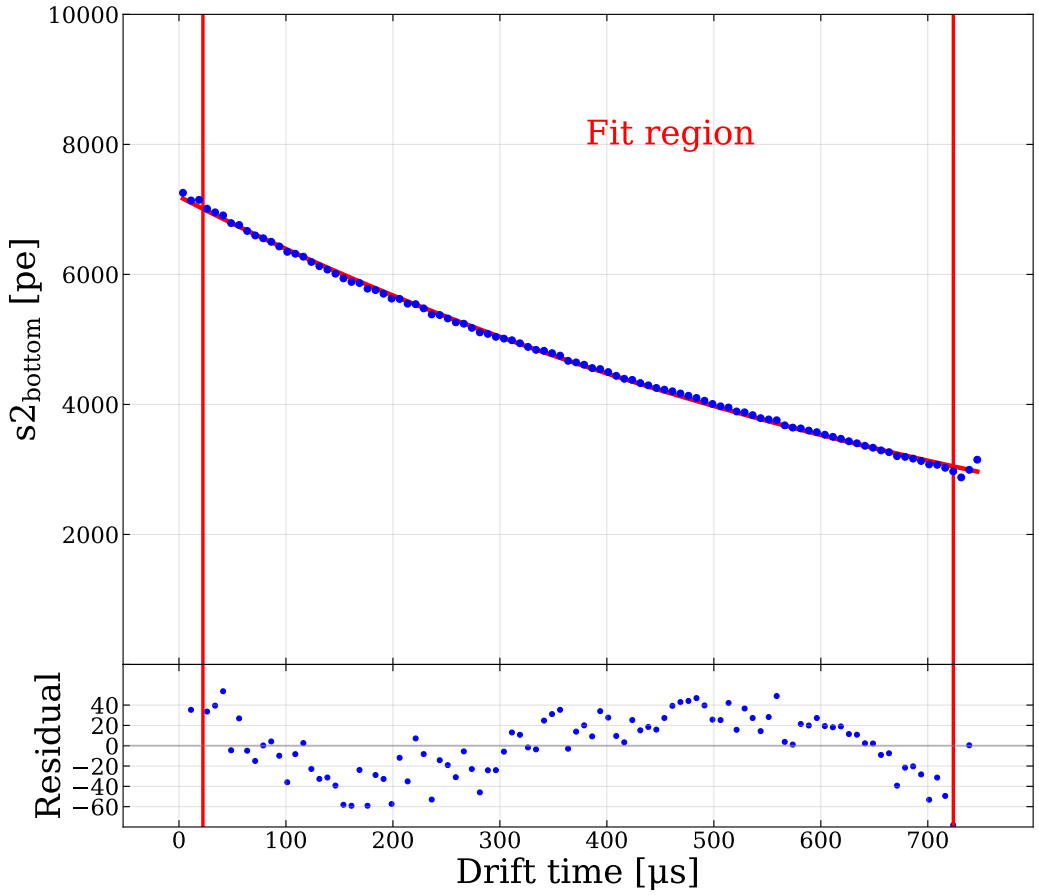

Figure 4.7.: *Exponential fit to the mean $S2_{bottom}$ of ^{83m}Kr with values obtained from the Gaussian fits in each of the 100 time slices. As can be seen in the residuals, there seems to be a systematic effect and a simple exponential fit does not describe the distribution of ^{83m}Kr as well as this is the case for ^{37}Ar, as shown in Fig. 4.6. The top and bottom three slices were removed from the fit region due to low statistics.*

For this reason, XENON1T eventually replaced the QDrive pumps in an upgrade by magnetically driven piston pumps in its gas system, built of screened material, which reduces the amount of radon by 40 % [80, 81]. Despite this reduction, the rate of the remaining ^{222}Rn content during the ^{37}Ar calibration period is high enough to allow a lifetime study. The decay energy, with a value of 5,590 MeV, is much higher than the previously examined sources and similar to the decay energy of 6,3 MeV of ^{220}Rn. Additionally, it needs to be considered that it decays via an α-decay and not an electron or γ-emission.

^{218}Po is the daughter nucleus of ^{222}Rn with a half-life time of 3.05 min and a decay energy of 6.115 MeV. Due to the applied x-y correction, the events of these two sources can be separated and evaluated individually, providing two additional electron lifetimes.

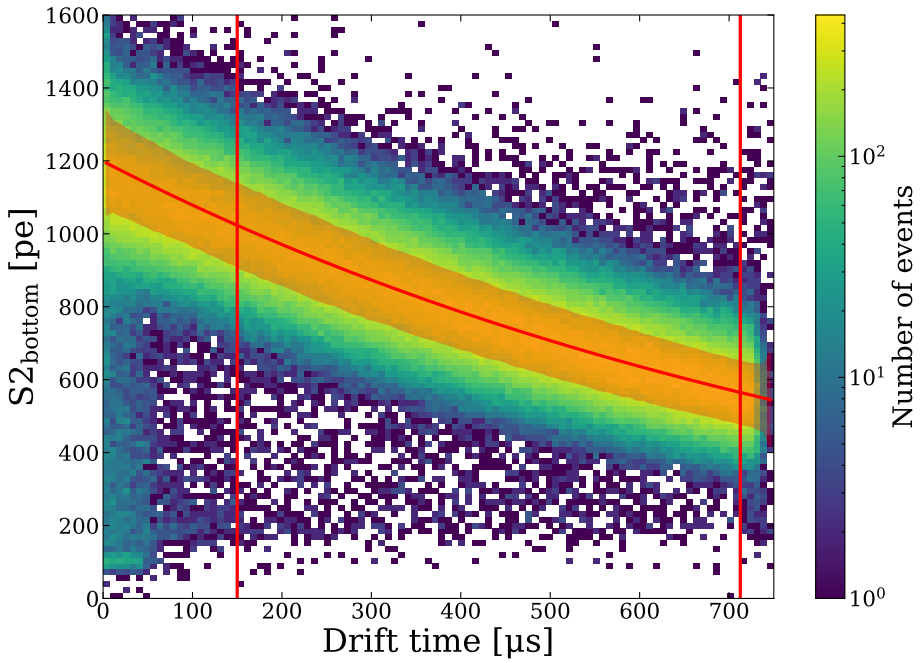

(a) *Argon*

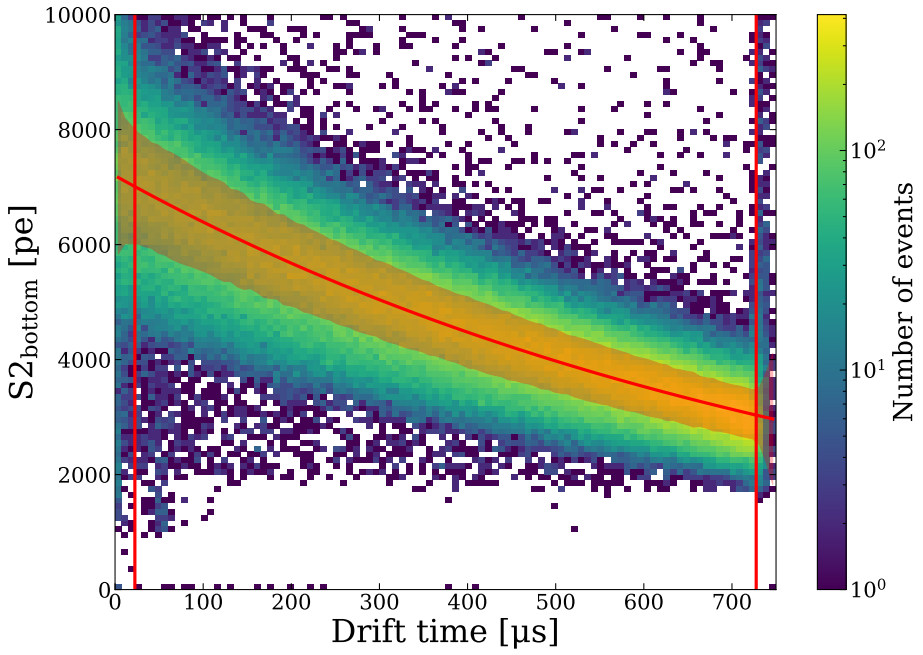

(b) *Krypton*

Figure 4.8.: *Direct comparison of the results from the ^{37}Ar and ^{83m}Kr fits. The 2D histogram shows the data in the $S2_{bottom}$ vs. drift time space and the red line shows the fit results from the time slicing. The vertical lines mark the data range used in the fit. The orange highlighted region represents the $\pm 1\sigma$ width of the Gaussian fits in each time slice.*

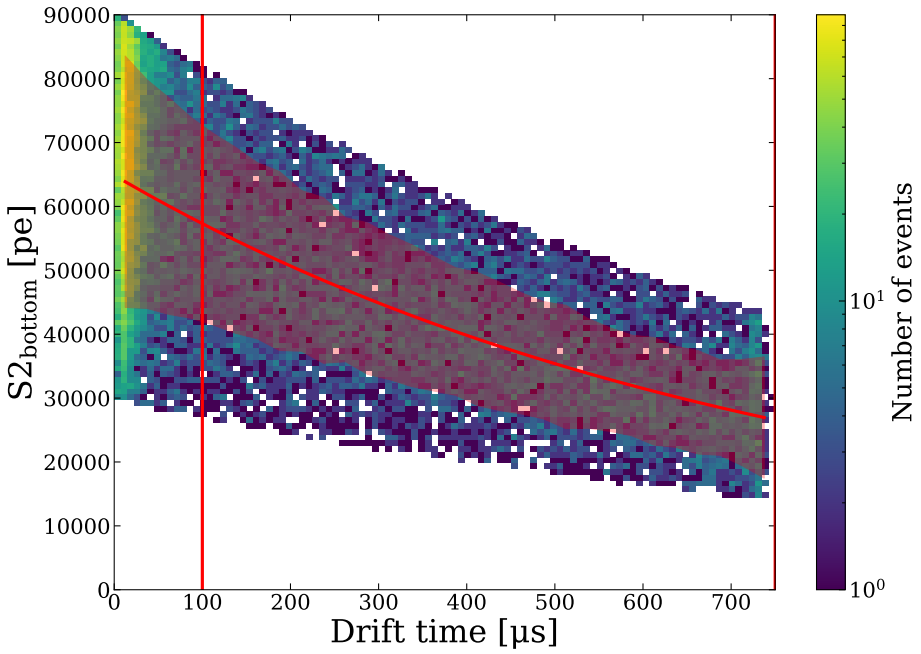

(a) ^{129m}Xe

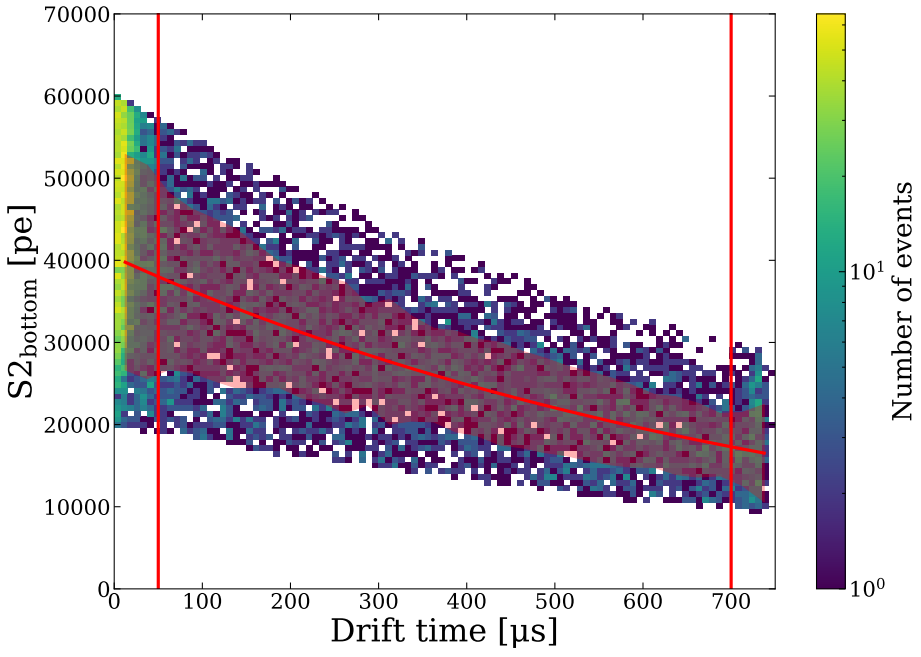

(b) ^{131m}Xe

Figure 4.9.: *Direct comparison of the results from the ^{129m}Xe and ^{131m}Xe fits. These isotopes are created as a side effect of neutron calibrations of the TPC, not as a main calibration source. Therefore the statistics are much lower than for the regular sources (^{37}Ar and ^{83m}Kr). To account for this and still have enough statistics for a reasonable Gaussian fit, the drift time range is divided into only 30 slices for these isotopes. Due to surface effects, the top regions are not included in the fit. The slice fit plots for these isotopes can be found in App. B.3 on page 198 in Fig. B.6 and Fig. B.7 for ^{129m}Xe and ^{131m}Xe, respectively.*

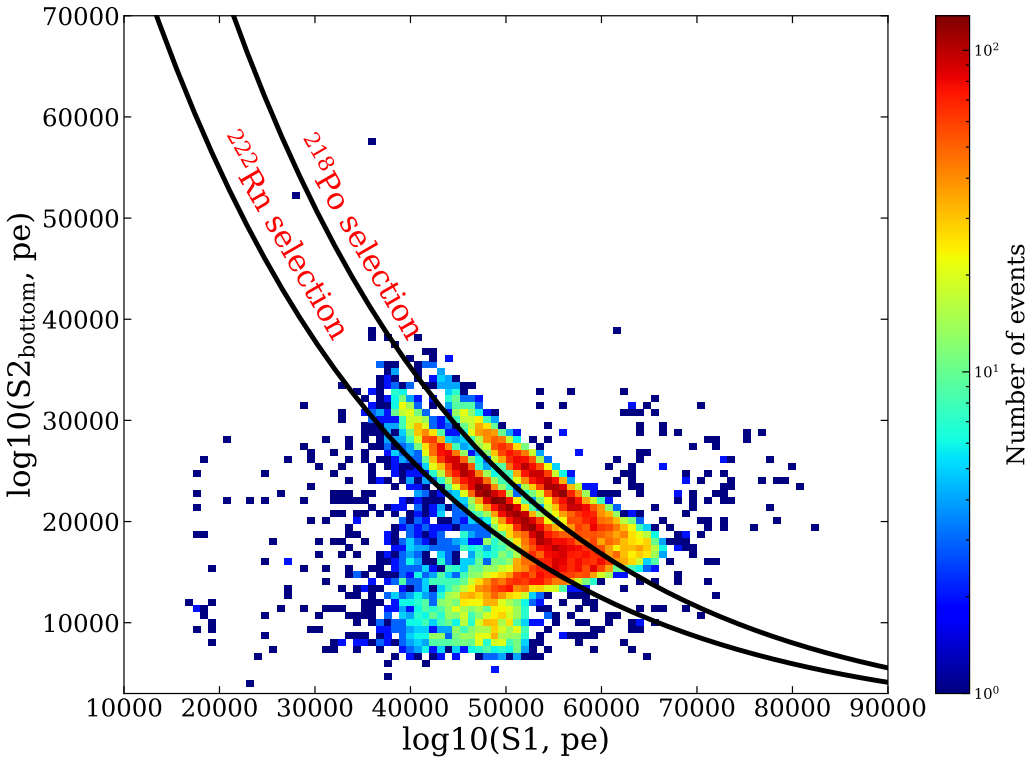

Figure 4.10.: *Data selection in the high energy region for the α-decaying isotopes ^{222}Rn with an energy deposit of 5,590 MeV and ^{218}Po with a deposit of 6.115 MeV. After the application of (x, y)-spatial correction maps on the S2, both peaks can be distinguished. Two manually adjusted exponential functions are used to select the events for each of the two components.*

The data selection was done in the S1/spatial-corrected-S2$_{bottom}$ space as can be seen in Fig. 4.10. The black lines highlight the selection area. They are based on empirical exponential functions:

$$S2 = A \cdot e^{-\frac{S1}{B}} \tag{4.3}$$

The parameters were chosen by eye to match the event distribution and are A = 155000/B = 27000 and A = 115000/B = 27000 for the upper and lower line respectively.

With these two selections, the electron lifetimes are measured to be (658.29 ± 0.59) μs and (765.64 ± 1.23) μs for ^{218}Po and ^{222}Rn, respectively.

Comparing the results for the electron lifetimes of the various sources indicate a systematic effect. The most apparent assumption would be an energy dependence as the electron lifetime decreases with increasing decay energy, as is shown in Tab. 4.2 and Fig. 4.12.

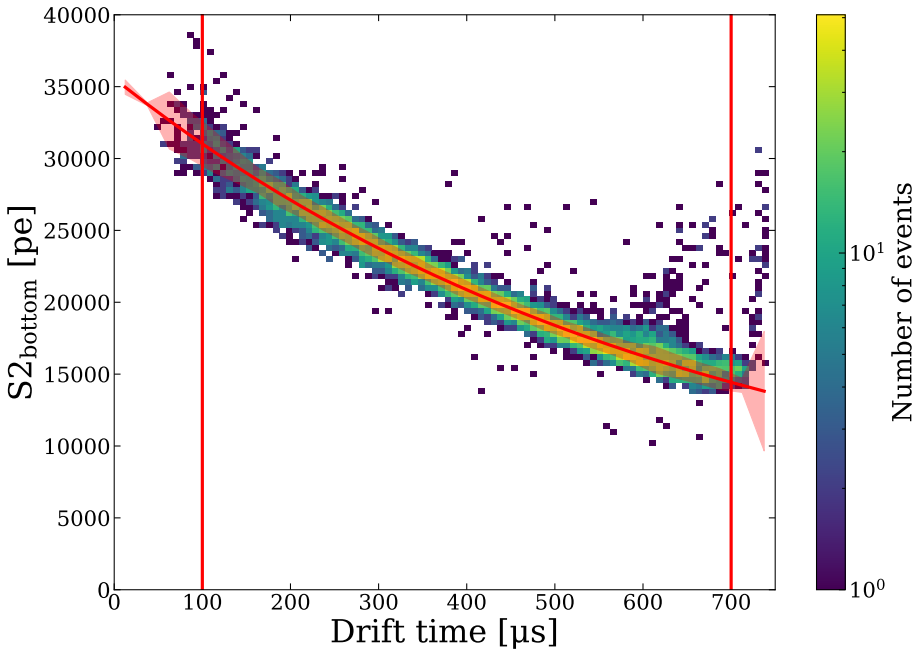

(a) ^{218}Po

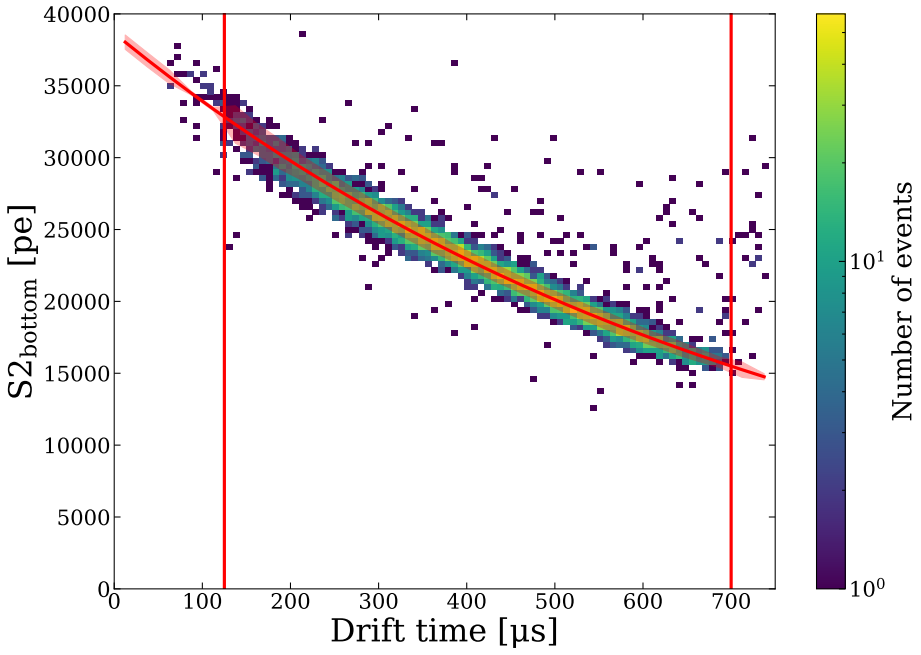

(b) ^{222}Rn

Figure 4.11.: *Direct comparison of the results from the ^{218}Po and ^{222}Rn fits. The vertical red lines represent the fit range, only the time slices between the lines are taken into account for the fit. Due to low statistics, similar to the xenon isotopes, the drift time was only divided into 30 slices. The upper and lower parts of the TPC had to be excluded, as the Gaussian fits in these time slices did not converge due to the very low statistics. The slice fit plots for these isotopes can be found in App. B.3 on page 198 in Fig. B.8 and Fig. B.10 for ^{129m}Xe and ^{131m}Xe, respectively.*

Isotope	Energy	Decay type	Electron lifetime [μs]
^{37}Ar	2.82 keV	Auger e$^-$	947.00 ± 0.176
^{83m}Kr	41.5 keV	e$^-$ + γ	842.16 ± 0.13
^{131m}Xe	163.9 keV	e$^-$ + γ	825.78 ± 4.90
^{129m}Xe	236.1 keV	e$^-$ + γ, 2γ	747.93 ± 2.65
^{222}Rn	5.590 MeV	α	765.64 ± 1.23
^{218}Po	6.115 MeV	α	658.29 ± 0.59

Table 4.2.: *Summary table of the isotopes used to determine the electron lifetimes.*

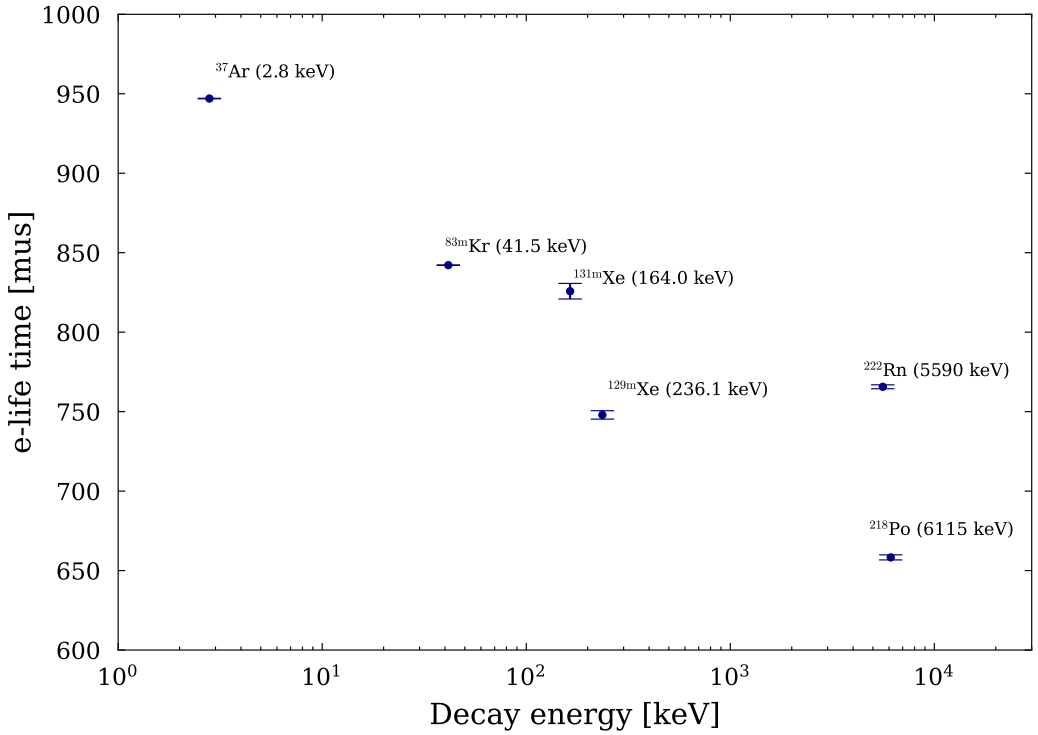

Figure 4.12.: *Direct comparison of the electron lifetime results from the different sources discussed in this section. Based on the observed correlation between the electron lifetime and the decay energy, a dependence between these to observables can be assumed.*

It is, however, not plausible to assume that the decay energy influences the drift loss of electrons throughout the TPC. The main quantities influencing the electron lifetime are the purity of the xenon and the drift field.

To observe such an effect, a constant 'purity gradient' needs to be permanently present inside the TPC volume. As the xenon is constantly recirculated by the purification system this reason can be excluded.

A more reasonable assumption is a different rate of electron production in the ionisation and recombination process during the interaction, which needs to be position

dependent. One important detector parameter that varies over the TPC volume and can influence the electron production process in this way, is the electrical drift field applied in the TPC. A further study on this topic is presented in the next section.

Impact of field non-uniformities on the electron lifetime

The XENON1T detector uses a drift field to transport the electrons freed in interactions to the liquid-surface interface, where they are extracted and produce the S2 signal. Due to geometry effects and wall charge-up, the applied drift field is not perfectly homogeneous. Simulations show variations in the field strength up to 20 % in the relevant regions, as is shown in Fig. 4.13. In part, deviations from uniformity were caused by the fact that the cathode high voltage could not reach the design value,

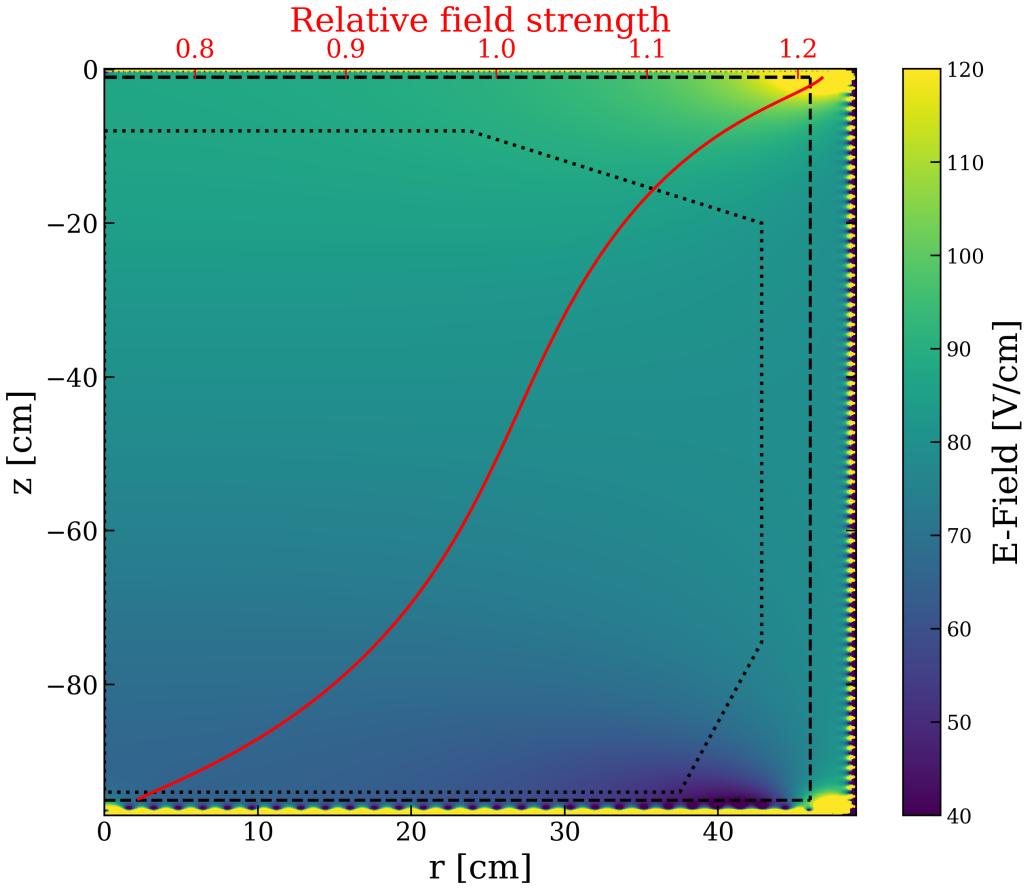

Figure 4.13.: *Simulation of the drift field in the XENON1T detector. The black dashed lines show the selected region for the relative field strength calculation, the dotted line shows the fiducial volume. This is necessary to exclude the strong field variations that appear near the edge of the detector and otherwise would dominate the mean value. The red line shows the relative change of field strength, averaged over r, as a function of z. Field simulation done by Junji Naganoma.*

resulting in a significantly reduced field strength.

These field variations not only determine drift path and velocity of the electrons, but also affect the recombination rate at the interaction site. In regions with a weaker field the recombination rate is higher, hence a larger S1 signal is created, while less electrons are freed and drifted, resulting a smaller S2.

The NEST can be used to simulate the effect of different field strengths on the charge yield. The results of these simulations is shown in Fig. 4.14 and shows the relative charge yields for a selection of some of the used calibration sources over a range of fields. The relative charge yield is calculated with respect of a field strength of 82 V/cm, which is the mean value used during the XENON1T science run considered in this analysis. As can clearly be seen, the higher energy interactions from ^{83m}Kr and ^{131m}Xe are more affected by field variations than the low energy ^{37}Ar source, which varies by less than 5 % between 60 V/cm and 95 V/cm.

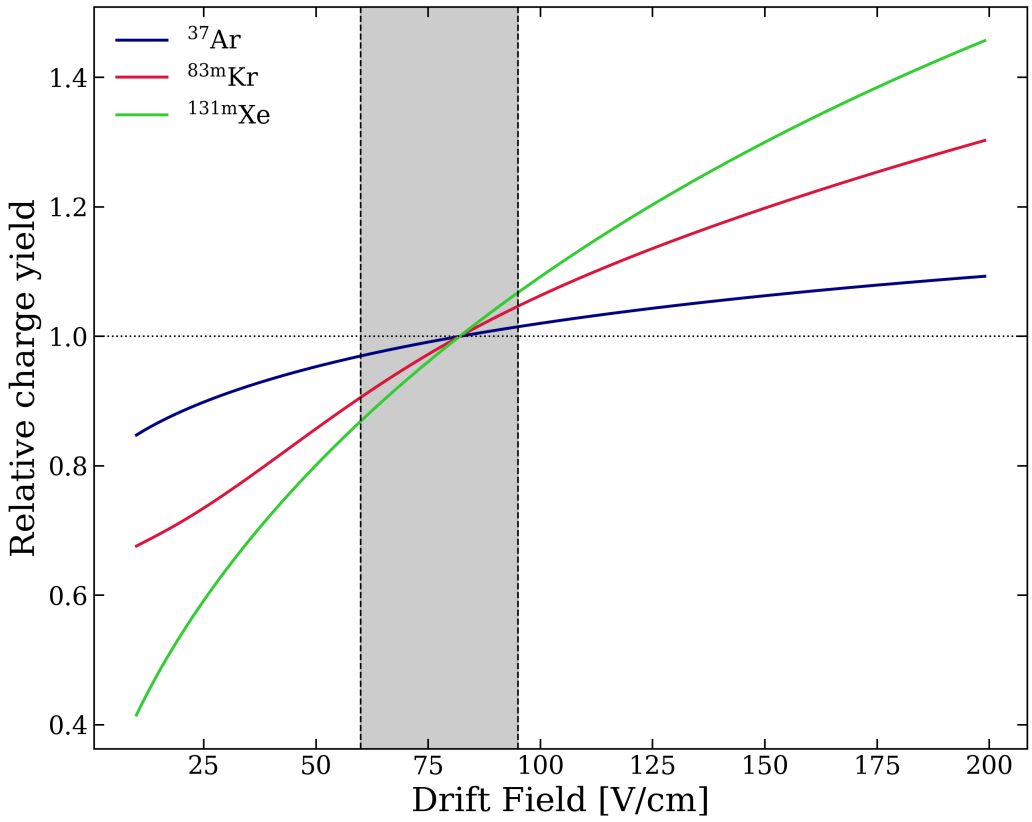

Figure 4.14.: *Relative charge yield changes of different sources in varying drift fields. The values are calculated in relation to a field of 82 V/cm, which is the mean drift field applied in the XENON1T TPC. Clearly ^{37}Ar is the least affected and shows the smallest variations, while with increasing decay energy the relative yield changes increase with changing fields. The grey marked region marks the range in field strengths present in the TPC.*

Fig. 4.15 shows this relative charge yield change in dependence of drift time, using the field variations resulting from simulations, which are shown as a red line in Fig. 4.13. Based on the simulation, field variations between 60 V/cm and 95 V/cm occur over the full height of the TPC, when averaged over r. For each source and its energy, a relative correction factor in dependence of drift time (which has a direct relation to the z-position), again with a reference mean field of 82 V/cm, can be calculated, using NEST.

In Fig. 4.15 these field corrections are applied to the resulting fit curves from the slice fitting. To visualize the effect only the curves for ^{37}Ar and ^{83m}Kr are shown. As already implied in Fig. 4.14, the effect on the ^{37}Ar curve is minimal. The ^{83m}Kr however now has nearly the same shape, and thus it can be assumed, also a very similar lifetime constant, to the ^{37}Ar curve. The ^{83m}Kr curve is scaled down in S2 to

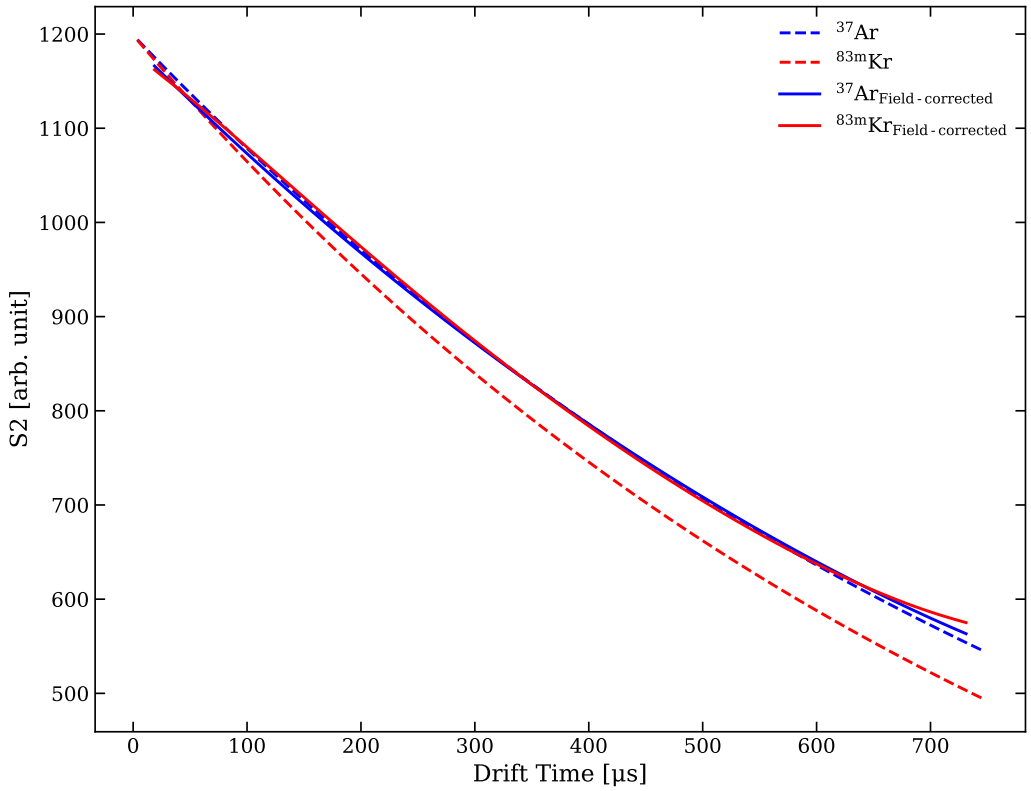

Figure 4.15.: *Relative charge yield changes of different sources in varying drift fields. For clarity only ^{37}Ar and ^{83m}Kr are shown. For a first prove of principles the fit result curves from Section 4.3 are corrected with the field correction. The dashed lines represent the shape of the uncorrected lifetime curves. The solid blue and red lines show the curves after the field corrections. Clearly visible is the much better agreement, indicating that after correction similar electron lifetime can be expected from both (and also the other) sources. Note that the ^{83m}Kr curves are scaled down in S2 to allow direct comparison with ^{37}Ar.*

the ^{37}Ar value at zero drift time to allow a direct shape comparison.

To verify the assumption that field effects are the main reason for the observed variations in electron lifetimes, the procedure described in Section 4.3 is repeated, taking the field corrections into account. The mean S2 values are field corrected, before the exponential fit is applied to extract the electron lifetime. This procedure is performed for the corrected ^{37}Ar, ^{83m}Kr as well as the xenon isotopes ^{129m}Xe and ^{131m}Xe. After correction the resulting electron lifetimes of the different sources are much more similar, as shown in Tab. 4.3. For completeness, the plots of the fit results are shown in the appendix on page 202.

Isotope	Energy [keV]	Lifetime (no correction) [μs]	Lifetime (field corrected) [μs]
^{37}Ar	2.82	947.00 ± 0.18	921.30 ± 0.19
^{83m}Kr	41.5	842.16 ± 0.13	915.89 ± 0.18
^{129m}Xe	236.1	747.93 ± 2.65	931.69 ± 6.81
^{131m}Xe	163.9	825.78 ± 4.90	937.37 ± 9.32

Table 4.3.: *Summary table of the electron lifetimes before and after field correcting the S2 values. After the field corrections, the different sources yield much more uniform results.*

It should also be mentioned, that in case of ^{83m}Kr, the observed structure in the residuals of the fit on the uncorrected data, shown in Fig. 4.7 is no longer observed after the field correction is applied, indicating that ^{83m}Kr is affected by the field variations.

A direct comparison between ^{83m}Kr data before and after field correction, and their fit residuals, is shown in Fig. 4.16. Similar structures in the residuals are not observed for the xenon lines, which may be caused by the low statistics of the data used for this analysis.

It should also be mentioned, that in case of ^{83m}Kr, the observed structure in the residuals of the fit on the uncorrected data, shown in Fig. 4.7 is no longer observed after the field correction is applied, indicating that ^{83m}Kr is affected by the field variations. A direct comparison between ^{83m}Kr data before and after field correction, and their fit residuals, is shown in Fig. 4.16. Similar structures in the residuals are not observed for the xenon lines, which may be caused by the low statistics of the data used for this analysis.

In conclusion, the main reason for different electron lifetimes is found in the non-uniformities of the drift field of the TPC. The variations in the field cause variations in the resulting charge yields, which impacts the measured electron lifetime. This highlights the importance of a good understanding of the applied fields in the detector and also promotes an improved correction of the data in the future. It also highlights an important feature of ^{37}Ar, as this source, as shown by our data and in agreement

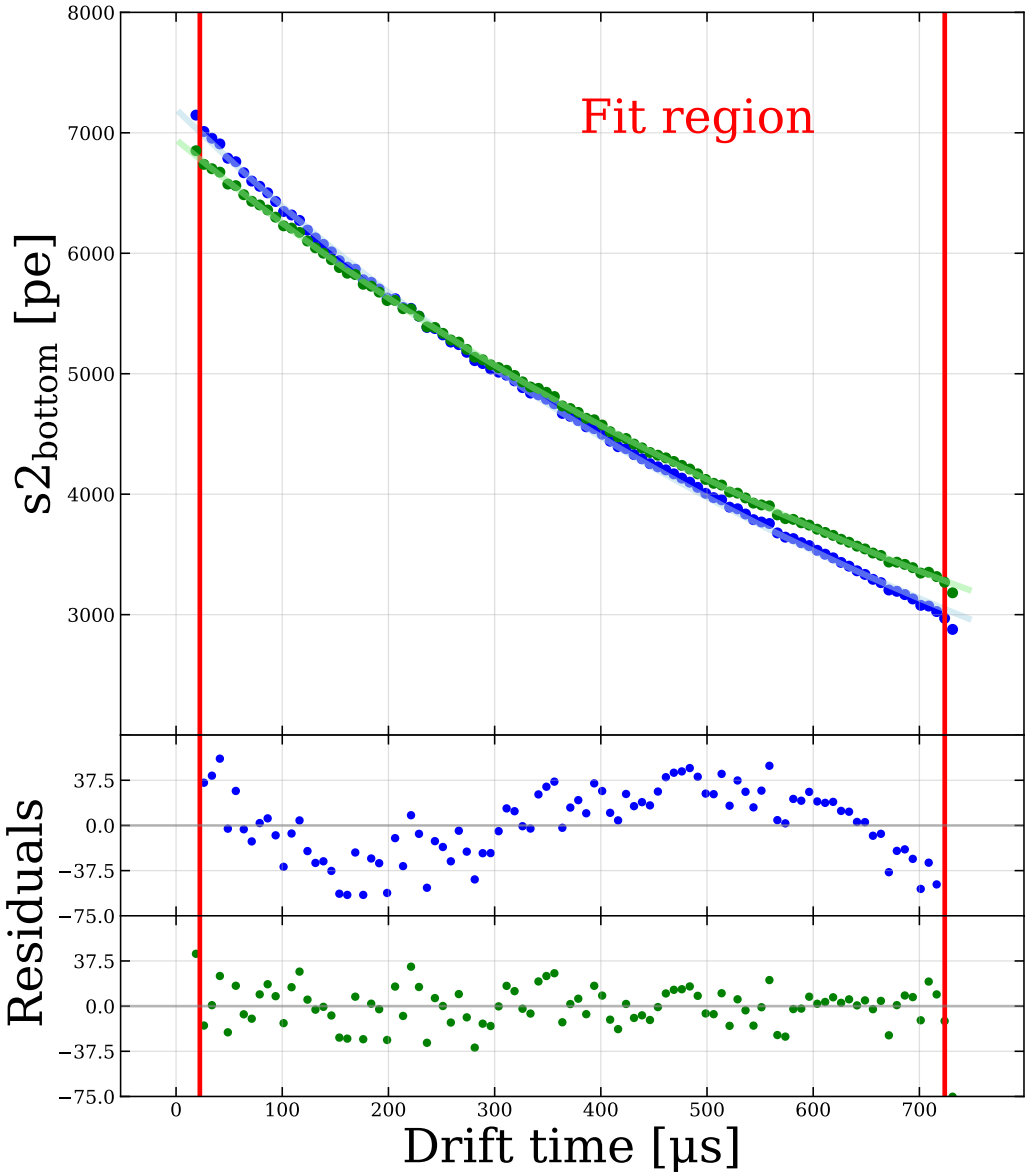

Figure 4.16.: *Comparison of the fit to ^{83m}Kr data before (blue) and after (green) field correction. Besides a different time constant of the fitted exponential function, which now results in an electron lifetime similar to the one of ^{37}Ar, the residuals now do not show the systematic anymore that was observed before. This indicates that already ^{83m}Kr is influenced noticeably by the field inhomogeneity and should be corrected.*

with NEST, is barely affected by field variations and thus provides an electron lifetime close to the true value, even without the proper correction applied.

Anomaly in the electron lifetime of ^{37}Ar in the top region of the TPC

A feature unique to the ^{37}Ar source is a kink observed in the electron lifetime curve. As can be seen in the previous section in Fig. 4.6, the S2 size deviates from the expected exponential behavior in the top 20 cm of the TPC. This feature is not observed for the more energetic calibration sources like ^{83m}Kr, ^{129m}Xe and ^{131m}Xe, suggesting an energy dependence of this effect. The fact that it appears only in a certain spatial region of the detector, namely the top 20 cm, indicates some detector-related reasons.

Two effects were found to be responsible for the observation:

- **^{37}Ar Signal width:**
  Due to the low energy of the ^{37}Ar interaction, the S2 width is small compared to the other calibration sources, with very short rise and fall times. As with all other signals, the S2 of ^{37}Ar produces AP signals with a short time delay in the $O(\mu s)$. As the S2 signals are usually longer than this time frame, the first APs are merged into the S2 and cannot be distinguished from the main S2 signal. This causes a bias for all S2s, but since the AP size is expected to be proportional to the main S2 causing it, the bias is the same for all S2s. The low-energy signature of ^{37}Ar with its short duration allows for a clear enough separation between the main S2 and the following AP signal, so the event builder of XENON1T can separate these two signals. As a result the ^{37}Ar S2s are actually *not biased* and thus smaller in size. This of course must be considered for all S2s from such low-energy interactions and must be taken into account in further analysis.

- **Signal widening by diffusion:**
  The effect described above is only visible for interactions in the top region of the TPC, where the signals are narrow. For long drift times diffusion broadens the electron cloud $\propto \sqrt{t_d}$. At a depth larger than $\approx$20 cm, the width of the main S2 broadens to a point where the AP cannot be separated anymore by the event builder from the main S2 and thus they are merged into one combined S2 again.

To enable a coherent analysis, a way to correct for the observed effects must be found. Diffusion at some point smears out any peak enough to merge it with its AP. As this effect makes it impossible to distinguish them afterwards, one can instead bias the ^{37}Ar data artificially, making them directly comparable to the rest of the data. This can be done by merging the ^{37}Ar S2 with its AP.

Simple selection of afterpulse candidates

The first step in applying a correction to the data is a suitable selection of events that need to be corrected. To generally select ^{37}Ar interactions, only events with an uncorrected S1 area smaller than 100 pe and an uncorrected S2 smaller than 5000 pe are selected.

The effect of too small S2 areas is predominantly observed in the top region of the TPC. Yet a threshold-like selection in the z-coordinate does not help as a continuous transition from events with separated APs to events with merged APs is expected.

Another selection criterion is the time delay between the S2 and a potential following signal. After event building and peak classification, it is common for a waveform to contain more than one peak classified as S2. While events with two similar-sized S2s are removed before analysis (see S2SingleScatter-cut in the cut list explained in Sec. 4.1), events with smaller secondary S2s are kept. The second largest S2 is also saved in the standard minitrees, so these can directly be used for this analysis.

A suitable selection can now be made in the delay time between the largest S2, which is assigned as the main S2 to the event, and the second largest S2 of an event. Fig. 4.17 shows this parameter plotted against the drift times (= equivalent to the z coordinate) for a selection of ^{37}Ar events.

These plots show a very prominent population of secondary S2s with a delay time shorter than 7.5 μs (indicated by the red line). This selection criterion is chosen by eye with the expectation in mind that the secondary S2s should be uniformly distributed in the TPC, independent of their z-position. This is indeed the case for the lower part of the TPC (with drift times $> 300\,\mu$s), whereas the population in the lower left corner is identified as S2s with separated AP.

As the kink in S2 vs. drift time was only observed for ^{37}Ar data, this population is expected to not be present for the other calibration sources. Fig. 4.18 shows the same plot for ^{83m}Kr data. Due to the two-step decay of ^{83m}Kr the secondary S2 delay is shorter compared to ^{37}Ar, so the selection threshold is set to 4.25 μs. Below this line only a negligible number of events are selected for AP correction, following expectations. For completeness, there are also the plots for ^{129m}Xe and ^{131m}Xe given in the appendix B.5 on page 206.

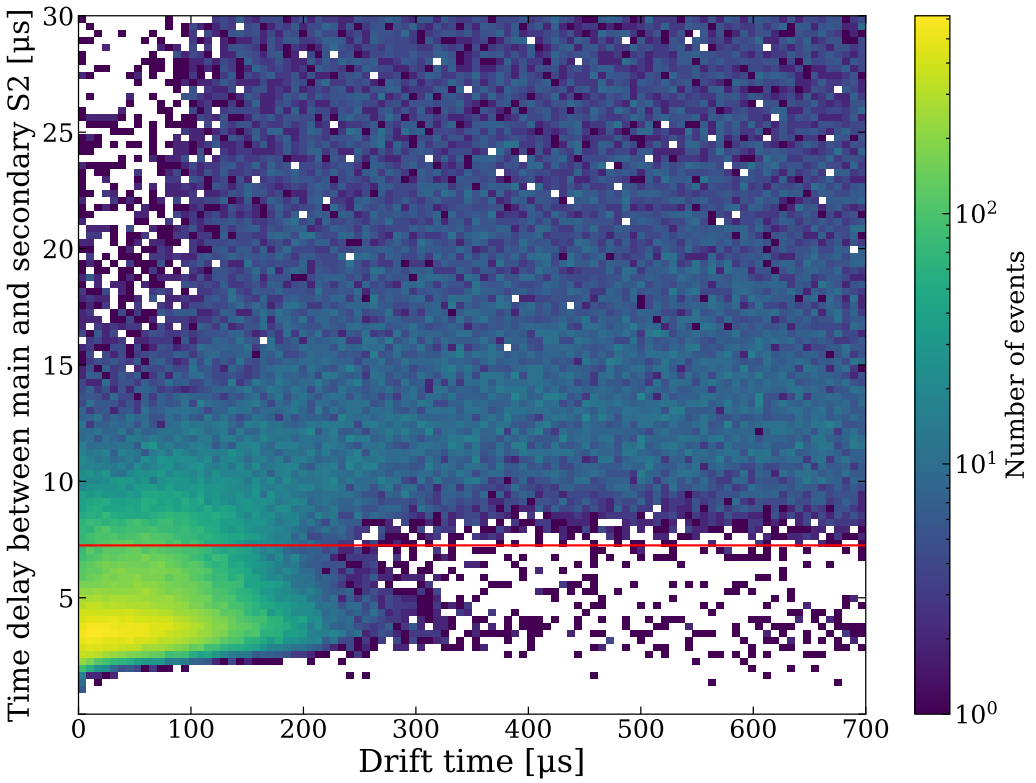

Figure 4.17.: *Simple selection of AP events in the time delay parameter. The threshold is set at 7.25 µs, shown as the red line. Every event with a delay between main* S2 *and* second_largest_S2 *smaller than this threshold is selected to be AP corrected. The delay time is plotted against the drift time to show the largest population fulfilling this condition has only short drift times, which locates these events at the top of the TPC. Obviously, this is not a very clean selection as part of this population bleeds above the threshold line and thus these events are not selected. The large population with a time delay* $< 5\,\mu s$ *are photo-ionization events from the gate. As the secondary S2 of these events dominate in the upper part of the TPC, the secondary S2s with a higher delay are not included in this data selection, which explains the gap in the upper left corner.*

For the selected events below the thresholds the AP corrections are now applied, replacing the old S2 value with the sum of the old S2 and the secondary S2:

$$S2_{AP} = S2 + S2_{second\_largest} \tag{4.4}$$

After applying this correction, the kink in the electron lifetime estimation plots should vanish. Fig. 4.19 shows the results using the AP-corrected $S2_{AP,bottom}$ values vs. drift time. The anomaly observed at the top of the TPC is no longer present. On the contrary, the residuals reveal a slight over-correction in the region of interest.

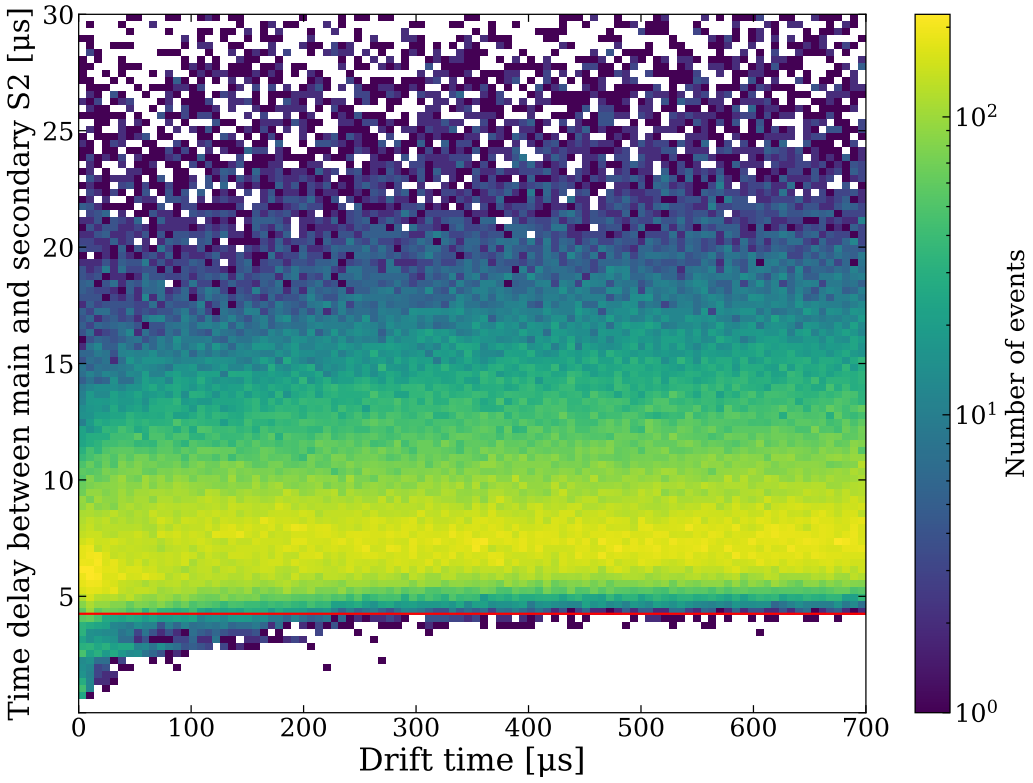

Figure 4.18.: *Simple selection for ^{83m}Kr. A lower threshold (time delay $< 4.25\,\mu s$) is used compared to ^{37}Ar, which is caused by the two-step decay of the ^{83m}Kr isotope. Below the threshold, only a few events close to the liquid-gas interface are selected for AP correction.*

One reason for this might be the very primitive way of AP candidate selection. As can be seen in Fig. 4.17, the selection threshold in the time delay cuts into the observed population. Despite this *incomplete* selection, the low drift time region already seems to be over-corrected in the lifetime plot, indicating that not every peak in this population is actually a real AP peak. Therefore, a more refined way of finding and selecting AP candidates must be found.

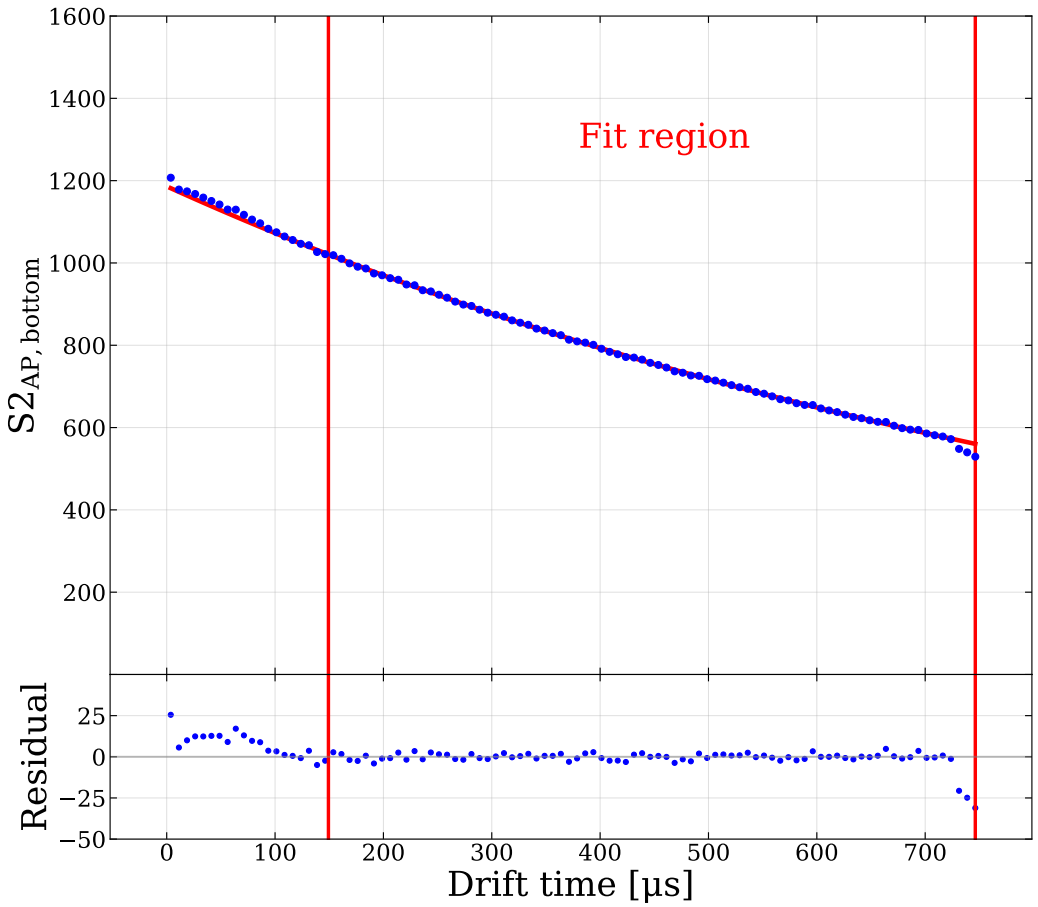

Figure 4.19.: $S2_{AP,bottom}$ *vs. drift time plot with the AP correction applied. When compared to the uncorrected data, as shown in Fig. 4.6, the anomaly at the top of the TPC is no longer present. The residuals of the plot actually show a slight over-correction in comparison to the expected exponential behavior.*

Improved afterpulse candidate selection

The first step is to provide a better selection of AP candidates. In the first simple correction, the standard minitrees were used. They provide the so-called *second_largest_s2*. As the name suggests this is the second largest S2 found in the waveform of an event, but this does not necessarily need to be a proper candidate. As an example: the second largest S2 might have a delay to the main S2 which is larger than the threshold, so it gets discarded and the main S2 is not corrected. Yet, it might be possible that a smaller (for instance the third largest S2), yet significant peak identified as S2 is present in the waveform, within the delay time window. With this first selection, this constellation is ignored and the event is not corrected.

To improve here, a special AP-correction-minitree was introduced, also providing the three largest S2 peaks within 15 μs of the main S2. This time window was chosen based on an AP study of the used PMTs in the TPC. As larger signals can induce

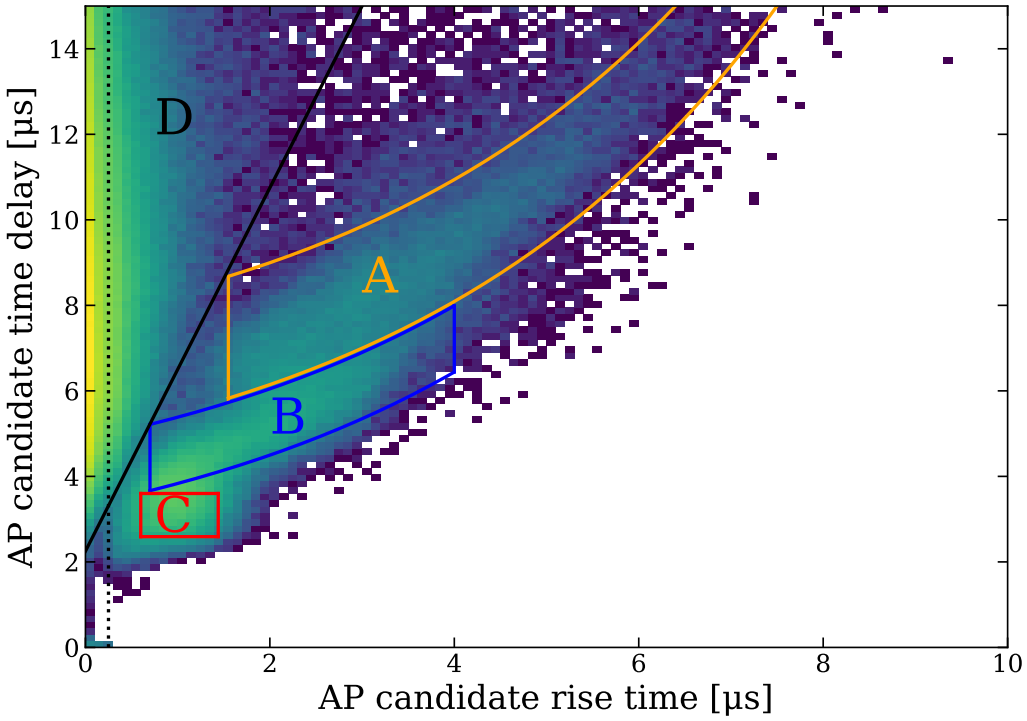

Figure 4.20.: *Time delay vs. rise time of the first AP candidate for ^{37}Ar data, the closest secondary S2 after the main S2. Clearly visible are four major populations, identified with A to D. The selection criteria are chosen by eye. Population D contains signals identified as S2s, but with a much too short rise time compared to the typical S2 in XENON1T. The origin of the populations A to C is further investigated in the text. For the final AP correction, all events with AP candidates right of the population D line and the dotted line and below population A are used.*

AP signals, which in return can induce new APs and so on, and up to three APs are taken into account, this threshold of 15 μs was chosen.

Additionally, the AP selection was moved to another data space. One dimension of interest is the time difference between the main S2 and the following AP. The other dimension chosen is the rise time of the AP candidates. As the typical shape of S2, and thus the typical rise times of S2s are well known, this choice also offers the possibility to also remove events with nonphysical shapes from being used as a correction. The distribution of the first AP candidates for ^{37}Ar data is shown in Fig. 4.20. The secondary AP S2 candidate shows a much weaker shape of these populations, whereas the third shows barely any other population besides population D. The corresponding plots can be found in Figs. B.18 and B.19 in the appendix on page 205. Due to the negligible number of peaks in these selections, only the primary AP candidates are considered for correction.

Four major populations are clearly visible. The population D on the left with very low rise times consists of the already mentioned nonphysical events, considered to be

accidentals identified as S2 and thus end up in this selection. Their rise time of the order of 100 ns, however, differs greatly from the one expected for a regular S2, with typical values of the order of 1000 ns.

The three remaining populations seem to be real signals identified as S2s. To identify the source of these populations, a simple selection of the core distribution of each population was applied and their spatial distribution evaluated. As shown in Fig. 4.21 the main S2 signals of population A have a certain spatial distribution in the x-y-plain. These correspond to the locations of PMTs which are known to have a higher AP rate. This is also visible for the distribution of the AP candidates which are concentrated on the high-AP rate PMT positions. The main S2s of population B are far more uniformly distributed. This is also true for the position of the first AP signal although they are also more evenly distributed. The main S2 of population C shows a somewhat inverse distribution when compared to population A. Also for this population the AP candidates are spread more uniformly as was observed for population B.

The same analysis is applied to ^{83m}Kr events. To select interactions caused by ^{83m}Kr decay, all events with an uncorrected S1 between 145 pe and 630 pe are selected. In the S2 space an area between 5000 pe and 25000 pe is selected. This is a rather large energy range selection but, in uncorrected space, the signals are greatly distorted, mainly caused by the drift losses and missing position corrections. The distribution of the AP candidates in the time delay vs. rise time space is shown in Fig. 4.22. For ^{83m}Kr the distribution of the first AP candidates looks quite different from the one of ^{37}Ar as there is one major population visible, containing nearly all events, which is named population E. Besides this, only a very small population F is visible with shorter delay times between the main S2 and the AP candidate.

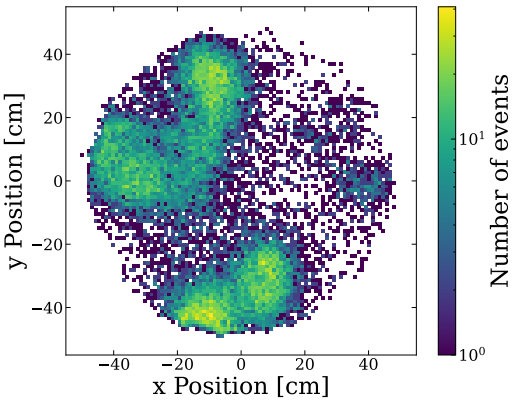

(a) *Population A, main S2*

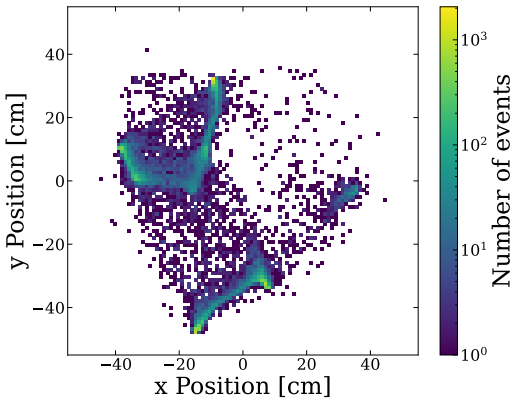

(b) *Population A, first AP candidate*

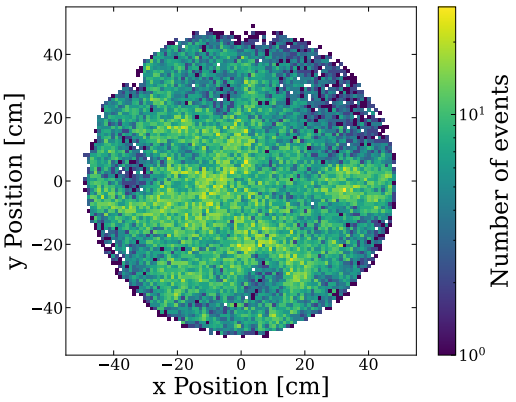

(c) *Population B, main S2*

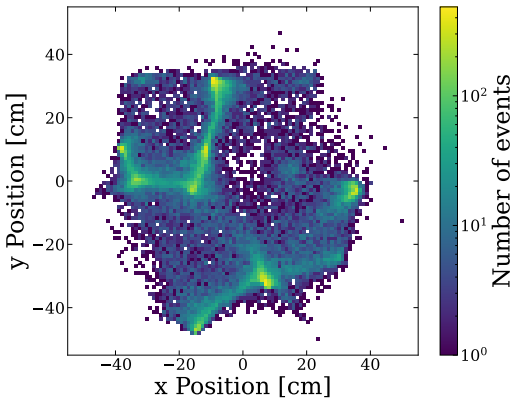

(d) *Population B, first AP candidate*

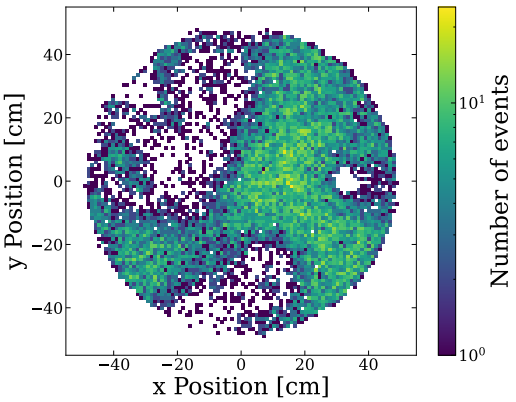

(e) *Population C, main S2*

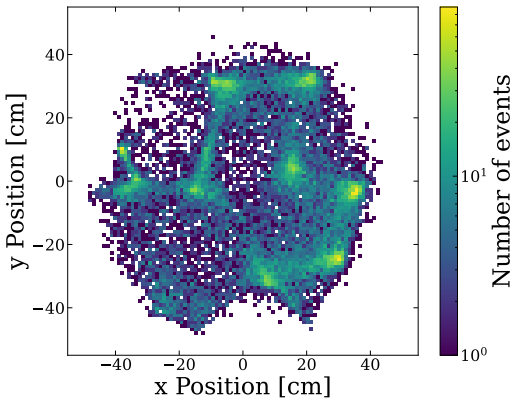

(f) *Population C, first AP candidate*

Figure 4.21.: *Distributions of the events of the three AP populations from Fig. 4.20 in the x-y-plane. The main S2s of population A are concentrated on positions of PMTs with a higher AP rate. This also accounts for the corresponding AP. The main S2s of population B are evenly distributed, while population C shows an inverse distribution in x-y when compared to population A. The APs identified for these events are more evenly distributed than for population A, but they are still concentrated at the AP-intense PMT positions.*

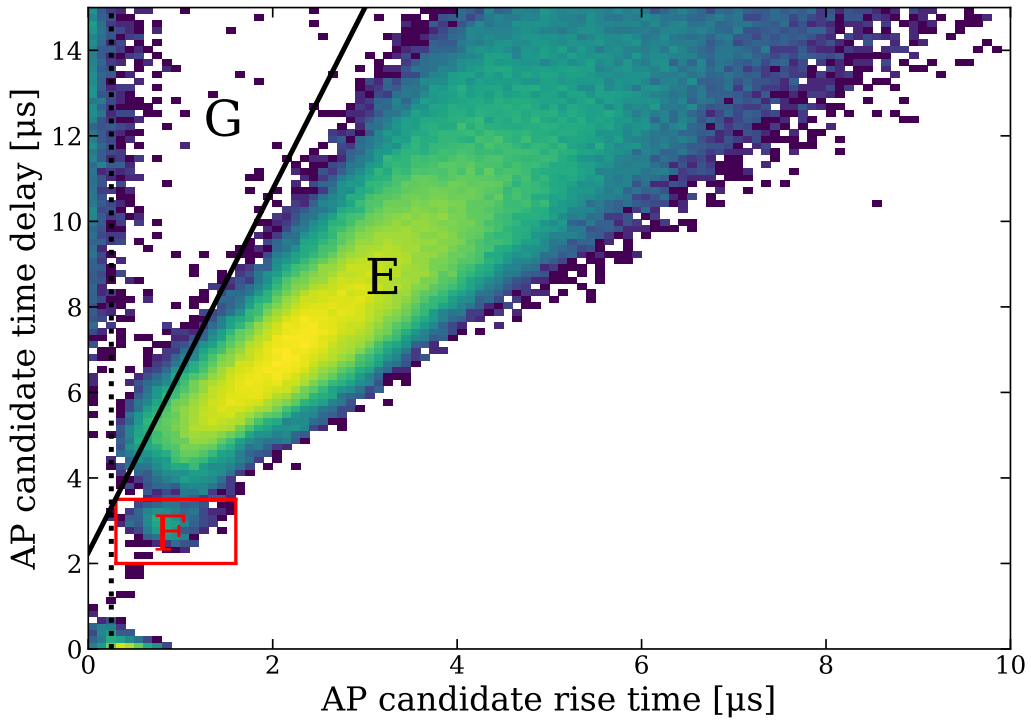

Figure 4.22.: *Time delay vs. rise time of the first AP candidate for ^{83m}Kr data, the closest secondary S2 after the main S2. It has a different structure when compared to ^{37}Ar. Most of the AP candidates are part of population E with higher time delays, besides them only a small population at lower delay times at 3 µs is visible, named F. The black solid and dotted lines show the same selection criteria as for ^{37}Ar. All events above and to the left of the lines (population G) are discarded as accidental events.*

When looking at the corresponding x-y-distribution of the related main S2, the events of population E are far more equally distributed compared to the ^{37}Ar populations. Merely the smaller population has a similar distribution to ^{37}Ar and is only present in the top region of the TPC. In the distribution of the AP candidate positions the locations of the AP intense PMTs are still clearly visible, but even here the events are far more homogeneously distributed in x and y, as can be seen in Fig. 4.23.

The main difference between the AP candidates of both sources is visible when looking into the z distribution of the main S2, which is shown in Fig. 4.24. As expected, the candidates for ^{37}Ar for all three populations are present at the top of the TPC, while the parent S2 of the candidates of the major ^{83m}Kr population are equally distributed throughout the whole depth of the detector. This indicates another origin for the population E candidates than for the ones of ^{37}Ar. Only the small population F has a similar distribution to the one observed for ^{37}Ar, but the number of events contributing to this population is negligible compared to the total number of ^{83m}Kr events.

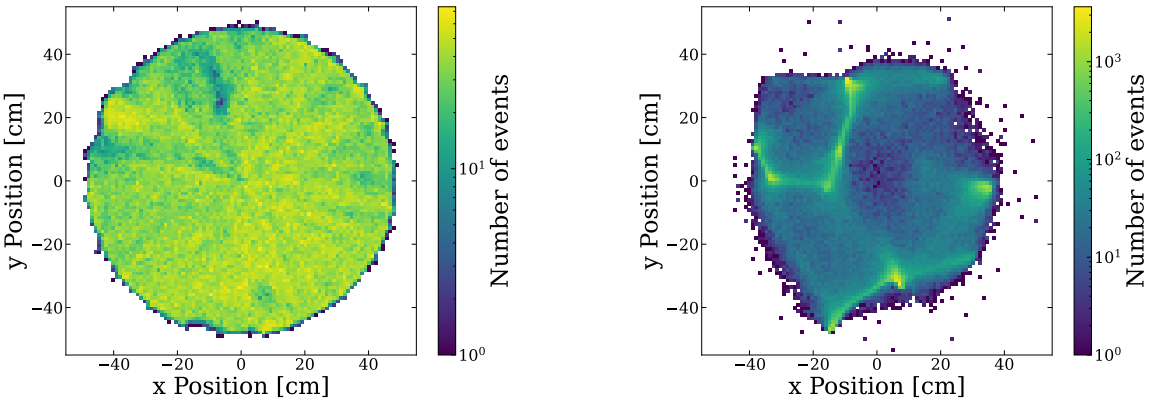

(a) *Population E, main S2*

(b) *Population E, first AP candidate*

Figure 4.23.: *Distributions of the events of the main AP population (E) in the x-y-plane for ^{83m}Kr. The main S2 is mostly equally distributed, as expected. The first AP candidate is also more equally distributed than in the ^{37}Ar distributions. Similar to the other selections, the positions of AP intense PMTs are still visible. The number of events for population F is too low to show any insightful distributions and are therefore not shown.*

Due to the distribution of the events in population E of the ^{83m}Kr data, these events can be excluded as AP candidates as they are spread equally throughout the height of the TPC. The remaining ^{83m}Kr population, as well as all three ^{37}Ar populations, are concentrated in the top region, as expected for AP-candidates. Population A, however, shares a similar shape to the excluded ^{83m}Kr population E in the time-delay vs. rise-time data space. Also some of the events belonging to A reach far deeper into the TPC than the peaks of the other two ^{37}Ar populations. To test which effect this has on a possible correction, the ^{37}Ar peak data was one time corrected with populations A, B and C, and one time with populations B and C candidates only. Applying the correction also here means replacing the S2 with the sum of the S2 and the AP candidate.

For both corrections, the electron drift time analysis was redone. In both cases, the obvious anomaly observed for top events has vanished. When applying the exponential fit (using the same fit ranges as before the corrections), however, the ABC correction shows a slight over-correction in the residual, while the BC correction fits better. This is shown in Fig. 4.25.

Based on this result and the shared time-delay vs. rise-time data space of populations A and E, only events with an AP candidate in populations C and D are corrected. The resulting electron lifetime from the AP corrected ^{37}Ar data is $(948.826 \pm 0.083)\,\mu$s, which in the end results in an electron lifetime of $(913.669 \pm 0.082)\,\mu$s after the field correction is applied.

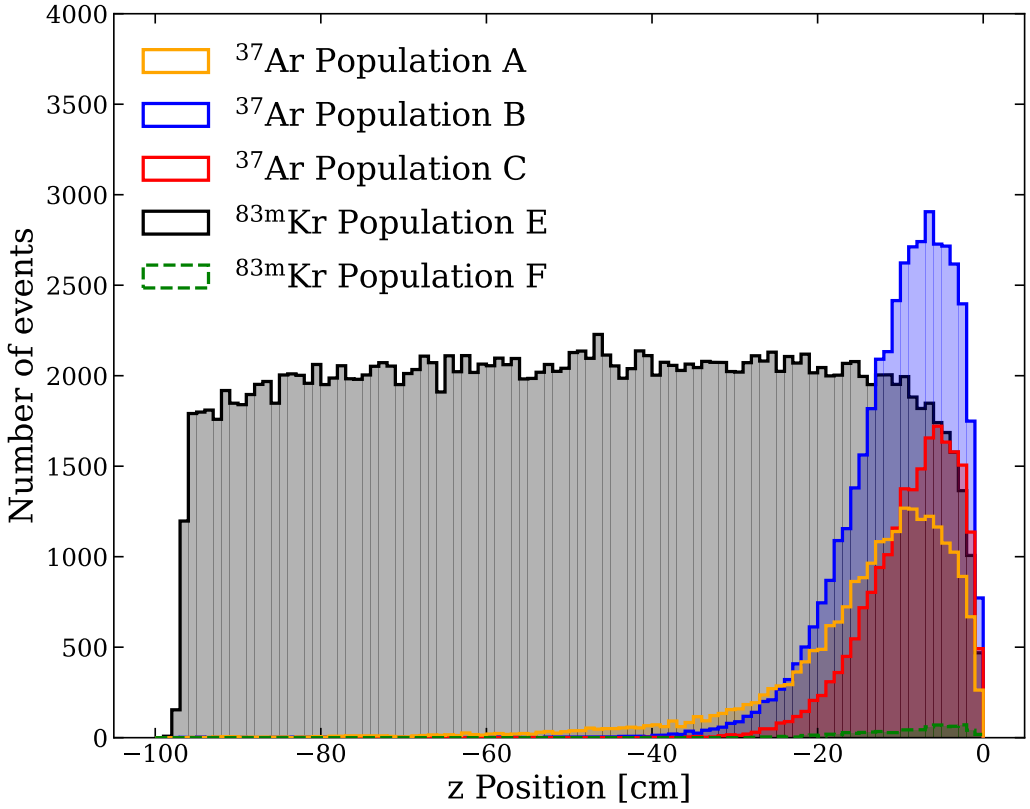

Figure 4.24.: *Z-distribution comparison for the first AP candidates of ^{37}Ar and ^{83m}Kr. Four populations (A, B, C and F) are concentrated in the top region of the TPC, while population E is equally distributed throughout the complete detector. Due to this, population E peaks are not considered AP-candidates. Also, the population A peak distribution reaches deeper into the TPC. As they also share a similar shape in the time-delay vs. rise-time data space, their suitability for AP corrections needs to be examined further.*

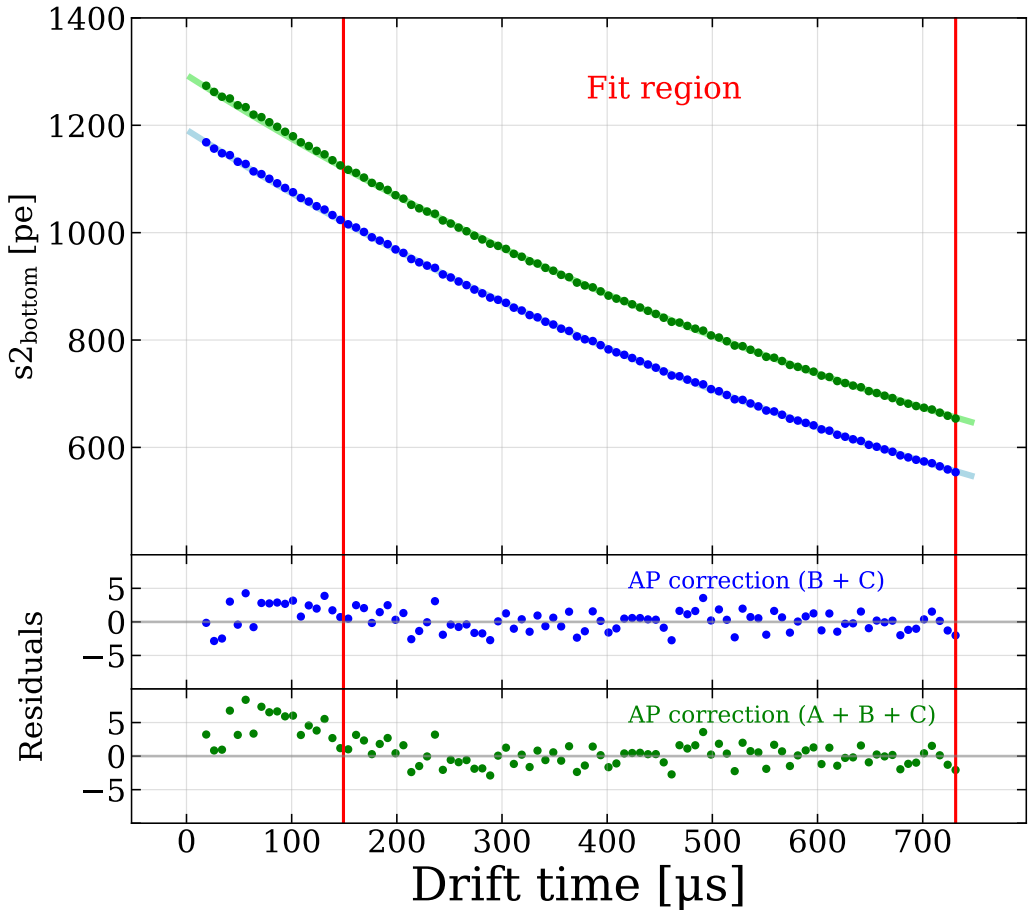

Figure 4.25.: *Direct comparison of both corrections. The blue data is corrected using candidates of populations B and C, the green includes also population A corrections. An exponential is fitted to both datasets. The residuals for the BC correction fit very well, while the ABC correction shows a small over-correction. This result, in combination with similar data space distributions of populations A and E, leads to the conclusion to apply only the BC candidates as AP corrections. Note that the ABC data is offset by 50 pe for better visibility.*

4.4. Fitting the signal distribution in S1-S2

For this analysis, the ^{37}Ar events are pre-selected in the S1/S2 space with the same criteria as for the lifetime estimation. Similar to the lifetime estimation, only the bottom part of the S2 ($S2_b$) signal is used. To extract information like the total energy measured, the mean cS1- and $cS2_b$ -values need to be determined. This can be done by fitting the event distribution in the cS1-$cS2_b$ data space. In a first attempt, one assumes the events to be normally distributed in both parameters cS1 and $cS2_b$. Hence the first attempt to fit the data was facilitating a standard 2-dimensional Gaussian distribution. The parameterization used in this work is as follows:

$$G(x,y) = A \cdot e^{-a(x-x_0)^2+2b(x-x_0)(y-y_0)+c(y-y_0)^2} \tag{4.5}$$

with the parameters A = amplitude of the distribution and a, b and c containing the σ_x and σ_y values of the 2D-Gaussian, as well as the tilting angle θ, which describes the anti-correlation of cS1-cS2:

$$a = \frac{cos^2\theta}{2\sigma_x^2} + \frac{sin^2\theta}{2\sigma_y^2} \tag{4.6}$$

$$b = -\frac{sin(2\theta)}{4\sigma_x^2} + \frac{sin(2\theta)}{4\sigma_y^2} \tag{4.7}$$

$$c = \frac{sin^2\theta}{2\sigma_x^2} + \frac{cos^2\theta}{2\sigma_y^2} \tag{4.8}$$

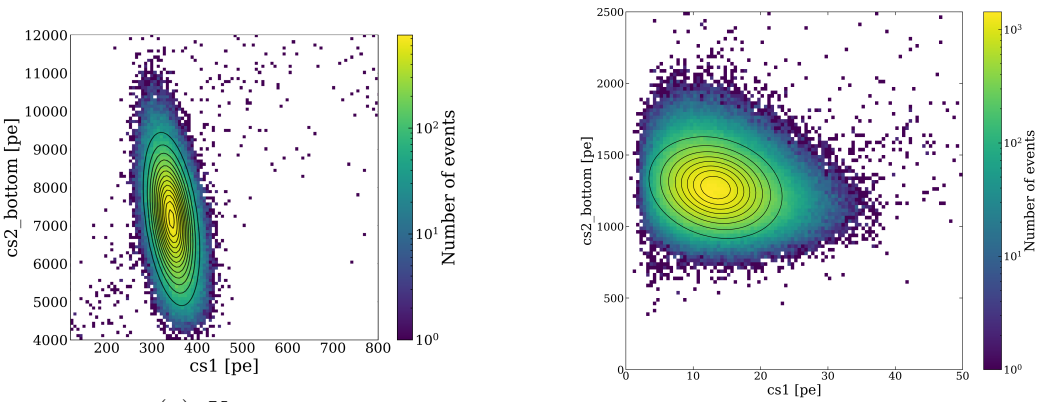

(a) *Krypton*

(b) *Argon*

Figure 4.26.: *cS1-cS2 distribution for a single voxel for ^{83m}Kr and ^{37}Ar, corrected with the electron lifetime based on ^{83m}Kr. The contours show the fit result of a simple 2D-Gaussian fit to the data. Fig. (a) shows the result for ^{83m}Kr which is well described by the Gaussian. In Fig. (b) the result is shown for ^{37}Ar, which shows a strongly deformed peak that is not well described by the fit.*

This Gaussian shape provides a good fit for the other calibration sources used previously, e.g. ^{83m}Kr, where it fits the distribution quite well, as shown in Fig 4.26.

When looking at the ^{37}Ar data, however, the event distribution looks distorted and not Gaussian alike. After consideration, three main contributions to the distortion in this event distribution are identified:

1 **Applied corrections:**
The corrections applied to the measured data are based on a calibration with ^{83m}Kr. This works fine for energies in the same order of magnitude as Krypton events. But as shown in Section 4.3, the electron drift time is dependent on the interaction energies, caused by the field inhomogeneities. Consistent with the other analysis of XENON1T, all S2 signals are corrected using the ^{83m}Kr lifetime. Application of this correction to the ^{37}Ar data, however, leads to an over-correction, resulting in too high $cS2_{bottom}$ values for the lower part of the TPC. More details about this can be found in section 4.5.

2 **Detector threshold:**
The energies observed from ^{37}Ar are very low and are influenced by the detection threshold. The number of photons observed from prompt scintillation in the S1 signal ranges from 2 pe up to 30 pe. As this range overlaps with the known threshold, the ^{37}Ar data allows for testing the threshold of the detector, one of the reasons this calibration source was chosen.

3 **Statistics:**
For ^{37}Ar the number of photoelectrons in each event is low enough that the expected distribution might not yet be Gaussian in shape but rather reflect the underlying Poisson and binomial processes. To account for this, asymmetric distributions are used to describe the S1 distribution.

4.5. Modeling the S1-S2 signal distribution

Similar to ^{83m}Kr, the large statistics, uniformity and line emission of the internal ^{37}Ar source permits the study of the spatial dependence of the detector response near the threshold. To this end the TPC volume is divided into voxels of equal volume. A 2D map was created, dividing the x-y-plane into equally sized sectors. This map is similar to the maps used to create the x-y-correction maps (for instance the one based on ^{83m}Kr), but designed to be easily manageable. The algorithm was written in a flexible way, so that only the number of rings and the total radius have to be given. The program then creates the map and assigns a sector number to each event, based on its x-y-coordinates. An example of such a map, created with 3 rings (the central area counts as ring 0) is shown in Fig. 4.27.

Additionally, the division in z is done simply by a selection in the z-coordinate. This allows for a fast (voxel-)data selection in the later analysis. With this map and

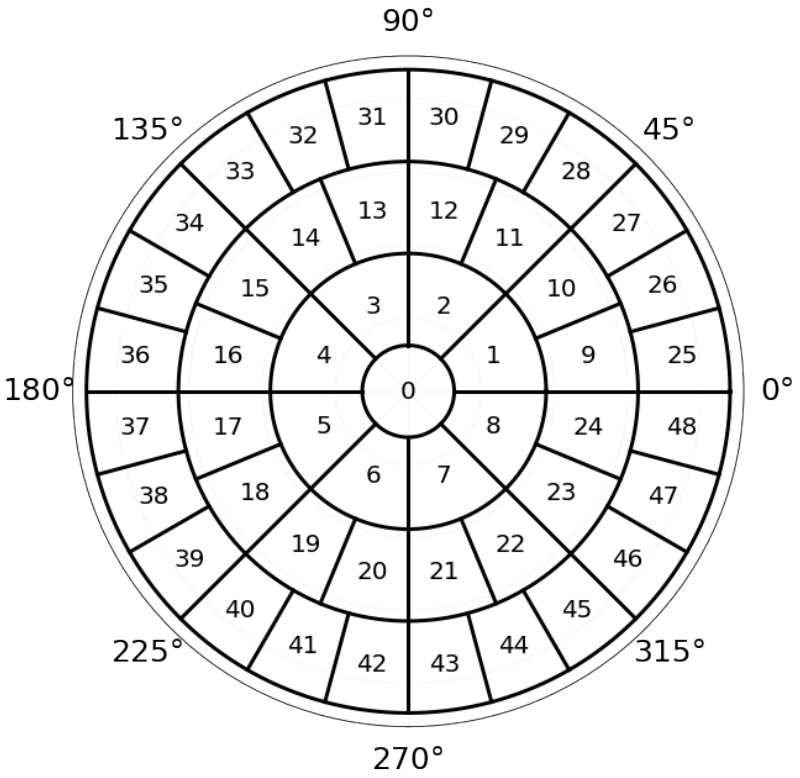

Figure 4.27.: *Section map showing the subdivision of the x-y-plane of the TPC, in this case featuring three rings of equally sized sections around a central section.*

.

a division of the TPC into 6 equal slices in z, each voxel contains around 5000 events, enough to allow a 2-dimensional fit.

For ^{37}Ar it was observed that the position of the mean cS1/cS2$_b$ shifts when data from voxels at different z positions of the detector are selected, as shown in Fig. 4.28. This should not occur after the corrections are applied. Regardless, this feature was observed for ^{37}Ar, especially when keeping the x-y-position fix, but varying z. This effect is reason for the distorted signal shapes for ^{37}Ar as shown in Fig. 4.26b. For comparison, Fig. 4.29 shows the same data, but this time corrected with the electron lifetime obtained from argon. The ^{37}Ar lifetime corrected S2 from the bottom of the TPC is equally widened than the ^{83m}Kr lifetime corrected data, an effect caused by diffusion during the electron drift through the detector. The mean value of the ^{37}Ar corrected S2 distribution, however, varies much less. This clearly shows the over-correction effect caused by the ^{83m}Kr lifetime correction, which has a much lower value than the one found for ^{37}Ar. Due to the ^{37}Ar longer lifetime, the drift losses are lower. Correcting then with the ^{83m}Kr lifetime leads to an over-correction of the S2s, especially at the bottom of the TPC.

Despite this finding, to be able to directly compare the results with other XENON1T analyses, the ^{83m}Kr-based correction is used in this analysis, unless otherwise noted.

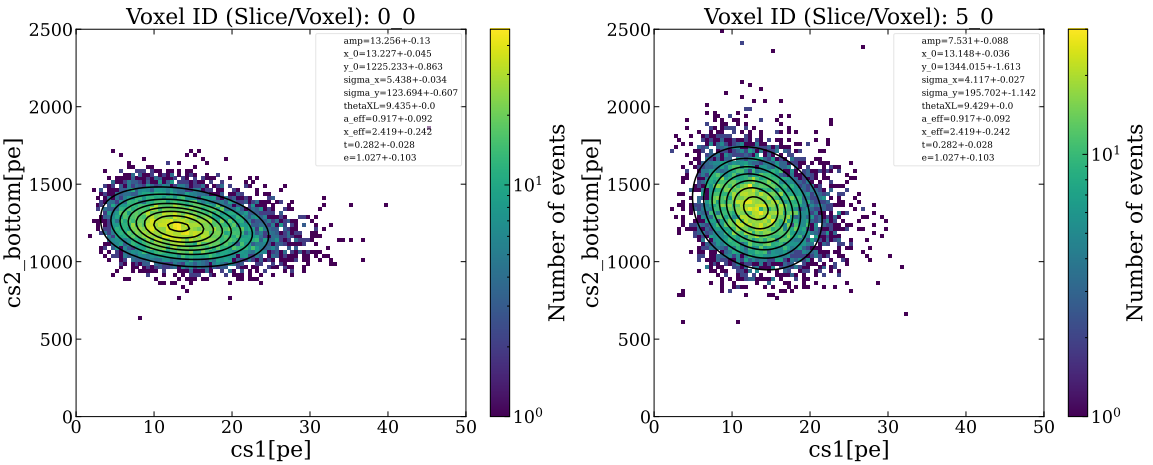

(a) *Top of TPC.* (b) *Bottom of TPC.*

Figure 4.28.: *Comparison of cS1-cS2$_b$ signal shape between a voxel from the top of the TPC (from z = -10 cm to z = -25 cm) to a voxel from the bottom of the TPC (from z = -85 cm to z = -100 cm). The smearing in S2 width is caused by diffusion. The shift in the mean of the S2$_b$ distribution from 1225 pe (top) to 1344 pe (bottom) is induced by the S2 (over-)correction with the electron lifetime based on ^{83m}Kr. As shown in in Section 4.3, this is caused by differences in e^--generation due to differences in the electric field. The contours shown indicate the shape of the 2D function used for fitting.*

Even with a finer voxelisation, reducing the distorting impact of over-correction (in each of the individual voxels), or applying a correction based on the ^{37}Ar lifetime, the signals are found to be still not purely Gaussian. There is still a clearly visible asymmetry in the S1 distributions. This asymmetric 2D-distribution can, however, be described much better with a 2D-Gaussian, which is skewed in the S1 component:

$$G(x,y) = A \cdot e^{-a(x-\xi)^2+2b(x-\xi)(y-y_0)+c(y-y_0)^2} \cdot \left[1 + erf\left(\frac{\alpha \cdot (x-\xi)}{\sigma_y\sqrt{2}}\right)\right] \tag{4.9}$$

Facilitating this S1-skewed version of a Gaussian, the mean S1 is not directly given as the parameter ξ, but can be calculated with:

$$x_0 = \xi + \sqrt{\frac{2}{\pi}}\frac{\alpha\sigma_x}{\sqrt{1+\alpha^2}} \tag{4.10}$$

Where α is the parameter describing the skewness of the Gaussian. A skewness of 0 leads to a classical symmetric Gaussian. Fig. 4.30 shows a qualitative comparison between a normal Gaussian and skewed Gaussian distributions with different values for the skewness. The parameters a, b and c in Eq. 4.9 are identical to the parameters of the simple 2D-Gaussian.

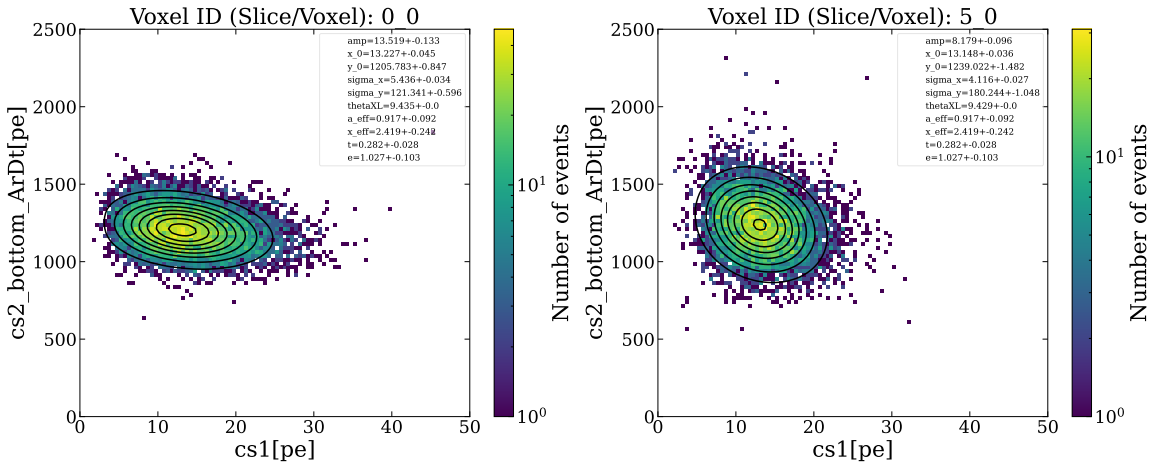

(a) *Top of TPC.* (b) *Bottom of TPC.*

Figure 4.29.: *Same data selection as in Fig. 4.28, this time with* ^{37}*Ar lifetime corrected S2. The diffusion effect is the same, the shift however between the mean signal from 1205 PE (top) and 1239 PE (bottom) is much smaller, showing also clearly the over-correction caused by the* ^{83m}*Kr -based lifetime.*

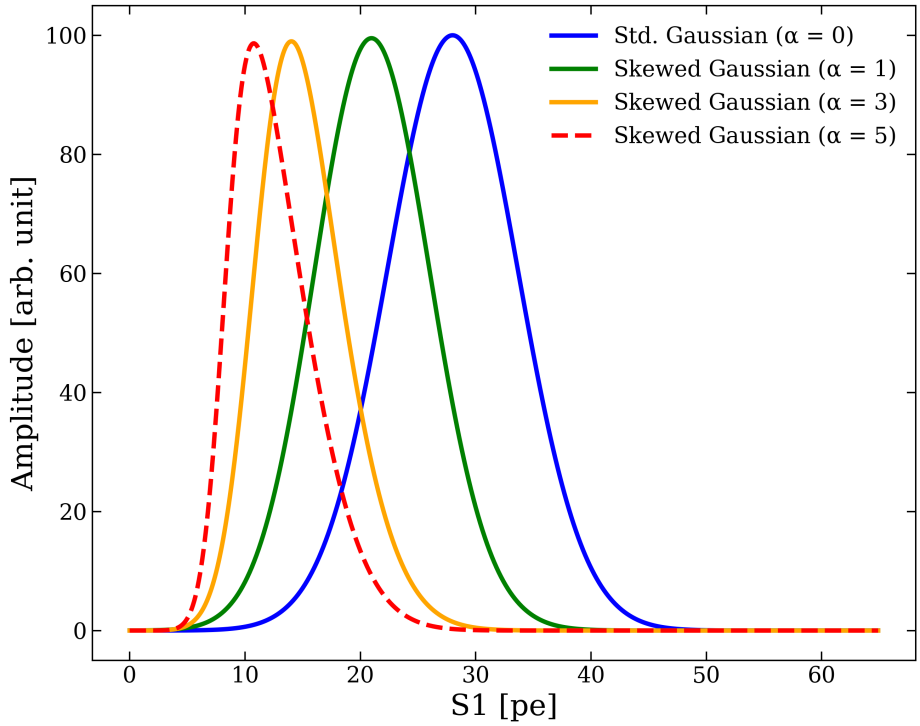

Figure 4.30.: *Shape comparison between skewed Gaussian and standard un-skewed (α = 0) Gauss-distributions.*

.

Yet the shape of the skewed Gaussian, although already much closer to the event distribution than a simple 2D Gaussian, still does not fit the left, low pe side of the S1 distribution. Here we have to consider an additional effect introduced by the detector, a detection threshold, which is discussed in the next section.

4.6. Signal threshold in S1

A significant loss in detection efficiency for S1 signals can be observed for weak S1 signals with less than 5 pe, where smaller efficiency losses are already affecting the signals smaller than 10 pe. The mean of the S1 signal of ^{37}Ar is well above this value, yet the signal distribution extends below that value. Therefore this efficiency has to be modeled and included in the 2D fit, as it will affect the minimization process of the model function and as such lead to wrong results, mainly in the S1 parameter. To further investigate the mentioned effects, the initial simple and later the skewed 2D-Gaussian were modified with a threshold function. Initially, the threshold was modeled with a simple Fermi function:

$$F(x) = \frac{1}{1 + e^{-\frac{x - x_{thr}}{w_{thr}}}} \tag{4.11}$$

Applying the threshold to the 2D-Gaussian already improves the fit result, as can be seen in shape and residuals. The TPC threshold, however, can also be extracted from data based on the first science run of XENON1T. When plotted and compared to the function, the Fermi function does not describe the threshold very well, as is shown in Fig. 4.31. This is mainly caused by the asymmetric shape of the threshold. To achieve a better agreement with the data the function was changed to an asymmetric threshold, a combination of an error function to describe the stronger rising part and a hyperbolic tangent for the weaker part, where the function flattens out:

$$F(x) = a \cdot (0.25 \cdot (tanh(\tau \cdot (x - x_S) + 1)) \cdot erf(-\epsilon(x - x_S))) \tag{4.12}$$

The parameter a describes the efficiency, the parameters τ and ϵ define the shape of the $tanh$ and erf functions respectively and x_S gives the position of the threshold in pe. The parameter values are determined by a fit to the data points and are given in Table 4.4. For most of the analysis, unless noted otherwise, the parameters for the threshold are fixed in the 2D fits and cannot be altered by the minimizer. This was found to be necessary as otherwise the shape and positions of the threshold and the S1 component of the 2D-Gaussian were utilized by the minimizer to improve the fit of the left flank of the Gaussian. In some cases, this led to non-physical values for the fit parameters. An example of this is shown in the next section.

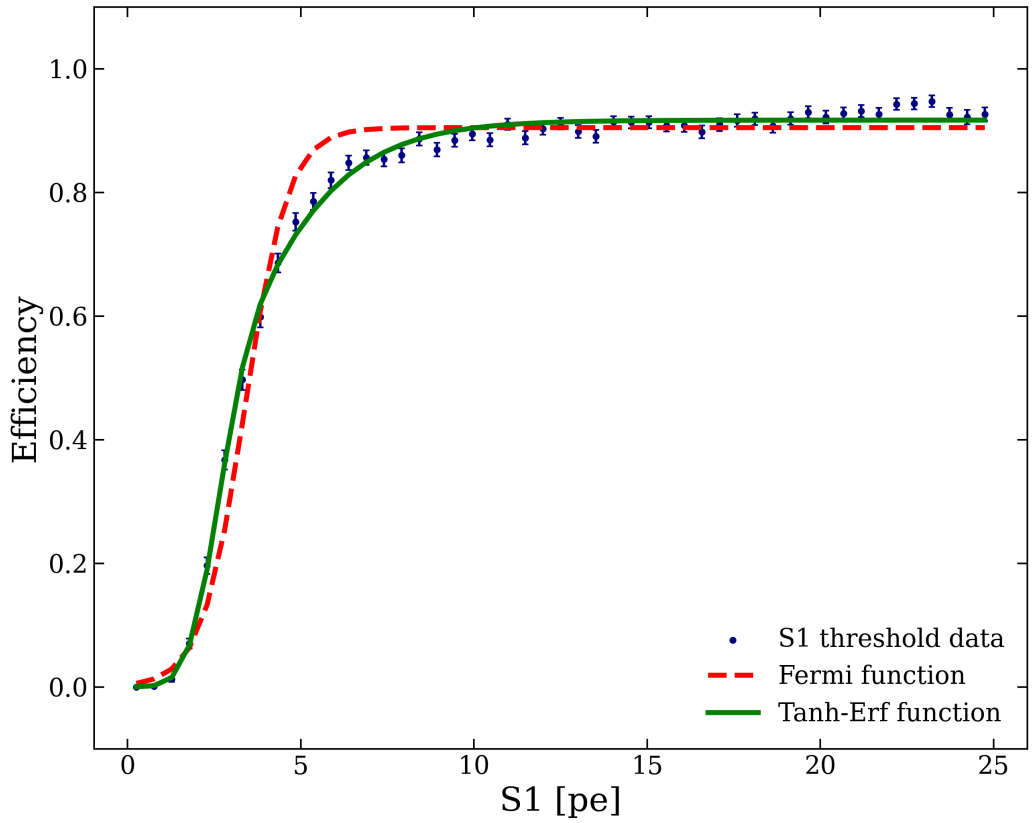

Figure 4.31.: *Functions used to model the threshold. The red function is the simple model, using a Fermi function, the green line shows the Tanh-Erf function as shown in Eq. 4.12. Both functions are fitted to the S1 threshold-data obtained by simulations and data-driven methods [82, 83]. The resulting fit parameters for the Tanh-Erf function are later used as fixed parameters in the 2D (Skew-)Gaussian fits to the calibration data in S1-S2 space.*

Parameter name	Value
a	0.9169 ± 0.0019
x_S	2.4187 ± 0.0238
ϵ	0.2821 ± 0.0081
τ	1.0271 ± 0.0488

Table 4.4.: *List of the fit parameters obtained from the fit of the Tanh-Erf function to the S1 threshold data. In the two-dimensional fits to the S1-S2 data, these values are fixed.*

4.7. Improved fitting of the signal distributions

In the first iteration, fitting employed the *curvefit* method included in the SciPY package of Python. This method uses χ^2 minimization for fitting. Later this was changed to minimizing a binned Log-Likelihood function, which allows Poisson statistics and empty empty bins to be taken into account, an important feature when events are distributed over a 5D dataspace in spatial voxels and S1/S2.

As we are in a regime with relatively low numbers of events we can assume that the entries in each bin follow a Poisson distribution:

$$P_i(n_i, \nu_i) = \frac{\nu_i^{n_i} \cdot e^{-\nu_i}}{n_i!} \tag{4.13}$$

Where n_i is the number of entries in the bin and ν_i the prediction by the model, in our case the 2D (Skewed-)Gaussian + threshold (or any other model function). With this, the Likelihood of obtaining the observed number of events n_i for each bin i is given by:

$$L = \prod_i P_i(n_i, \nu_i) = \prod_i \frac{\nu_i^{n_i} \cdot e^{-\nu_i}}{n_i!} \tag{4.14}$$

To get rid of the product the natural logarithm is introduced:

$$ln\, L = \sum_i ln\left(\frac{\nu_i^{n_i} \cdot e^{-\nu_i}}{n_i!}\right) \tag{4.15}$$

This can, utilizing Stirlings approximation $ln(n!) = n ln\, n + n + O(ln\, n)$ be rewritten as:

$$-2 ln\, L = -2 \sum_i \nu_i - n_i + n_i\, ln \frac{n_i}{\nu_i} \tag{4.16}$$

The factor 2 is introduced as $-2ln\, L$ is χ^2-distributed (in the case of Gaussian errors or large number of events) and thus can be used as a measure for the goodness of fits [84]. The Eq. 4.16 is the cost function minimized to find the best set of parameters describing the data. The realization of this procedure in Python is shown in appendix B.8.1 on page 215.

The starting values for the fit were determined by calculating the arithmetic mean of all cS1/cS2$_b$ signals in a voxel to get starting values for x_0 and y_0. The standard deviations of the cS1/cS2$_b$ distribution were used as initial values for σ_x and σ_y. The initial values for the rotation angle and the skewness were set to 0.01 and 2 respectively. These values were obtained from test fits and also provided stable fit results. The values a, x_S, τ and ϵ for the threshold were taken from the fit results given in Table 4.4.

Initially, it was intended to use the combination of the threshold function and the 2D Gaussian to also extract a position and shape for the threshold from the fit. Due

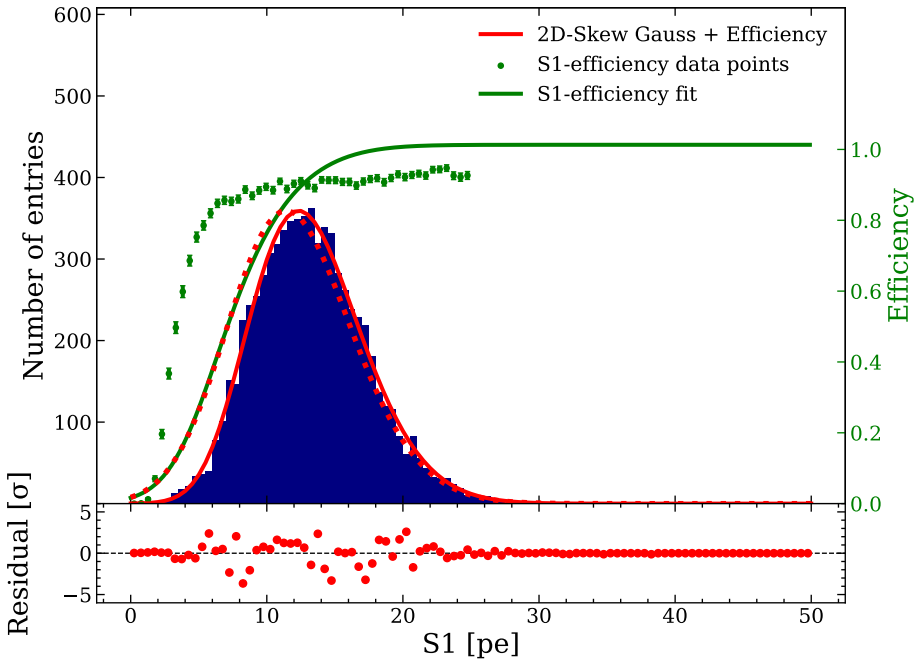

Figure 4.32.: *Example of an overcompensation of the fit with free threshold parameters. The combination of skewed Gaussian and threshold is shown as the red line, fitting quite well to the data. Taking a look at the contribution of both components reveals that the threshold in green is shifted to the right, with a position of* (4.83 ± 4.51) *pe, whereas the position based on data is at* (2.42 ± 0.02) *pe. The position of the Gaussian is shifted to lower values to compensate for the higher threshold position, as it is shown by the dotted red line. In this example, this leads to a difference in the cS1 result by more than one PE from 12.99 pe to 11.85 pe between fixed and free fit. The 2D contour plots for the free threshold and the fixed case with all the fit parameters can be found in Fig. B.20 in the appendix on page 206.*

to the way the function is constructed, the fitting routine tries to match the shape of the S1/S2$_b$ distribution, but because of the correlations of its parameters (S1- and threshold position) this approach proved to be prone to errors.

In the projection on the S1 axis, it is clearly visible that for the left side the skewed Gaussian alone only poorly describes the shape of the signal. The threshold is intended to catch this, and in most voxels the results for the threshold and peak position look reasonable. However, the resulting efficiency parameter a is vastly underestimated in most voxels.

In several voxels, however, the fitting result shows an "'overcompensation"': the threshold is shifted to higher values while the S1 mean is shifted to lower values. This results in a better match for the shape, but the values found for the threshold position and the resulting mean for the S1 are obviously wrong. An example of such an overcompensation is shown in Fig. 4.32, which also results in an unrealistic detector efficiency of larger 100 %. This of course also raises doubts on the robustness of the

results for the other voxels.

As a result of these tests, the threshold parameters were fixed in the next steps. The TPC volume was divided into 6 equally thick slices in z, and a voxel map with 2 rings was chosen. This results in a total of 25 voxels per slice or 150 voxels in total. To extract the mean S1 and $cS2_b$, the event-distribution of each voxel is fitted with a combined 2D-Skewed-Gaussian ($G(S1, cS2_b)$; Eq. 4.9) and threshold ($F(S1)$; Eq. l4.12) function:

$$G'(S1, cs2_b) = F(S1) \cdot G(S1, cS2_b) \tag{4.17}$$

The 2D fit is performed in the S1-$cS2_b$ data space. The uncorrected S1 is used as the basic threshold data is also extracted in uncorrected S1. After the fit the mean value is corrected, using the XENON1T S1 correction map. To get the corresponding correction value, the 3-dimensional correction map is divided into the same voxels as the data. For each voxel, the mean correction value is calculated and then applied to the mean S1 to obtain the mean cS1. The correction values used are given in appendix in Table B.2 in addition to the fit results.

An example fit for one voxel is shown in Fig. 4.33. The upper plot shows the event distribution in S1-cS2 with a contour plot of the 2D skewed Gaussian. The lower plot depicts a projection of the event distribution and the fitted function on the S1 axis. The fit itself is performed in the 2D data space. Additionally, the threshold function is shown to give an idea of how much the shape of the fit function is influenced by the threshold.

Mean of fit results	
Parameter	Value [pe]
$S1$	13.044 ± 0.131
$cS2_b$	1302.575 ± 12.324
Normalized signals	
Parameter	Value [pe/keV]
$S1/E_{Ar}$	4.625 ± 0.044
$cS2_b\ /E_{Ar}$	461.906 ± 4.636

Table 4.5.: *The mean of the fit results obtained from the individual voxel fits is given in the upper part of the table. The S1 values are obtained in the uncorrected space, as the used threshold function is also defined in the uncorrected data space. The resulting signals normalized to the line energy of 2.82 keV are shown in the lower half of the table.*

A table containing the fit results for all voxels and all skew-Gaussian parameters (except for the threshold, as these are fixed) can be found in Table B.2 in the appendix on page 217.

The global mean S1 and $cS2_b$ are then calculated using the mean values of the $S1/cS2_b$ obtained in each voxel. The light and charge yield for ^{37}Ar is given by dividing the obtained results for S1 and $cS2_b$ by the energy of the interaction, which for ^{37}Ar is 2.82 keV. The resulting numbers are given in Table 4.5.

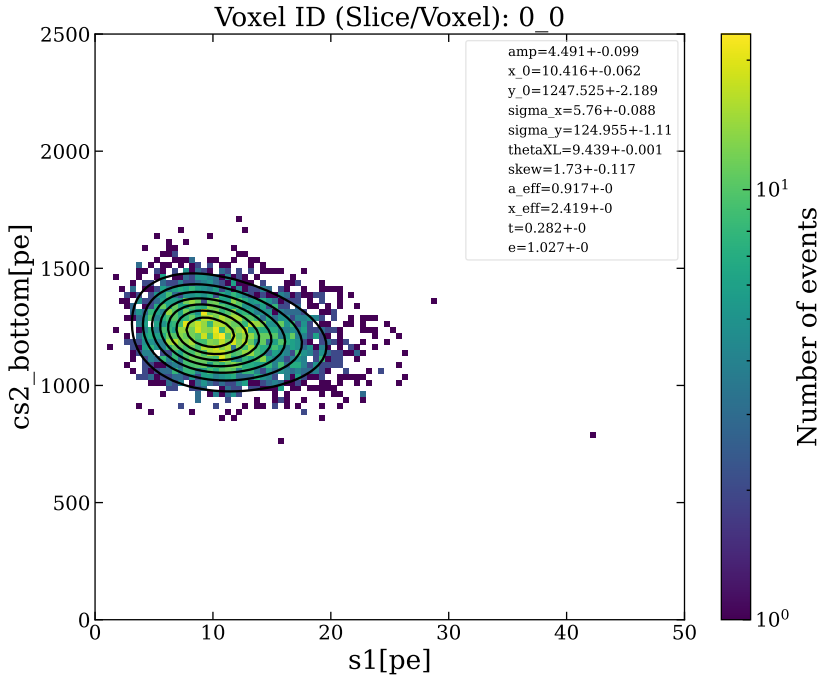

(a) *2D-Skew Gaussian fit to voxel data.*

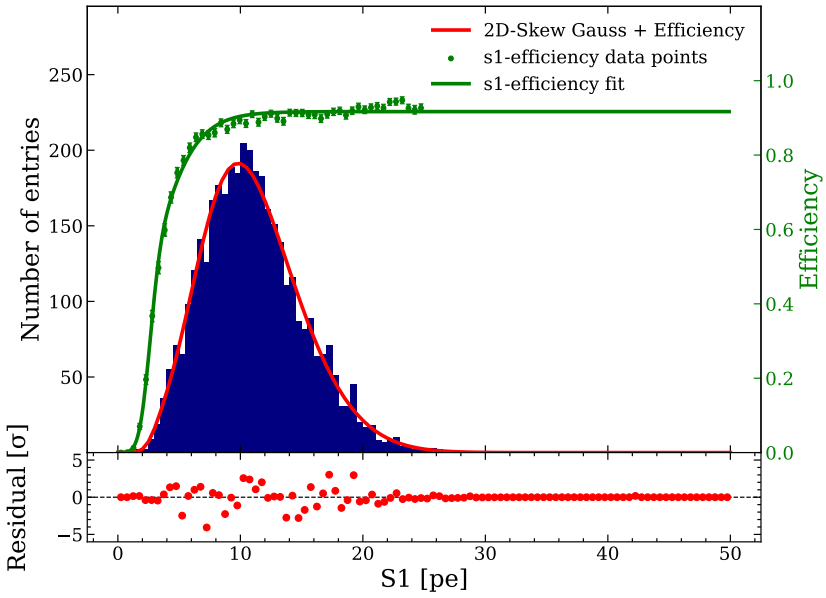

(b) *1D projection on S1 axis.*

Figure 4.33.: *Example of one voxel fit from the top of the TPC (slice 0) in the center (voxel 0). The top figure shows the contours of the 2D fit to the data and the resulting fit parameters for this voxel. The bottom figure shows the projection on the S1 axis. Also shown is the shape of the threshold (arbitrarily scaled for visibility), to give an idea of how much the shape in S1 is influenced by the threshold.*

4.8. Determination of photon and electron gain factors for XENON1T

Besides ^{37}Ar, ^{83m}Kr is used to estimate the detector-dependent photon gain g1 and electron gain g2. Additional calibration lines, considered background in dark matter search, can also be used. This also includes the two meta-stable xenon lines, which were already used in the electron lifetime measurements. Other sources include the ^{60}Co line at a higher energy of 1332.5 keV, and a ^{214}Bi line at 609 keV, which is part of the decay chain of ^{222}Rn, a background source permanently emanating from detector materials.

Fig. 4.34 shows the Doke-plot for XENON1T, plotting the (normalized to line energy) cS2 vs. cS1 signals of various calibration sources. ^{83m}Kr is found in the lower right corner with an energy of 41.5 keV. With increasing energy the light yield reduces and the charge yield increases, so that the sources are found alongside a linear relation with a negative slope. ^{37}Ar behaving counter-intuitively, as it is found at very low light yield and high charge yield values in the upper left corner. The reason for this behaviour is explained in Chapter 2.1.

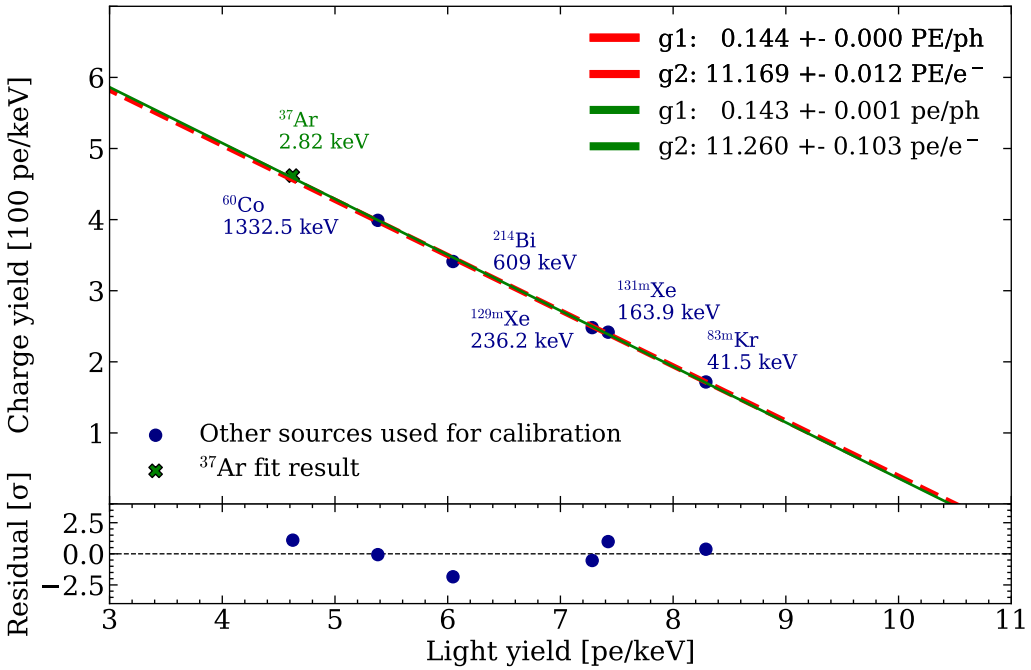

Figure 4.34.: *Doke plot to estimate the light and charge gain factors of the XENON1T detector. The red dashed line shows the fit through previously used calibration sources. The green line shows a fit including the new source ^{37}Ar. It fits the previous data very well, verifying the light and charge gain factors values used in older XENON1T analyses.*

The resulting light- and charge yield values for XENON1T, including the new calibration point from ^{37}Ar are given in the following table:

Parameter	Value
Photon gain $g1$	$0.143 \pm 0.001\,\mathrm{pe/ph}$
Electron gain $g2$	$11.260 \pm 0.103\,\mathrm{pe/e^-}$

Table 4.6.: *Photon gain g1 and electron gain g2 values resulting from the Doke fit in Fig. 4.34.*

With the fit results for cS1 and $\mathrm{cS2}_b$, given in Table 4.7, the detector-independent photon yield PY and electron yield EY can be calculated. These values are specific for xenon for excitation with the ^{37}Ar decay energy of 2.82 keV and an applied drift field of 82 V/cm:

Parameter	Value	NEST
LY_{Ar} Light yield	$32.27 \pm 0.52\,\mathrm{ph/keV}$	
CY_{Ar} Charge yield	$41.02 \pm 1.06\,\mathrm{e^-/keV}$	

Table 4.7.: *Resulting xenon-specific light and charge yields for an interaction energy of 2.82 keV (electronic recoil) at an applied drift field of 82 V/cm.*

4.9. Combined energy fit for the ^{37}Ar peak

A simple test to verify the values for g1 and g2 obtained in the Doke plot is to calculate the combined energy scale (CES). This can be done with Eq. 2.10 with a W-value of 13.7 eV. The resulting energy peak for the selected data is shown in Fig. 4.35 for electronic recoils. The peak is fitted with both, a Gaussian and a skewed Gaussian function. As with the S1 distribution, the skewed Gaussian describes the shape of the energy peak much better than the symmetric Gaussian. The resulting mean of the skewed Gaussian is (2.81 ± 0.02) keV, which is well in agreement with the expected value of 2.82 keV, marked with the dotted line.

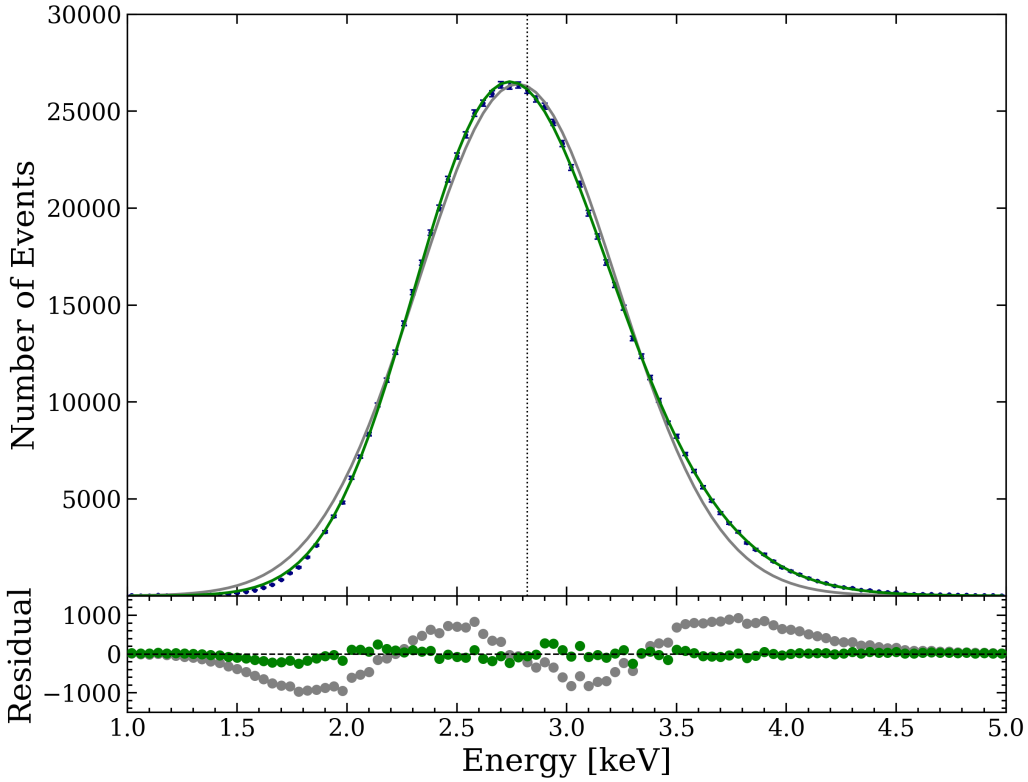

Figure 4.35.: ^{37}Ar *energy peak reconstructed using the g1/g2 values obtained from the fit in the Doke plot in Section 4.8. The peak is fitted with a Gaussian (grey) and a skewed Gaussian (green). Also for the energy peak, the skewed Gaussian shows a much better agreement with the data (blue), as can clearly be seen in the residuals. The position is well in agreement with the expected value of 2.82 keV, as indicated by the dotted line.*

4.10. Energy resolution for ^{37}Ar

With the mean value and the width of the energy peak fit obtained in Section 4.9, the energy resolution σ/E for the XENON1T detector can be calculated. Similar to the mean value, the width of the skewed Gaussian is not directly given by a fit parameter. It can be calculated with:

$$\sigma = \omega \cdot \sqrt{1 - 2 \cdot \frac{\alpha^2}{\pi \cdot (1 + \alpha^2)}} \tag{4.18}$$

Where ω is the skewed width obtained from the fit and α is the skewness. With the results obtained from the fit, the energy resolution is computed to be $(16.59 \pm 1.22)\,\%$. The uncertainty is propagated using Gaussian error propagation. The result is shown in Fig. 4.36 together with the resolution from other line sources.

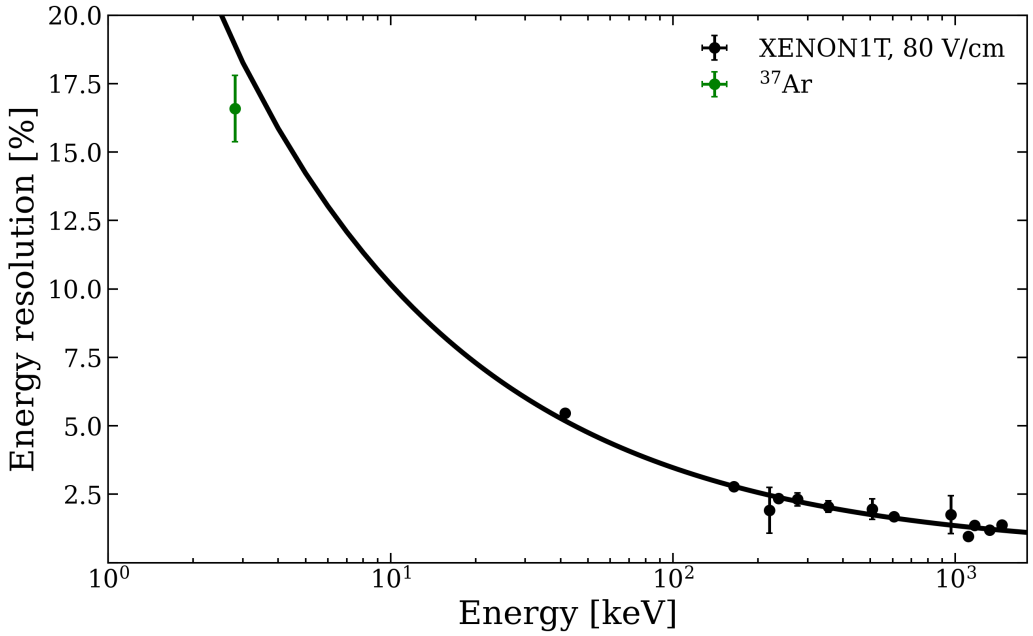

Figure 4.36.: *The energy resolution of the XENON1T detector at an energy of 2.82 keV, based on the ^{37}Ar calibration data. Several other sources are shown. The black line fit does not include the ^{37}Ar value. Due to the relative large error, the change of the curve by including the ^{37}Ar value in the fit is negligible. Plot recreated with data shown in [85].*

4.11. Single electron gain measurement

The single electron gain gives the amplification factor of the gas phase of the TPC. As this property is sensitive, among other things, to gas impurities, field-, and level fluctuations, it is monitored to ensure data quality.

This information can be extracted by examining the distribution of small S2 signals, which are most likely caused by single electrons. There is also no need for these electrons to be caused by an external or internal calibration source. Any random single electron can be used, they can, for instance, originate from field emission on the cathode, from photoionization of electrodes and charge traps, or from delayed electrons that were temporarily trapped on impurities or in the liquid-surface interface.

To access this information, the data needs to be reprocessed with a special minitree. The minitrees used in the standard analysis only contain a pair of one S1 and one S2 which are considered to belong to the same event. The S2 considered in this pairing is the largest in the event and thus is usually caused by clouds of multiple if not even hundreds, thousands, or even more electrons. As mentioned in the AP analysis, also the second largest S2s are saved, but these are usually much larger than a typical single electron peak. The small S2 signals, caused by single electrons, are therefore not showing up in these minitrees.

The special minitree called 'PeakExtractor' can be used to access all peaks contained in each event. For this analysis, 20 runs were used. These contain 13.7 million peaks classified as S2. For comparison, the standard minitrees of the same runs contain only 512000 events, consisting of a pair of the largest S1 and largest S2. Based on these numbers, every recorded event contains on average 26 peaks classified as S2.

The gas amplification factor is sensitive to local field variations which can be caused by small differences in the thickness of the gas layer between the liquid-gas interface and the anode. Two major contributions of these variations are:

- **Mesh sagging:**
  The anode in XENON1T is actually not a mesh, but a steel frame with tensioned parallel wires. The electric field between gate and anode, gravity, and limited tension, results in wire sagging in the center region of the TPC, where the wires are the longest. This tension limit is chosen to provide minimal sagging, but also be loose enough to not risk damage to the wire during the cool-down and filling of the TPC. During detector cool-down, the wires contract much faster than the frame they are fixed to. If the static tension is already too high this shrinking may cause plastic deformation of the wire, resulting in a worse, permanent sagging when the detector is in its cold running condition. In the worst case the wire could even break, rendering the detector inoperative, as a broken wire might cause shortcuts with other meshes or the field cage.

- **TPC tilt:**
  The TPC is hanging inside a cryostat, which is floating inside a water tank. Despite all movement being restricted by the support structure and the position being fixed with high precision during the setup of the experiment, small uncertainties resulted in a small tilt of the detector, with a significant impact on the gas amplification factor. To provide a reference: the maximum in height difference between two opposing sides of the detector was found to be (0.63 ± 0.01) mm in [86].

To observe (x, y)-spatial variations in S2 gain, the surface of the TPC is divided into sectors, as presented in Section 4.5.

Single electrons are identified in the dataspace of the parameters *n_hits* and *range_50p_area*, where *n_hits* is the number of PMTs contributing to the peak and *range_50p_area* is the width of the peak in ns, containing 50% of the area.

Fig. 4.37 shows the single electron S2 distribution in this dataspace with two different selection ranges: one appropriate to Science Run 0 (SR0) data, which for the later data used here cuts into the single electron distribution due to a different field configuration, and a new selection to avoid this issue. Both selections are given in Table 4.8.

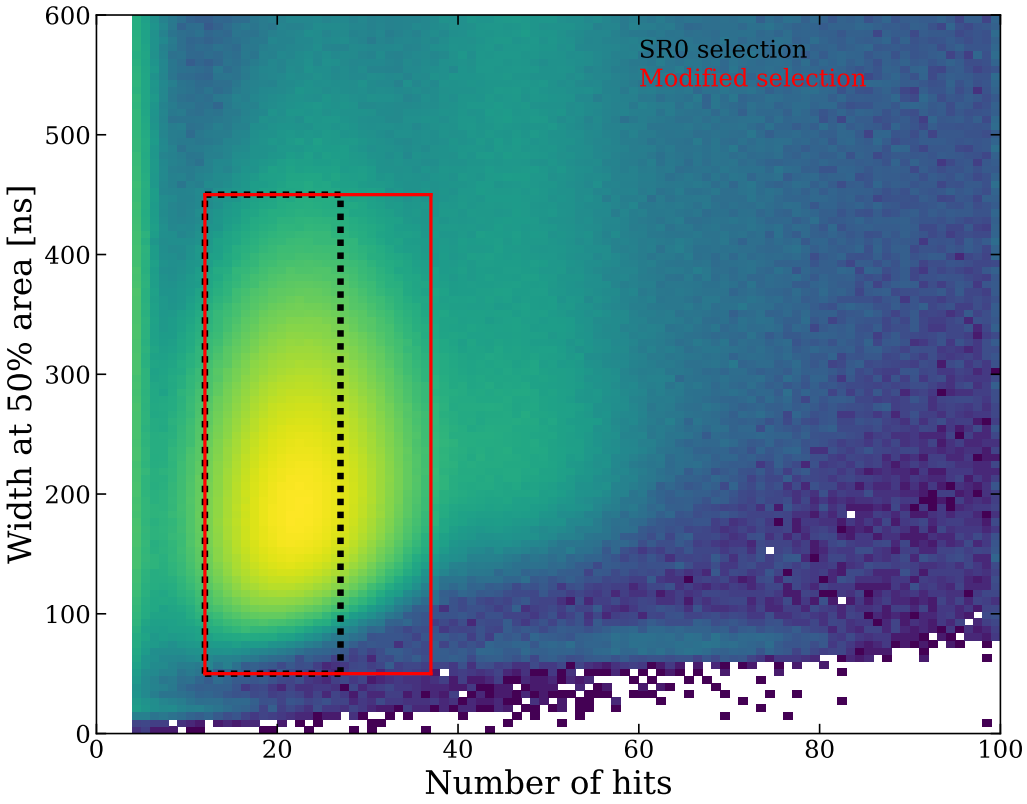

Figure 4.37.: *Single electron S2 selection in the 'range_50p_area' vs. 'n_hits' data space. Shown are two different selection ranges: an older one used in Science Run 0 (SR0), which later cuts into the single electron distribution, due to changed detector conditions. To correct for this, a larger window for the 'n_hits'-parameter was chosen.*

	n_hits		range_50p_area	
Selection	Min	Max	Min ns	Max ns
SR0	12	30	50	450
Modified	12	36	50	450
No selection	All data is used			

Table 4.8.: *List of selection cuts applied to the single electron S2 population.*

To extract the single electron gain, the mean of the S2 area is needed. For this the data with the modified selection are used. The distribution is not well described by a Gaussian, as a first fitting attempt revealed. To compensate for the asymmetry, the distribution was also fitted with a skewed Gaussian function:

$$G_{Skew}(x) = a \cdot e^{-\frac{(x-\xi)^2}{2\sigma}} \cdot (1 + erf(\alpha \cdot \frac{x-\xi}{\sqrt{2}\sigma})) \tag{4.19}$$

Exactly like for the 2D case, as introduced in Section 4.5, the mean of the Gaussian

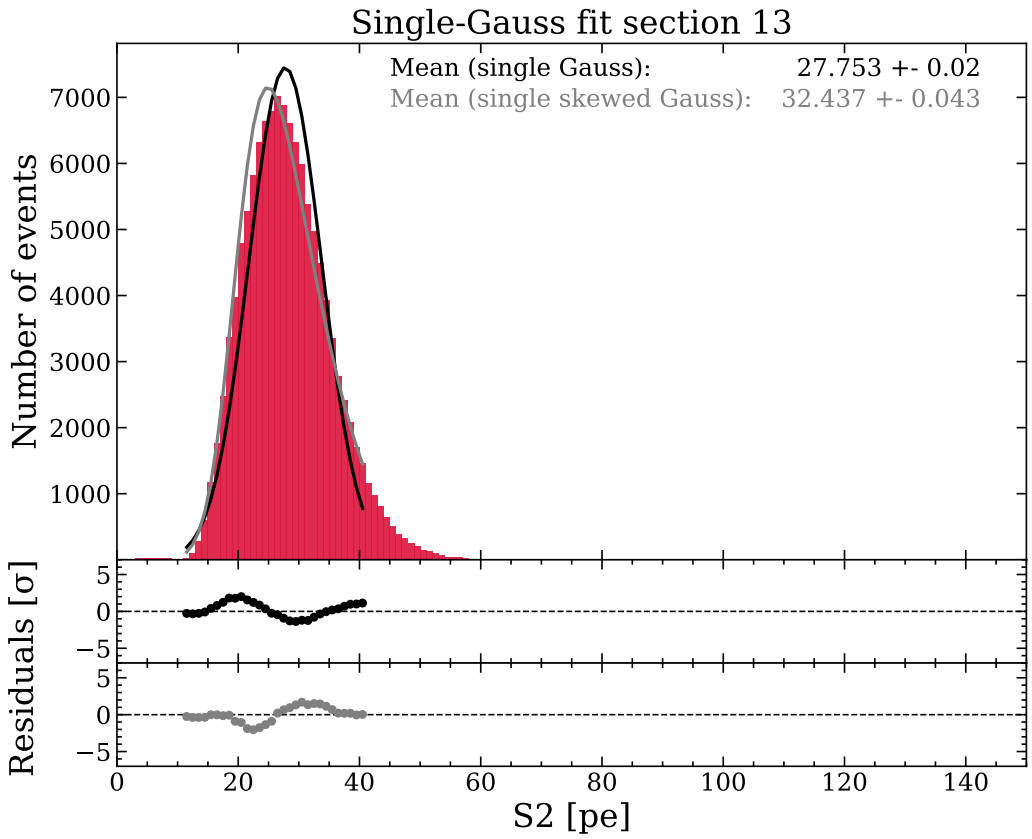

Figure 4.38.: *Single Gaussian fits on data selected with modified selection criteria. Neither the normal Gaussian nor the skewed Gaussian describe the shape very well. Additionally, the results for the mean of both fit functions can differ significantly.*

is not directly given by the parameter ξ, but it can be computed with:

$$x_0 = \xi + \sqrt{\frac{2}{\pi}} \frac{\alpha \sigma_x}{\sqrt{1+\alpha^2}} \tag{4.20}$$

The fit with the skewed Gaussian, however, also does not describe the S2 distribution very well. A direct comparison of both fits is shown in an example of one section in Fig. 4.38. Both functions show a relatively strong shape bias in the residuals.

The same fit procedure was also applied to the raw data, without any selection at all. In this case also other peaks are included, for instance, the two-electron peak, which is also visible in Fig. 4.37, directly right of the modified selection at a number-of-hits value of approx. 50. The raw data contains all peaks detected, this includes also the S2 later paired into events, which can consist of hundreds and thousands of electrons and is therefore not visible in the plot. These only make up a very low fraction and can be neglected. The one with lower numbers (like 2 or 3 electrons), however, can influence the shape and thus are taken into account by fitting a sum of Gaussians to the distribution. A fit with three Gaussian is shown in Fig. 4.39,

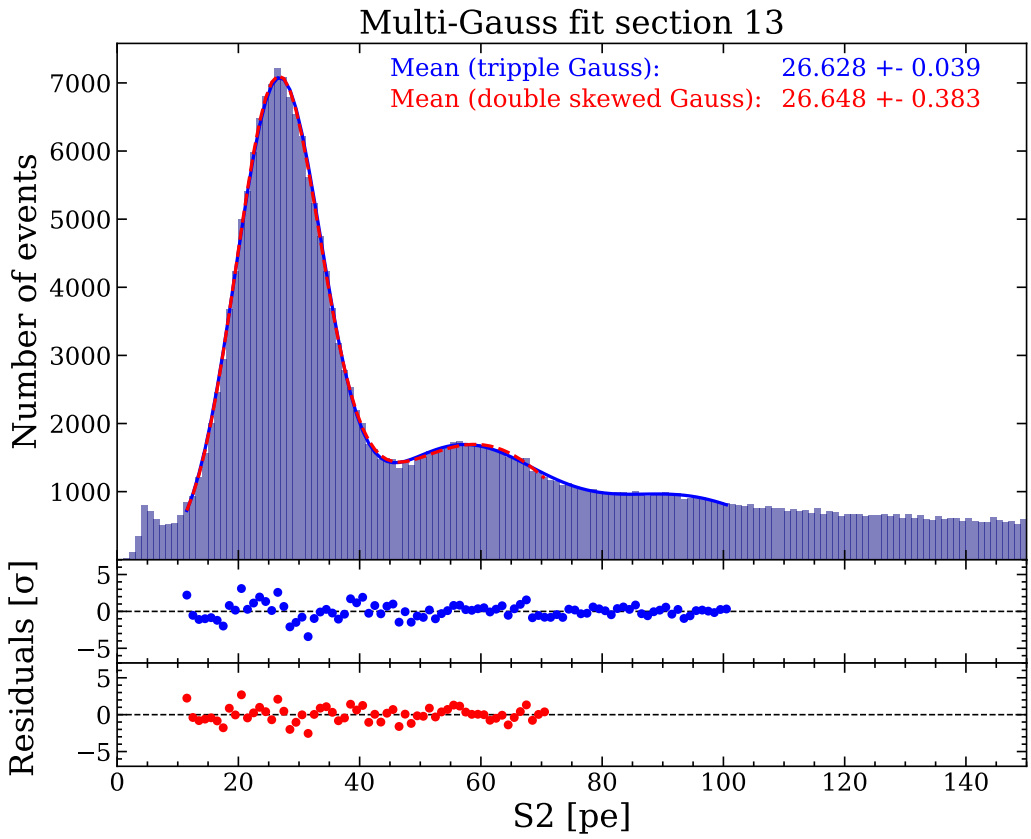

Figure 4.39.: *Summed Gaussian fit on all data of a single section (see Fig. 4.27) without further selection. The first fit consists of a sum of three normal Gaussians with free parameters. The S2 distribution is described well, without a shape bias as it was observed for the single peak fits. A fit with a sum of 2 skewed Gaussians (with a reduced fitting range) results in a very similar position for the S2 peak.*

featuring quite satisfactory residuals.

A test with a sum of 3 skewed Gaussians was very unstable, resulting partially in very low or high values for the skewness parameter and as such tampered with the mean position of the first component. When reduced to a sum of 2 skewed Gaussians, with a reduced fit range, this fit works more reliably. Also, the fit results are more similar to the simple Gaussian fits, with a nearly identical result in the shown example. The maximum observed difference of the S2 area was 0.5 pe over all 49 sectors.

Due to the stability issues observed for the skewed Gaussian fits and the nearly identical results for both variants, the triple-Gaussian results are used in further analysis.

The mean values of the first Gaussian from each of the section fits are arranged in the map shown in Fig. 4.40. A detector tilt is clearly visible. This map includes all effects having an influence on the signal amplification, including mesh sagging, TPC tilt, and even detector geometry effects, but is independent of the electron extraction

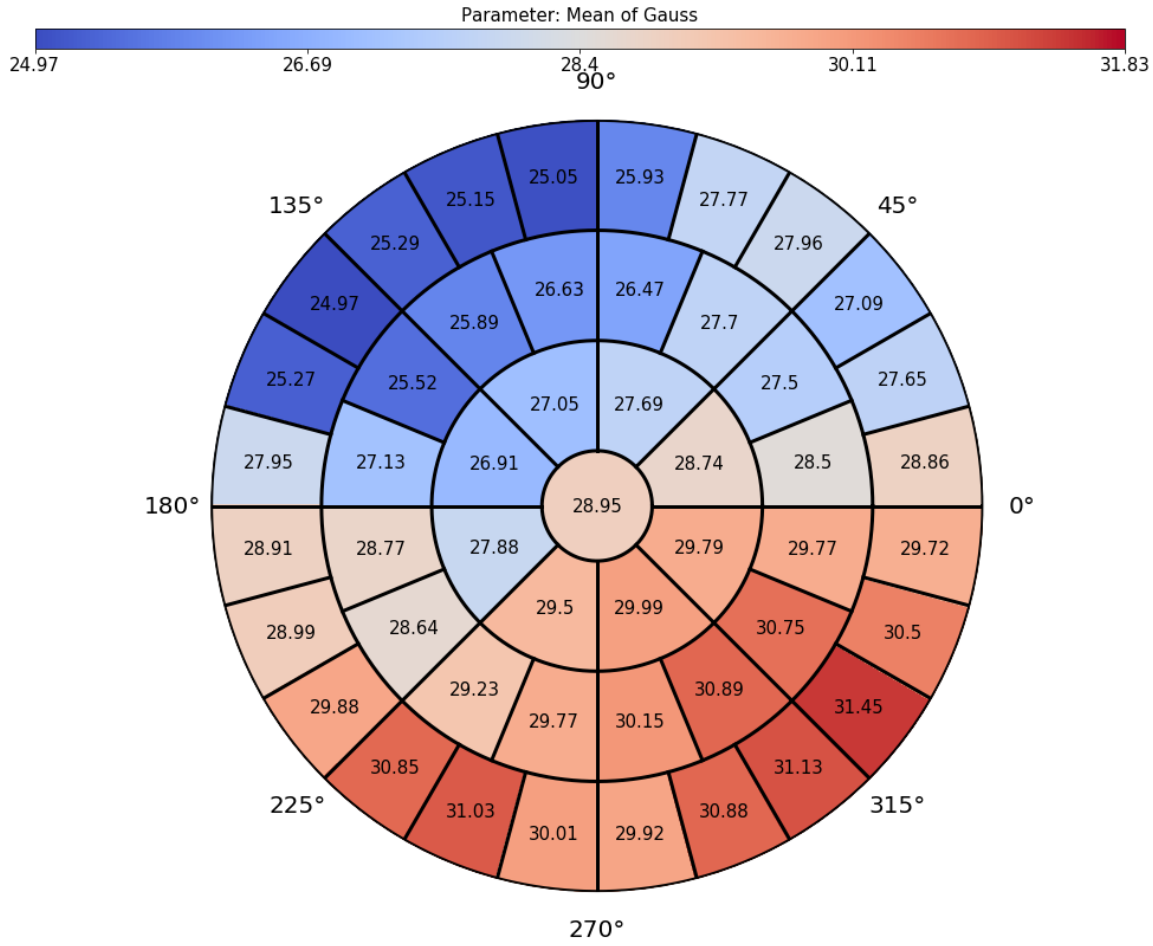

Figure 4.40.: *Section map for the single electron S2 gain. Clearly, a difference in gain between the two sides of the detector is visible. This indicates a variation of the strength of the extraction field or the electron path length in the electroluminescense region, caused by a variation of distance between the anode and the liquid surface, which points to a slight tilt of the TPC.*

.

efficiency. The average over all sectors yields a mean value for the single electron S2 gain of 28.949 ± 0.036 pe.

4.12. Alternative charge yield calculation

The charge yield can also be calculated directly, based on the ^{37}Ar S2 data, without the involvement of other calibration sources. This method is based on the corrected S2 signal, including the spatial and drift-time corrections, using the fit result found in Section 4.7. For this fit, only the cS2 from the bottom array was used. As now

the full S2 signal is needed, this value is corrected with the mean fraction f_{aft} [1] of all events included in the selected volume.

The mean number of electrons freed by an interaction of 2.82 keV, e.g. the charge yield can be calculated with:

$$N_e = \frac{\mu_{cs2_b}}{\epsilon_{ext} \cdot G \cdot (1 - f_{aft})} \tag{4.21}$$

Parameter	Value	Source
f_{aft}	0.637	mean of data selection
$cS2_b$	1302 ± 12 pe	fit on ^{37}Ar , see Section 4.4
ϵ_{ext}	96.4 %	official value for SR0
G	28.949 $\pm$ 0.036	single electron gain, see Section 4.11

Table 4.9.: *List of values used to obtain the charge yield directly from the ^{37}Ar data. The value of the extraction efficiency is taken from [87, 88].*

Table 4.9 lists the values needed for the charge yield calculation. The value for the single electron gain G is the one obtained in Section 4.11. The area-fraction-top (AFT) value f_{aft} is calculated as the mean of the AFT of the individual events.

The extraction efficiency ϵ_{ext} is based on an analysis done by the XENON collaboration. With these values, the electron yield can be calculated:

$$EY^{Ar} = (45.59 \pm 1.23)\frac{e}{keV} \tag{4.22}$$

The value found is significantly larger than the one obtained from the results of the Doke plot, which was 41.02 ± 1.06 e/keV. The main reason for this is the used lifetime correction based on the calibration with ^{83m}Kr . As ^{37}Ar data was found to be over-corrected, this leads to a too large estimation for the S2, which directly impacts the value of the electron gain. Refitting the ^{37}Ar data, this time corrected with the electron lifetime calculated in Section 4.3, results in a mean $cS2_b$ of 1239.6 $\pm$ 2.3 pe. With this value, the electron yield is calculated to be:

$$EY^{Ar}_{ArLT} = (43.39 \pm 0.28)\frac{e}{keV} \tag{4.23}$$

This result is already closer to the value found earlier with the Doke plot, the disagreement is however still significantly larger than the calculated uncertainties. As it was shown during the analysis of the ^{37}Ar data, ^{37}Ar is sensitive to various effects, so these values based on one source alone should not be considered as robust as the one obtained from the Doke plot, which takes measurements of multiple sources into account.

[1] fraction of the S2 signal seen by the top PMT array to the total *area-fraction-top*

One possible explanation is the use of the electron extraction efficiency based on other analyses, as detector conditions might have changed since theses analyses have been performed.

4.13. S2-only analysis

The analysis so far focused on the most frequent decay, the K-shell capture at 2.82 keV. With a branching ratio of 8.7 % (see Fig. 3.1) the L-shell transition also produces a significant number of interactions. As the decay energy of this transition is at 0.27 keV, this offers the opportunity to calibrate the detector at even lower energies.

As it was shown in the previous sections in Fig. 4.33, the K-shell interaction is already affected by the S1-detection threshold of XENON1T. For the L-shell interaction with a decay energy of 0.27 keV, the mean number of produced scintillation photons, using NEST for computation, is well below one photon, as shown in Eq. 3.1. Taking the light collection efficiency and the detection threshold of XENON1T into account, no detection of an S1 signal from this transition is to be expected.

According to NEST, the expected number of electrons at a drift field of 82 V/cm is $\sim$73 e^-/keV or $\sim$20 electrons in total. With the single electron amplification in the gas phase, an S2 signal on the order of $\sim$150 photons can be expected, which is well detectable with XENON1T. To analyze L-shell events, only the S2 signals are used and the requirement to have a valid S1 in an event is dropped. This so-called *S2-only* analysis was already used in XENON10, XENON100, and XENON1T in the search for light dark matter [89, 90, 91].

For the first ^{37}Ar calibration performed in XENON1T, the S2-only analysis of the data was analyzed by Andrea Molinario and Emanuele Angelino at the University of Torino [2]. For completeness of the results of the ^{37}Ar calibration, the results of this analysis are summarized here, with additional information presented in [92, 93].

With the S2-only method, S2 signals down to a size of 90 pe, equivalent to $\sim$3 extracted electrons, are evaluated. This lower threshold is chosen to reduce background from single- and few-electron events from the analysis. As an upper limit 5000 pe is chosen, as no larger ^{37}Ar -based signals are expected. In parallel to the L-shell events, also the K-shell events are analyzed with this method to provide a crosscheck. This is of particular interest as lowering the detection threshold came with the cost of loosing the 3D-position reconstruction. The determination of the x-y-position of an interaction is still possible, but due to the loss of the S1 and thus the drift time information, the z-position can not be extracted in this analysis directly. However, there is a relation between the depth of the interaction and the S2-signal width due to electron diffusion during drift. The direct effect of the two different selection methods are shown in Fig. 4.41.

For this selection, a subset of data was used, including data taken after the ^{83m}Kr

[2] INAF-Astrophysical Observatory of Torino, Department of Physics, University of Torino and INFN-Torino, 10125 Torino, Italy

source was closed and before the distillation started. A total of 6.9 days of data, taken between day 7 and day 14 after the first injection, are used. For further data selection, similar cuts as in the search for light dark matter are applied [39, 94].

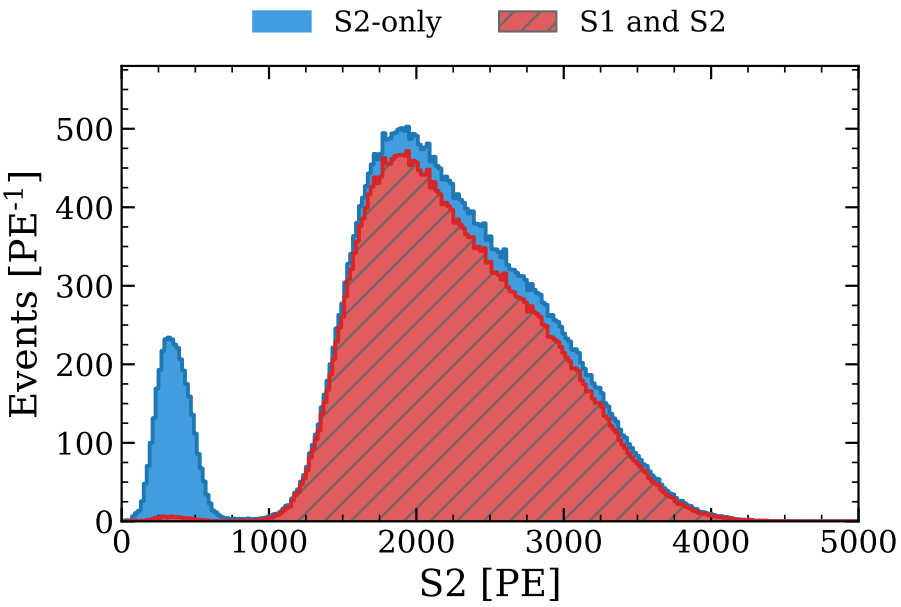

Figure 4.41.: *Comparison of the effect of both data selection types. The red distribution shows events selected in the S1-S2 data space, where nearly no events of L-shell interactions are selected. The blue distribution shows the events when the requirement of an existing S1 is dropped. Here the L-shell events appear, but also the number of K-shell events is increased slightly by events that were not accounted as valid before due to a missing S1. The non-Gaussian shape of the K-shell S2 is caused by the missing z-position correction. For increasing depth of interaction, the mean of the S2 slightly changes to lower values due to losses during electron drift. Additionally, the width of the S2 signal increases due to diffusion. The combination of the mentioned effects results in the observed shape for the K-shell peak.*

Data selection

To minimize the impact of field inhomogeneities, only events within a radius R $<$ 26.5 cm are used, which is a much tighter selection than the 47 cm used in the S1-S2 analysis. Another cut applied to the ^{37}Ar data is a selection in S2-width. Its selection range was modified compared to the light dark matter search, now passing all events with an S2 width between [300, 4000]. Although the z-position cannot be measured directly over the drift time, it can still be addressed via the S2 width as this is caused by diffusion of the electrons during drift. Therefore the S2 width cut removes events interacting near the top and bottom of the detector.

Further, a cut on the S2-area-fraction-top parameter is applied. This cut was slightly modified, removing events with a signal fraction of larger 69 % seen by the top PMT array. Signals with this structure are usually caused by interaction in the gas phase.

If an event contains more than one S2 with similar characteristics to the main S2, it is targeted by the cut to remove multiple scatters (although it is most likely only a random similarity as multi-scatter events are highly unlikely at these energies) and as such rejected.

Events are also checked for S1 signals and possible pairings with the main S2. If one possible pairing coincides with a z-position that fits with an interaction on the cathode, it is also excluded.

Fit model

As can be seen in Fig. 4.41, the detector response for single S2 signals, especially for the K-shell events, cannot be simply described by a (skewed) Gaussian model as for the S1-S2 analysis. This is a result of the missing z-information and thus missing drift-time correction.

Instead, a parametric model is used to describe the detector response. In this model, the S2 spectrum is modeled in three steps. In the first step, the expected rate for a certain number of produced electrons $r_p(n_e)$ is calculated. This number depends on the energy of the interaction type rates R_K and R_L (as the model is used for both, the K- and L-shell decay), and the branching ratio between the different decays and their respective electron yields EY_K and EY_L. In the second step the rate $r_p(k, z)$ for different numbers of extracted electrons k is calculated. This is highly dependent on the interaction depth z and as such dependent on the electron drift velocity and electron lifetime. Finally, the extraction efficiency is also applied to get the rates for k extracted electrons. In the last step the S2 rate $R(S2, z)$ based on $r_p(k, z)$ is calculated, using the single electron gain and applying reconstruction bias and smearing in dependence of the x-y-position of the interactions. The later mentioned parameters are extracted either from simulations (reconstruction bias) or are based on calibration (x-y-smearing). A more detailed description is provided in [92].

The acceptances of the above cuts are applied to the model before applying the fit to the data. In this fit five parameters are free to vary, namely the decay rates R_K and R_L, the electron yields EY_K and EY_L, and the electron lifetime. The latter is left free to provide an independent verification for the values obtained in chapter 4.3.

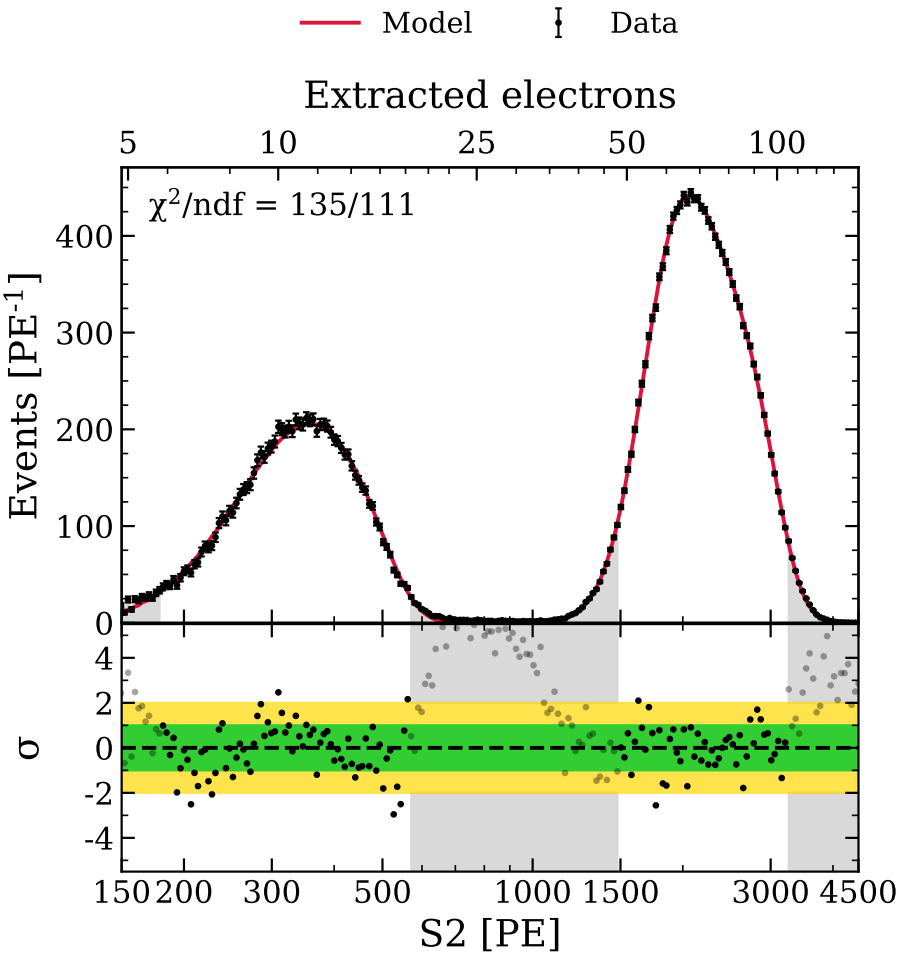

Figure 4.42.: *The best-fit model (red line) is shown together with the data (black. points). The lower panel shows the residuals of the fit. The grey regions show the areas that are excluded from the fit. The fit-relevant regions were chosen such that 95% of the peak areas are included in the fit. The regions outside this selection are excluded as the model does not describe the tail regions of the peaks very well, a fact which is also reflected in the residuals in these regions. Note the logarithmic x-axis.*

Results

The combined K- and L-shell decay S2 spectrum and the result of the model fit to the data is shown in Fig. 4.42. Both peaks are fitted simultaneously with the model. Only the central regions of the peaks (containing 95 % of the peak area) are included in the fit. The tails of the peaks are excluded, marked as grey regions, as they are not described well by the model. Overall, the fit is in good agreement with the data, resulting in a reduced $\chi^2/ndf = 135/111$.

The best fit parameter provides results for the electron yield for both decays, the L-shell:

$$\mathrm{EY}(0.27\ \mathrm{keV}) = 68.0^{+6.3}_{-3.7}\ \mathrm{e}^-/\,\mathrm{keV} \tag{4.24}$$

and for the K-shell:

$$\mathrm{EY}(2.82\ \mathrm{keV}) = 40.0^{+2.7}_{-2.2}\ \mathrm{e}^-/\,\mathrm{keV} \tag{4.25}$$

Additionally, the K- and L-shell event rates, which were also free parameters, can be used to calculate the branching ratio of the two decay modes. This results in a value of:

$$\mathrm{L/K} = (10.11 \pm 0.44)\,\%\,, \tag{4.26}$$

which is in good agreement with the expected value of 9.67 % [70]. This result confirms a good understanding of the S2 detector response at both ^{37}Ar decay energies.

4.14. Electron and photon yield in liquid xenon from the ^{37}Ar calibration

Based on the analysis in the S1-S2 data space and the analysis based on S2-only, new values for the photon and electron yield of ^{37}Ar were obtained. The data was taken at the standard running conditions of the XENON1T detector at a drift field of 82 V/cm. Fig. 4.43 shows the results obtained and presented in this work in comparison to other measurements of xenon-based detectors. The results for the 2.82 keV interaction are generally in good agreement with other measurements, especially with the CH_3T based measurement from the LUX experiment [95]. The largest disagreement is observed when comparing the result with the ones obtained with PIXeY, although this data was taken at higher drift fields [72]. A better agreement is achieved with the results of the Xurich II TPC, which was operated under similar conditions as XENON1T [96].

The S2-only analysis adds a data point for the electron yield in the sub-keV range, where only two other experiments contributed so far, measuring a value below the one predicted by NEST.

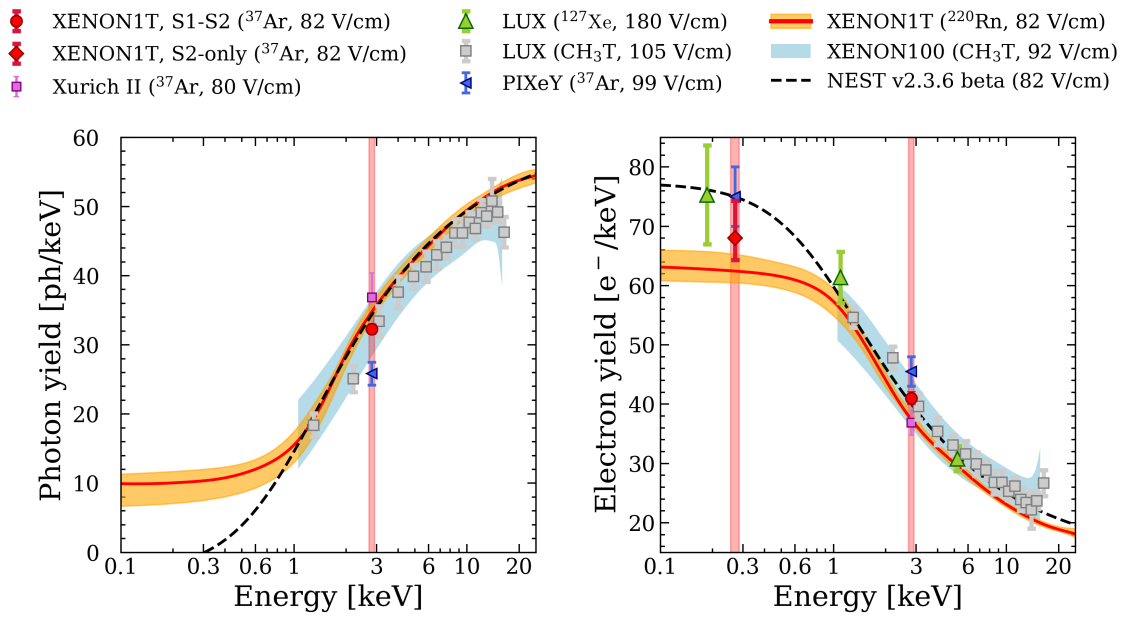

Figure 4.43.: *Summary plot for the photon and electron yields obtained during this first calibration of the XENON1T detector with ^{37}Ar. The results are shown together with ER measurements of other xenon-based detectors in a similar energy regime. These include results from LUX, based on CH_3T and ^{127}Xe [97], and measurements of the smaller Xurich II and PIXeY TPCs. Also shown is a XENON1T measurement based on ^{220}Rn as well as an older result from XENON100 based on CH_3T [68, 98].*

4.15. Impact of ^{37}Ar calibration on the XENON1T low-energy electronic-recoil excess

In 2020 the XENON collaboration published a paper describing an excess for electronic recoils at very low energies observed in XENON1T [77]. In this paper, the ER data taken during the first science run of XENON1T is fitted with a sophisticated background model including the standard background sources present in LXe detectors like ^{85}Kr and ^{214}Pb, a daughter of ^{222}Rn which is emanated from the detector materials. The model also includes components based on decays of unstable and meta-stable xenon isotopes that are produced during a neutron calibration of the detector. Even a solar neutrino component is part of the model, which when fitted to the data, showed a 3.3 σ deviation from the expectation in the 1-7 keV region. After the exclusion of systematic and instrumental effects, several signal models were examined to describe the excess. In the following a summary of the possible causes of the excess is given as discussed in the XENON1T excess paper. The signal models discussed are:

- **Tritium contamination:**
  Tritium is the heaviest hydrogen isotope, which decays via β-emission and has a half-life time of 12.3 years. With a Q-value of 18.6 keV, it can be a source for the observed excess. Tritium can be introduced into the system via the capture of atmospheric hydrogen into the materials used in the construction of the detector. Atmospheric hydrogen can be activated by cosmic radiation, but it can also be produced by spallation processes of cosmogenic produced neutrons on xenon even in the underground facilities of the LNGS.

  The fit of the model to the rate results in a tritium concentration which would be an equilibrium between emanation and removal, as tritium, predominantly present in the form of HTO or HT, would be removed by the getters. Additional limits on the tritium content are given by the achieved electron lifetimes, as the tritium compounds would have a significant impact on the achieved value. In conclusion, as no direct measurements of the tritium concentrations were performed during the run-time, tritium can neither be confirmed nor excluded as a background.

- **Solar Axions:**

  Introduced as a solution to the strong CP problem [99], axions, under certain circumstances, also provide good candidates for dark matter. From cosmological and astrophysical observations it can be concluded that the axions, which were created in the early Universe, have masses well below the keV range and thus cannot be observed with XENON1T [100, 101, 102]. Solar axions however, for example from the isotope ^{57}Fe, which is relatively abundant in stars, would deposit energies in the low keV range [103], which is well inside the detection range of XENON1T. A much more detailed explanation of the coupling strengths and the axion flux components that contribute to this model can be found in the XENON1T excess paper [77].

- **Neutrino Magnetic Moment:**

  Due to the observation of neutrino oscillations, the SM needs to be extended to include the neutrino mass. As a result it will also have a magnetic moment [104]. From the SM, a value for the magnetic moment of $\mu_\nu \sim 10^{-20}\mu_B$ can be calculated, with μ_B being the Bohr magneton. Current detection limits based on solar and reactor neutrino measurements are in the order of $10^{-11}\mu_B$, observations based on astrophysical observations reach one order of magnitude lower [105].

  An enhanced magnetic moment in the order of $10^{-11}\mu_B$ would be in the detection range of XENON1T. In the case of the XENON1T analysis of the low ER excess the expected neutrino spectrum would be added to the background model, including the effects expected from elastic neutrino scattering. As for the other

candidates a more complete explanation and additional sources on this topic can be found in the XENON1T excess paper [77]

- **^{37}Ar contamination:**

  The ^{37}Ar decay energy is exactly in the ROI of the excess. Therefore possible ways of an ^{37}Ar contamination were also examined to explain the excess. Only two possible ways of an ^{37}Ar contamination were identified to be able to impact the data in the observed magnitude.

  The first is an initial contamination of the used xenon. Due to the time difference between the filling of the TPC and SR1, the time period during which the data used in this analysis was taken, and taking the half-life time of ^{37}Ar of 35 days into account, it is expected that the amount of ^{37}Ar left after natural decay is negligible. Additionally, as previously shown, ^{37}Ar is removed during krypton distillation, so that any leftover from an initial ^{37}Ar contamination can be excluded.

  A second possibility is continuous contamination by ^{37}Ar present in the air via a leak. The leak rate of the XENON1T system can be estimated based on the ^{nat}Kr increase in the system after distillation. Based on a measurement of the ^{37}Ar concentration in the experimental hall, a ^{37}Ar rate of < 5.2 events/(t·y) is expected, while a rate of > 65 events/(t·y) is needed to explain the excess [106].

During the calibration with ^{37}Ar, more specifically when obtaining the electron lifetime with ^{37}Ar, it was observed that for low-energy interactions the S2 signals are reconstructed smaller than expected. As shown in Section 4.3, it was found that for small signals the main S2 and following APs may be separated and thus missing in the S2 peak saved in the minitree. As shown in the XENON1T excess paper, when fitting a peak to the excess, the best fit is obtained with a peak at an energy of 2.3 keV, which is well within the range where the AP issue might affect the analysis [77].

Besides the AP correction to the data, the fit model for a single peak contribution used was changed from a simple Gaussian to a skewed Gaussian. This is also based on the observations made during the ^{37}Ar analysis, as discussed in Section 4.5.

The implications of these corrections on the data and fit are shown in Fig. 4.44. As shown, the impact on the data, especially in the excess region is negligible. Although the effect of changing the fit function on the shape is minimal, the best-fit peak energy moves from 2.3 keV which resulted from a Gaussian to 2.4 keV for the updated model with a skewed Gaussian peak.

An answer to the question, if the excess is really a signal or if it was just a statistical fluctuation, was one of the most anticipated results after the upgrade to XENONnT. For the XENONnT result, a total exposure of 1.16 tonne×years was used. In this data, the achieved background level is roughly a factor 5 lower than the one achieved in XENON1T, as can be seen in Fig. 4.45. No peak or excess, however, is observed in XENONnT using a blind analysis. As no excess has been found, new limits were set and parameter space was excluded for the before-mentioned models. As a result,

some sort of contamination, most likely with tritium, was responsible for the excess in XENON1T. In this case, the absence of a signal in XENONnT would result from improved cleaning and prevention measures, especially regarding tritium, taken during material selection and construction of the detector [107].

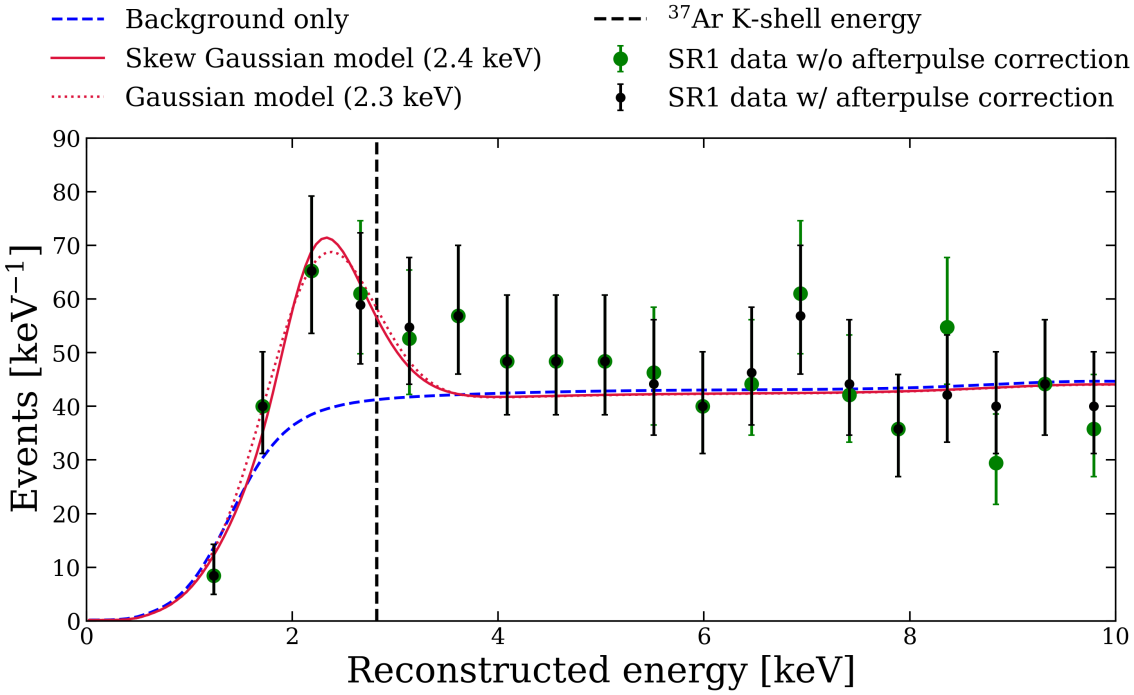

Figure 4.44.: *Impact of the corrections learned from the ^{37}Ar calibration. The data are corrected for the afterpulse effect (black points vs. grey points), which only shows a minimal effect at very low energies below 6 keV. Additionally, instead of a simple Gaussian peak a skewed Gaussian is used to fit the excess (solid red line vs. dotted red line). Overall the impact on the excess when applying the corrections is negligible. For completeness the energy of the ^{37}Ar decay is shown, which also has a significant offset compared to the best-fit results, discouraging ^{37}Ar as the source of the excess, besides all the other arguments already pointed out. The data re-analysis shown in this plot was performed by Evan Shockley.*

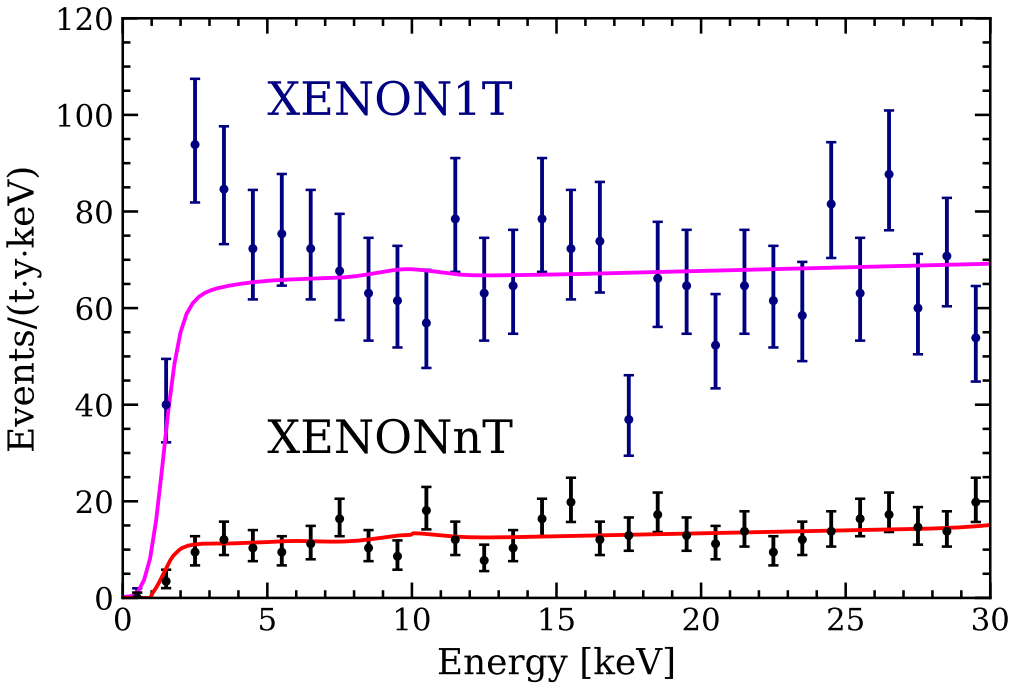

Figure 4.45.: *Direct comparison of data from XENON1T (blue points) and XENONnT (black points), fitted with the corresponding background models only. It is clearly visible that the background level in XENONnT is about a factor of 5 lower than the one from XENON1T. Also, no excess is observed in XENONnT. Composition plot created by Jingqiang Ye [77, 107].*

4.16. Summary and conclusion

After an initial rate-based analysis, presented in the previous chapter, the distillation process is re-analyzed, this time using a proper ^{37}Ar event selection to calculate the event rate. The resulting rates are fitted with a simple exponential model. The fit results in a distillation time constant of $\tau = 1.972 \pm 0.013$ days, which means a reduction of rate by a factor of ten every 4.543 ± 0.030 days. After this first calibration, the background event rate at the ^{37}Ar energy was reached again after 24 days of continuous distillation. This time span is considered reasonable for removal, rendering this a viable source between science runs, not only at the end of the experiment. This is actually realized between SR0 and SR1 of XENONnT.

Calculating the electron lifetime based on ^{37}Ar data results in a lifetime of $(947.00 \pm 0.18)\,\mu$s. This value significantly differs from the one used so far for corrections, based on data taken with ^{83m}Kr , which has a value of $(832.62 \pm 0.43)\,\mu$s. It was found that the electron lifetimes differ due to field inhomogeneities. These inhomogeneities not only affect the drift times of electrons but also the ratio of produced electrons and photons during an interaction. Applying a field correction to the S2 results in very similar values for the electron lifetime of different sources at different interaction

energies. The newly computed values are very close to the corrected one of ^{37}Ar with a lifetime of $(921.30 \pm 0.19)\,\mu$s.

In the next step, the charge and light yields of ^{37}Ar were calculated. To achieve this, a suitable model for the asymmetric shape of the S1-S2 distribution was developed. This included the use of a two-dimensional, skewed Gaussian function. Additionally, due to the very low energy and therefore very small S1 signal, the detection threshold of XENON1T needs to be accounted for. As the shape of the signal was found to be strongly position dependent, causing an additional distortion of the signal peak, the TPC-volume was divided into smaller sub-volumes, which were fitted individually. The resulting mean values for the light and charge yield were found to be $4.625 \pm 0.044\,\mathrm{pe/keV}$ and $461.906 \pm 4.636\,\mathrm{pe/keV}$. These values for ^{37}Ar were added to the so-called Doke plot, including already a variety of other calibration sources, where a fit, now including the ^{37}Ar data results in the detector-dependent photon and electron gain of $0.143 \pm 0.001\,\mathrm{pe/ph}$ and $11.260 \pm 0.103\,\mathrm{pe/e^-}$, respectively. From these, in turn, the detector-independent photon and electron yields for the ^{37}Ar energy of 2.82 keV can be calculated to be $32.27 \pm 0.52\,\mathrm{ph/keV}$ and $41.02 \pm 1.06\,\mathrm{e^-/keV}$, respectively.

Besides the main K-shell peak at 2.82 keV, also the L-shell peak at the smaller energy of 0.27 keV was analyzed. For this, a special data format was needed, as events at this energy do not have a valid S1-S2 pair. In this analysis, based solely on the S2 signal, an electron yield of $68.0^{+6.3}_{-3.7}\,\mathrm{e^-}$ keV is found. To validate the procedure, also the K-shell peak was reevaluated and an electron yield of $40.0^{+2.7}_{-2.2}\,\mathrm{e^-}$ keV was found, in agreement with the value found in the analysis of the combined S1-S2 signal.

As the ^{37}Ar decay energy is in the range of interest (ROI) of the XENON1T excess, these data were re-evaluated taking the findings of the ^{37}Ar analysis into account. This especially addresses the AP correction for low energy data and the usage of a skewed Gaussian function to model the excess, instead of a symmetric one. Although some event numbers are changed by the AP correction, the positions and magnitude of the excess remains unaltered.

In conclusion, the calibration with ^{37}Ar offer a novel, complementary calibration source with applications similar to the already used ^{83m}Kr source. Compared to ^{83m}Kr, ^{37}Ar is comparatively insensitive to field effects and uniquely provides a calibration point for the S2-only analysis with its L-shell decay at 0.27 keV. Additionally, due to the much lower energy close to the XENON1T detection threshold, ^{37}Ar highlighted some areas in the analysis chain, that needed improvement to properly describe low-energy events, including AP correction, field correction and a skewed Gaussian-based peak modeling. These factors are already included in the improved analysis routines used in XENON1Ts successor XENONnT, where a short outlook is given in the next chapter.

5. ^{37}Ar Calibration of the XENONnT detector

In 2021 the next generation detector XENONnT was commissioned. Based on the same working principles, it introduced a significantly larger TPC with a diameter of 1.328 m and a height of 1.485 m. This allows for the usage of an increased active Xenon mass of 5.9 t, which in turn results in a higher fiducial volume which is increased from 1.3 t to 4.18 t [59]. The infrastructure needed to operate XENONnT is directly inherited from XENON1T as it was already foreseen during the construction of XENON1T. The muon water tank and the outer cryostat as well as most of the gas purification and storage system are reused.

There are, however, some additions to improve detector performance and adapt to the higher detector mass. A liquid purification stage and an online radon distillation column were added to further increase xenon purity as well as a second storage facility to accommodate the larger amount of xenon used [108, 109]. An additional Cherenkov detector was added in the water tank to veto neutrons, which can mimic WIMP signals in the TPC (XENONnT paper in preparation). Another upgrade is a permanent ^{37}Ar injection branch added to the calibration system, enabling a ^{37}Ar calibration in between science runs without additional hardware work besides ampule exchange.

This system upgrade is presented in chapter 5.1, the first calibration procedure is explained in Section 5.2, and Section 5.3 gives a first outlook on the data analysis in XENONnT.

5.1. Calibration system upgrade in XENONnT

With the upgrade to XENONnT, the ^{37}Ar calibration system was permanently integrated into the calibration system. The main working principle of the system remained the same, as well as the main components, which were reused from the XENON1T system. The arrangement, however, was optimized, based on the experience with the first calibration performed in XENON1T.

The ampule opening system using a guillotine mechanism as shown in Fig. 3.5 stayed unchanged. The system was rearranged in such a way that after the ampule opening the first dilution is into a small VCR cross (DV-Cross) and after that into the activity camera volume. An additional cold trap (CT-A) was added after the camera volume, allowing evacuation of cross and camera volume and thus creating an active flow of the ^{37}Ar -Xe gas mixture. This has proven to be much faster and

more efficient for mixing than relying on diffusion only. This arrangement of the first rough dilution volumes also allows for the repeated filling of these two volumes from the ampule volume, which is helpful in case of a weaker source or if larger injections are needed. The camera setup was not operational during this first calibration, but the volume of the camera is crucial in achieving a sufficient dilution from the very high rate source of order $\mathcal{O}(100\,\mathrm{kBq})$ to the needed activity for the detector of order $\mathcal{O}(10\,\mathrm{Bq})$.

The regulating valve intended for fine dosing with continuous activity selection was removed. On the one hand, this kind of valve is not designed to close tight (although the one used in XENON1T was modified to achieve this), on the other hand, during the XENON1T calibration it became clear that this feature is not necessary.

Instead, a fixed arrangement of four valves with well-known volumes in between them was used for dosing. As all the volumes were evacuated via the second cold trap (CT-B) and thus gas transport was achieved via flow and not diffusion, the dilution process proved to be very reliable and is based only on the volume ratios. A pressure measurement is not necessary, but a pressure transducer is still present if the filling status of the system needs to be checked. Fig. 5.4 shows a schematic of the new arrangement together with the realization at the experimental site. Tab. 5.1 gives the possible injection strengths for an initial ampule activity of 100 kBq.

Volume Name	Volume [cm^3]	Activity (target) [Bq]	Activity (calibration) [Bq]
Ampule container	182	100000	37635
Activity camera	327	2224	837
DV-Cross	4.14	15.68	5.90
DV-A	3.2	8.69	3.27
DV-B	1.26	3.42	1.29

Table 5.1.: *Volumes of the system that are used to dilute the activity and the resulting dosing step size based on an initial ampule activity of 100 kBq, the target activity of the irradiation. The volumes are extracted from the CAD models of the setup and the valves. The error of the volumes is neglected here, as they are estimated to be much smaller than the uncertainty for the activity of 10%, based on experience from irradiation in the Mainz TRIGA reactor. Activities at the time of calibration (corrected for the natural decay of ^{37}Ar) are given in the right column, thus representing the estimated activities used for the dosing during the calibration of XENONnT.*

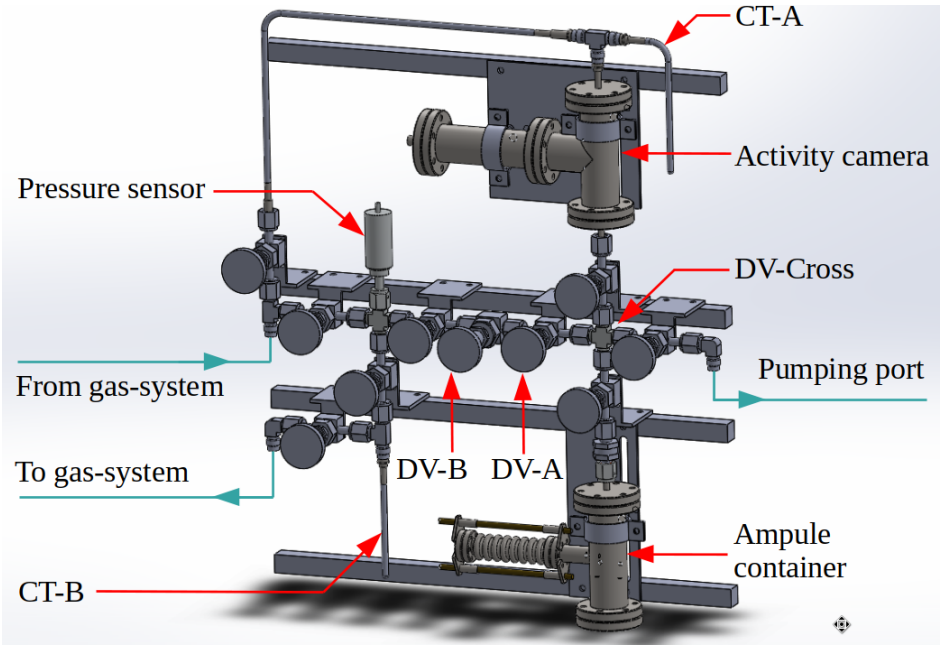

(a) *CAD-scheme of the new ^{37}Ar dosing system.*

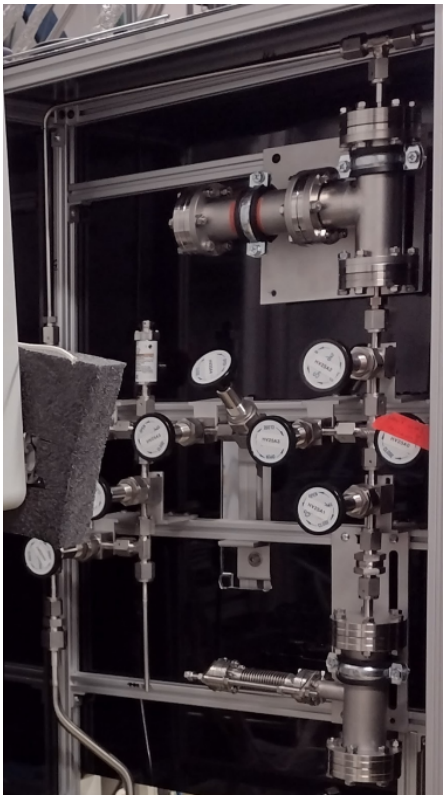

(b) *Picture of the new ^{37}Ar dosing system.*

Figure 5.1.: *New dosing system for XENONnT, now permanently installed in the calibration section of the gas recirculation and purification system.*

5.2. First ^{37}Ar calibration in-between science runs in XENONnT

The first ^{37}Ar calibration in between science runs in XENONnT was done in December 2021 after the first science data collection of the XENONnT detector. The actual calibration started 43 days after the irradiation of the ampule, which was again targeted to achieve 100 kBq. This delay reduced the overall activity in the ampule to approx. 37.6 kBq based on the argon half-life of 35 days. This of course also reduces the injection step sizes to the new expected values given in Tab. 5.1.

As the injection system was new, as well as much of the detector and detector infrastructure had changed compared to the calibration in XENON1T, the first injections were planned to be small to test the detector response. A second reason for this slow approach is the fact that the absolute activity contained in the ampule cannot be measured beforehand, thus a careful approach to the desired calibration rate is chosen. This second reason, however, is valid for every new ampule produced, making this first slow rate increase at the beginning of a calibration a mandatory step.

Injection	Time [d:hh:mm]	Injected Activity [Bq]	Cumulative Injected Activity [Bq]
1	0:00:00	1.3	1.3
2	0:04:17	3.3	4.6
3	0:22:11	5.9	10.5
4	1:04:52	10.3	20.8
5	1:23:10	41.7	62.5
6.1	2:23:19	40.8	103.3
6.2	3:00:43	39.8	143.1
6.3	3:03:53	33.2	176.3
7	6:03:42	37.9	214.2

Table 5.2.: *Injection steps performed in the first ^{37}Ar calibration of the XENONnT detector. As in XENON1T, a series of small injections was performed to verify the order of magnitude of the activation in the ^{37}Ar ampule, followed by larger steps to increase the measured rate to the target activity. The size of injections also takes the reduction of the source volumes into account. Injections 5, and 6.1 are injected from the same dosing volume, but they are also filled from the camera volume, which for the later refill of course contains less activity than before, thus the reduction from 41.7 Bq to 40.8 Bq between these two injections.*

Learning from the XENON1T calibration, ^{37}Ar has shown to be a valuable source that can be used for cross-checking many different analyses or calibrations. One main goal of this calibration is the creation of correction maps directly comparable in detail to the one resulting from weekly ^{83m}Kr calibrations. To achieve this approximately 10^7 events are needed. The time frame given for the full rate calibration, excluding the

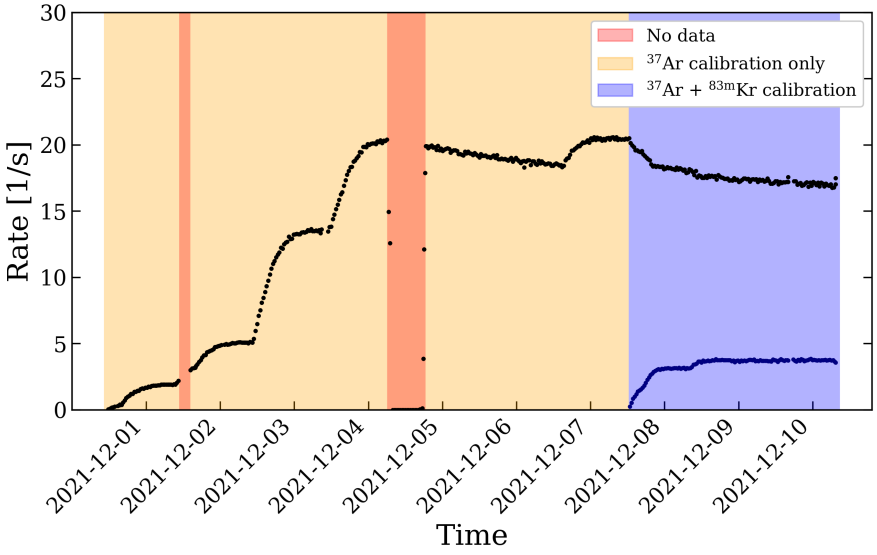

(a) *Injection phase of the ^{37}Ar calibration.*

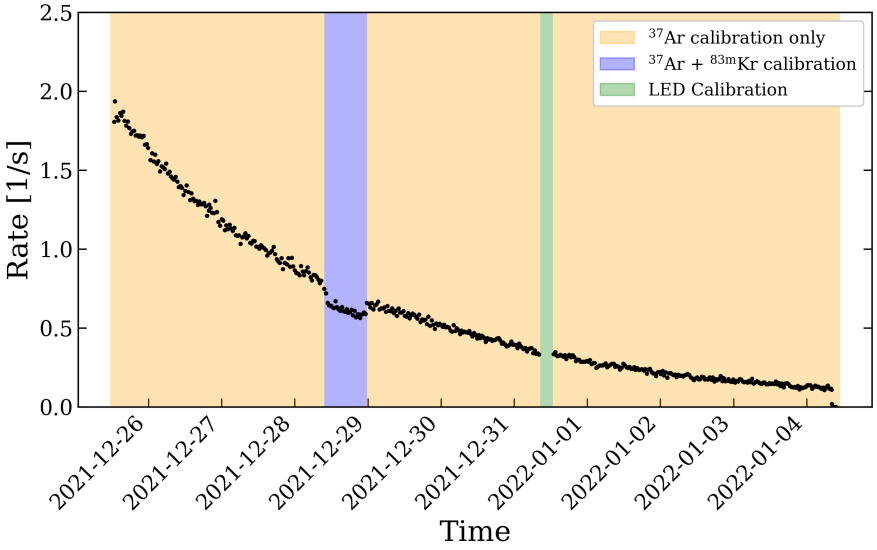

(b) *End of the distillation phase.*

Figure 5.2.: *Calibration of the XENONnT detector with ^{37}Ar . Shown are the mean rates per data run, with a simple source selection in S1-S2 space, for the two sources ^{37}Ar and ^{83m}Kr with black and blue data points, respectively. Fig. 5.4a shows the rate increase for each of the injection steps listed in Table 5.2. During the red-marked time windows, no ^{37}Ar data is available due to technical issues of the detector. Also, a pile-up effect is observed as soon as the ^{83m}Kr source is added, with a sudden reduction in the observed ^{37}Ar rate. Fig. 5.4b shows the end of the distillation, with the expected exponential reduction in rate. A ^{83m}Kr calibration with a high rate (not shown) was performed during this episode, resulting again in a rate reduction caused by pile-up.*

activity trial phase, was 4 days of data taking. These were also split into two modes: two days of ^{37}Ar data only and two days of ^{37}Ar in parallel with an open ^{83m}Kr source, to allow direct comparison between both sources at the exact same detector conditions. Due to pile-up effects the planned injected rates are not expected to be directly observed, at least not for higher rates.

5.3. First look at XENONnT data

The general approach of analyzing the data in XENONnT is identical to XENON1T. Before the data analysis, a series of cuts is applied to reduce background and identify and remove bad events. The cuts are very similar in function to the ones applied in XENON1T but adapted to the different detector conditions of XENONnT. Therefore only a short summary and explanation is given here.

A first set of cuts is applied to ensure data quality. This includes a check that the recorded events are not too close in time to run boundaries or other hardware-related vetos. This avoids splitted (between datasets) or incomplete events caused by a too high rate. It is also checked that at least 3 PMTs have contributed to a signal and that one of the designated S1 or S2 of an event actually created a trigger, otherwise the event is considered an accidental coincidence and is discarded.

Further cuts are applied addressing directly the event attributes. Each peak of an event (S1 and S2) is checked for its shape, light pattern in the PMT arrays, and the number of PMTs that contributed to the peak. These cuts try to eliminate falsely classified single electron and gas events, for example.

The XENONnT data taken during the ^{37}Ar calibration period is shown in Fig. 5.3. The event distribution in corrected S2 vs. corrected S1 data space is shown after the basic quality and peak cuts are applied. The data includes the ^{37}Ar peak, which is visible in the lower left corner at 15 pe in S1 and 1800 pe in S2. ^{83m}Kr peaks are visible at 300 and 400 pe in S1 and 8000 pe in S2, due to the double decay structure of ^{83m}Kr .

An extra complication is introduced in XENONnT by the design of the gate electrode. To minimize wire sagging and the possible resulting field distortions, the gate has two transverse supporting wires below the actual electrode wires. These wires have caused larger than anticipated field distortions, resulting in strong effects on event position and gas amplification [110]. A simple solution to minimize their impact is to remove the affected events via a cut. This cut removes all events within a certain distance from the wires. While this increases data quality it also comes with a large reduction of detector volume, as the wires are close to the center of the TPC. The effect of the wires on the reconstructed event distribution and the cut effect is shown in Fig. B.29 in the appendix on page 225.

One major difference in the operational conditions between XENON1T and XENONnT is the applied drift field. While in XENON1T a field of 82 V/cm was applied, a field of only 23 V/cm was achieved in XENONnT [110]. This results in a

higher photon yield and therefore a lower charge yield compared to XENON1T, as shown in Fig. 2.1 in Chapter 2.1. For an ^{37}Ar interaction therefore larger S1s and smaller S2s are to be expected, compared to XENON1T. Another factor influenced by the field is the drift speed of the electrons. Besides the larger distances due to the increased height of the detector, the lower field will additionally increase the drift time of the electrons.

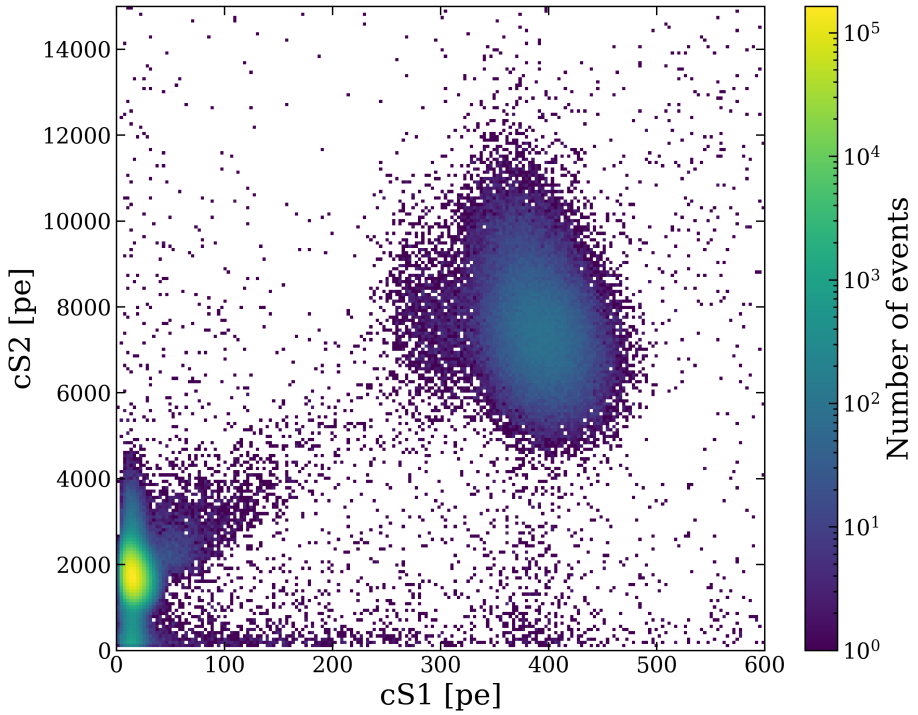

Figure 5.3.: *Data taken during the ^{37}Ar calibration run of XENONnT. Besides the ^{37}Ar source also ^{83m}Kr was injected simultaneously. The ^{37}Ar peak is visible in the lower left corner at an S1 of 15 pe and an S2 of 1800 pe. The ^{83m}Kr peaks are visible at an S2 of 8000 pe and S1 values of 300 pe and 400 pe for the 32 keV and 41.5 keV line, respectively. For the ^{83m}Kr events, most of the 32 keV line and the 9 keV line are removed by the single scatter cuts.*

Electron lifetime in XENONnT

For the electron lifetime estimation, data selection is done in the same way as in the previous XENON1T analysis. An energy region is selected by selecting events within a certain area in the S2 vs. S1 space. For ^{37}Ar all events with an S1 $<$ 50 pe and 500 pe $<$ S2 $<$ 4000 pe are considered. Due to the lower field and larger dimensions of the TPC, the drift time is much longer, with a maximum drift time of 2.2 ms, compared to 750 μs in XENON1T.

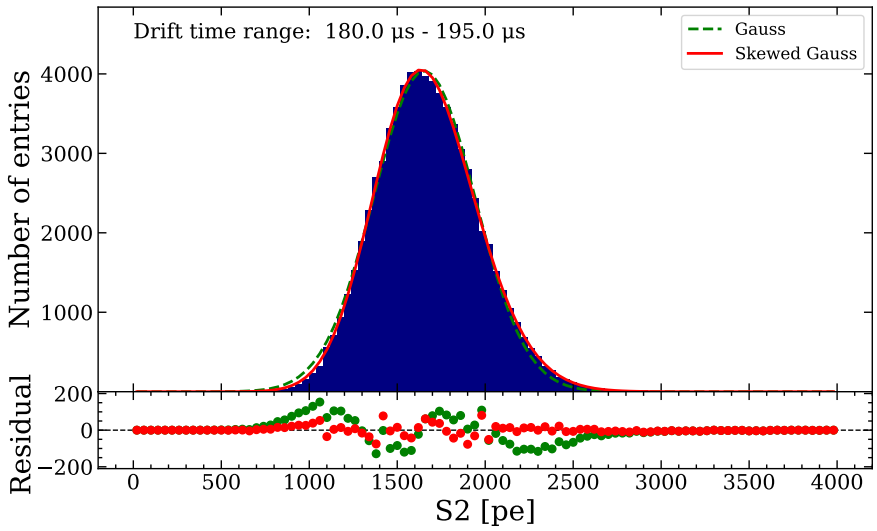

(a) *Example fit of one time slice.*

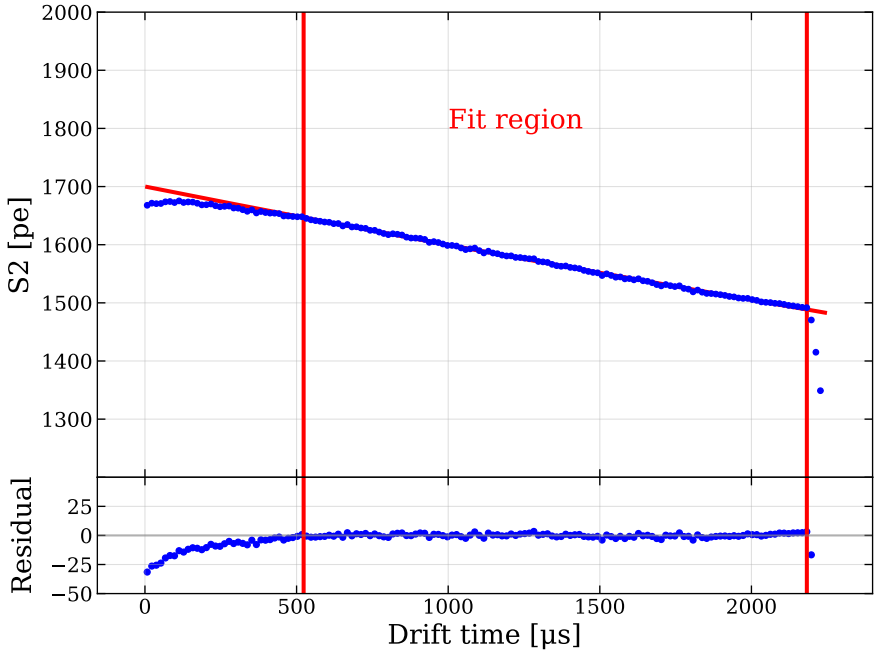

(b) *Exponential fit on S2 size for electron lifetime estimation.*

Figure 5.4.: *Electron lifetime estimation for XENONnT. Fig. 5.4a shows an example of a time slice fit. Clearly, the skewed Gaussian fits the shape better than the normal Gaussian function. Fig. 5.4b shows the exponential fit to the mean values obtained in the slice fits, resulting in an electron lifetime of (16425 ± 13) µs. As uncorrected data is used, the same feature of a missing AP correction as in XENON1T is observed for the top region of the TPC.*

The procedure applied is the same as in XENON1T. The drift time is divided into 150 time intervals. In each time interval the event distribution is fitted, an example is shown in Fig. 5.4a. A normal and a skewed Gaussian function are used as fit models, whereas the skewed Gaussian model achieves a better agreement with the data, as is visible in the residuals.

The mean values resulting from the fits are plotted against the drift time and fitted using an exponential function. The most striking difference to XENON1T is the loss of S2 area over time. Despite the much longer drift time, the loss is much weaker. This is a result of the additional xenon purification facilities added in the upgrade, that were mentioned already earlier. This is also reflected in the resulting life time constant from the exponential fit. For XENONnT, the electron lifetime is computed to be $(16425 \pm 13)\,\mu$s. This is a factor 18 longer than XENON1T and nearly a factor 8 longer than the maximum drift time in XENONnT. The fit is shown in Fig. 5.4b. XENONnT has thus achieved the longest electron life time in a LXe TPC.

The electron lifetime is extracted from the uncorrected S2. Similar to XENON1T, the ^{37}Ar data in the top part of the TPC is affected by the missing AP in the S2 size reconstruction.

S1-S2 distribution

When looking at the data in S1-S2 space and comparing the uncorrected and corrected events, there is a major difference between the two detectors. The effect of the corrections is much more prominent in the XENON1T data than in the XENONnT data, as shown in Fig. 5.5. The main reason for this is the much longer electron lifetime achieved in XENONnT. In XENON1T, the lifetime was of similar length as the drift time of the electrons, resulting in a significant loss of electrons. In XENONnT the lifetime is a factor of 8 greater than the drift time. In XENONnT the ^{83m}Kr based lifetime is still used as the basis for corrections, but due to the long lifetime the effect of over-correction, as observed for ^{37}Ar data in XENON1T, is not observed.

The already mentioned complication caused by the transverse support wires of the gate is also visible here in the form of a population with higher S2 values. Figures 5.5b and 5.5d still show a remnant of this population, visible for S2/cS2 $> 3000\,$pe, although the cut to remove the events close to the wire has already been applied.

Notice the greater mean cS2 signal in XENON1T peaking around $\sim 3500\,$pe, compared to the one of XENONnT at $\sim 1800\,$pe. This is mainly caused by the higher extraction efficiency in XENON1T of $\epsilon_{ext} = 96.4\,\%$ compared to the one of XENONnT with $\epsilon_{ext} > 70\,\%$ near the perpendicular wires and $\epsilon_{ext} \sim 53\,\%$ in the rest of the area [111].

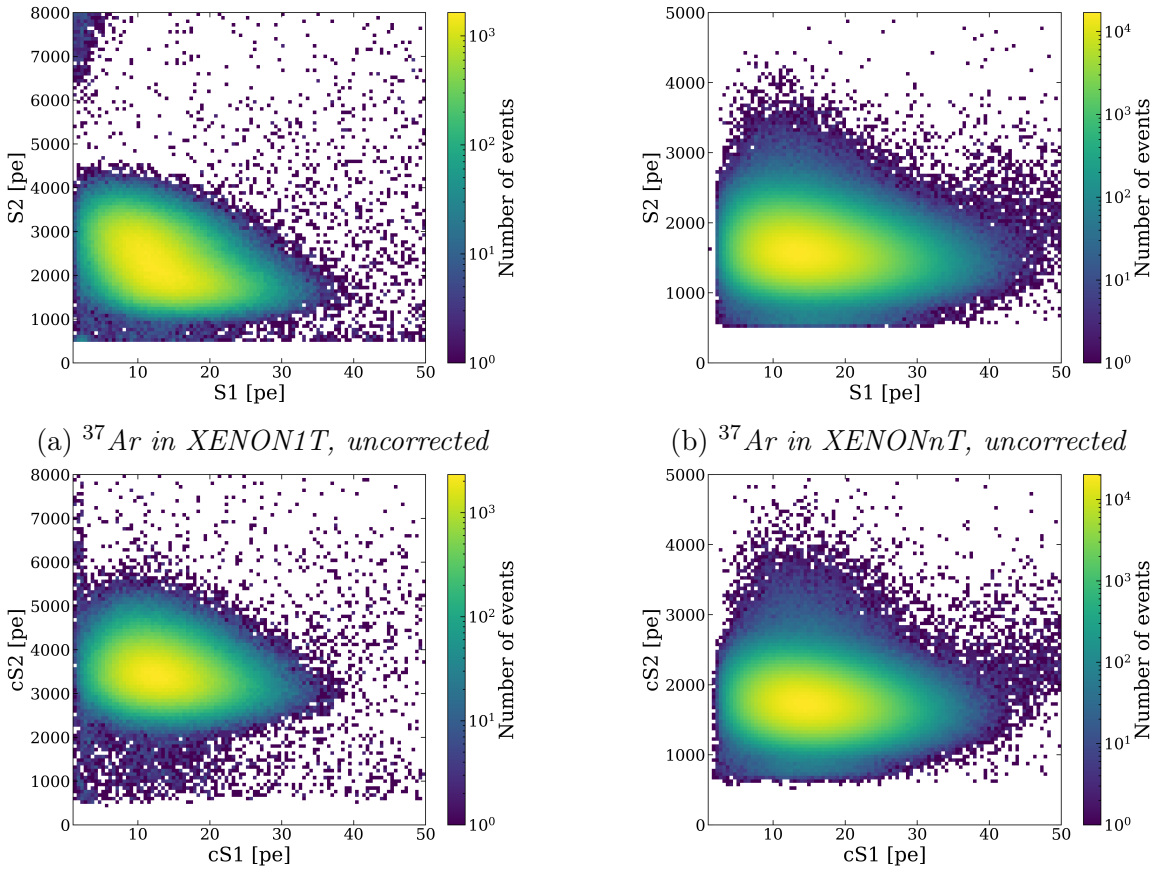

(a) ^{37}Ar *in XENON1T, uncorrected*

(b) ^{37}Ar *in XENONnT, uncorrected*

(c) ^{37}Ar *in XENON1T, corrected*

(d) ^{37}Ar *in XENONnT, corrected*

Figure 5.5.: *Direct comparison between* ^{37}Ar *data taken by XENON1T (left) and XENONnT (right). The impact of the corrections on the shape of the event distribution is much smaller in XENONnT than in XENON1T, mainly due to the much longer electron lifetime. Also as* ^{37}Ar *and* ^{83m}Kr *result in more similar lifetimes, the over-correction observed in XENON1T is negligible in XENONnT. Despite the applied wire-cut, the effect of the transverse support wires is still visible. The small excess in the XENONnT* ^{37}Ar *distribution at around cs1* $\sim$ *10-20 pe, cS2* $\sim$ *3000 pe is a remnant of the population caused by the wires, which is already strongly reduced by the cut.*

5.4. Summary and Outlook

After the successful calibration of XENON1T with ^{37}Ar and, more importantly, the successful removal thereafter, the calibration with ^{37}Ar was also performed in the XENONnT detector. This time the calibration took place between SR0 and SR1 of XENONnT, with a successful removal before the start of SR1. The system used for injection is now permanently installed into the calibration system and can be used for repeated calibrations after a new ^{37}Ar ampule has been installed.

After calibration, the ^{37}Ar data was used to estimate the electron lifetime in the

new detector. It was found to be much longer than in its predecessor XENON1T, due to several upgrades in the xenon purification system. The lifetime for ^{37}Ar was found to be $(16425 \pm 13)\,\mu$s, in agreement with other sources [107]. In addition to being a complimentary calibration source to ^{83m}Kr at low energies, the calibration (already of XENON1T) with ^{37}Ar introduced several improvements in data analysis. Low energy modeling was changed from a pure Gaussian to a skewed Gaussian and the importance of field and AP correction was highlighted [107].

As indicated after the XENON1T calibration and confirmed with the first calibration in XENONnT, this type of calibration can be performed in between science runs. The preparations on site require minimal work, only replacing a flange holding the ampule, followed by a pumping period of a few days to clean the calibration volumes. A few days of data taking are enough to reach a sufficient amount of data for creating correction maps and measurement of the electron lifetime. This is followed by a distillation period of about three weeks to remove the ^{37}Ar from the system, reaching the pre-calibration background levels again. The whole process can be completed within four weeks, where during most of the (distillation) time other tasks, tests, and upgrades can be realized in parallel. The benefits gained by this calibration have already shown to be worth the time invested, so future calibrations are expected to be included in between science runs, to further monitor and validate detector conditions in XENONnT.

6. Semiconductor photon detectors

6.1. Introduction

This chapter will introduce the working principles and properties of semiconductor-based photon detectors with a focus on SiPMs. These sensors were investigated as they are potential candidates to replace the PMTs in a dual-phase xenon TPC to improve position reconstruction and radio purity. For this, they have to satisfy certain criteria, such as sufficient sensitivity for xenon scintillation light and manageable dark count-, crosstalk- and afterpulse rates.

The basic working principles of photodiodes, the smallest building block SiPMs are made of, are described in Section 6.2. This is followed by a description of the complete SiPM composition.

Section 6.3 summarizes various characteristics of SiPMs, like signal gain, afterpulsing, crosstalk, and dark count rate and their dependence on the applied bias voltage. These properties need to be characterized for each sensor individually to properly understand and interpret the response of the sensor when used in an experiment.

6.2. Working principle of SiPMs

Basic principles of solid-state photon detectors

A SiPM is a solid-state detector capable of detecting single photons. It is based on the working principle of a photodiode operated with a reversed bias voltage. A simple photodiode consists of two layers of differently-doped semiconductors. For example, photodiodes, like most modern electronics, are based on silicon which has four electrons that are used to form a lattice. In the crystal the atoms are close enough together so that their electron orbitals start to overlap, forming energy bands. The relevant bands for electrical conductivity are the valance band, where the electrons are bound to the atom and the conduction band where they can move freely through the crystal. In electrical conductors these two overlap, allowing an easy transition for electrons from the valence band to the conduction band. An electrical insulator has a large band gap in the order 10 eV, prohibiting electrons from entering the conduction band, also by thermal excitation. Silicon, a semiconductor has a small band gap of 1.11 eV [112]. An example of the different band structures is shown in Fig. 6.1. The band gap value can be used to estimate the minimal energy a photon needs to provide to lift an electron into the conduction band.

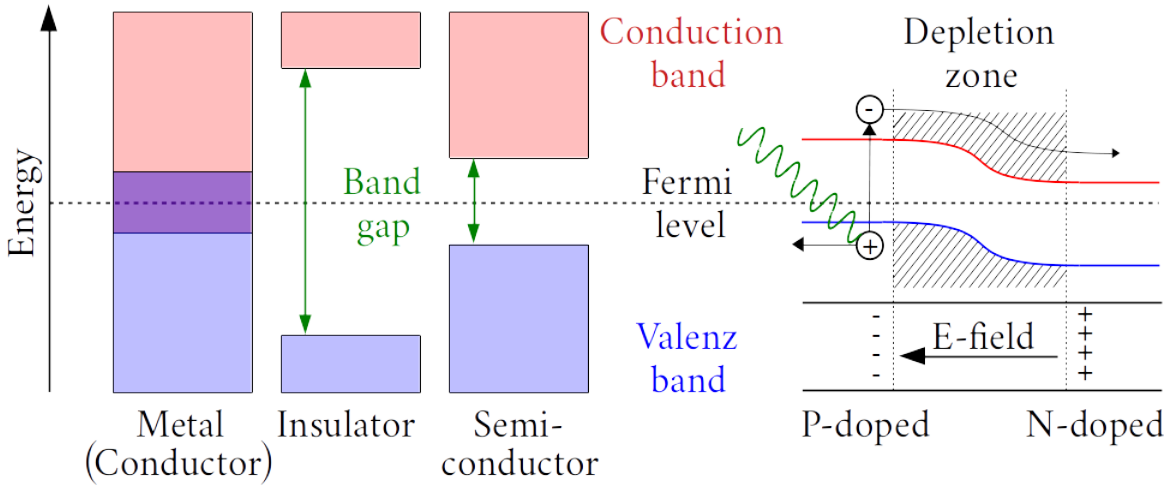

Figure 6.1.: ***Left:*** *Comparison of band structures for metals (conductors), insulators and semiconductors. The bands are created by the overlapping orbitals of neighboring atoms in the crystal structure. For conductors, the valence- and conduction bands are overlapping and electrons can change freely between them. For insulators the band gap is usually in the order 10 eV. The band gap of semiconductors is smaller, allowing a transition of the electron with a lower energy deposit, e.g. by a photon or thermal excitation.* ***Right:*** *Band bending at a P-N-junction due to doping. An incoming photon can create an electron-hole-pair, and the created charge carriers move according to the present electric field. The formation of the depletion zone and the resulting fields is shown in more detail in Fig. 6.2.*

Doping is achieved by introducing impurities into the material with a different amount of electrons in the outermost orbital compared to the bulk material. Doping can be achieved with a material with five or more electrons in its outer orbital, leaving electrons free to traverse the lattice. In this case, the semiconductor is called N-doped and the impurities are called donors, as they provide free electrons (which are the majority charge carriers) in the N-region. On the other hand, if an impurity with three or fewer outer electrons is introduced, a hole (missing electron) in the lattice is formed (and acts as the majority charge carrier) in the P-region, which creates a so-called acceptor in this P-doped semiconductor.

SiPM structure

If a P-N-junction is created by bringing a P- and N-doped material in contact, the free electrons of the N-region move to the P-region to fill the holes. This leaves a region in between the materials without free charge carriers, called the *depletion zone*. This movement of electrons also leaves positive donors in the N-region and negative acceptors in the P-region, creating an electric field that slows down this process until an equilibrium state is reached, as it is shown in Fig. 6.2a. The width of the depletion zone between P- and N-doped material is increased by applying an

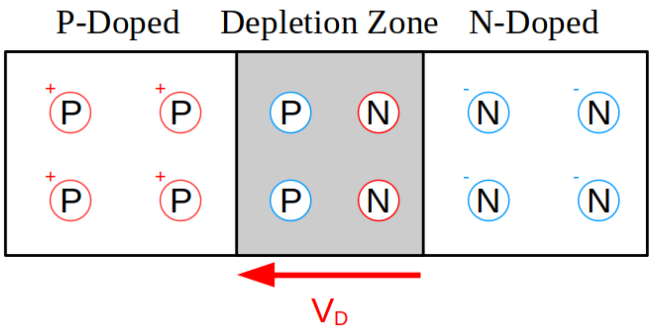

(a) *P-N-junction in equilibrium.*

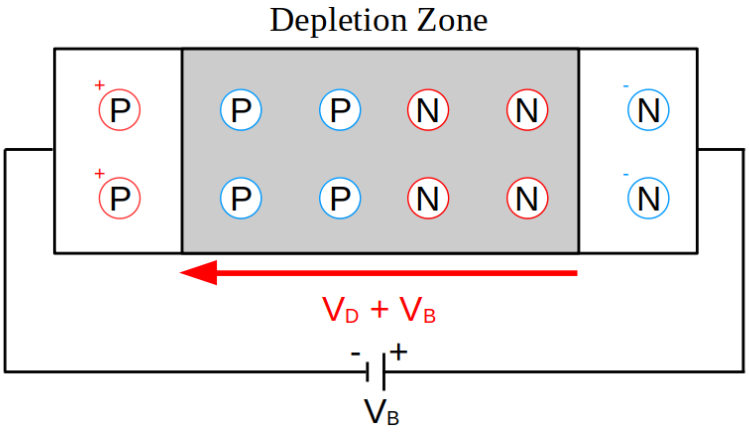

(b) *P-N-junction with applied reversed bias voltage.*

Figure 6.2.: ***Top:*** *P-N-junction in equilibrium with the depletion zone formed, when the electrons of the donors are filling the acceptors and no free major charge carriers are available.* ***Bottom:*** *Increased depletion zone due to an reversed bias voltage V_B applied from the outside.*

external bias voltage, increasing the electric field in this region, as shown in Fig. 6.2b.

The field strength in the structure can also be specified by different doping densities. The top layers of a cell usually consist of a highly doped N-P-junction (high doping usually is indicated by N^+ or P^+), followed by a less doped layer (N^- or P^-). The first provides a strong electric field and acts as an amplification region, the latter acts as a larger absorption region, with a weaker field, strong enough to drift the electrons to the amplification region, without producing barely any additional electron-hole pairs itself. A schematic of the typical structure of a SiPM, together with the electric field strengths, is shown in Fig. 6.3.

To create a signal, the energy of the incoming photon needs to be large enough to create the electron-hole-pair, i.e. it needs to have enough energy to lift an electron from the valence band into the conduction band. This creates an electron-hole pair via the photo effect inside the depletion or absorption zone. The major charge carriers are now accelerated by the combined electric field created by the formation of the

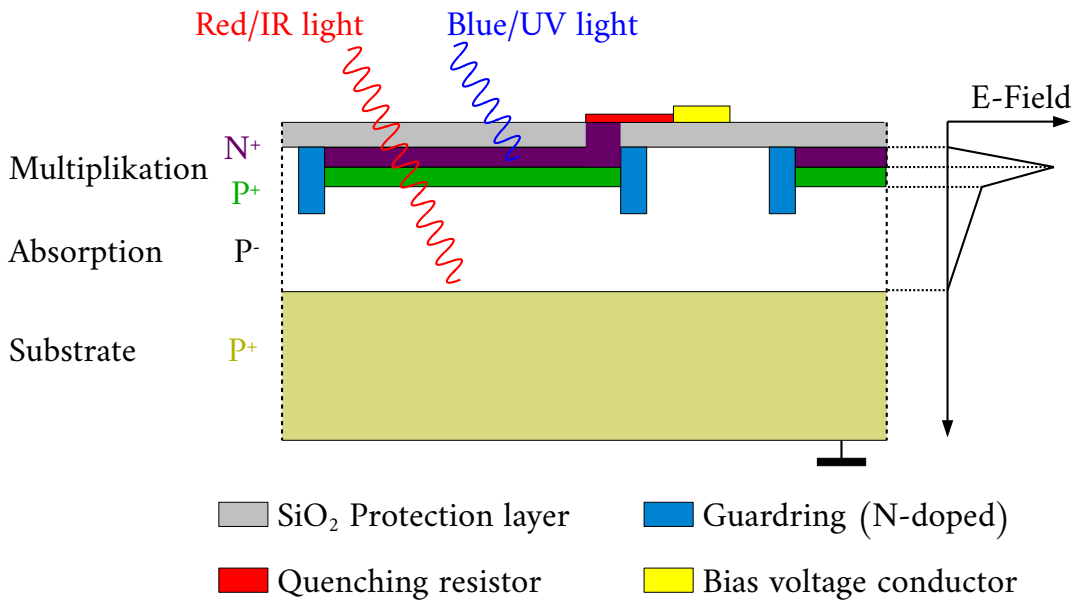

Figure 6.3.: *Structure of a SiPM. The top layer consists of SiO_2, acting as a physical protection. Directly below is a highly doped N^+-P^+-junction, which provides a strong field and acts as charge multiplication region. Below is a less densely doped region which increases the absorption volume of the sensor. A guard ring structure is added to prevent early-edge breakdown, provide improved isolation between cells, and enhance field shape. A thick substrate layer acts as a basis for the structure. The bias voltage is provided by conductive strips on top of the SiO_2, connected to the avalanche photo diode (APD) via a quenching resistor to avoid self-discharge. Red/near-infrared photons can penetrate deep into the structure and are absorbed in the absorption layer. Blue/UV photons are mostly already absorbed in the top layers and cannot reach the absorption region. Switching to a P^+-on-N^+ structure can increase sensitivity for these wavelengths. Figure adapted from [113].*

depletion region and the applied bias voltage. Gaining energy from the strong field in the depletion zone, the charge carriers create additional electron-hole pairs.

Depending on the field strength two things can happen: The amount of charge carriers that can be collected is either proportional to the number of initial electron-hole pairs (and therefore photons) or for strong fields, a complete discharge occurs. The first case is called *proportional mode* and achieves low signal gains on the order 10, the latter is called *Geiger* mode which can achieve very high gains in the order of 10^6. The Geiger mode is ideal for detecting weak signals down to single photons, but it is also a binary mode where every photon causes a full breakdown and therefore an equally sized signal. A diode specifically designed to operate in this mode is called an avalanche photo diode (APD).

The width of the band-gab between the two top layers is dependent on the doping,

but primarily on the materials used. The materials therefore determine the wavelength the diode is sensitive to. Further, the sensitivity for different wavelengths can be enhanced by the order of the doped layers. In a so-called N-on-P (the top layer is N-doped) arrangement, as shown in Fig 6.3, a higher sensitivity for long wavelength in the red/near-infrared region is achieved, as the red/near-infrared photons can penetrate deep into the APD structure and interact within the absorption layer. Blue/UV photons are often already absorbed in the top layer of a APD. Switching to a P-on-N arrangement changes the polarity, and therefore the drift direction, in the top part of the APD and thus enhances the sensitivity for blue/UV photons [114].

SiPMs are based on the function principles of APDs operated in Geiger-mode (short GAPD). They consist of a matrix of GAPDs, each with a typical size between 25 - 50 μm. The SiPMs themselves are typically available in sizes between $1 \times 1\,\mathrm{mm}^2$ and $6 \times 6\,\mathrm{mm}^2$. A picture of such an array is shown in Fig. 6.4.

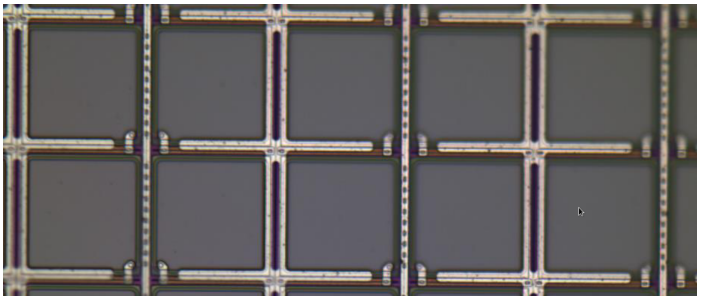

Figure 6.4.: *Picture of the structure of a SiPM on the example of the KETEK sample. The grey areas are photo sensitive, limited by power connections and optical separators. This picture was taken with the confocal microscope of the Prisma Detector Lab of the University of Mainz by Daniel Wenz.*

Simple electronic modeling of SiPMs

The individual GAPDs of a SiPM, also called cells or pixels, are connected in parallel as sketched in Fig. 6.5a. For example, a $6 \times 6\,\mathrm{mm}^2$ device with 50 μm pixel size features about 14400 pixels.

Due to its structure, each pixel has its intrinsic capacitance C_P and, in case of a discharge, also an intrinsic resistance R_P. To avoid a continuous, self-sustained discharge, a quenching resistor R_Q is usually added to allow the pixel to return to the equilibrium state. Its resistance is chosen such that $R_Q \gg R_P$. The equivalent circuit that can be used to describe the discharge of an individual cell operated in Geiger mode is shown in Fig. 6.5b.

Due to this arrangement, the SiPM combines the high gain of a GAPD, which enables single photon detection, with the capability to detect multiple photons with individual pixels. If multiple pixels are hit simultaneously, a summed signal is provided by the SiPM. As the individual pixels are designed to achieve very similar gains, the

summed signal allows direct access to the number of photons that hit the SiPM (under the assumption that a single pixel was not hit by two photons). An example of such a hit spectrum is shown in Fig. 6.6.

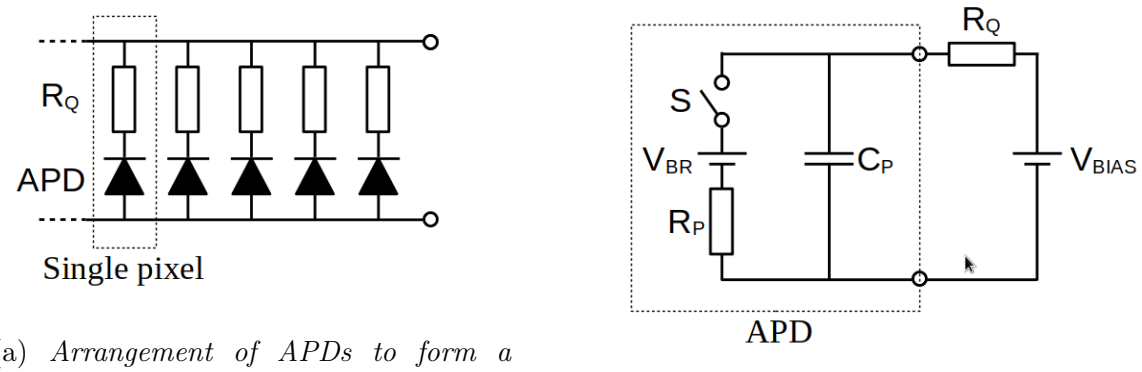

(a) *Arrangement of APDs to form a SiPM.*

(b) *Equivalent circuit of a pixel.*

Figure 6.5.: ***Left:*** *Equivalence circuit of a SiPM, consistent of parallel connected single pixels, each equivalent to an APD. This results in a summed output signal in case multiple pixels are triggered at the same time.* ***Right:*** *Equivalent circuit of a single SiPM pixel (APD), realized with a capacitor C_P and the internal resistance R_P. An additional quenching resistor R_Q is added to avoid continuous discharge of the pixel. Closing the switch S represents an incoming photon.*

6.3. Characteristic properties of SiPMs

Based on the structure and material used in the SiPM, the sensors have some intrinsic characteristics that define their performance in an experiment. On the one hand properties like the signal gain and the photon detection efficiency (PDE) define the performance in detecting signals. On the other hand, flaws in the used materials or physical effects like dark counts produced by thermal excitation or signals from one cell triggering the neighboring cells (crosstalk), impact the data quality. In the following, a short explanation and summary of the most important characteristics is given. These properties of the SiPMs have to be known and calibrated to be used in detectors such as a LXe TPC.

Breakdown voltage

The breakdown voltage is the minimal value of the applied reverse bias voltage at which a photon can initiate a breakdown process. To achieve higher signal amplification (gain), the devices are usually operated several volts above the breakdown voltage. The breakdown voltage can vary slightly between individual SiPMs and needs to be known to ensure proper operation. It can be determined with several methods:

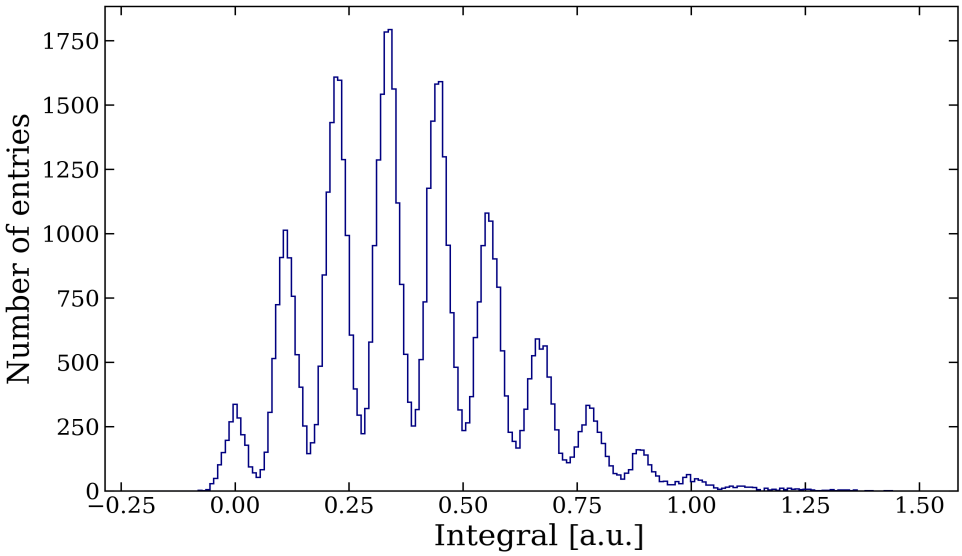

Figure 6.6.: *Example of a hit spectrum for a SiPM (taken with a Hamamatsu S13370). The plot shows the spectrum of the signal integrals. The photon count is visible as each photon hitting a new cell adds a certain amount of charge to the signal, resulting in the equidistant peaks in the hit spectrum. The peak distance reflects the gain of the SiPM and depends on the applied overvoltage.*

- **Gain-breakdown voltage measurement:**

  The method shown here is based on the signal amplification. In the charge spectrum of the SiPM signals, an example is shown in Fig.6.6, the amplification is given by the difference ΔQ of the integrated voltage signals (which are proportional to the charge) between consecutive peaks (defining the gain in charge per photoelectron). This corresponds to signals given by the number of triggered cells. This amplification is measured for multiple bias voltages at controlled temperatures. In a plot of ΔQ versus the bias voltage, a linear fit to the data points determines the breakdown voltage V_{BR} by its intersection with the x-axis. This method is simple and does not need extra equipment, but multiple measurements at different bias voltages must be performed to collect enough data points. It should also be ensured that the achieved statistics are high enough and a low-intensity illumination is applied to the SiPM to create a meaningful spectrum. This method was utilized on a test sample as shown later in Section 7.8.2.

- **I-V-curve:**

  This method is based on the measurement of the I-V curve of the device. When plotting the curve in log(I) against the applied voltage, the inflection point is defined as V_{IP}. An example of such a plot is shown in the appendix, see Fig. B.21. The difference between V_{IP} and V_{BR} is constant for a specific device.

First using the gain measurement (see below) to find V_{BR} for a device and after that, the I-V method to find V_{IP} allows the calculation of the value $V_{IP} - V_{BR}$ for this type of device. For a device of the same model, V_{BR} can now simply be calculated by subtracting this value from the measured V_{IP}. As V_{IP} can be measured much faster with a simple I-V-scan in the voltage area-of-interest than compared to a gain scan for multiple bias voltages, this method is especially useful when multiple devices of the same model need to be characterized [114, 115].

Gain

The gain of the SiPM is the amplification achieved by the sensor and is the factor that relates the number of detected photons with the charge signal, i.e., the number of electrons produced in the discharge caused by one photon. Based on the equivalent circuit for a single cell as shown in Fig. 6.5b, the gain can be derived from the charge released when discharging the intrinsic cell capacity C_P when the bias voltage $V_{BIAS} = (V_{BR} + V_{OV})$ is applied. The gain is then given by the charge in the capacitance for a voltage difference of V_{OV}:

$$G(V_{OV}) = \frac{C_P \cdot V_{OV}}{e} \tag{6.1}$$

where e is the elementary charge. A shift of the breakdown voltage due to temperature variations can greatly affect the gain as it varies the overvoltage accordingly for a fixed bias voltage. An exact knowledge of the breakdown voltage at the operating temperature is therefore mandatory for a stable signal gain if no compensation circuit is used.

For a fixed overvoltage, the temperature dependency of the gain is based on the temperature dependency of the cell capacitance.

Afterpulses

It is possible that during avalanches single charge carriers get trapped in impurities and are released after a short delay. These delay times are usually on the order of tens of nanoseconds. In case they occur during the recharge of a cell they are usually smaller than a 1 pe signal and can be easily suppressed with a signal threshold. If they occur after the cells have fully recharged, they reach the same pulse height as a 1 pe signal and are indistinguishable from a real signal.

The afterpulse rate increases with higher overvoltage. The higher voltage creates more charge carriers which increases the probability of one getting trapped accordingly.

The trapping times of the charge carriers are exponentially distributed, resulting in most of the trapped carriers being released directly after the initial breakdown. It is also expected that the release probability increases with increasing temperature.

Therefore, the expected delay of afterpulses indistinguishable from real signals to occur is shorter at higher temperatures [116].

Crosstalk

During a charge carrier avalanche, not all participating carriers produce additional carriers. Their energy can also be released in the form of a photon, which can reach neighboring cells. There it can trigger an additional avalanche, artificially increasing the measured signal by 1 pe (also more are possible, albeit much less likely) compared to the number of photons hitting the SiPM. This effect is called *optical crosstalk*. In case the photon created in the avalanche hits the depletion zone of the neighboring cell directly, the additional cell will directly contribute to the summed signal. This effect is called *prompt* crosstalk. It is also possible to create a charge carrier outside the depletion zone. This charge carrier first has to drift into the depletion zone via diffusion and then creates a *delayed* crosstalk signal. Even though this effect is strongly suppressed due to the charge carrier having to survive the drift without being neutralized, it can occur. Similar to the afterpulses these signals are indistinguishable from real signals.

In more recent SiPM models so-called *optical trenches* are added to absorb these photons. These trenches are, for instance, filled with metals to provide optical isolation and as such greatly reduce the crosstalk probability [117].

The before-mentioned effects are also refered to as *direct* crosstalk, as they are based solely on processes inside the SiPM. Often SiPMs are used in direct contact with other optical materials like scintillators or are equipped with protective windows. In this case, photons created in an avalanche can also leave the SiPM and can then be reflected into another cell to create an additional signal. This effect is refered to as *external* optical crosstalk.

Dark counts

Dark counts are signals where the avalanche is not started by an incoming photon. Several mechanisms can cause dark events [118]:

Thermal excitation: The avalanche leading to a detected signal is created by thermal excitation in so-called *generation centers*. These can be impurities or defects in the crystalline structure. As the event is triggered by thermal excitation, reducing the temperature of the device can greatly reduce the probability of such a transition.

Trapped charge: This is the same mechanism as described for the afterpulses, with trap times so long it cannot be related to an actual event.

Diffusion: The avalanche is triggered by a charge carrier which diffuses into the active region of the pixel. This is similar to the mechanism described for delayed crosstalk, but the charge carrier does not necessarily need to be created by another cell interaction.

Band-to-band tunneling: This effect is based on internal field emission of electrons, which primarily happens on impurities in the lattice structure. This effect contributes only at applied bias voltages larger than 1 V above the breakdown voltage [118].

In general, the dark count rate is directly related to the applied overvoltage, usually showing an exponential increase for larger overvoltages [116].

Photon detection efficiency

The PDE is defined as the fraction of incident photons that create a signal in the SiPM, and thus is a measure of the sensitivity of the device.

The PDE includes the quantum efficiency, i.e., the probability P(QE) of a photon interacting inside the active region of the SiPM. This value is influenced by the reflectivity of the material and the thickness of the optical layers and as such is strongly dependent on the wavelength of the photons. Thick layers especially influence short wavelengths as they have a short absorption length in silicone and therefore a low resulting quantum efficiency. This is a major issue for the detection in the VUV-regime since these wavelengths are often already absorbed in the protective coating of the devices. On the other hand, longer wavelengths might just penetrate thinner depletion zones and interact too deep, reducing the efficiency of the device at those wavelengths.

The second factor contributing to the PDE is the avalanche starting probability P(AV), as not every electron-hole pair initiates an avalanche. For instance, the initial charge carriers can be delayed by impurities or close to a transition layer, allowing self-quenching of the cell before a sufficient potential difference is reached to create a measurable signal [119].

The third contribution is the fill-factor (FF) of the SiPM. This is the percentage of the actual active region of the device. As shown in Fig. 6.4, a significant part of the surface of the individual cells is covered by the electrical connections necessary to apply the bias voltage. As their size is given by the used technology, different total pixel sizes result in different FFs, whereby larger pixels therefore usually are more efficient. Reducing the spacing between the pixels increases the FF at the cost of increased direct crosstalk. As mentioned before, this can be partially negated with the introduction of optical trenches, which can reduce the needed amount of cell separation [117].

The PDE value is then given as the product of the individual components:

$$PDE = P(QE) \cdot P(AV) \cdot P(FF) \tag{6.2}$$

Signal linearity

Another property of the sensor is given by its linearity, which states the relation between the output signal of the sensor in relation to the input of the sensor:

$$Linearity = \frac{\text{Real Output}}{\text{Ideal Output}} \tag{6.3}$$

For a linear behavior a value of 1 is expected, while a value < 1 shows nonlinear behavior. For a low number of photons, a linear behavior is anticipated and the output signal is expected to be proportional to the number of photons hitting the active area of the sensor, only limited by its PDE:

$$N_{fired} = N_{photons} \cdot PDE \tag{6.4}$$

For a higher number of photons, however, deviations are expected, as photons might hit cells again before they are recharged. This effect can be modeled with [120] (for the case that the light pulse is shorter than the recharge time):

$$N_{fired} = N_{pixel} \cdot \left(1 - e^{\frac{-N_{photon} \cdot PDE}{N_{pixel}}}\right) \tag{6.5}$$

As can be seen in Eq. 6.5, the number of available pixels N_{pixel} within the illuminated area plays an important role in the estimation of the linearity of a device. A value that typically is given is the number of photons at which the deviation from the ideal response is larger than 10 %. An example is shown in Fig. 6.7 for a Hamamatsu S13360, taken from [120].

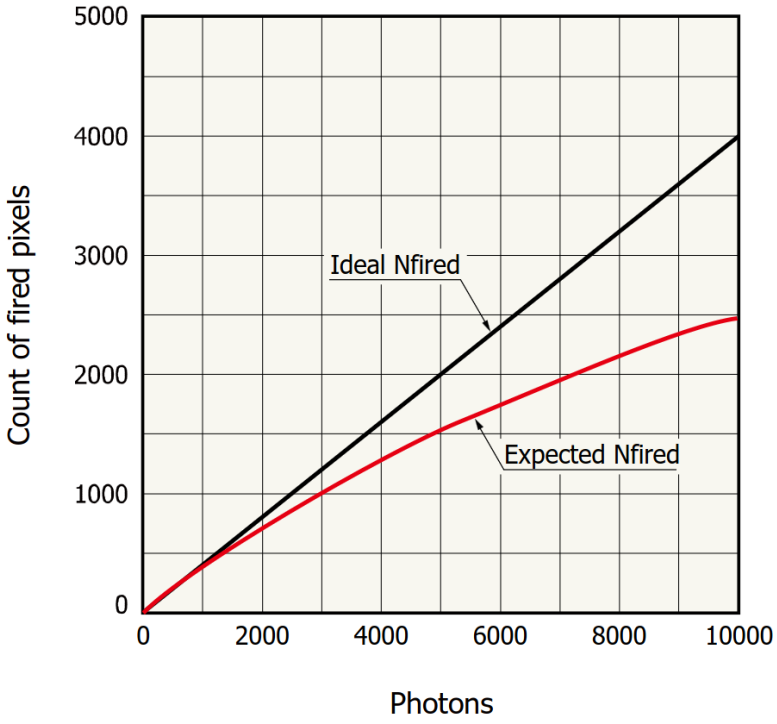

Figure 6.7.: *The nonlinearity of SiPM signals for high photon counts. The values shown are from a Hamamatsu S13360-3050, a* $3 \times 3\,\mathrm{mm}$ *device with* $50\,\mu\mathrm{m}$ *pixel size and therefore 3600 pixels. For this device, the 10 % deviation from the ideal response is reached with about 2000 photons. Figure from [120].*

7. Design and construction of a test setup for SiPM characterization

7.1. Introduction

In this chapter, the design of a test setup for SiPM characterization is explained. Three different SiPM models were initially tested and are shortly introduced in Section 7.2. The setup design and its functionalities are shown in Section 7.3. The setup allows illumination of the SiPM samples with light from an external source, guided to the sensors via optical fibers, as well as the utilization of xenon scintillation light, produced in situ with an ^{241}Am source immersed in liquid xenon. The operation of the setup requires additional infrastructure. This includes a gas purification system, which is briefly described in Section 7.4.

The equipment needed to operate the SiPMs is presented, including the power supply (Section 7.5) and the readout circuitry (Section 7.7). A special focus was placed on the signal amplification, as for weak signals the amplifier should be as close to the SiPM as possible. A possible place is close to the sensors within the clean xenon gas environment at around -100°C, which puts extra requirements on the hardware in terms of outgassing and temperature stability. A prototype amplifier board satisfying the temperature requirements was developed and tested as shown in Section 7.6. A first successful test run with liquid xenon was carried out and a preliminary analysis of the data for the most promising of the three tested samples is shown in Section 7.8. Finally, the chapter is summarized in Section 7.10 with a brief outlook on the future use of the setup and its impact on the upgrade of the local dual-phase xenon TPC.

7.2. SiPM Samples

Three samples of analog SiPMs were used during the tests. One sample type was provided by Ketek, and two different sample types by Hamamatsu, of the 3rd and 4th generation respectively. All devices received a special treatment or were designed specifically to provide an increased sensitivity in the VUV regime.

KETEK sample

The sample provided by KETEK is a wafer cutout without housing and interface. The device has a total size of 6.46×6.45 mm^2, of which 6×6 mm^2 is the active and sensitive area. On the rim, pads for voltage and ground connections via wire bonding are located. The pixel size of this device is 50 μm, resulting in a total of about 14400 pixels per sensor. As the sensors were not packaged, a base for mounting, bias voltage supply and signal readout had to be provided. For the tests, a simple printed circuit board (PCB) was designed on which the SiPM was glued with an epoxy suitable for high vacuum application. The electrical connections were realized with wire bondings to the pads of the SiPM. On the backside of the PCB an SMA connector is used to supply the bias voltage and to read out the signal at the same time. The PCB was made from a ceramic-teflon compound to ensure low outgassing and thus high vacuum compatibility. A picture of the device, glued to the PCB, is shown in Fig. 7.1 on the right.

Two samples were provided by KETEK. They are prototypes derived from a commercial product and received a surface treatment to increase UV sensitivity, with no further information on the procedure provided by KETEK.

Hamamatsu MPPC model S10943

The second device tested was the 3rd generation Hamamatsu Multi-Pixel Photon Counter (MPPC) model S10943, a device already in use at the MEG II experiment in a liquid xenon environment [121]. They are provided in a ceramic package consisting of 4 devices, each $6 \times 6\,\mathrm{mm}^2$ in size. The pixel size is 50 μm, so the sensor structure is very similar to the KETEK device. The signal of each individual SiPM is read out by two pins in the corresponding corner on the back side of the package. A picture of the device is shown in Fig. 7.1 on the left, and a technical drawing of the device is given in Appendix B.7 on page 209.

Hamamatsu MPPC model S13370

The third device tested was the Hamamatsu MPPC model S13370, a 4th generation SiPM. Compared to the 3rd generation it features optical trenches to lower the crosstalk probability. Like the S10943 they are provided in a ceramic package, but containing only one sensor with a size of $3 \times 3\,\mathrm{mm}^2$. Similar to the S10943, the signals are read out via two pins on the back side. A picture of the device is shown in Fig. 7.1 in the middle.

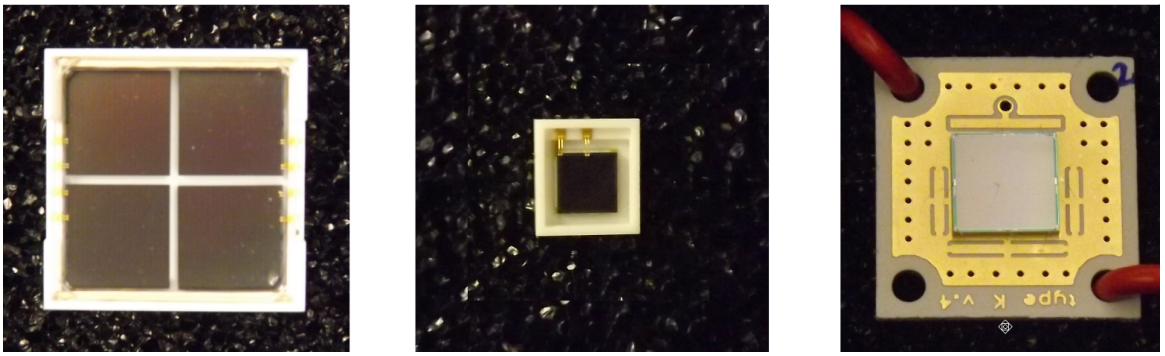

Figure 7.1.: *Pictures of the SiPMs tested. Left: Hamamatsu S10943, four SiPMs with a size of $6\times6\,mm^2$ in one ceramic package. Middle: Hamamatsu S13370, a single SiPM of size $3\times3mm^2$ in a ceramic package. Right: KETEK sample of size $6\times6\,mm^2$ on a ceramic-teflon board.*

7.3. Test setup design for measurements in liquid xenon

As the SiPMs are planned to be used in a liquid xenon environment, the characteristics of the devices need to be tested as close as possible to the conditions present in a dual-phase xenon TPC. Therefore the characterization needs to be performed at liquid xenon temperatures of about -100°C with the sensors immersed in liquid xenon. The sensors are supposed to detect scintillation light emitted by xenon so the photon detection efficiency at VUV wavelengths has to be determined.

A new setup was designed to test as many of these properties in parallel and also to test multiple sensors simultaneously. The setup was placed within a cryostat for better thermal insulation. Xenon liquefaction is achieved by cooling with liquid nitrogen. A CAD-drawing of the setup is shown in Fig. 7.2. The major components (from top to bottom) are:

- A copper disc providing the necessary cooling power.
- A rotary disc with with four latching positions orientated towards the SiPM test samples.
- The illumination cylinder providing different illumination settings for the sensors.
- The bottom flange with mounted holders for up to three SiPM samples. An additional Hamamatsu R6850 1"-PMT is mounted and used for reference measurements.
- At the bottom, a pipe feedthrough is mounted to extract liquid xenon for purification. A fiber feedthrough passes flashes from a pulser-powered light emitting diode (LED) light to each sensor for gain calibration.

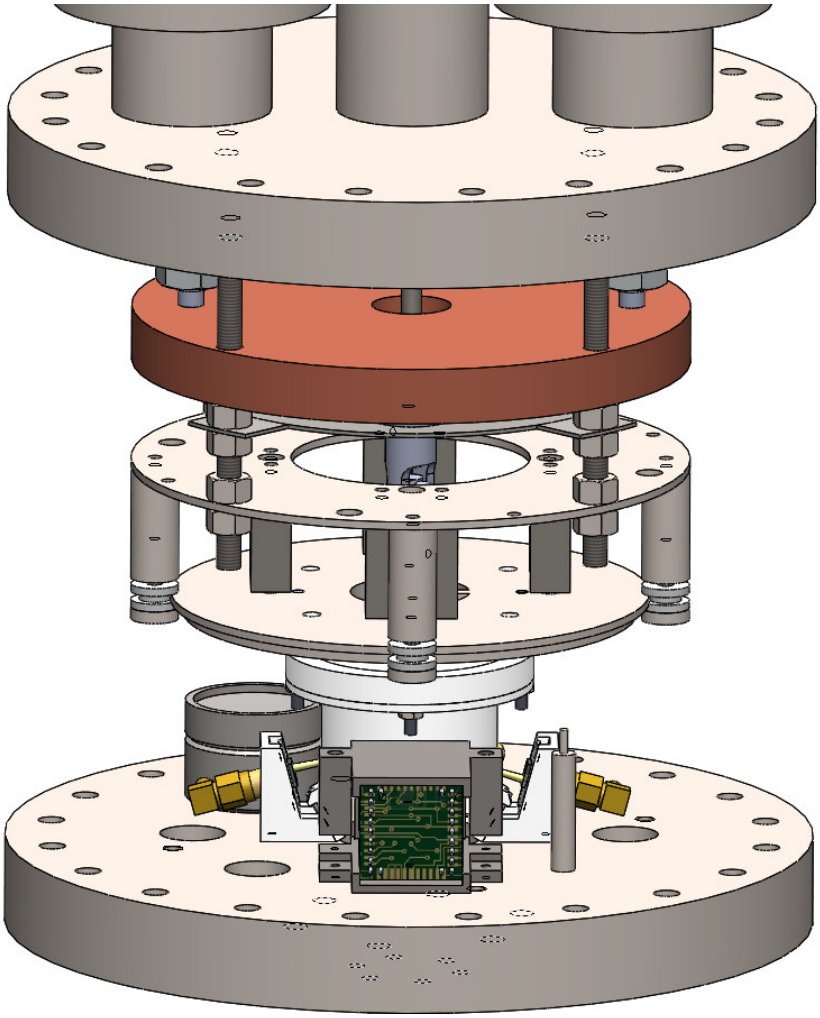

Figure 7.2.: *CAD drawing of the test setup designed for SiPM characterization. The reddish part below the upper flange is the hollow copper disc which is cooled down with liquid nitrogen to liquefy the xenon in the test chamber. The rotatable double disc structure below contains an arresting mechanism that allows certain positions (every 45°, eight possible settings) to ensure that the cylinder holes are facing the sensors. The white cylinder contains the radioactive ^{241}Am source. On the bottom flange, the sensor holders are visible. To the left and right of the cylinder (and also behind, but not visible here), SiPM holders can be seen. In the center the holder for the Hamamatsu R6850 1" PMT is visible. The cylindrical structure on the left behind the sensor holder is a feedthrough used for sensor data readout. Not visible here: through the center of the bottom flange fibers are fed into the volume to allow LED illumination for calibration via Polytetrafluoroethylene (PTFE) light diffusers in front of each sensor.*

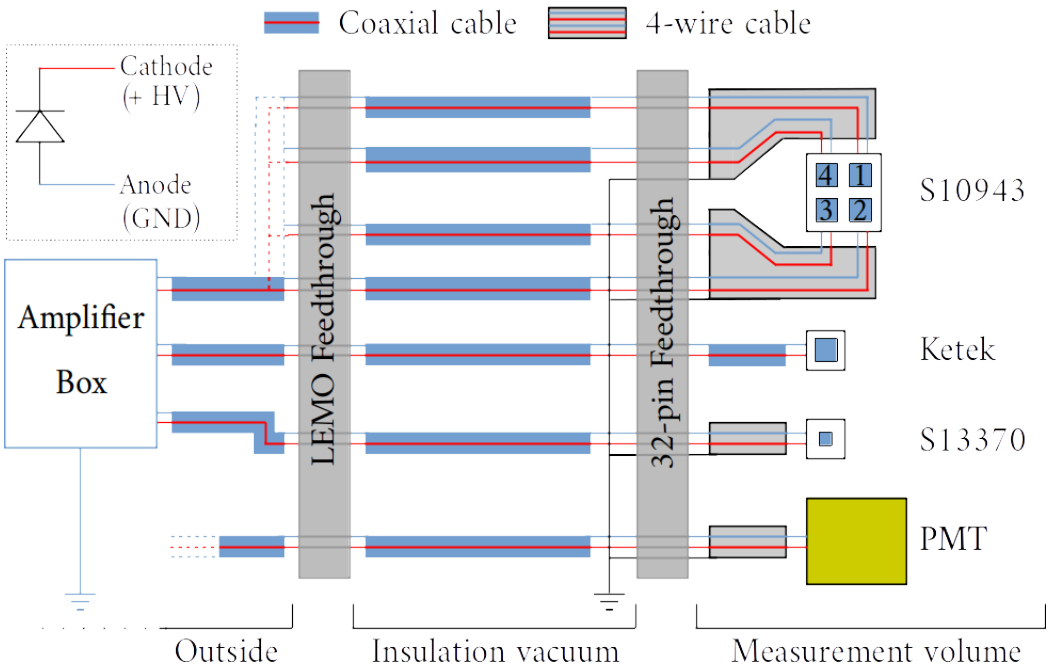

Figure 7.3.: *Cable connections and grounding scheme inside the test vessel. In the measurement volume cables with low outgassing are used to avoid contamination of the xenon. The SiPMs and the PMT are connected with a PTFE-coated 4-wire cable (sharing one shield), except for the KETEK, which is connected with a Kapton-coated coaxial cable. The signals are transferred to the insulation vacuum via a 32-pin feedthrough. Each anode, cathode, and shield uses its own pin. In the insulation vacuum the (inner-)shields are grounded, the signals/bias lines are connected via coaxial cables (the anodes are connected as shields, the cathodes, providing the bias voltage through the inner core). The connection from the insulation vacuum to the outside is done via a custom made 7-line LEMO-feedthrough. The further connection to the amplifiers and following electronics is done via standard coaxial cables. The amplifier box is further explained in 7.6 and following sections.*

Cooling In the upper part, a hollow copper disc is flushed with liquid nitrogen, which provides the necessary cooling power to liquefy the xenon by evaporation. The cooling power is controlled by limiting the gaseous nitrogen flow on the outlet with a mass-flow controller. Due to the comparatively high mass of the copper disc of 1.5 kg the system reacts very slowly to changes in the setting, but it also provides a very stable temperature during the measurement campaigns.

A typical cooling cycle starts with filling the system with xenon at approximately 2 bar and switching on the cooling by starting the nitrogen flow. The following day more xenon is added to the now pre-cooled system and liquefaction starts. This requires more cooling power, which is provided by increasing the nitrogen flow. After a few hours of stabilisation, the measurement window starts. After the measurement, the xenon is recuperated. This process is shown in Fig. 7.4, where the stable temper-

ature conditions of the system during the measurement period are visible. With a constant set-point for the nitrogen flow, the temperature of the cryostat stays stable for nearly 24 h, the whole duration of the measurement.

Once the xenon is liquefied, the system needs permanent supervision to avoid damage from over-pressure or loss of xenon in case of a cooling system failure.

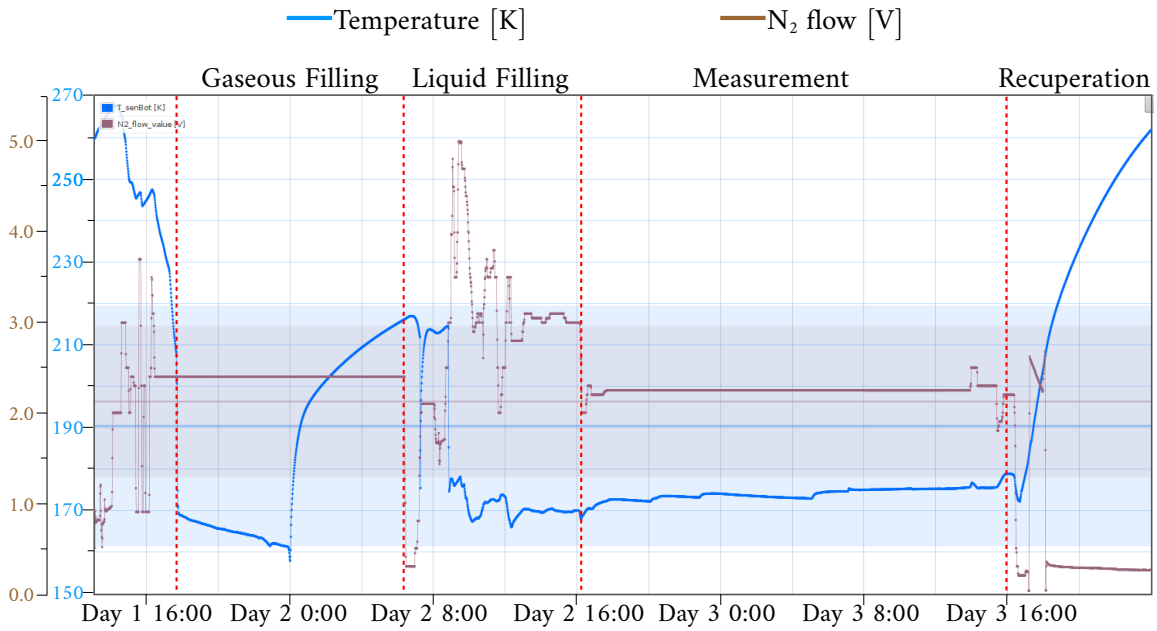

Figure 7.4.: *The typical cooling cycle of a measurement run. The cycle can be divided into multiple segments, starting with the pre-cooling phase, where the system is filled only with gas. This is followed by filling with additional gas and liquefaction. After stabilization, the measurement can take place. After the measurement, the gas is recuperated into the gas bottles.*

Illumination cylinder The illumination cylinder provides the various test illuminations for the sensors. It is connected to the rotary disc which can be rotated manually from the outside via a rotary feedthrough to set the illumination level. The rotary disc has eight latching positions which are aligned with the sensors. In the center, supported by eight fins and fixed with a spring, the ^{241}Am source is placed, as shown in Fig. 7.5. During a measurement, the setup is filled until the disc is completely submerged in liquid xenon. The liquid level is measured with a *discrete levelmeter*, an array of PT100s that show a temperature drop when they submerge in the liquid xenon, thus indicating the filling level.

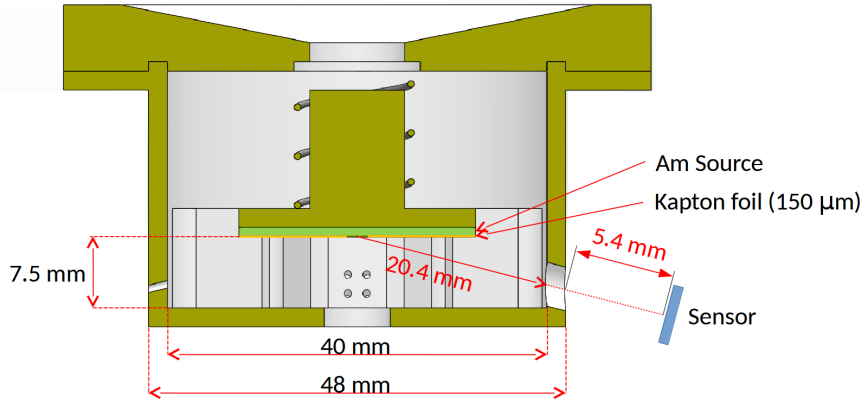

Figure 7.5.: *Cross section of the illumination cylinder. Shown are the dimensions and the position in relation to the sensors. In the center, the source is placed, which is fixed with a stamp and a spring from the top. The disc with the source is partially covered by a Kapton foil which acts as a collimator for the excitation light.*

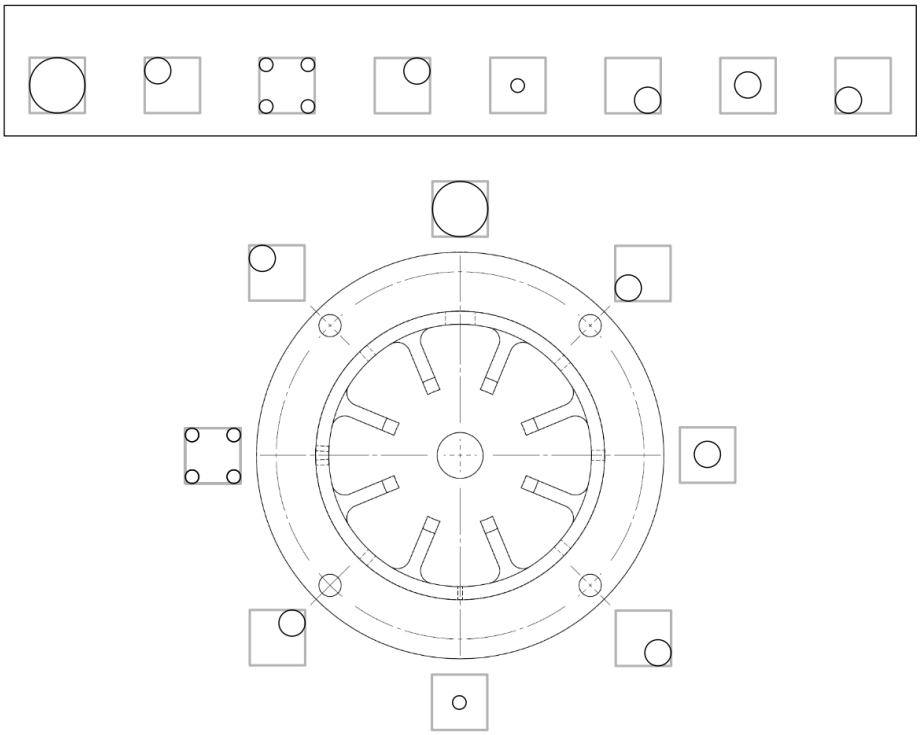

Figure 7.6.: *Hole sequence of the illumination cylinder in the center of the setup. On the inside, the fins separating each hole are visible. They were introduced to reduce stray light outside of the cylinder. Additionally, they act as holding structures of the metal disc which contains the* ^{241}*Am source.*

Hole size	Diameter	Area	Coverage of sphere (%)	# Photons emitted	# Photons on sensor (mean)
Large	4.5 mm	63.62 mm^2	1.22	3816	53
Medium	1.5 mm	7.07 mm^2	0.135	422	5
Small	0.8 mm	2.01 mm^2	0.038	118	1
4-holes	0.8 mm	8.04 mm^2	0.154	481	4

Table 7.1.: *Sizes of the holes in the illumination cylinder. Also given are the estimations of the number of photons that are expected to reach the sensors, assuming uniform emission. These are based on the decay energy of* ^{241}Am *and the expected photon yield for this energy based on NEST.*

The cylinder is mounted in between the sensors and has eight holes/hole-combinations that can be used to choose the illumination strength or the position to be illuminated on the sensors. The hole sequence in the cylinder walls is shown in Fig. 7.6, Table 7.1 shows the combination of holes that face the various sensors at the same time.

Electronic noise issues During the first test runs signal crosstalk between sensors and also ground loop issues were observed. The signal cross-talk especially happens between the PMT and the SiPMs, even when the SiPMs were not powered. To avoid these effects during the measurements, all signal lines received new shieldings as shown in Fig. 7.3. As the PMT itself seemed to be the source of EM-noise, a copper sheet shielding was placed around the PMT.

Fig. 7.14 shows the noise induced on the SiPM lines by a PMT signal before and after the addition of the new shielding. In App. B.27 on page 212 a picture of the added PMT shielding is shown.

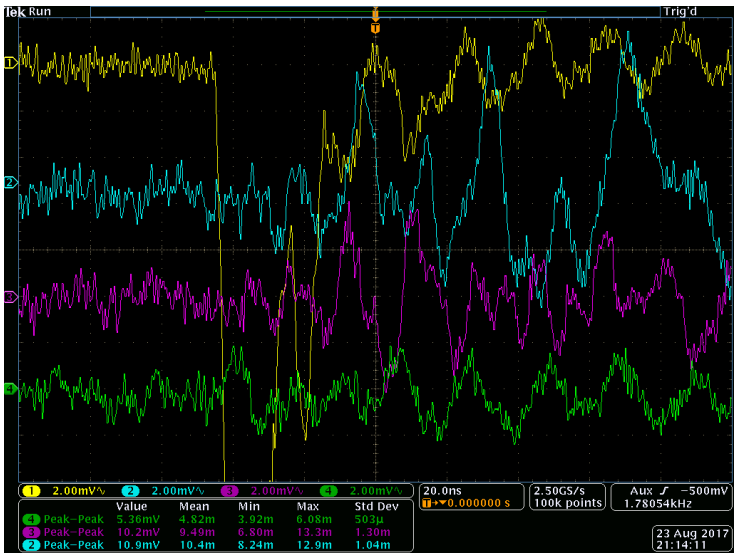

(a) *Before shielding.*

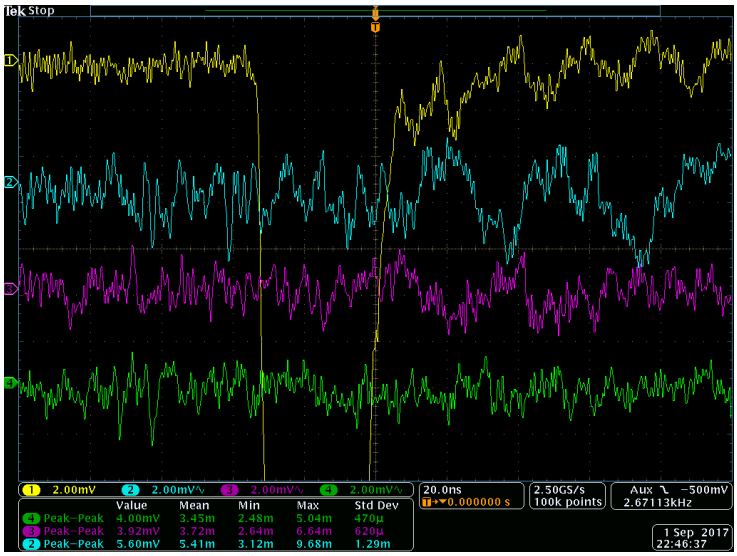

(b) *After shielding.*

Figure 7.7.: *Comparison of the noise levels observed on the SiPMs when the PMT detects a signal. The SiPMs were not powered during this test. Shown are screenshots taken from an oscilloscope, where the PMT signal is shown in yellow. The blue, purple and green lines are the Ketek, the Hamamatsu S10943 and Hamamatsu S13370 SiPMs, respectively. How the signal transmitted by the PMT induced the noise in the SiPMs is unclear. The top picture shows the effect before the copper shielding was installed, the lower picture after the installation of the copper shield. There is still an effect visible, albeit at a smaller scale.*

7.4. Gaseous xenon infrastructure

For the operation of the test-setup with xenon, a certain infrastructure is needed to fill and recuperate the xenon, as well as keep it clean. In the lab, we used a gas purification and storage system, which is shown in Fig. 7.8.

The system uses a membrane pump (Type: MX-808ST-S, Enomoto Micro Pump Mfg. Co., Ltd.) for recirculating the gas. Theoretically, it can achieve a maximum flow of 25 standard-liter per minute (slpm), but due to the flow resistance of the getter, which is used to purify the gas, the realized flow is much lower. The getter used is a SAES® MonoTorr heated getter, model PS3-MT3 for rare gases, utilizing a heated zirconium-alloy based cartridge to trap impurities. The maximum efficiency for this type of getter and for xenon is also achieved at a much lower flow of only 3 slpm. The flow is measured using a Teledyne Hastings Metaline HFM-300 flowmeter (FM) with a maximum measurement range of up to 30 slpm (xenon). As the FM only measures the flow rate the flow has to be set manually with a needle valve.

The system contains two gas bottles with a volume of 20 l. When filling the system, a pressure reducer is used to throttle the gas bottle pressure of approximately 70 bar down to the filling and operating pressure of about 2 - 2.5 bar. The bottles are made of aluminum, as they need to be cooled down with liquid nitrogen below the freezing temperature of xenon for recuperation. The xenon in the bottles is frozen and the pressure is reduced down to a few mbar [122]. In this way, the gas flows back from the higher pressure in the test setup into the bottles. In this way, none of the relatively expensive xenon (compared to argon or krypton) is lost and can be reused in future measurement runs.

Although we do not need a very high purity of xenon as we only use it to produce scintillation light and no drifting of electrons is needed as in a TPC. However, to maintain the purity of the gas, the system was mounted with a high cleaning level and a getter is used during measurement runs.

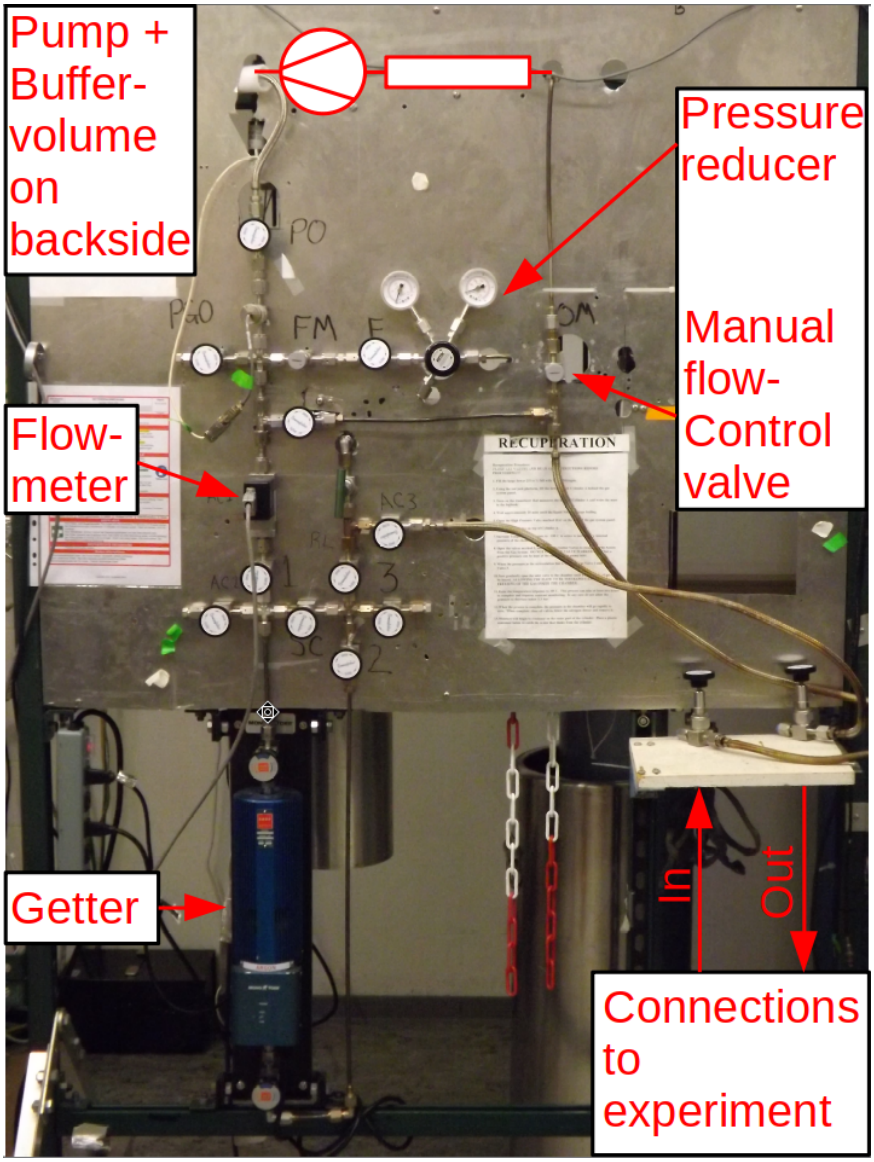

Figure 7.8.: *Picture of the gas recirculation system used for the SiPM measurement. The pump is placed on the back side of the panel. The two gas storage bottles (20 l capacity each) are hanging on the back side on load cells (view blocked by the metal sheet), which allow monitoring of the mass of the stored gas. In the middle to the left on the front side the flow meter is visible, the needle valve next to it is used to set the flow rate manually. On the front the pressure reducer is visible, which is used when filling the attached experimental setup with xenon from the bottles. This is necessary, since the pressure of xenon in the bottles at room temperature is around 72 bar, which is far higher than the operating pressure of the setup, which is usually operated with pressures between 2 to 3 bar. For the case of an uncontrolled pressure increase, a rupture disk with a burst pressure between 3.6 and 4.4 bar is present on top of the test vessel.*

7.5. Sensor power supply

Multiple power supplies are needed to provide the voltage for the photosensors, since the Hamamatsu R8520 PMT has a higher voltage requirement than a SiPM. The PMT requires a supply voltage of 900 V to achieve a signal gain of about 10^6 [123]. In this measurements, the PMT was powered with an Iseg NHQ series NIM-standard power supply module.

The SiPMs have significantly lower voltage requirements. The Hamamatsu S10943 is operated at a breakdown voltage between 60 to 80 V, the S13370 at 48 to 58 V. The data sheets for the Hamamatsu SiPM can be found in Appendix B.7 on page 210.

The operating voltage of the Ketek samples is even lower than the ones of the Hamamatsu models with a breakthrough voltage between 25 to 30 V [124], plus an over-voltage of up to 4 V.

The SiPMs, both the Hamamatsu and KETEK models, are powered by the CAEN Model A 1510 12 Channel HV board. This device offers 12 individual, floating channels that can provide a bias voltage between 0 and 100 V [125].

7.6. Low temperature amplifier for SiPM measurements

Design of the amplifier board

To ensure signal quality, the SiPM signals should be amplified as close to the sensor as possible. For the future application in a xenon TPC this means operation at liquid xenon temperatures of around -100 °C. For this purpose, a simple amplifier was developed with the goal to achieve an amplification factor of 5 to 10.

The final version was planned to be operated inside the xenon volume in contact with gaseous xenon. To preserve the purity of the detector medium xenon (which is needed to drift electrons in the liquid phase with minimal loss when operated in a TPC), the board needs to be constructed from vacuum-rated materials. Using the same ceramic-teflon compound that was used for the KETEK SiPMs bases would be a possible solution. Additionally, using ceramic-based electronic components (for example ceramic-based capacitors) would minimize the impact on xenon purity.

The first test boards were built from commercial parts on standard PCB material. The main component of the board is an AD8009 AR amplifier intergrated circuit (IC). On the test boards, only a standard IC with a plastic housing is used, which is in general not suitable to be used in a xenon environment. This also applies for the resistors that are used, as they were not tested for vacuum suitability.

The schematic of the amplifier board is shown in Fig. 7.9, the layout and the actual implementation are shown in Fig. 7.10. It includes a section with low-pass filters for the AD8009 AR power supply, which requires a dual voltage supply of ± 5 V. The signal amplification section of the board was designed in a flexible way in order to

allow it to be used with multiple configurations. It is possible to configure it for AC- or DC-signal readout on the return line of the signal, dependent on whether a decoupling capacitor or a direct connection (0 Ω -resistor) is placed on the positions marked with A or B in the schematic. Further, an AC readout on the bias line is possible by placing a capacitor at position C.

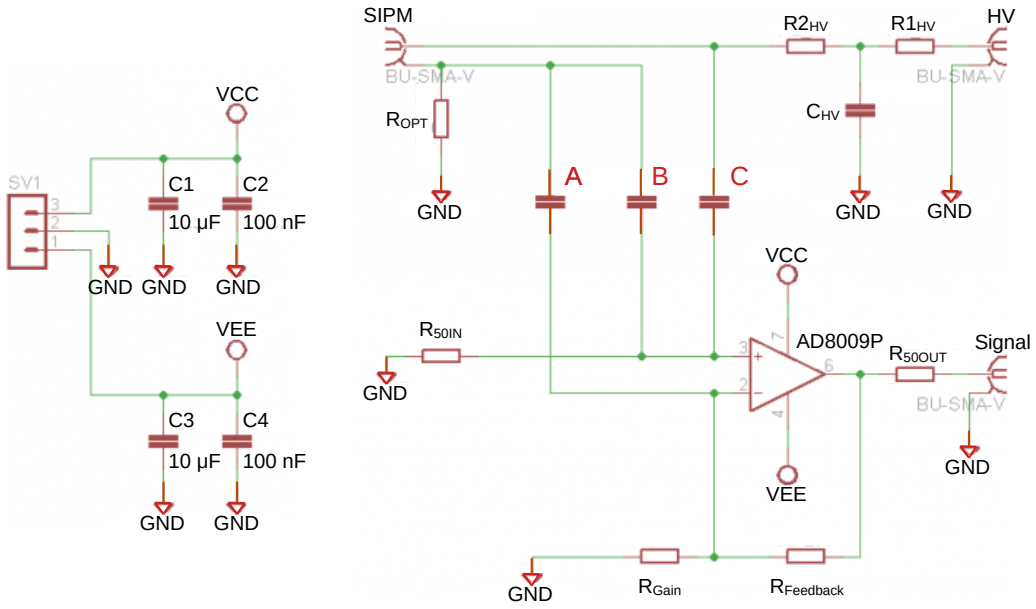

Figure 7.9.: *Schematic of the amplifier board build for the SiPM measurement. The left part shows the low-pass filter for the power supply of the AD8009. The right part shows the part used to amplify the signal from the SiPMs (connected to the upper left connector). The board was designed to be used in multiple configurations, dependent on the component placement. Placing a decoupling capacitor or a direct connection in either position A, B, or C allows for an AC or DC coupling of signals on either the SiPM return or bias line, respectively. The amplification of the board is determined by the resistance ratio between the resistors R_{gain} and $R_{Feedback}$, with an intended value of 10.*

The power supply input for the SiPM is also equipped with a low-pass filter to reduce possible noise from the SiPM power supply. The resistor placed in position R_{IN} has a high impact on the baseline position. A resistor with a too high resistivity can severely limit the dynamic range of the amplifier. For a resistor value of 1000 Ω for example, it was found that it shifted the baseline to the maximum amplifier output voltage, preventing any useful output.

The signal amplification factor of the AD8009 is determined by the ratio of the values of the two resistors R_{Gain} and $R_{Feedback}$. The values of these resistors, as well as the values of all the other components, can be found in Tab. B.1 in the appendix. The values given there are for the board configuration used in the SiPM measurements

presented in the following sections.

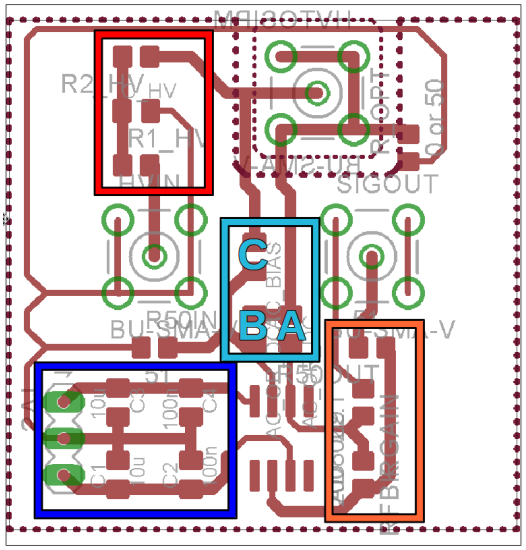

(a) *Layout plan of amplifier board*

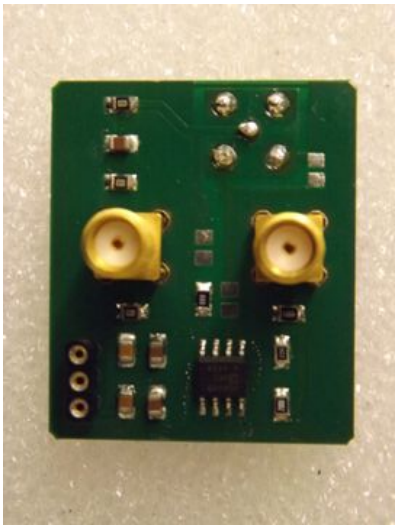

(b) *Picture of amplifier board (DC coupled on return line)*

Figure 7.10.: *Implementation of the amplifier board. The left figure shows the design layout of the board. The dark blue marked area contains the AD8009 AR power supply low-pass filter. In the red area, the SiPM power supply low-pass filter is placed. The type of readout is determined by component placement in the light blue area. Possible are AC and DC coupled readout on the return line (Positions A and B) and AC coupled readout from the SiPM bias voltage line (Position C). In the orange marked area, the resistors defining the amplification are placed. The right figure shows a realized board. The SMA connector for the SiPM is on the backside of the board. The version shown here utilizes a DC coupling on the return line (realized by a 0 Ω 'resistor' at position B).*

Test of the amplifier board

As later versions of the board are meant to be used as close as possible to the sensors and as such most likely in a cold environment, the first version of the board was tested at different temperatures to evaluate the temperature dependence of its amplification properties. For this test, continuous sinusoidal signals at different frequencies, provided by a frequency generator, were applied to the amplifier board. The input signal was applied with an amplitude of 10 mV. The amplitude of the output signal was measured using an oscilloscope. From the ratio of the output to the input signal the amplification was calculated. This measurement was performed for continuous sinusoidal input signals with a frequency of 0.2/0.5/1/5/10/20/30/40 and 50 MHz. This procedure was repeated for different temperatures. To achieve this, the amplifier was placed inside a containment, which was flushed with gaseous nitrogen. In this way,

measurements were taken at room temperature (≈ 293 K), 273, 240, 212 and 157 K. The last temperature is well below the usual operation temperature of the liquid xenon detector of around 170 K. The result of this measurement is shown in Fig. 7.11. As can be seen, it shows consistent behavior at all temperatures for the tested frequencies, thus we consider the board to be very temperature stable and therefore do not expect any signal degradation at lower temperatures.

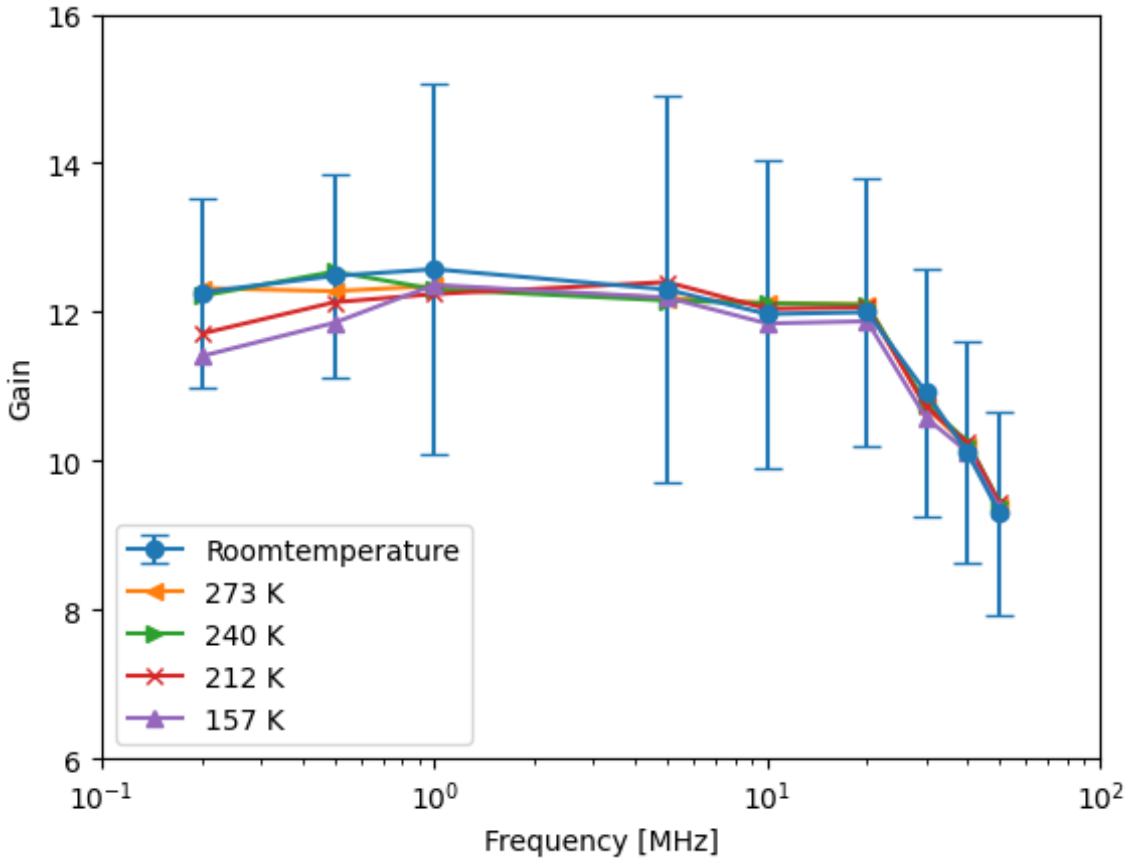

Figure 7.11.: *Measurement of the amplifier board response to sinusoidal signals with different frequencies at various temperatures. The test results show only a minimal impact of the ambient temperature on the amplification, thus the board is considered to be temperature stable. Errors are only shown for the room temperature measurement for the reason of visibility but the errors are of the same size for the other temperatures.*

7.7. Signal readout

Three identical boards were used in the measurement as a first amplification stage for the three SiPM samples. The boards used were configured for AC readout on the bias line. The complete configuration list is given in the appendix in Table B.1 on page 213. The amplifiers were placed in a metal box to add an additional shielding

and thereby reduce the noise level. The layout of the box is shown in Fig. 7.12, a picture is shown in the appendix in Fig. B.28 on page 214. All cable feedthroughs in this box were floating in order to avoid ground loops. An additional braided shield was added later to all coaxial cables connecting the test setup with the amplifier box to further reduce the noise level. The box also contains additional low-pass filter boards on the SiPM power-in line to reduce the ripple on the bias voltage provided by the SiPM power supply (CAEN Model A 1510, 12 Channel power supply).

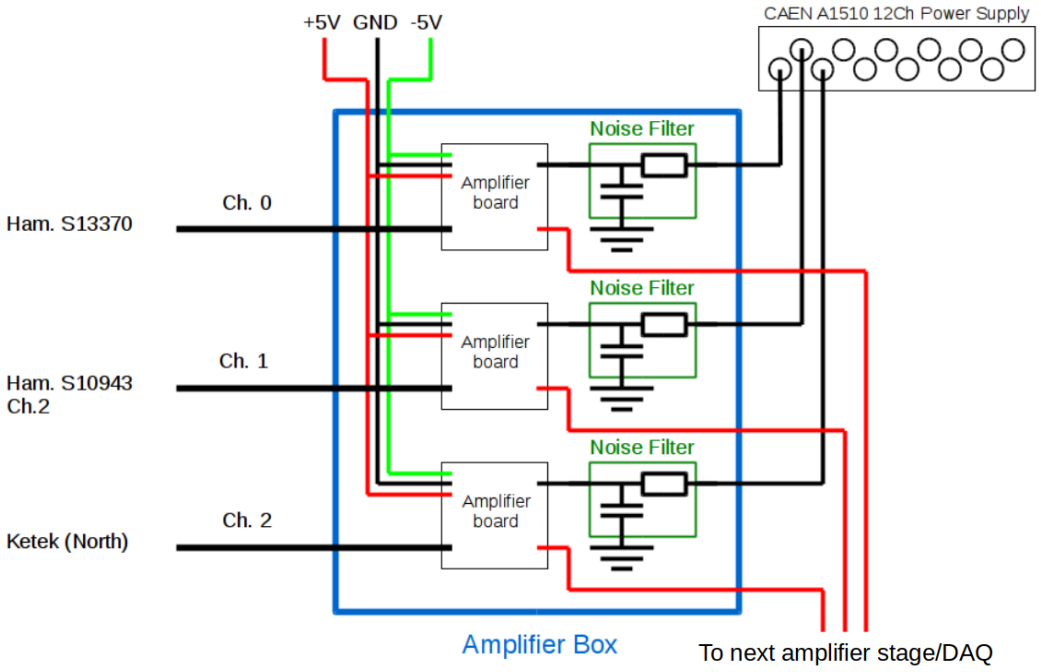

Figure 7.12.: *Layout of the box used in the test setup. The amplifier boards are housed in a metal box for shielding. The box contains additional low-pass filters for the SiPM power to remove the voltage ripple of the CAEN power supply.*

The signal was further amplified using a type KN2104 NIM amplifier, adding another amplification factor of 5. The fan IN/OUT module is needed to change the polarity of the signals to negative, as the KN2104 requires input signals with a negative polarity [126].

The PMT signal was amplified using only the KN2104. The signal was later split and one of the lines was connected to the digitizer. The other line was fed into a discriminator to create a trigger signal for the digitizer. This trigger was used for the detection of xenon scintillation light where the PMT provided the signal trigger for all sensors.

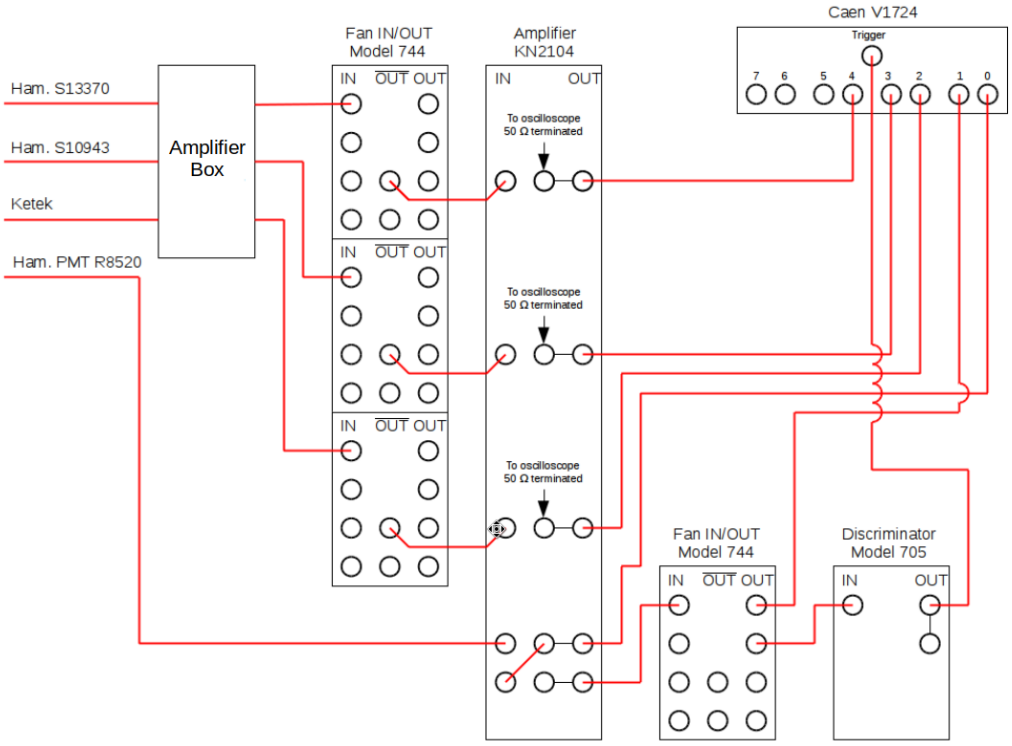

Figure 7.13.: *Readout chain for the SiPM and PMT signals during the measurement. The SiPM signals are first amplified by the boards with a factor of 10, followed by a second amplification of 5 by the KN2104 board. The PMT is amplified only by the KN2104 board, followed by a signal split to provide a trigger signal for the digitizer. This option is only used when* ^{241}*Am created xenon scintillation light is measured. For an LED measurement, the trigger signal is provided by the pulse generator powering said LED.*

7.8. First Measurements of SiPM samples

7.8.1. Signal shapes for the SiPM samples

In a first test, the three samples were operated in the setup with LED illumination to evaluate their signal quality. The samples were supplied with an arbitrary voltage above the breakdown voltage given in the respective data sheets. The pulse generator setup is sketched in Fig. 7.15.

The KETEK samples showed very erratic behavior, including large baseline fluctuations in the same order of magnitude as the signals. This is shown in Fig. 7.14a. Compared to the KETEK samples the Hamamatsu samples of both models showed a waveform as expected from a SiPM: a short signal rise followed by an exponential signal decay back to the baseline. Signal examples for the S10943 and S13370 are shown in Fig. 7.14b and Fig. 7.14c, respectively.

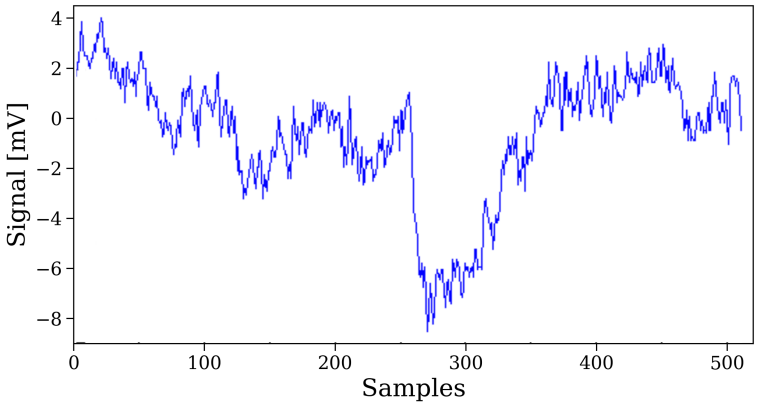

(a) *Waveform example for the KETEK sample.*

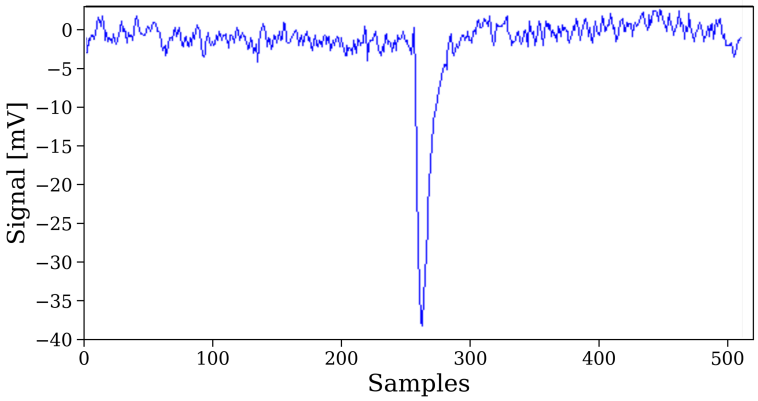

(b) *Waveform example for the Hamamatsu model S10943 sample.*

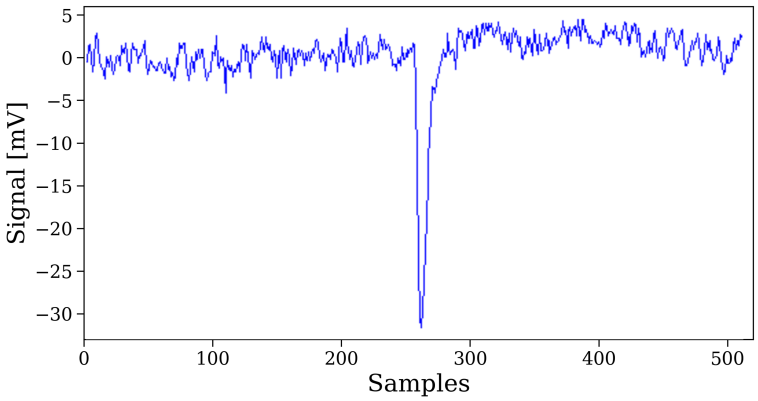

(c) *Waveform example for the Hamamatsu model S13370 sample.*

Figure 7.14.: *Qualitative comparison of signal shapes for the three tested SiPM models. The KETEK model shows erratic behavior with a very unstable baseline, making gain estimation and also later use unfeasible. Both Hamamatsu samples show clean signals. One digitizer sample corresponds to 10 ns sampling time.*

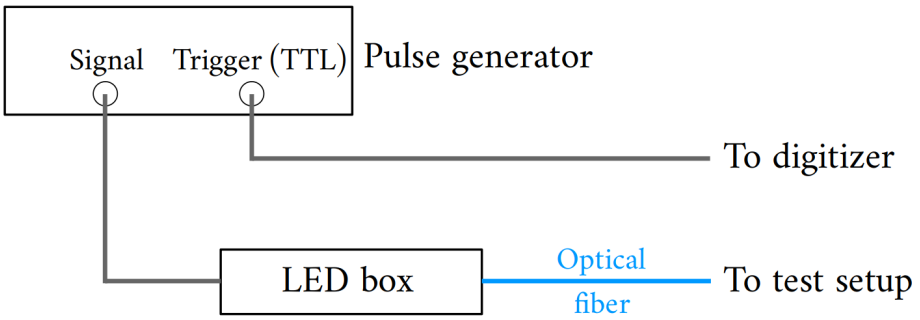

Figure 7.15.: *Setup for a LED measurement. A pulse generator (AVTECH model: AVI-V-HV1-C) powers a LED inside a light-tight box, which is coupled to an optical fiber. The fiber is connected to the test setup. The pulse generator additionally provides a trigger signal in form of a TTL (transistor-transistor logic) pulse [127].*

The signals observed from the KETEK samples were comparatively long, with no clear exponential tail. The shape in most cases might also be strongly affected by the baseline fluctuation, which made automatic peak-finding a challenge. The baseline instability, however, made it impossible to compute the peak integral and therefore the charge produced by a signal cannot be estimated. As no charge spectrum can be derived, there was no possibility to estimate the gain from these devices.

As this behavior was only observed for the KETEK samples, and exchanging the readout hardware (amplifiers, filters) with the Hamamatsu samples showed no improvement, it was concluded that the KETEK SiPMs itself were the source of the instability. As explained in Section 7.2, the KETEK samples received a surface treatment to increase UV sensitivity. It is assumed that this treatment damaged the SiPMs (or at least some individual pixels) in an unknown way, which results in the observed behavior. This assumption, however, could not be confirmed.

Based on these observations, no further tests were done with the KETEK devices. Regarding future updates of the MainzTPC, the newest generation of SiPMs should be used and further tests were focused on the newer Hamamatsu model S13370.

7.8.2. Determination of breakdown voltage

The breakdown voltage can be determined by measuring the gain of the SiPM at different bias voltages and utilizing the linear relation between applied bias voltage and observed gain. For this measurement, the light was provided by a LED via the optical fiber in front of the SiPM.

The gain can be extracted from the photon count spectrum with a fit function consisting of a sum of the number of Gauss functions equal to the number of observable photon peaks observed in the spectrum. The peak distance in this function is a common parameter of all Gauss functions, e.g. the x-position of the second Gaussian is two times the x-position of the first and so on. An additional Gauss is added to fit the pedestal peak around $x = 0$:

$$G_{Photon} = a_{PD} \cdot e^{\frac{x-\mu_{PD}}{2\sigma^2_{PD}}} + a_{P1} \cdot e^{\frac{x-\mu_P}{2\sigma^2_{P1}}} + a_{P2} \cdot e^{\frac{x-2\mu_P}{2\sigma^2_{P2}}} + ... \tag{7.1}$$

where a are the amplitudes of the Gauss functions for the pedestal (PD) and photon peaks ($P\#$), σ the standard deviation and μ_P the gain. An example of such a fit with 8 photon-peaks plus pedestal is shown in Fig. 7.16.

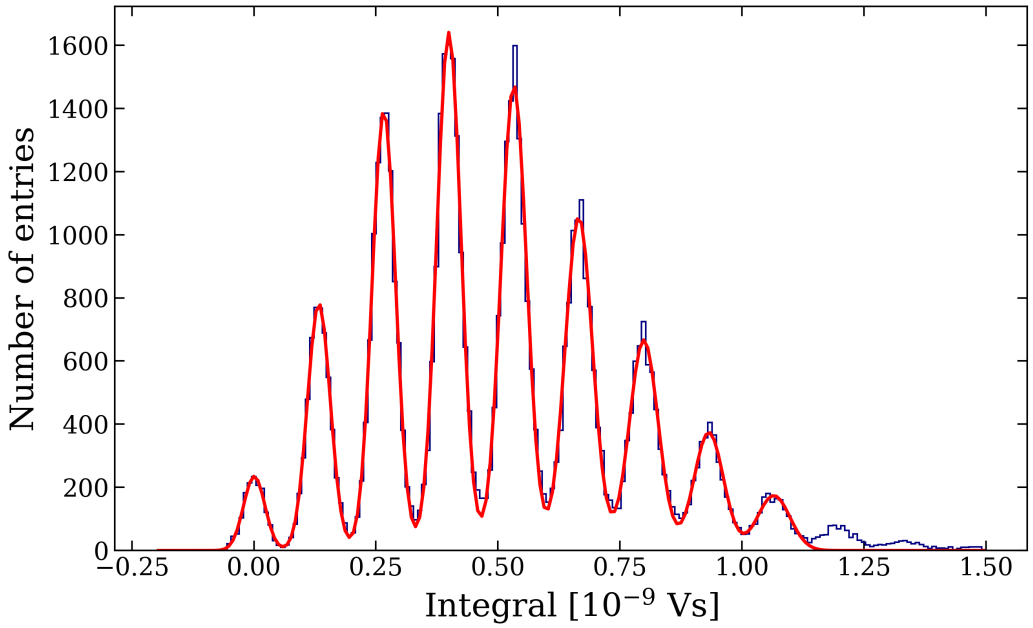

Figure 7.16.: *Example of a spectrum fit with a Gaussian for the pedestal peak plus one for every photon-peak. The spectrum was taken with the Hamamatsu S13370 with an applied bias voltage of 47.76 V at a temperature of 175 K.*

The gain values obtained can be plotted against the bias voltages they were recorded with, as shown in Fig. 7.17. A linear fit is used to calculate the breakdown voltage. For the S13370 a value of (44.73 ± 0.05) V was found at an operating temperature of around 175 K.

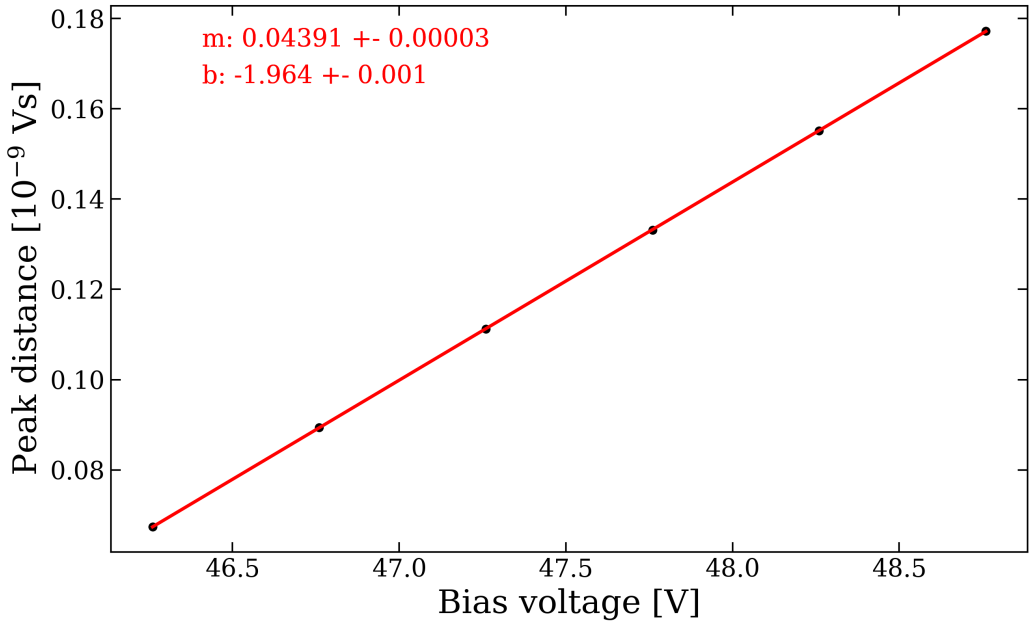

Figure 7.17.: *Linear fit of the obtained gains at different applied bias voltages. The fit function was of shape* $y = m \cdot x + b$. *The resulting parameters from the fit are shown in the plot. The resulting breakdown voltage* V_{Bd} *from the extrapolation to zero at the y-axis is* (44.73 ± 0.05) *V at a temperature of 175 K.*

7.8.3. Gain

The absolute gain of the SiPMs can be calculated by converting the peak distances from the spectra that were obtained in the last section, into a charge. The voltage amplified by the board drops over the resistor R_{OPT} with a value of 100 Ω. This type of resistors usually have a precision in the value of ± 1 %.

Additionally, the value needs to be corrected for the gain factors of the amplifiers. The total intended gain is 50, but a relatively high uncertainty of 10 % was assumed. Although the amplifier boards are outfitted with the same components, their individual gain factors were not evaluated separately, which is why this large uncertainty is assumed.

The resulting values from the previous steps are now divided by the elementary charge to get the gain of the SiPM:

$$G_{SiPM} = \frac{\Delta P}{R_{OPT} \cdot G_{AMP} \cdot e} \tag{7.2}$$

where ΔP is the peak distance (in Vs), R_{OPT} the resistance, G_{AMP} the gain of the amplifiers, and e the elementary charge. The error is computed via error propagation. The results for different illumination strengths are shown in Fig. 7.18. The achieved gains are close to the value of $2.25 \cdot 10^6$, which is given in the datasheet for the S13370 provided by Hamamatsu (see Appendix B.25).

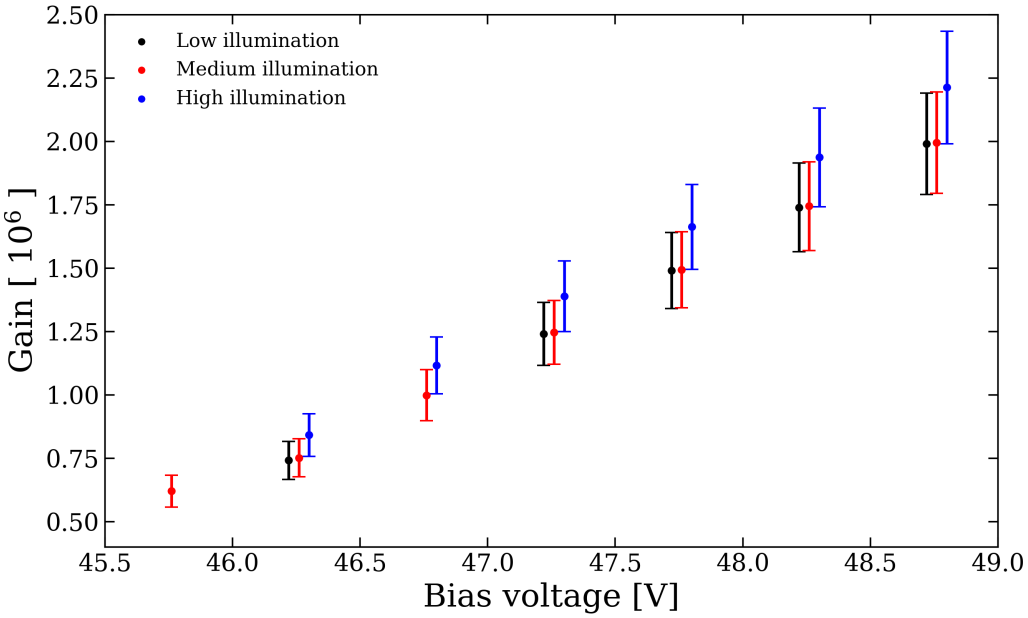

Figure 7.18.: *Gains of the S13370 SiPM for different illumination settings. Only data points with successful Gaussian fits of the spectra are included. The data points are taken at the voltages of the red positions, the other measurements are slightly offset for better visibility.*

7.8.4. Correlated noise measurement

The correlated noise refers to a combination of the previously mentioned effects of afterpulses and crosstalk. These effects increase the number of detected firing cells compared to the real number of hitting photons, i.e., to an overestimation of the number of hitting photons. For a sufficiently low photonflux a Poissonian distribution is expected for the number of detected photons (on a perfect sensor). Afterpulsing and crosstalk distort this distribution and shift it to higher numbers.

Starting with the multi-electron spectral fits as in Fig.7.16, the integral over each Gaussian peak provides the number of counts k in that peak. The results are plotted in a histogram as shown in Fig. 7.19. The effects of afterpulsing and crosstalk are clearly visible when a standard Poisson distribution is plotted over the photon distribution:

$$P(k;\mu) = \frac{\mu^k e^{-\mu}}{k!} \tag{7.3}$$

The pedestal peak can be used to calculate the parameter μ, which is the expectation value for the number of photons to produce signals in the SiPM. The probability for a zero photon event is given by:

$$P(0;\mu) = e^{-\mu} = \frac{N_{Zero}}{N_{Total}} \tag{7.4}$$

where N_{Zero} is the number of events without any detected photons and N_{Total} is the number of all waveforms. Therefore:

$$\mu = -ln\left(\frac{N_{Zero}}{N_{Total}}\right) \tag{7.5}$$

Comparing a Poisson distribution plotted with this parameter μ to the recorded data shows the aforementioned shift as shown in Fig. 7.19. The residuals show an overestimation in event numbers for lower photon counts and an underestimation for higher photon numbers.

The effects of afterpulsing and crosstalk are taken into account by a generalized Poisson distribution. Here, it is assumed that every event produces a Poisson distributed number of succeeding events (with probability λ) until all branches arrive at their final event. This distribution is given by [128]:

$$P(k;\mu,\lambda) = \frac{\mu\cdot(\mu+\lambda\cdot k)^{k-1}e^{-(\mu+k\cdot\lambda)}}{k!} \tag{7.6}$$

A fit of this generalized Poisson distribution to the recorded photon distribution is shown in Fig. 7.19. Compared to the normal Poisson distribution the generalized one describes the shape of the photon distribution very well, as visible in the residuals. The combined afterpulse/crosstalk probability is then given by the fit parameter λ.

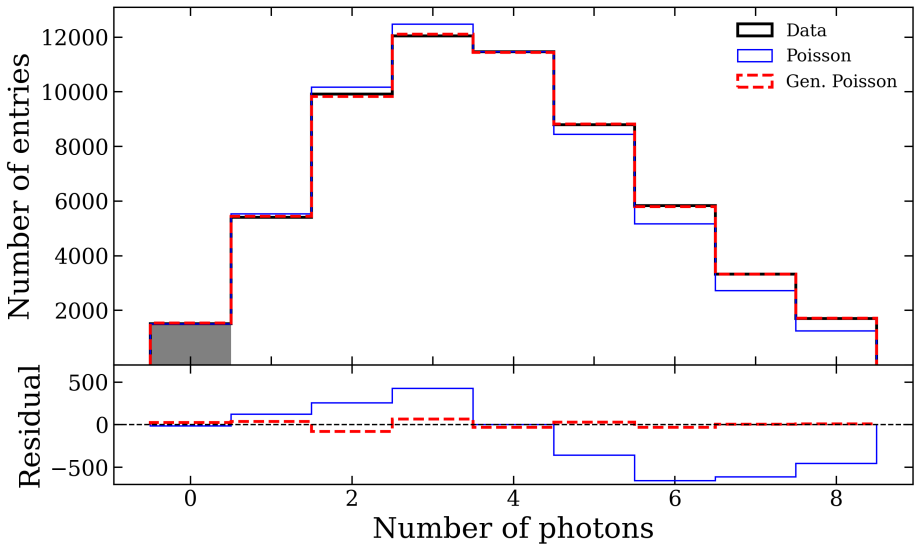

Figure 7.19.: *Photon-count spectrum taken with the S13370. A comparison of the data (black) with a standard Poisson distribution (blue) shows the effects of afterpulsing and crosstalk as the distribution is shifted towards higher photon counts. A fit with a generalized Poisson distribution (red), which includes additional branching events, shows a much better agreement and allows direct extraction of noise probability.*

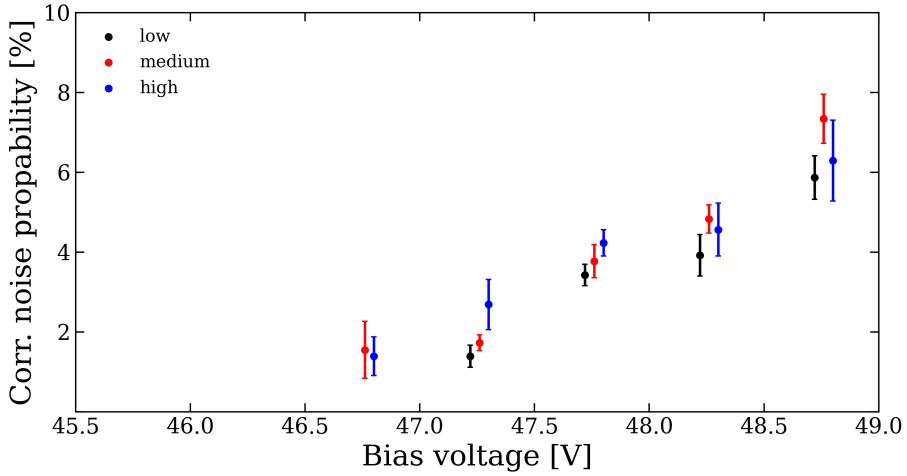

Figure 7.20.: *Results for the correlated noise probabilities resulting from fits of the photon count spectra with a generalized Poisson distribution. As expected the probability increases with higher bias voltage. Data was also taken for lower bias voltages, but the generalized Poisson fit did not converge on the photon count distribution. This is mainly caused by the largely overlapping Gaussians for low bias voltages, which distorts the count distribution. The results are shown for three different illuminations, taken at the same bias voltages (at the position of red data points). The other measurements are shifted slightly for better visibility only.*

This analysis was done for a range of applied bias voltages and also for three different illumination strengths. The resulting excess noise probabilities are plotted against the applied bias voltages which is shown in Fig. 7.20. As expected the noise probability increases with a higher bias voltage and behaves the same for different illumination strengths.

7.8.5. Dark count rate

The dark count rate of the SiPMs was determined in an extra measurement run. This was necessary, since the scintillation light produced by the ^{241}Am source in liquid or gaseous xenon was visible on the sensors even when the illumination cylinder was turned into a position where the openings did not directly face the sensors. Enough light was reflected on the bare steel vessel walls to significantly impact the measured rate.

To avoid this effect and perform the measurement without removing the ^{241}Am source, the dark count (DC) measurement was performed in a gaseous nitrogen atmosphere, where no scintillation light is to be expected. The nitrogen flow was tuned such that the temperature in the vessel was close to the temperature of liquid xenon. A PT100 from the discrete levelmeter was used to measure the temperature.

In order to be able to directly count the dark events a self-trigger circuit was con-

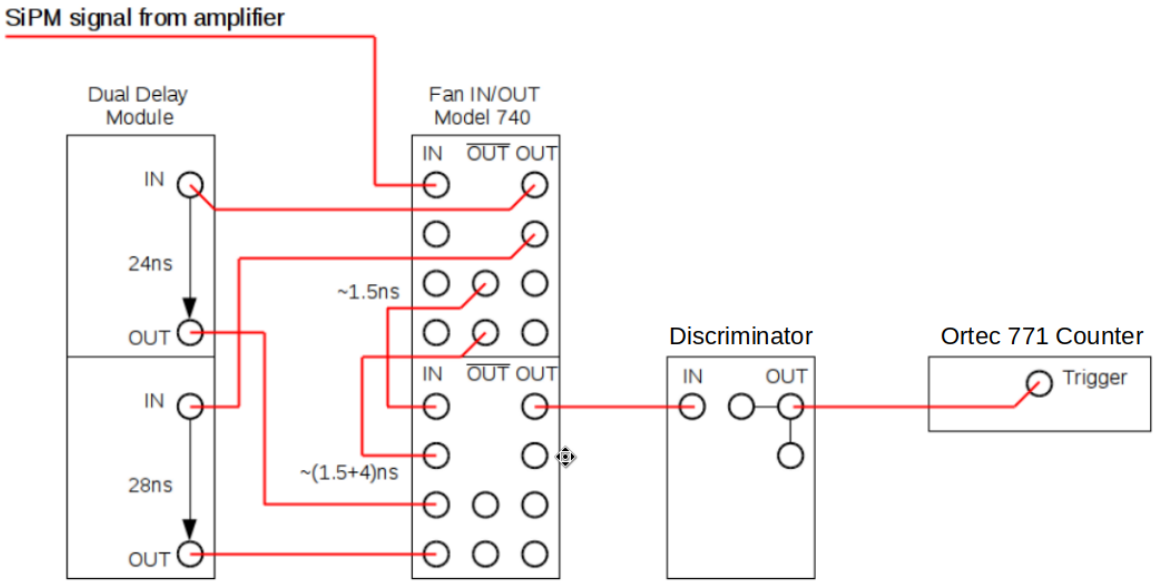

Figure 7.21.: *Readout and self-trigger configuration used to determine the dark count rate of SiPMs. The Fan IN/OUT module is used to add delayed versions of the signal to the waveform in order to eliminate high- and low-frequency oscillations. This allows the creation of a trigger signal by simply setting a threshold. This trigger is then used to count the number of dark events within a certain time window.*

structed utilizing Nuclear Instrumentation Modul (NIM)-boards. This was needed as a simple threshold was not reliable due to the baseline oscillations. To compensate for that, a 24 ns delayed version of the waveform was subtracted from the waveform itself. This eliminates oscillations with long wavelengths (also longer than the observed time window). The delay was chosen with respect to the signal rise time to ensure the signal strength is not significantly reduced. In a second step, this is repeated with a much shorter delay of 4 ns to reduce faster oscillations. The resulting summed signal provides a much more stable baseline so that a simple threshold set in a discriminator can be used to create a trigger signal. These triggers were fed into an Ortec 771 counting module to count the number of events created by the SiPM within a time window of 1 s. The counting setup is sketched in Fig. 7.21.

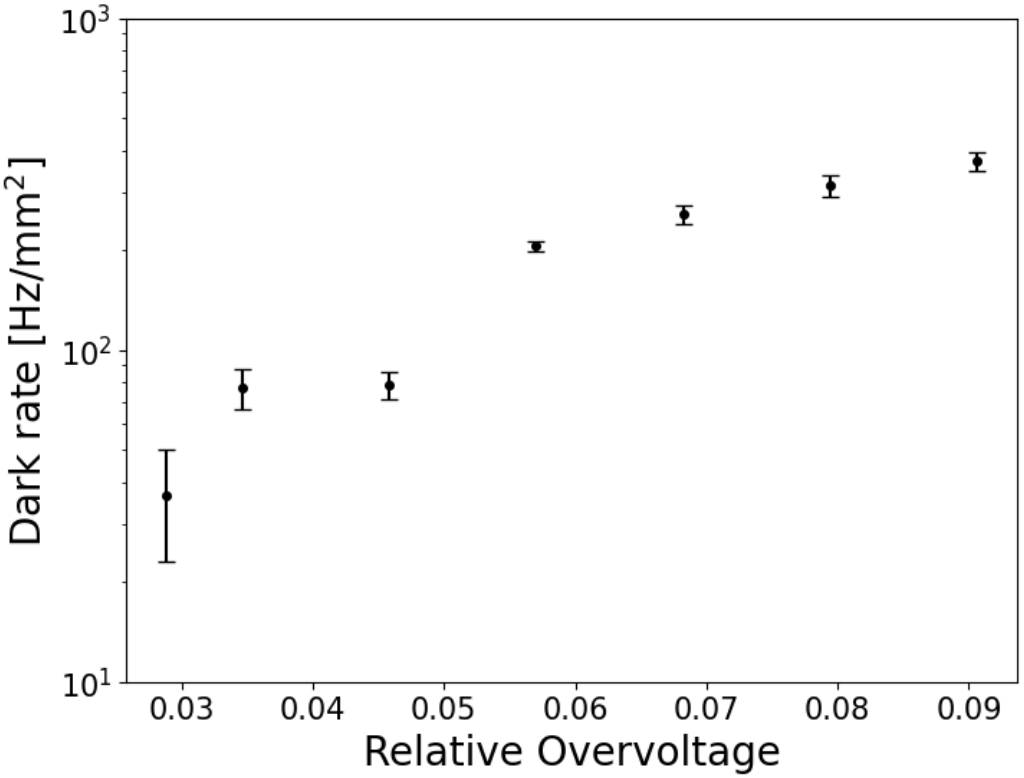

Figure 7.22.: *Dark count rates for the Hamamatsu SiPM of model S13370, measured at LXe temperatures. The DC rates were estimated for different over-voltages. One of the measurements does not follow the expected behavior, the reason for this is unknown. A large systematic uncertainty in this measurement is introduced by the measurement of the temperature, as the value was taken only in gas (the SiPM could be warmer, resulting in a higher DC rate).*

7.9. Measurements with xenon scintillation light

There was also data taken with xenon scintillation light instead of LED illumination, with the idea to trigger on the PMT, as shown in Fig. 7.13. The scintillation light is produced by an alpha particle from the decay of an ^{241}Am source immersed in the liquid xenon. Based on the decay energy of 5.5 MeV, more than 300000 photons are expected per decay, based on the mean energy of 17.9 eV (due to scintillation quenching), which is necessary to create a photon via an α-particle [45].

Due to the solid angle coverage of the illumination holes, using the largest opening towards the PMT, in the order of 1000 photons were expected on the PMT for each decay, a significant signal even when corrected for the quantum efficiency ($\approx$30 %). One order of magnitude less number of photons was expected for the SiPMs (due to the smaller opening facing the SiPMs for this orientation of the cylinder, see Fig. 7.6), which still is a significant signal.

The recorded spectra for the SiPMs, however, were dominated by the pedestal peak, with a total number of counts in the order of 100 for each photon-number peak for a total of 100000 events triggered by the PMT. This efficiency ratio between PMT and SiPM is far below the expectation and indicates a flaw in the design of the illumination arrangement, which needs to be reconsidered.

7.10. Summary, conclusion and outlook

In this chapter, the first steps in designing and building a test stand for SiPMs were described. With this setup first measurements were performed to characterize SiPMs. A test run was completed, in which the setup was successfully filled and operated with liquid xenon. During the run, data were taken with LED illumination of the sensors as well as with scintillation light of xenon which was created by an ^{241}Am source submerged in the liquid xenon, although the latter did not yield useful data and suggest some improvements are needed on the hardware.

Three different SiPM models were tested. The analysis was focused on the newest model S13370 from Hamamatsu. While preliminary values for correlated noise probabilities were calculated, the analysis needs to be refined to characterize afterpulsing and crosstalk probability separately. The dark count rate was determined in a gaseous nitrogen environment, as the reflected light from the xenon scintillation processes made a dark rate measurement in a liquid xenon environment unfeasible.

As shown in Section 7.8 the setup in its current state can be used to determine the basic characteristics of SiPMs, utilizing LED illumination. With focus on most recent Hamamatsu model S13370, values for the probabilities of correlated noise were measured in a liquid xenon environment.

Based on the experience gained during the test run presented, the setup is now (status during the writing of this thesis) used to characterize the Hamamatsu model S13371 SiPM. These are intended to be used in an upcoming update of the MainzTPC[1], replacing the current setup of a single upper PMT and APD assembly with a SiPM array to improve position reconstruction and also further test the feasibility of SiPMs in larger scale detectors like the upcoming dark matter projects DARWIN or XLZD.

[1]For further information on the two-phase xenon TPC located at the JGU see the PhD theses of Bastian Beskers [129] and Pierre Sissol [130]

A. Appendix: Applying a global fit to voxelized data to extract the S1 detection threshold

A.1. Motivation

The impact of the S1 threshold on the signal shape depends on the position of the interaction in the TPC. The S1 signal is mainly detected with the bottom PMT array. This means the uncorrected S1 signals produced close to the bottom array should be larger due to less loss of signal and thus less affected in shape by the threshold. A position closer to the center minimizes the impact of signal distortions caused by reflections of the S1 light off the TPC walls. Combining these effects the S1 signal should be the least distorted in the center and at the bottom of the TPC, but it is still expected to be asymmetric due to remaining threshold effects and low photon count numbers. This is confirmed when analyzing the fit results from different voxels of the TPC. A comparison of the projected shapes (in S1) is shown in Fig. A.1.

In this section an additional attempt to fit the data is made, this time utilizing a global fit to also extract the threshold parameters. In this case, each voxel is fitted with a 2D-skewed-Gaussian multiplied by a threshold, but the threshold parameters are the same for all voxels. This is realized by minimizing a global Log-Likelihood function. The cost function used is the sum of all the individual voxel Log-Likelihood functions. In this way, each voxel has its own set of parameters for the skewed 2D Gaussian but there is only one set of parameters for the threshold for all voxels.

This method has the advantage of giving only one, spatially independent result for the threshold. This result would be optimized taking the complete sensitive volume of the TPC into account. On the other hand, using the finest voxelization tested, results in a fit with a large number of fit parameters: with an x-y-division into 49 sectors and a z-division into 6 slices, there are 294 voxels in total. Each voxel is fitted with a 2D skewed Gaussian needing 7 parameters (amplitude, x, y, σ_x, σ_y the rotation angle Θ and the skewness α) plus the 4 global parameters defining the threshold. A fit with this voxelization thus would use 2062 parameters, so it is expected to be quite unstable and minimization would take long.

The starting values for the parameters were determined in the same way as before, determined for each voxel independently, and using the fit result shown in Fig. 4.32 as initial values for the threshold. In fact, the code was written in a way to reuse most of the functions already used previously.

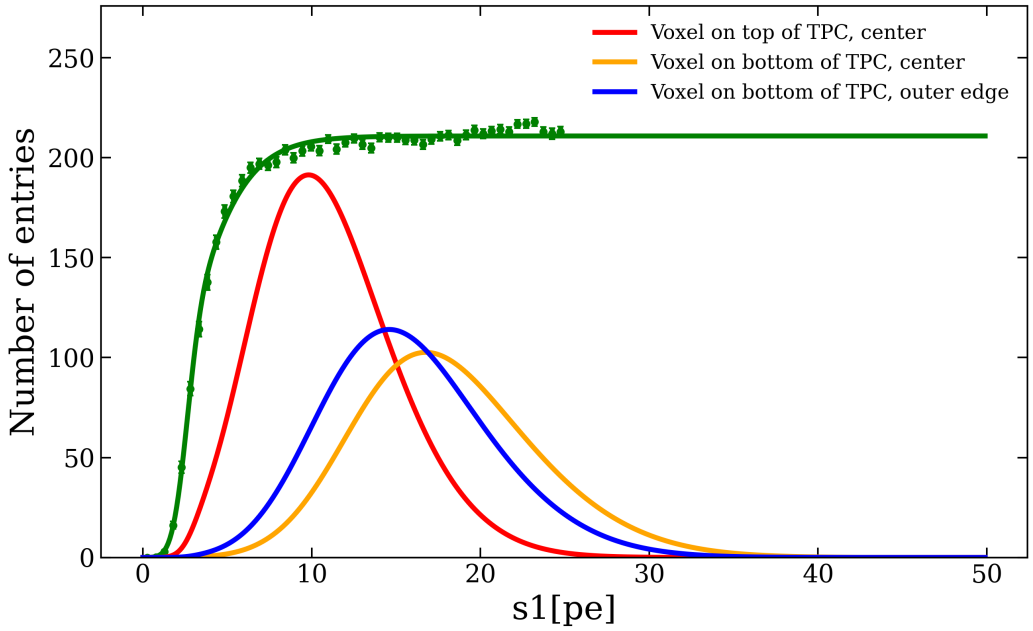

Figure A.1.: *Comparison of uncorrected S1 shapes in voxels at different positions in the TPC. The top voxel spans from -10 to -25 cm, and the bottom ones from -85 to -100 cm. The central voxel is a cylinder with a radius of 8.4 cm, the outer one is a ring-section ranging from a distance of 25.2 to 42 cm of the center of the TPC. As expected the lower central voxel has the largest S1. Going to the edge of the TPC already reduces the amount of detected photons, most likely caused by losses due to reflections and absorption at the TPC-walls. The top voxels have the lowest S1 values (all very similar to the shown example), confirming that their shape is much stronger influenced by the threshold (which is shown as the green line and data points for comparison, arbitrarily scaled for visibility).*

The only difference is a new function, building now a global cost function from the single voxel cost functions, and the output of this global function is minimized instead. This new function is shown in in the appendix on page 216.

A.2. Fit performance

A first run with a fine voxelization did not converge. Therefore a number of test runs with a much smaller amount of voxels were done. For a start, a series of fits was performed only by dividing the TPC volume into a different number of z slices.

The most obvious divergence observed was for the fit parameters of the threshold function. Especially the parameters describing the maximum efficiency and the position deviate from the initially fixed settings. In common for nearly all the fitting runs is an efficiency value, which was much lower than the experimental one, partially even resulting in negative values. The fits, when all parameters are left free, result in

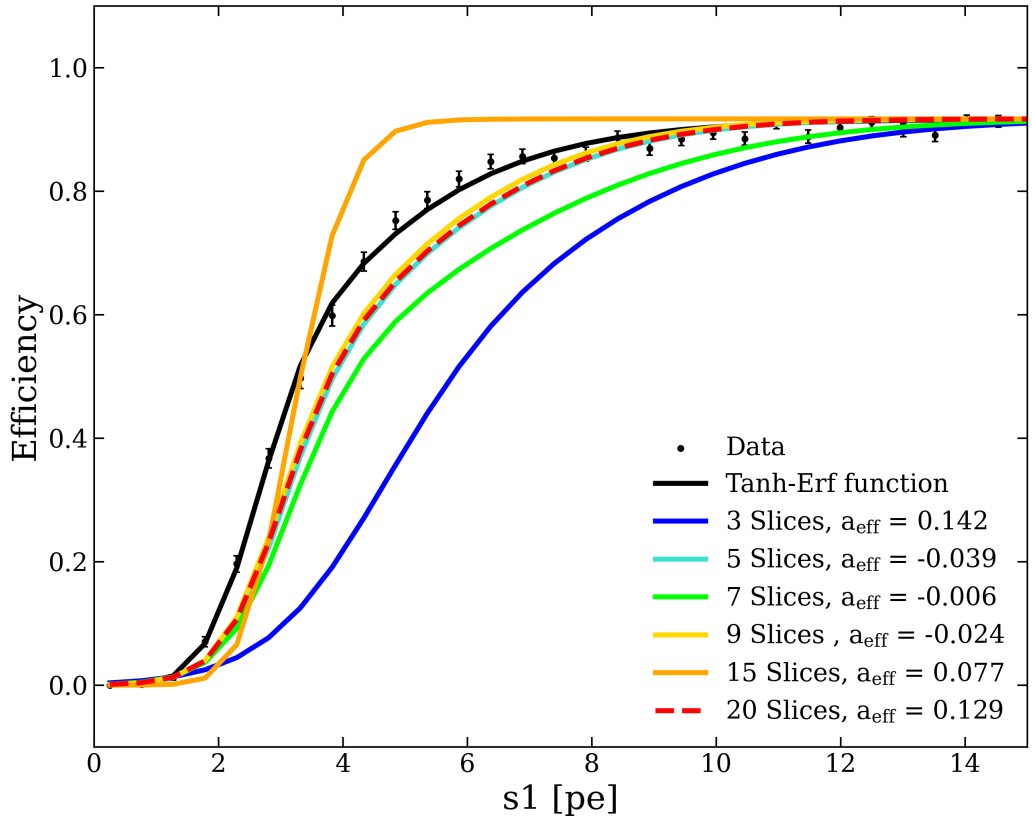

Figure A.2.: *Comparison of the threshold shape, based on the results of global voxel fits with a different number of slices, as the only voxelization is done in z. The black line is the fit to the XENON1T data. The results from the global fits are scaled to the same efficiency value to allow an easier shape comparison. Three fits (5, 7, and 9 slices) result in an actually* negative *efficiency parameter. Also, three of the resulting thresholds are otherwise very similar in shape (5, 9, and 20 slices). Their shape is very close to the fit at the data points but with a higher position at around 2.8 PE instead of 2.4 PE. The values of all the (threshold) fit parameters are given in Table A.1.*

a variety of fit parameters that all seem to describe the shape of the S1 distribution quite well. However, the results for especially the efficiency parameter, are unrealistic. There is a large deviation in the threshold shape (apart from the efficiency parameter) between the different fits. Fig. A.2 shows a comparison of the shapes for the different numbers of z slices. All results are scaled to the same efficiency to allow for a simpler comparison. Interestingly, results from three different divisions (5, 9, and 20 slices) result in a very similar shape and position, while others completely differ.

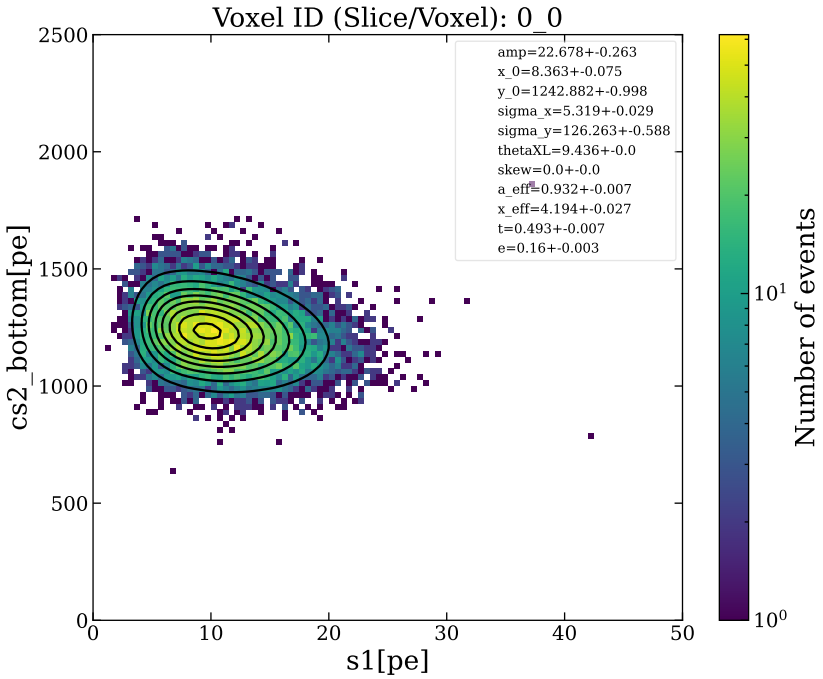

(a) *2D-Skew Gaussian fit to voxel data.*

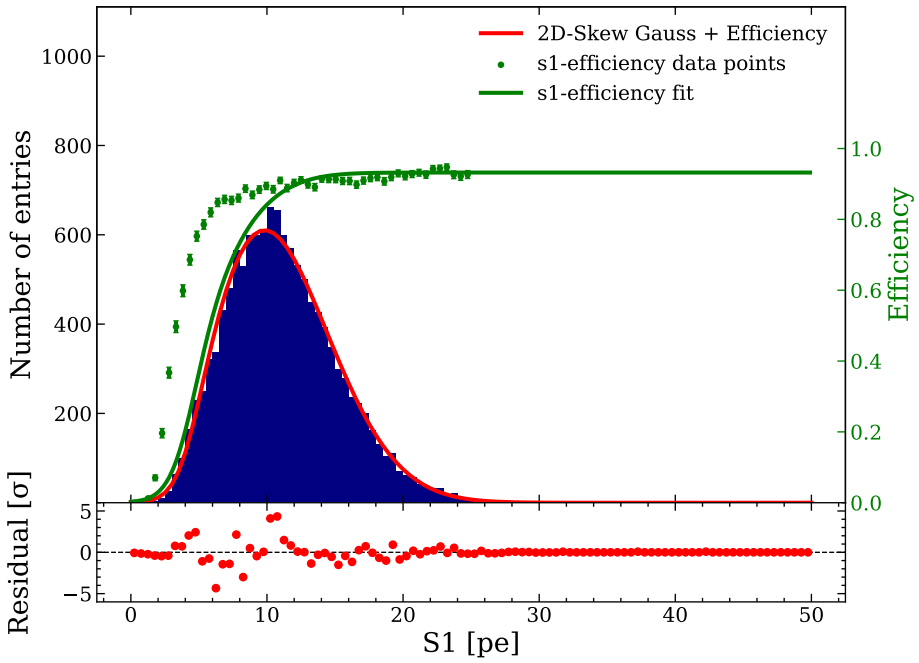

(b) *1D projection on S1 axis.*

Figure A.3.: *Example fit results from one voxel (from the top center of the TPC) when a global fit is applied to the ^{37}Ar data. For this fit, the TPC volume was divided into 36 equally sized voxels. All fit parameters were free, with shared parameters between voxels for the threshold. The shown example results close to the data (in green) in amplitude, but far off in position. Therefore the shape is threshold dominated and for compensation the Gaussian is shifted to lower values, resulting in a far to low value for S1 with (8.363 ± 0.075) pe.*

Additional fit attempts were made with a finer voxelization, dividing the x-y-plane into 9 sectors. Also with this configuration, the too low efficiency values were observed.

A possible solution could be to fix the efficiency parameter to the value obtained from the experimental data, this case was however covered by a free fit for a division of the TPC into 36 voxels (one ring map with 9 voxels, z division into 4 slices). As shown in Fig. A.3, the found global efficiency parameter has a maximum value of 0.932 ± 0.007, very close to the 0.917 ± 0.002 found with a fit to the threshold datapoints (see Fig. 4.31). The resulting S1 value of the distribution, however, is at a much too low value due to a very high threshold position at 4.194 ± 0.027 pe compared to the data-based 2.419 ± 0.024 pe. An additional attempt to fit only the central region of the TPC was made. Here, not the full diameter of the TPC was fitted, but only a cylindrical selection in the center, with a radius of 20 cm. With that selection, edge effects of the detector (for instance light collection efficiency variations due to reflection at the detector walls) on the signal shape should be avoided or minimized. This selection, however, did not improve the results.

	Threshold fit parameter			
Fit settings	a	x_S	ϵ	τ
Threshold only	0.917 ± 0.002	2.419 ± 0.024	0.282 ± 0.008	1.027 ± 0.049
0 Rings, 3 Slices	0.142 ± 0.003	4.082 ± 0.030	0.506 ± 0.006	0.158 ± 0.002
0 Rings, 5 Slices	-0.039 ± 0.002	2.823 ± 0.032	1.011 ± 0.036	0.204 ± 0.008
0 Rings, 7 Slices	-0.006 ± 0.002	2.951 ± 0.025	0.941 ± 0.032	0.154 ± 0.004
0 Rings, 9 Slices	-0.024 ± 0.002	2.774 ± 0.042	1.039 ± 0.032	0.214 ± 0.011
0 Rings, 15 Slices	0.077 ± 0.012	2.801 ± 0.037	0.230 ± 0.03	0.837 ± 0.028
0 Rings, 20 Slices	0.129 ± 0.002	2.801 ± 0.042	1.022 ± 0.038	0.205 ± 0.011
1 Ring, 3 Slices	0.033 ± 0.003	3.857 ± 0.033	0.562 ± 0.011	0.165 ± 0.003
1 Ring, 4 Slices	0.932 ± 0.007	4.194 ± 0.027	0.493 ± 0.007	0.160 ± 0.003

Table A.1.: *Comparison of the fixed parameters used in the local fits (individual fits for each voxel as it was done in Section 4.7) with the parameters obtained in various global fit attempts. A clear trend to very low values (even negative) for the efficiency parameter a can be observed, with generally higher position values x_S than the data based ones. An exception is the 1 Ring/4 Slice combination, which results in an efficiency very close to the data, but also here the position is at far too high values. This results mostly in too low values for the position, which is also shown in Fig. A.3.*

Based on the results presented in this section, the global fit, in its current state, does not result in reliable results. The shapes of the event distribution are well described, but the strong correlation between the threshold and S1 position prevents this method from resulting in a stable and reliable outcome.

One reason might be that the signal shape in S1 is not Gaussian at all due to the low photon number and it is better described with a smeared binomial or Poisson distribution and a threshold.

B. Appendix

B.1. XENON1T working principle

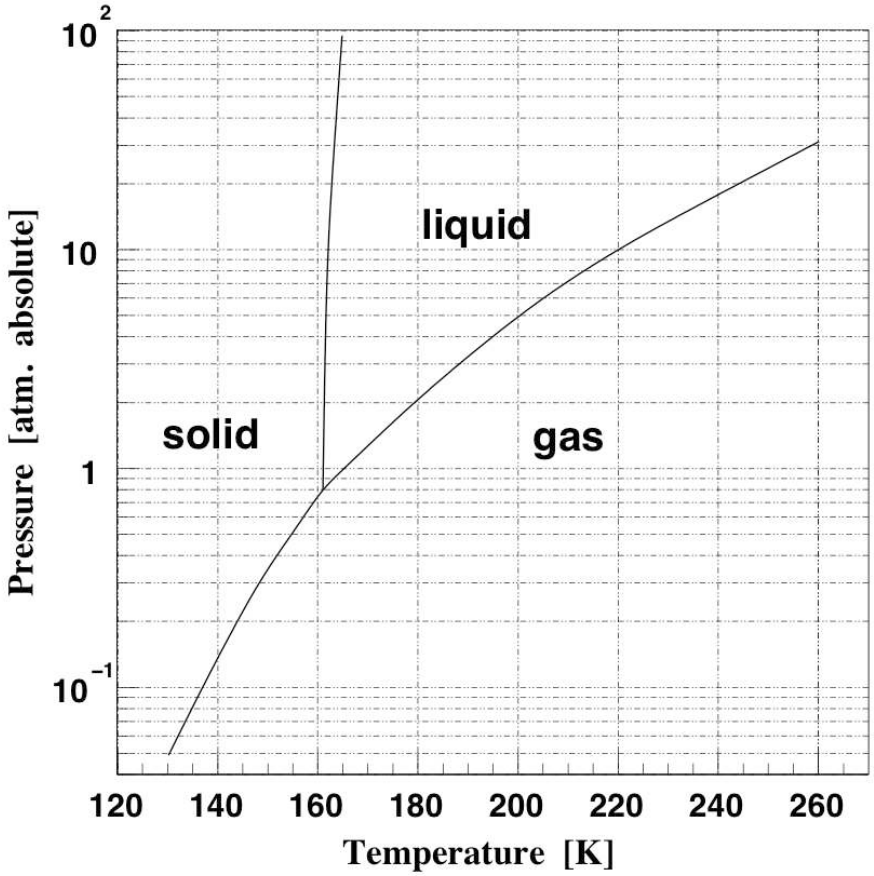

Figure B.1.: *Phase diagram of xenon. Plot taken from [45].*

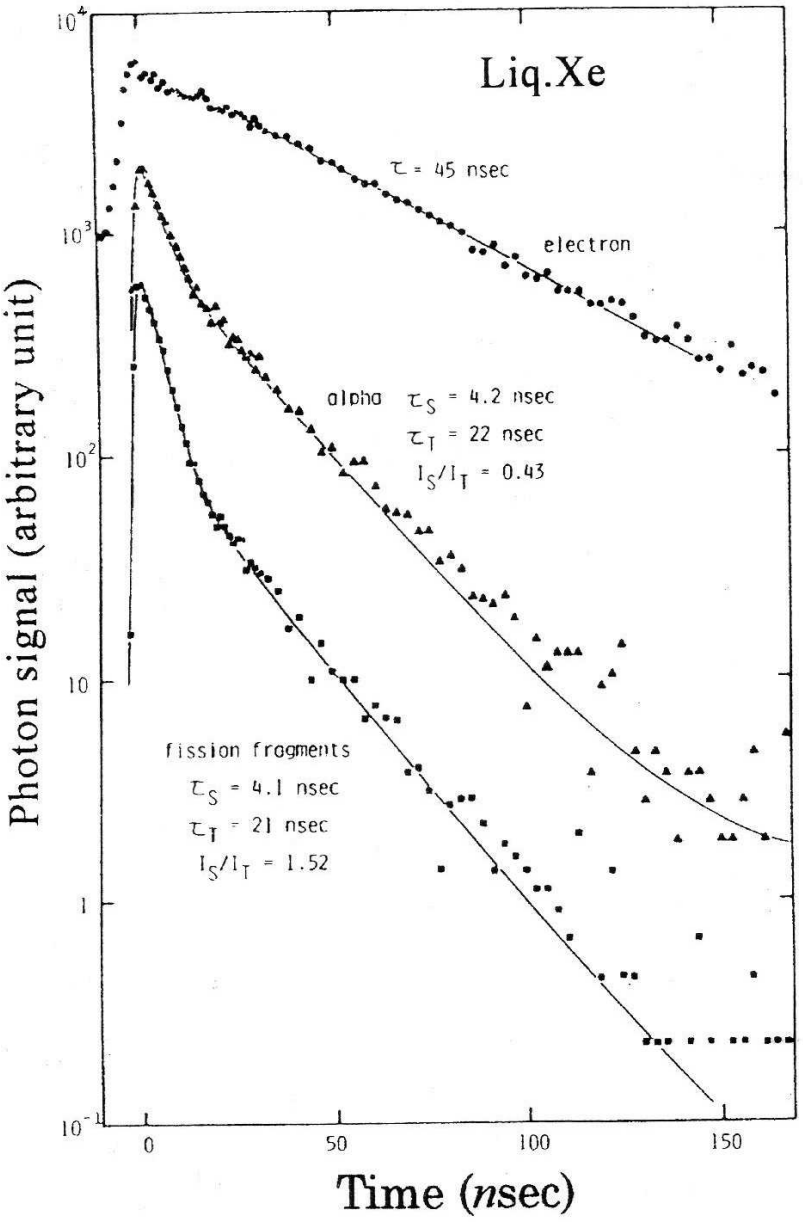

Figure B.2.: *Decay curves of liquid xenon for different types of exciting particles like electrons, fission fragments and alpha particles. The top curve is without applied electric field. It shows the two present decay time constants of ∼ 4 ns (limited by readout system) and ∼ 22 ns for the decay of the singlet and triplet state, respectively [45].*

B.2. XENON1T ^{37}Ar Distillation

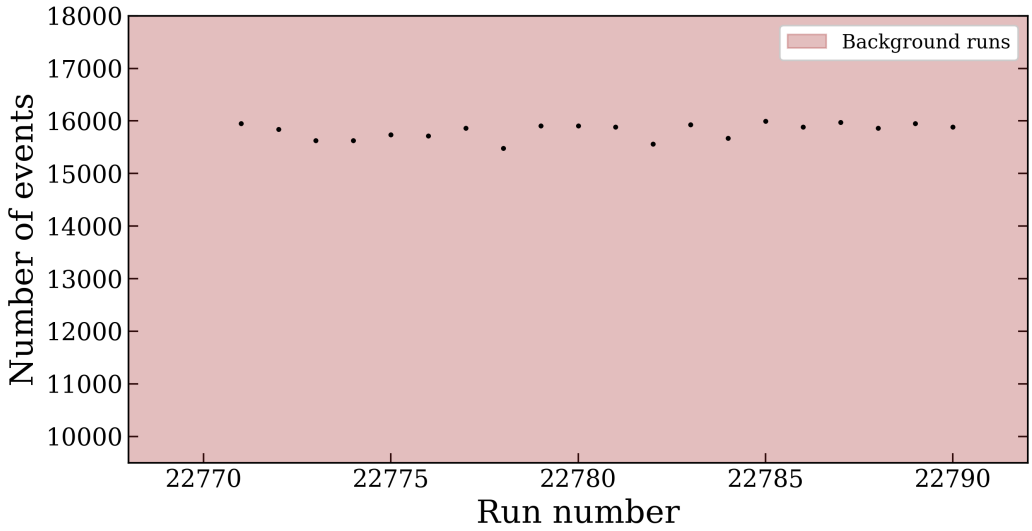

Figure B.3.: *The 20 runs used to estimate the background levels before the ^{37}Ar calibrations. A mean value of 15879.80 events/run are calculated from these runs. The number of useful runs was limited to this low number as detector conditions before these runs were different due to other tests.*

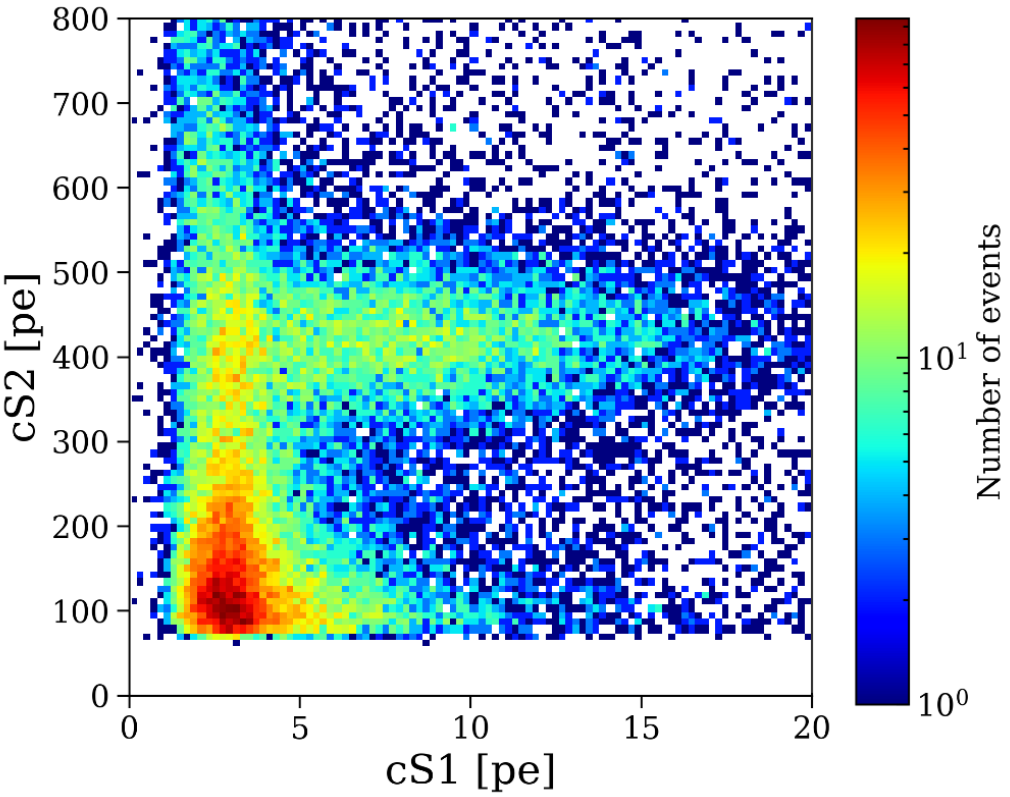

Figure B.4.: *Detail of the lower energetic 0.27 keV line of the ^{37}Ar decay. The events are clearly visible at cS2 ≈ 400 pe. The shown S2 in that regime are paired with random S1s, as the expected amount of light produced in this interaction is well below 1 pe. This peak also only shows up in the ^{37}Ar data sets and is not visible in the background data. 766 runs of ^{37}Ar data are accumulated in this plot.*

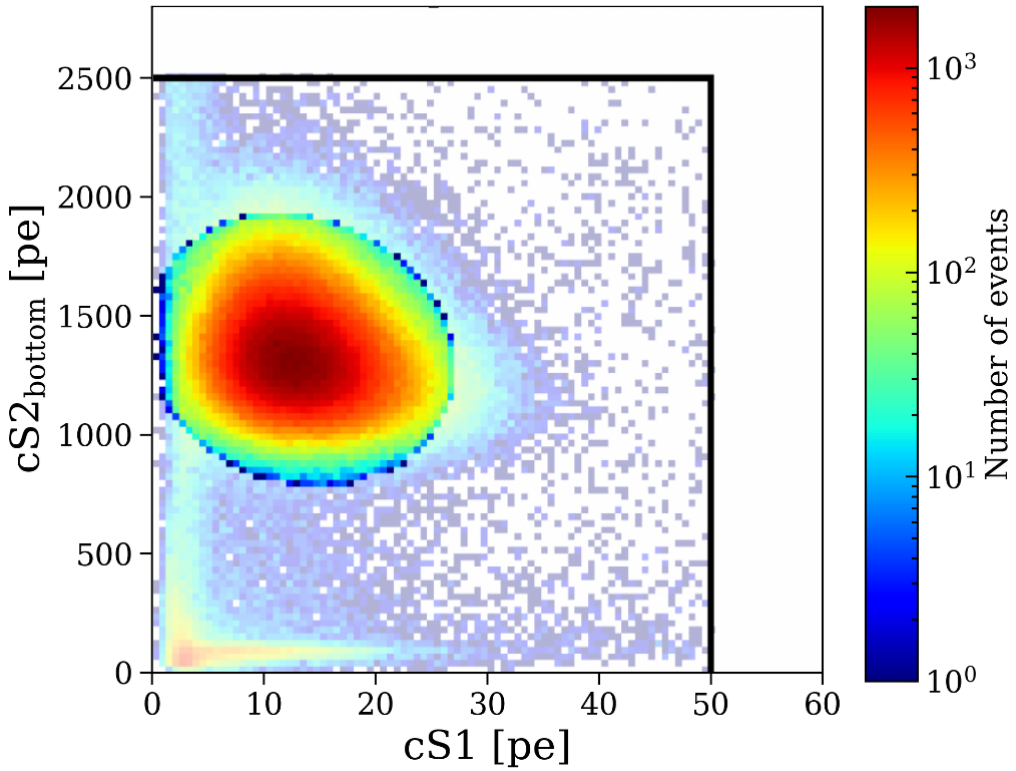

Figure B.5.: *Shape of the ellipsoidal event selection for the rate calculation, only the events in the highlighted region are used. The ellipsoidal shape was placed in way that it includes 99.6 % of the peak events. By selecting this way a much cleaner data sample is selected. This plot was created by Matteo Alfonsi.*

B.3. XENON1T Electron lifetime estimation

Raw S2$_{bot}$ fits

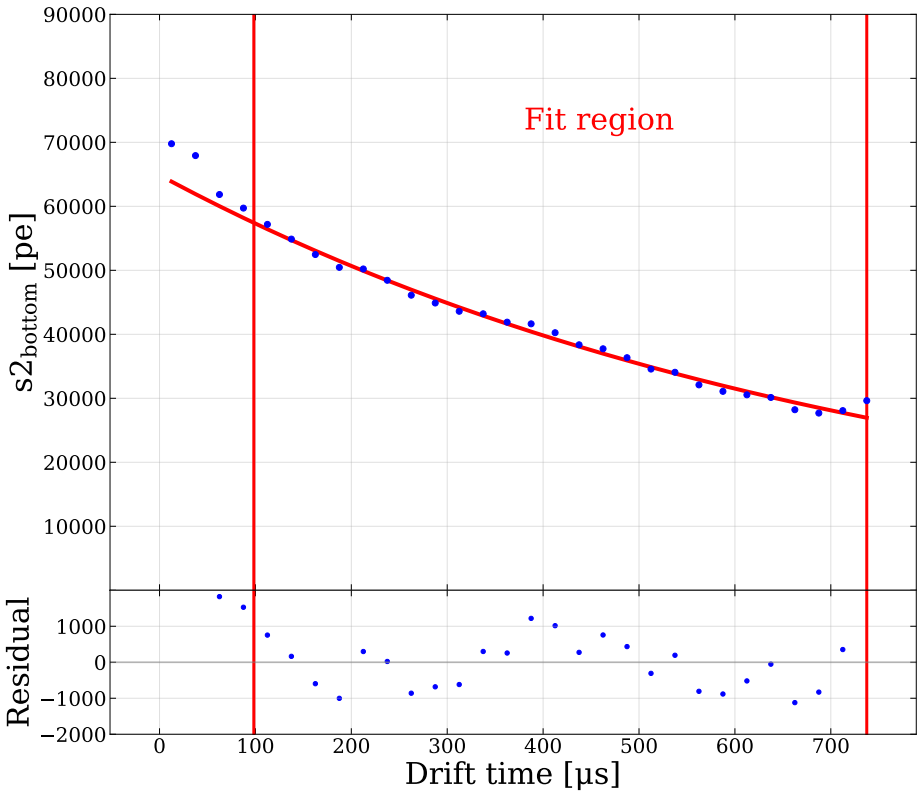

Figure B.6.: *Exponential fit to the mean $s2_{bottom}$ of ^{129m}Xe with values obtained from the Gaussian fits in each of 30 time slices. The large fluctuations are due to the low statistics of this source.*

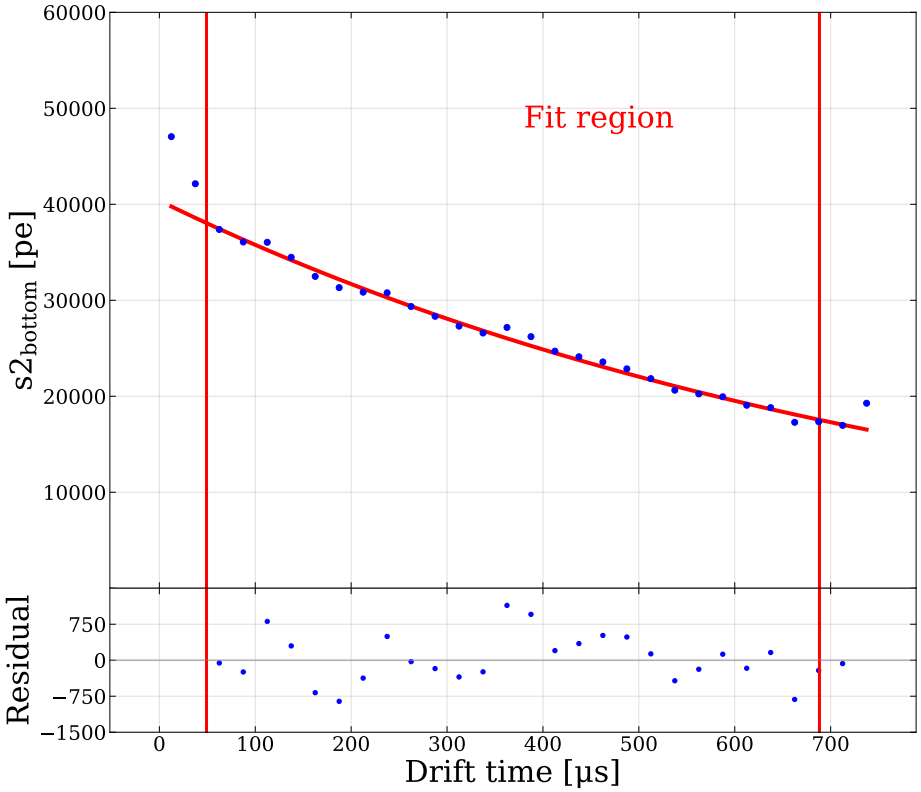

Figure B.7.: *Exponential fit to the mean* $s2_{bottom}$ *of* ^{131m}Xe *with values obtained from the Gaussian fits in each of 30 time slices. The large fluctuations are due to the low statistics of this source.*

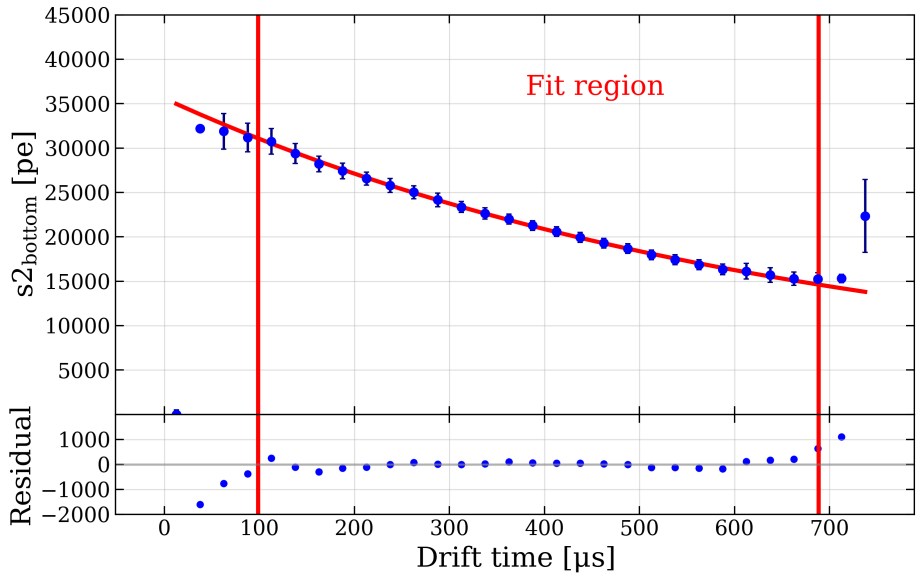

Figure B.8.: *Exponential fit to the mean $s2_{bottom}$ of ^{218}Po with values obtained from the Gaussian fits in each of 30 time slices.*

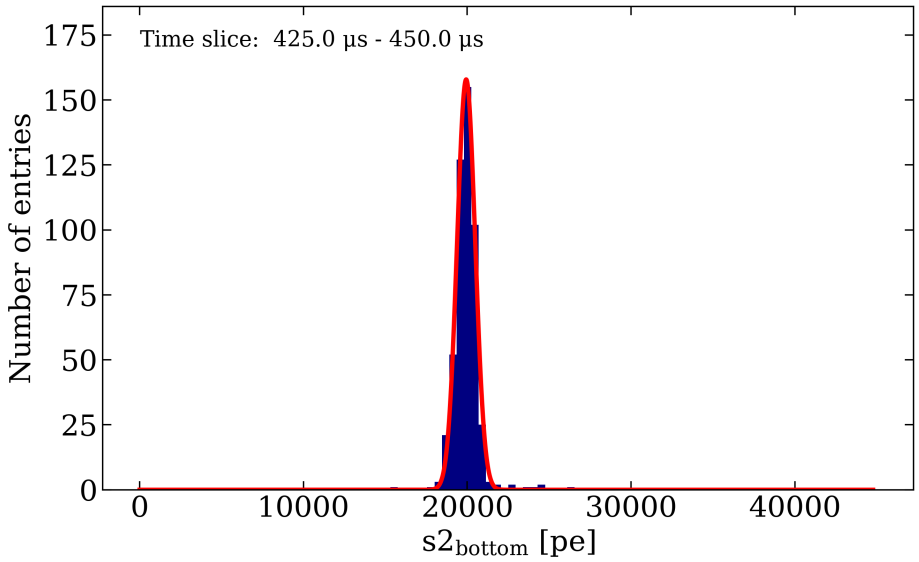

Figure B.9.: *Example fit of one time slice of ^{218}Po.*

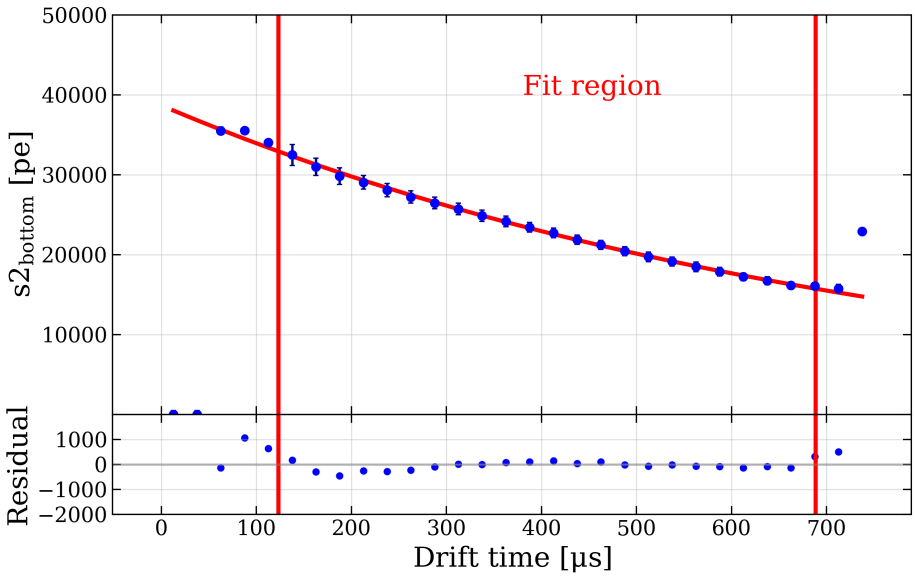

Figure B.10.: *Exponential fit to the mean $s2_{bottom}$ of ^{222}Rn with values obtained from the Gaussian fits in each of 30 time slices.*

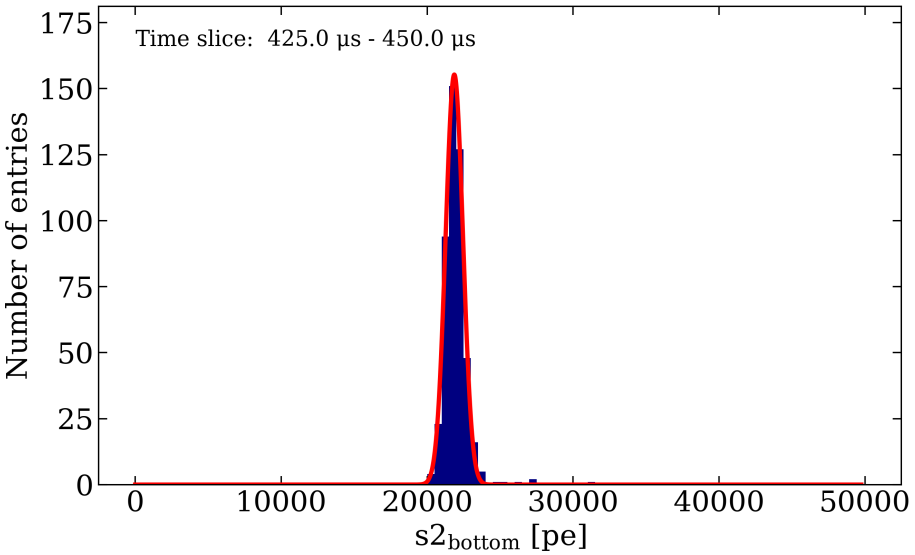

Figure B.11.: *Example fit of one time slice of ^{222}Rn.*

Field corrected $S2_{bot}$ fits

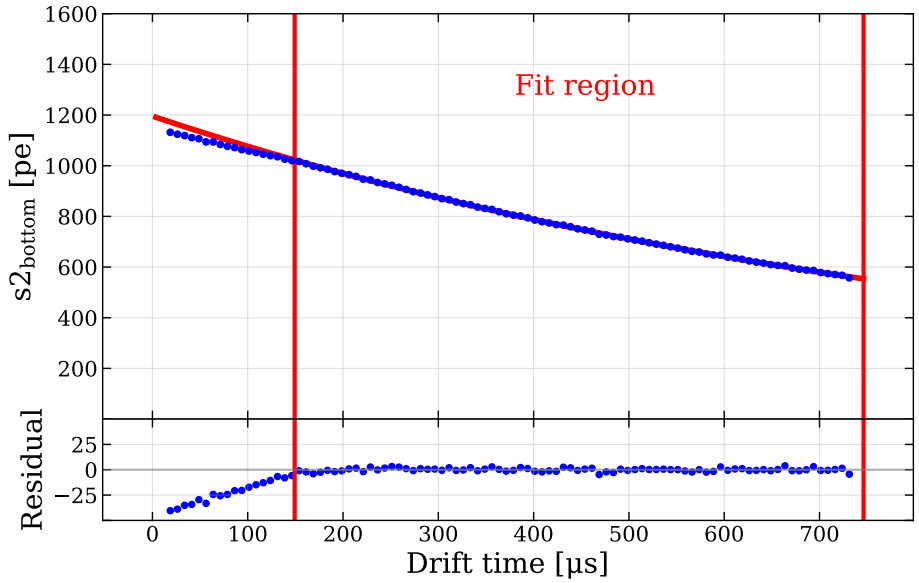

Figure B.12.: *Exponential fit to the field corrected mean* $s2_{bottom}$ *of* ^{37}Ar *with 100 time slices. The obtained lifetime is* $(921.30 \pm 0.19)\,\mu s$.

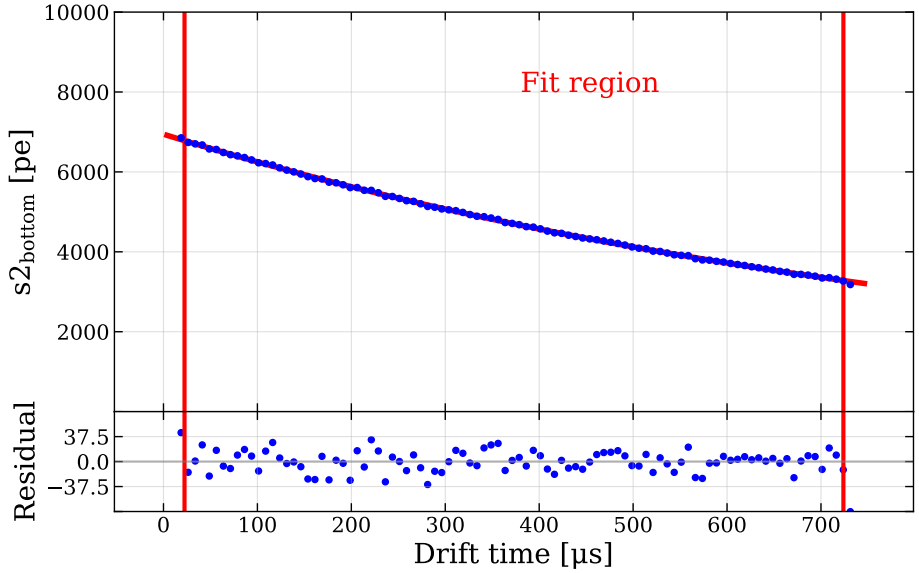

Figure B.13.: *Exponential fit to the mean* $s2_{bottom}$ *of* ^{83m}Kr *with 100 time slices. The obtained lifetime is* $(915.89 \pm 0.18)\,\mu s$.

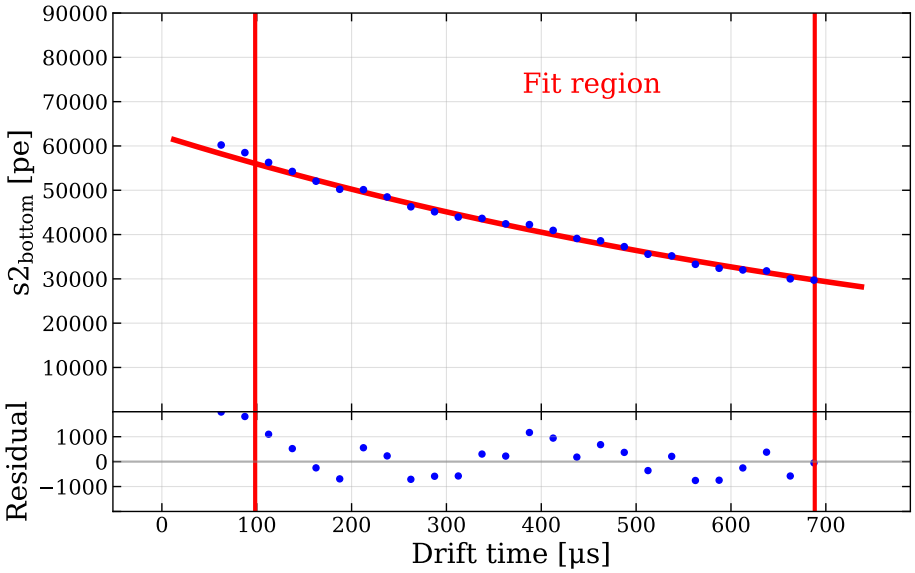

Figure B.14.: *Exponential fit to the field corrected mean $s2_{bottom}$ of ^{129m}Xe with 30 time slices. The obtained lifetime is (931.69 ± 6.81) µs.*

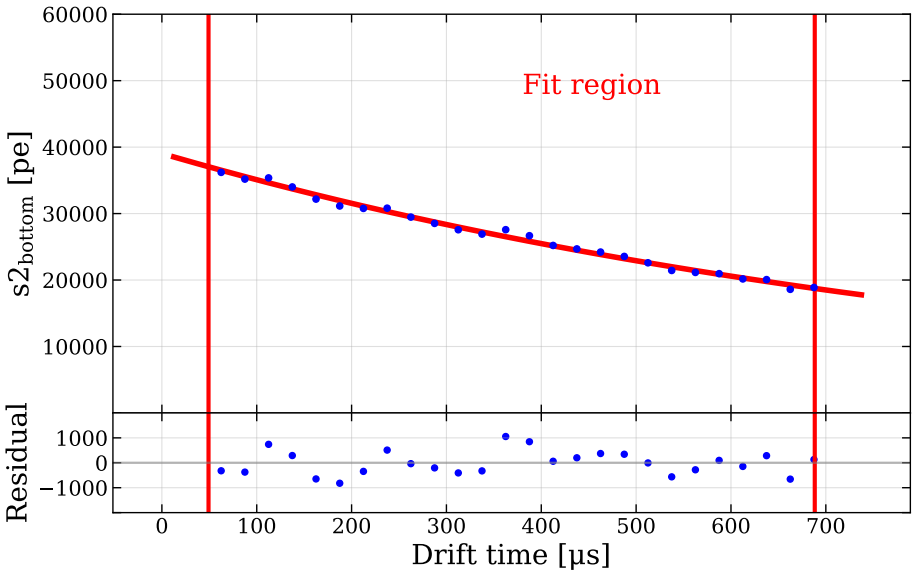

Figure B.15.: *Exponential fit to the mean $s2_{bottom}$ of ^{131m}Xe with 30 time slices. The obtained lifetime is (937.37 ± 9.32) µs.*

B.4. XENON1T Afterpulse correction

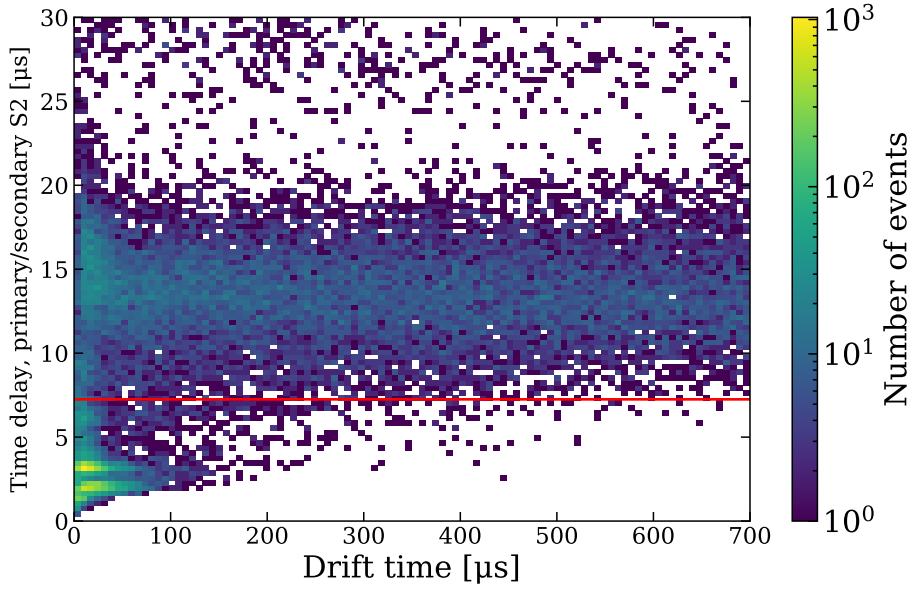

Figure B.16.: *Simple selection for ^{129m}Xe . The threshold used is identical to the one for ^{37}Ar . Below the threshold only a few events are selected for AP correction.*

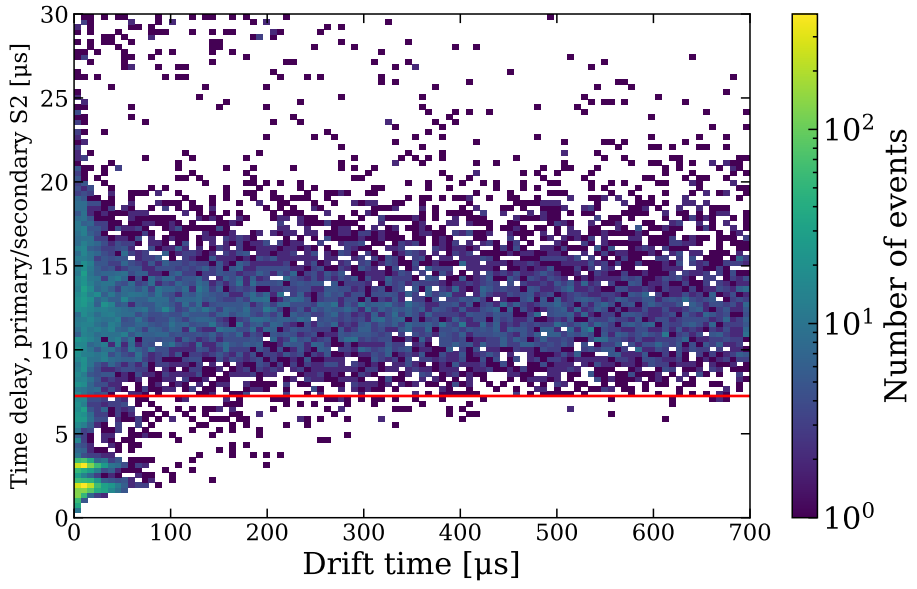

Figure B.17.: *Simple selection for ^{131m}Xe . The threshold used is identical to the one for ^{37}Ar . Below the threshold only a few events are selected for AP correction.*

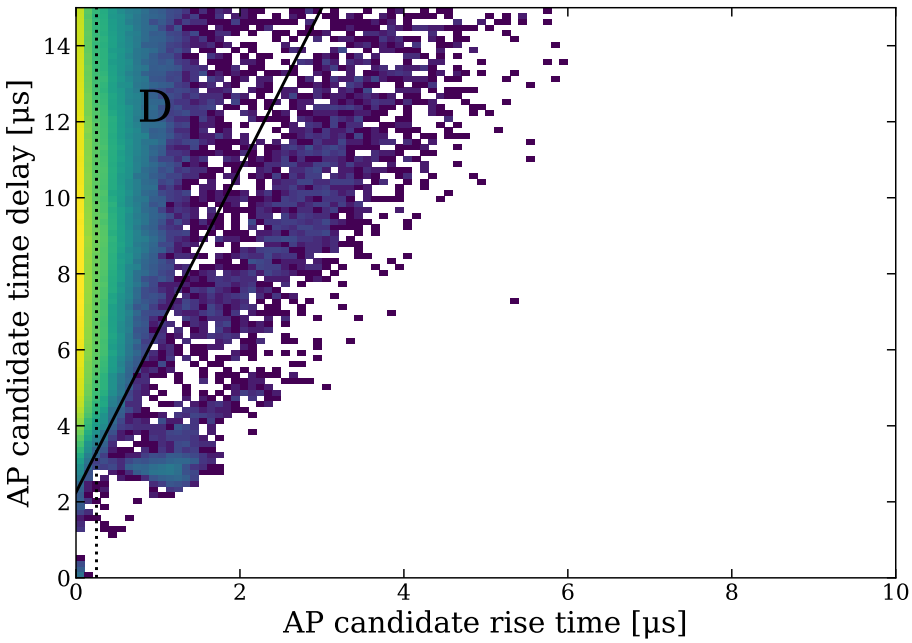

Figure B.18.: *Distribution of the second AP candidate of ^{37}Ar . The amount of peaks is already drastically reduced.*

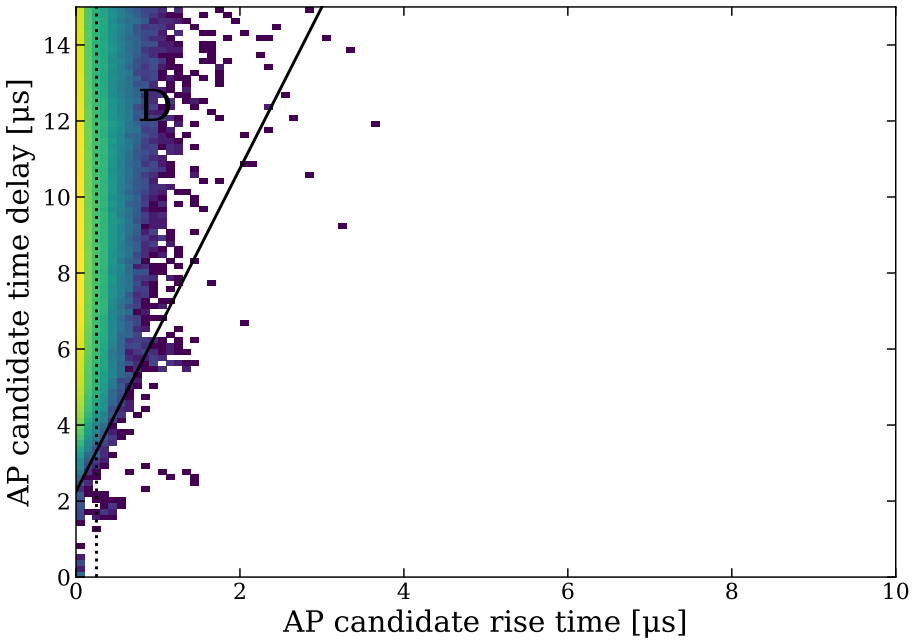

Figure B.19.: *Distribution of the third AP candidate of ^{37}Ar . Besides the accidental classified peaks with unusual rise times. no further peaks are present.*

B.5. XENON1T 2D-Fit plots

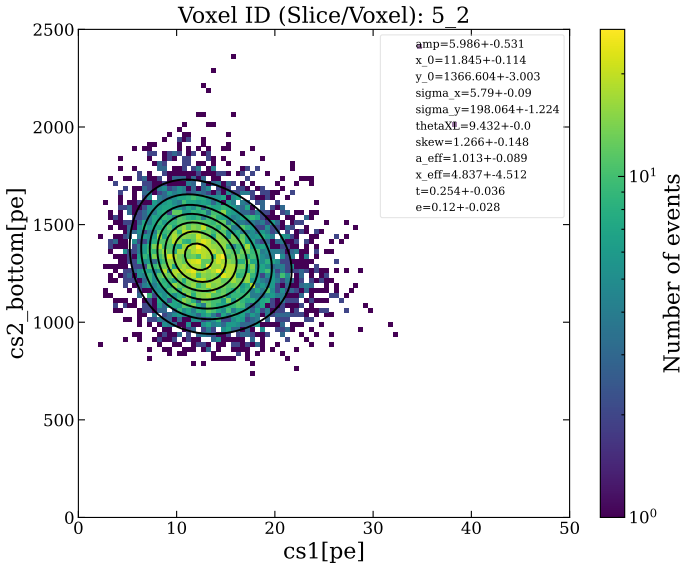

(a) *2D-Skew Gaussian fit to voxel data with free threshold parameters.*

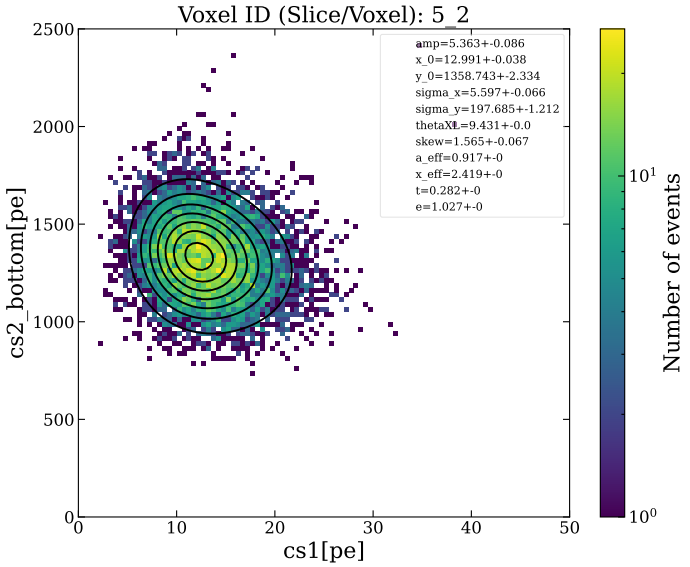

(b) *2D-Skew Gaussian fit to voxel data with fixed threshold parameters.*

Figure B.20.: *The two 2D-Skew Gauss fit examples show the same data with two different fits, one time with free threshold parameters (Fig. a) and one time with fixed threshold parameters (Fig. b). The contours indicate a good shape of both the fits, the fit parameters however reveal some unlikely values. Most prominently a detection efficiency of larger then 100 % in case of the free threshold fit. But also the cS1 results differ by more than 1 pe, a result of compensating the threshold position which is at a too high pe value.*

B.6. Additional plots: SiPM Introduction

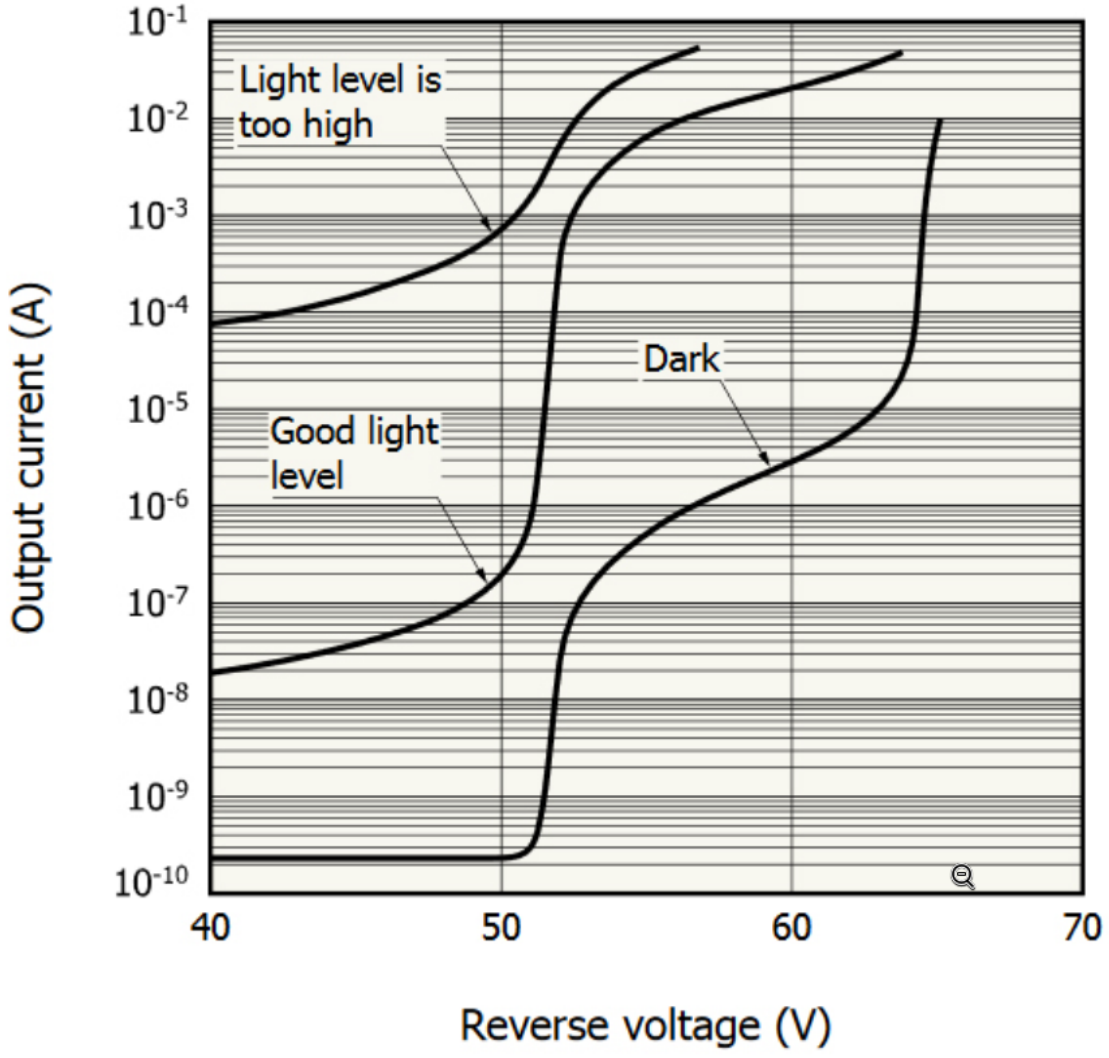

Figure B.21.: *Example of an I-V curve. The turning point in the curves can easily be determined and have a constant offset to the breakdown voltage. This can be used to characterize a large amount of SiPMs, as only a small voltage region needs to be scanned to determine a value for the breakdown voltages. Figure taken from [114].*

B.7. Additional plots: SiPM Setup

S10943-3186(X) TENTATIVE SPECIFICATIONS

■Specifications (Ta=25 deg C)

Parameter	Symbol	Condition	min	typ	max	Unit
Spectral response Range			--	130～900	--	nm
Peak sensitivity wavelength			--	430	--	nm
Pixel pitch			--	50	--	um
Effective photosensitive area /channel		Device Type A	--	5.95 x 5.85	--	mm^2
		Type B	--	5.70 x 5.60	--	mm^2
Recommended operating voltage range *2	Vop	at M=1.25×10^6	60	70	80	V
Vop variation between channels			--	0.3	0.5	V
Temperature coefficient of reverse voltage			--	60	--	mV/deg C
Detection efficiency *3	PDE	VR=V(M=1.25×10^6) λ=175nm, in a vacuum	20	25	--	%
Dark count/channel *4	ID	VR=Vop				
		Device Type A	--	7.0	21.0	MHz
		Type B	--	6.4	19.2	MHz
Terminal capacitance/channel	Ct	VR=V(M=1.25×10^6)				
		Device Type A	--	1200	--	pF
		Type B	--	1100	--	pF
Gain at Vop	M	VR=Vop	--	1.25×10^6	--	--

*2 Refer to the attached data for recommended operation voltage of each product.

*3 The detection efficiency acquired by photocurrent is affected by optical cross talks and after pulses.

*4 The dark current is attached to each product.

Figure B.22.: *Operational specifications and expected performance parameter of the Hamamatsu model S10943 MPPC. Information provided by Hamamatsu alongside the test samples.*

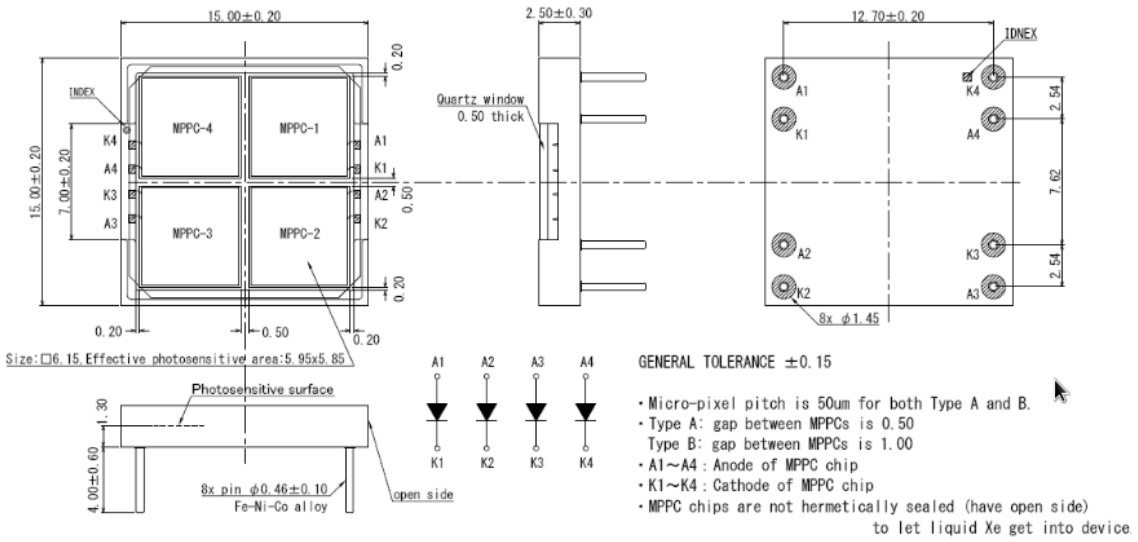

Figure B.23.: *Dimensional drawing of the Hamamatsu model S10943 MPPC, containing 4 separate SiPMs in one ceramic housing, protected by a quartz window to preserve UV-sensitivity. Drawing provided by Hamamatsu alongside the test samples.*

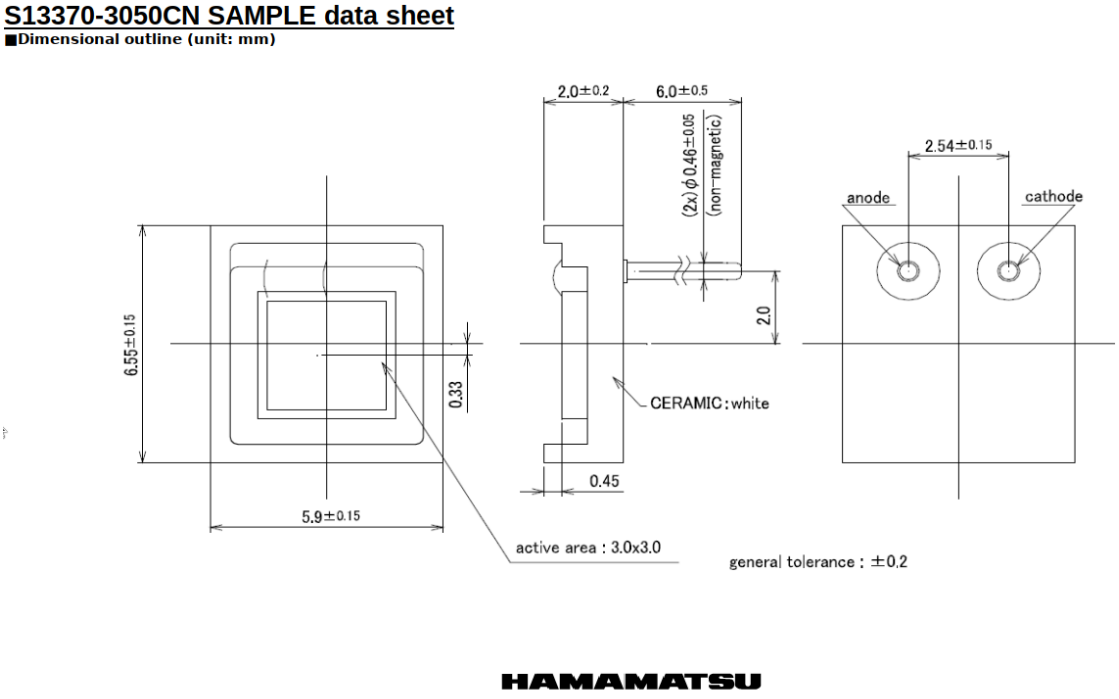

Figure B.24.: *Dimensional drawing of the Hamamatsu model S13770 MPPC, containing one SiPM in one ceramic housing. In this model no protective quartz window is present. Extract from the Hamamatsu datasheet [131].*

S13370 series

S13370 series are basic VUV-MPPCs with 4th generation (VUV4).

Sensitivity for 128nm (Liq. Ar)	Sensitivity for 178nm (Liq. Xe)	Low RI
✓	✓	

Structure

Parameters	S13370				unit
	-3050CN	-3075CN	-6050CN	-6075CN	
Effective photosensitive area	3.0 x 3.0		6.0 x 6.0		mm^2
Pixel pitch	50	75	50	75	μm
Number of pixels / channels	3600	1600	14400	6400	-
Geometrical fill factor	60	70	60	70	%
Package	Ceramic				-
Window	Unsealed				-

Absolute maximum ratings

Parameters	Symbol	S13370 series	unit
Operating temperature*1	Topr	up to +60	℃
Storage temperature*1	Tstg	-20 to +80	℃
soldering condition	Tsol	350 ℃ or less, once, within 3 seconds	-

*1: No condensation

Electrical and optical characteristics
(Typ. Ta=25 deg C, Over voltage=4.0V Unless otherwise noted)

Parameters	Symbol	S13370				unit
		-3050CN	-3075CN	-6050CN	-6075CN	
Spectral response range	λ	120 to 900				nm
peak sensitivity wavelength	λp	500				nm
Photon detection efficiency at λp*2	PDE	35	40	35	40	%
Break down Voltage	VBR	53 +/-5				V
Recommended operating voltage *3	Vop	VBR + 4				V
Dark count typ.		1.0		4.0		Mcps
Dark count max.		3.0		12.0		Mcps
Crosstalk probability	-	3	5	3	5	%
Terminal capacitance	Ct	320		1280		pF
Gain	M	$2.55x10^6$	$5.8x10^6$	$2.55x10^6$	$5.8x10^6$	-
Temperature coefficient of recommended reverse voltage	ΔTVop	54 (around the room temperature)				mV/℃

*2: Photon detection efficiency does not include crosstalk and after pulse.
*3: Refer to the data attached for each product.

Figure B.25.: *Operational specifications and expected performance parameter of the Hamamatsu model S13370 MPPC. Extract from the Hamamatsu datasheet [131].*

SiPM test setup sensor configuration

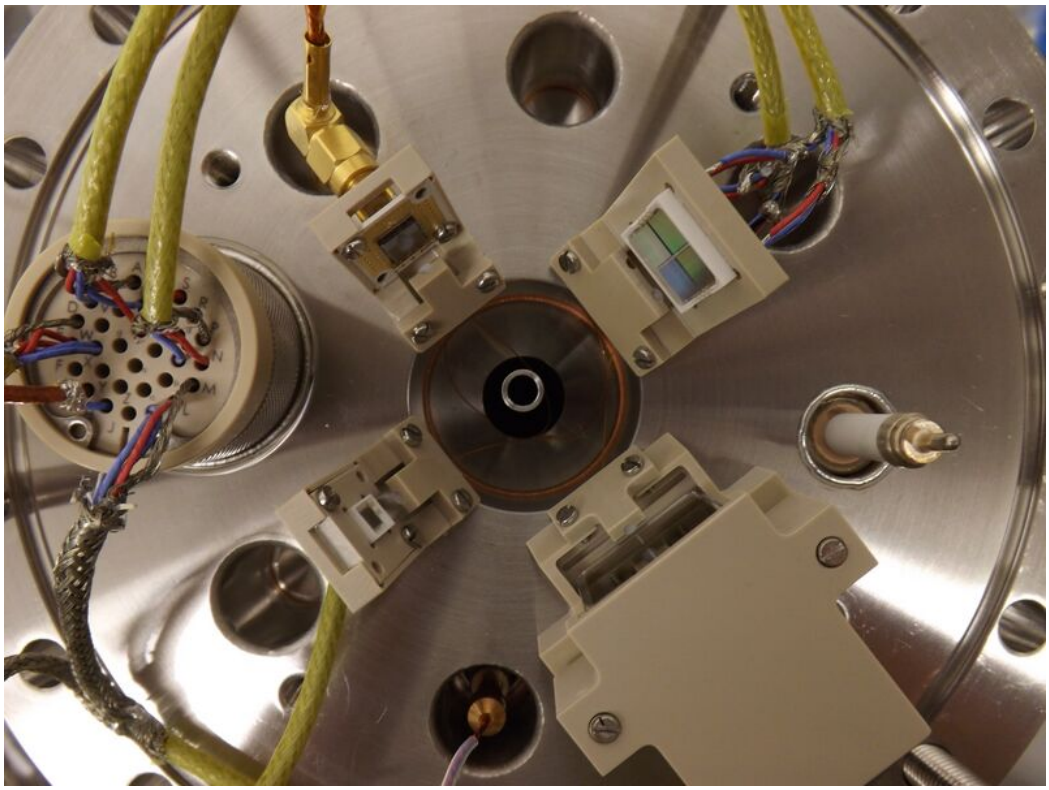

Figure B.26.: *Sensor configuration in the test setup during the measurement runs. In the upper right corner is the Hamamatsu model S10942, then (clockwise) the 1" PMT R8520 from Hamamatsu, the Hamamatsu model S13370 MPPC and in the upper left the sample from KETEK. As can be seen the signal from the KETEK is connected via a SMA connector, the cables for the Hamamtsu MPPCs are soldered to pins, where the MPPCs are plugged in. In the center the drain pipe for the xenon is visble. Also the fibers can be seen which lead to a small, hollow PTFE cylinder placed in front of every sensor, to provide a diffuse illumination for calibration.*

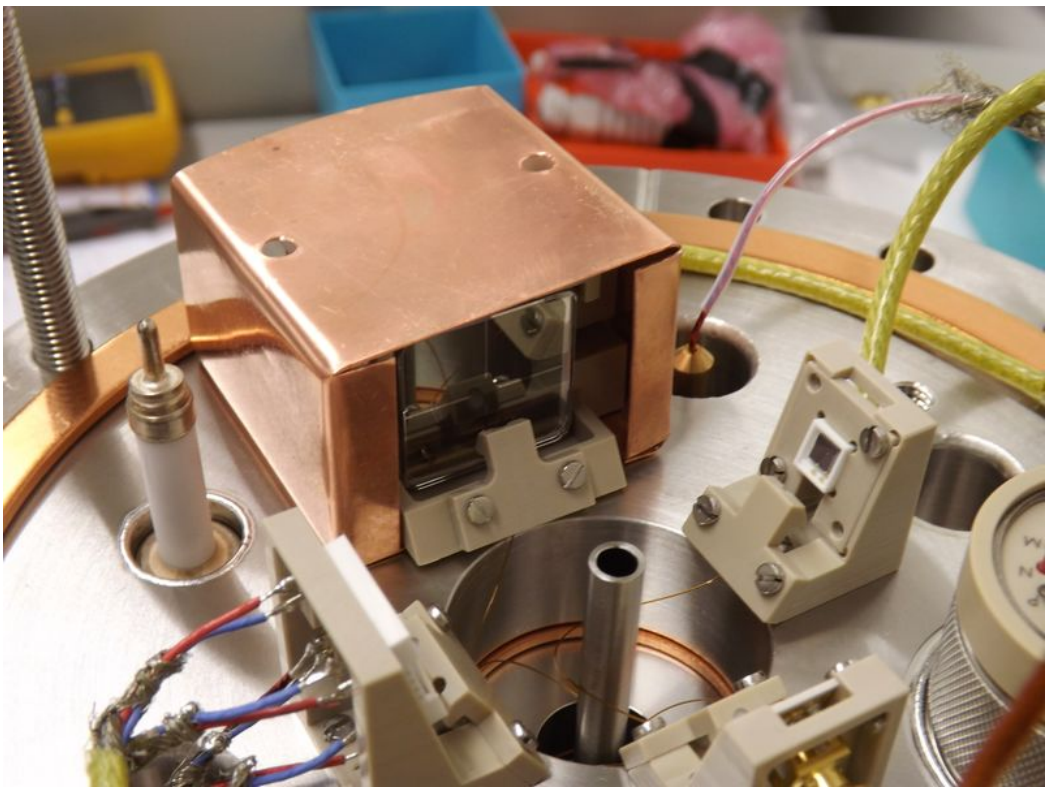

Figure B.27.: *The setup with the improved copper-sheet shielding around the PMT. This was necessary as the PMT induced massive baseline noise into the SiPM lines when detecting a signal.*

SiPM Amplifier

SiPM HV Filter	
$R1_{HV}$	$1\,k\Omega$
$R2_{HV}$	$1\,k\Omega$
C_{HV}	1 nF
Signal decoupling	
R_{OPT}	$100\,\Omega$
R_{IN}	$300\,\Omega$
A	open
B	open
C	$1\,\mu$F
Amplification	
R_{OUT}	$50\,\Omega$
R_{Gain}	$50\,\Omega$
$R_{Feedback}$	$1\,k\Omega$
AD8009 Power Filter	
C_1	$10\,\mu$F
C_2	100 nF
C_3	$10\,\mu$F
C_4	100 nF

Table B.1.: *Component values used on the SiPM amplifier boards, as shown in Figures 7.9 and 7.10, during the SiPM measurements. The board configuration was the same for all three SiPMs tested.*

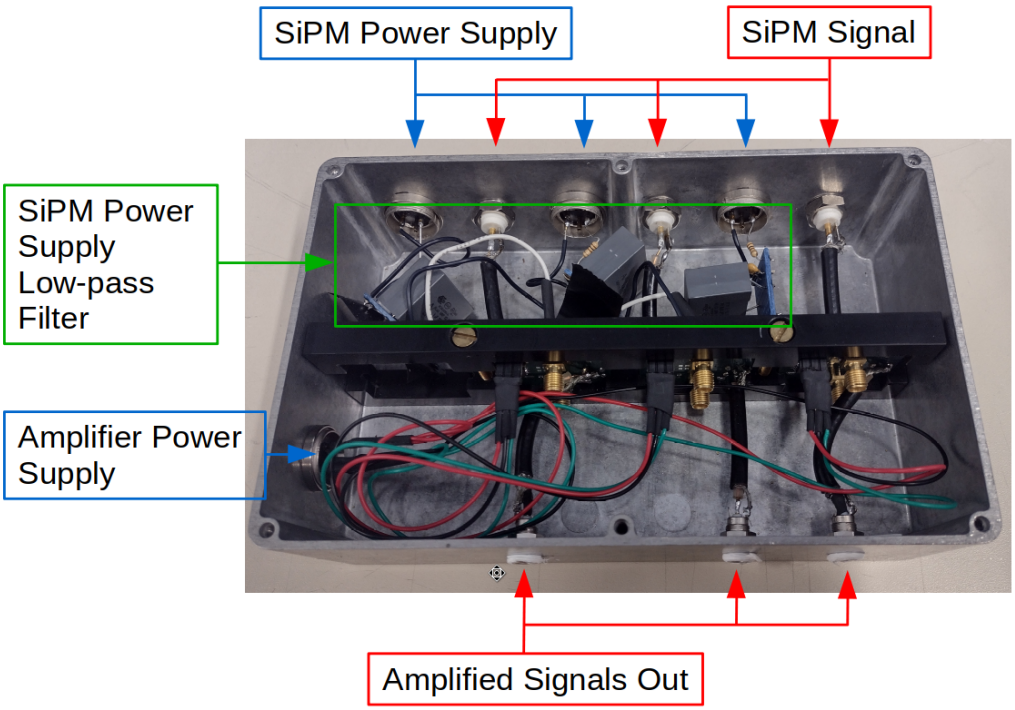

Figure B.28.: *Picture of the amplifier setup used during the SiPM data taking. The amplifier boards are mounted vertically between the two plastic bars in the middle of the box. In this picture also the additional low-pass noise filters for the SiPM-HV are seen to reduce the ripple of the CAEN Power supply (Model A 1510, 12 Channel). All cable feed-throughs are floating, either*

B.8. Code snippets for 2D fits

B.8.1. Likelihood class for voxel fits

This is a short description of the class that builds the Log-Likelihood function used to fit the two-dimensional S1-S2-dataspace. In general, this class offers the possibility to build a Likelihood function out of a variety of so-called `fitmodels`. The `fitmodels` include definitions for standard 2D-Gaussians and 2D-Skewed Gaussians, both with a threshold function included and without. This `fitmodels` include the model in standard form, as well as in a logarithmic form, as both are needed later. `xydata` contains the binning information in the form of a 2 dimensional mesh grid. `para_dict` is a dictionary that will contain all the parameter values from the fit. Each parameter name consists of its name and the voxel ID. `fitVarParas` and `fitGlobalParas` are lists of the parameter names that are variable (can be changed by the minimizer) and that are global, e.g. shared between all voxels, respectively. `func_code` contains a list of all parameters in the function. In a single voxel fit case, this is identical to the parameters of the used fit model. It becomes important in a global fit, as the likelihood function is built from multiple single voxel Likelihoods, so that the global Likelihood can contain up to several hundred individual parameters.

```
class global_LogL_cl:
    def __init__(self, fitmodel, xdata, para_dict,
                 fitVarParas, fitGlobalParas, func_code):
        self.fitmodel       = fitmodel
        self.xydata         = xydata
        self.para_dict      = para_dict
        self.fitVarParas    = fitVarParas
        self.fitGlobalParas = fitGlobalParas
        self.func_code      = iminuit.util.make_func_code(func_code)
        self.errordef = 1
```

In the following method the actual cost function, which will be minimized, is built, following the explanation given in Section 4.7. This cost function is created for one voxel and in the case of local fits (where each voxel is fitted for itself), this is the function that is returned to the minimizer for the fit.

```
    def logL_single(self, zdata, *paras):

        n_i = zdata
        n_i = np.array(n_i)

        v_i_exp = self.fitmodel[0](self.xydata, *paras)
        v_i_log = self.fitmodel[1](self.xydata, *paras)

        v_i = np.array(v_i_exp)
```

```
        lh_array = np.zeros(len(n_i))

        # use log function (also taking empty bins into
        #                   account with case selection):
        lh_array = np.where(n_i > 0, n_i*(np.log(n_i)-v_i_log)
                            + v_i_exp - n_i, lh_array)
        lh_array = np.where(n_i == 0,  v_i - n_i, lh_array)

        log_L = np.sum(lh_array)

        return 2*log_L
```

B.8.2. Update of Likelihood class to allow global fitting

Instead of just returning the local cost-function, this method builds a global cost function out of the individual voxels cost function. When the class is called for a global fit, the list of fit parameters and the data in each voxel are handed over in form of a dictionary. The corresponding parameters and data for each voxel are also assigned to the proper cost function. In the end, the global cost function (the sum of all individual cost functions) is returned to be minimized.

```
    def __call__(self, *paras):
        global_log_cost = 0

        for vox in range(len(self.para_dict['voxel_id'])):
            voxel_paras = ()

            # select voxel data:
            data = self.para_dict['data' + '_'
                   + self.para_dict['voxel_id'][vox]]

            # select voxel parameters from global parameter
            # tuple:
            for i in range(len(self.fitVarParas)):
                voxel_paras += (paras[vox * (len(paras)
                                - len(self.fitGlobalParas))//
                                len(self.para_dict['voxel_id']) + i],)
            for j in range(len(self.fitGlobalParas)):
                voxel_paras += (paras[len(paras)
                                - len(self.fitGlobalParas) + j],)

            # build global logL cost function
            global_log_cost += self.logL_single(data, *voxel_paras)
        return global_log_cost
```

The way the function is called determines if it is doing a global or local fit. In the case of a global fit, it is called with a dictionary which contains multiple sets of parameters and data, which is used to build the global cost function.

In the local fit case, the function is called with a dictionary, which contains only one set of parameters and one data set. The length of the global fit parameter list is zero and the global cost function is identical to the local one. In this case the program calling this class is looping over the voxels, creating individual cost functions for each voxel, which are minimized sequentially.

In the global fit case, only one fit is done, which includes one cost function and works with all voxel parameters and on all voxel data simultaneously. This fit takes some time to be minimized. For example, fitting globally with a TPC division into 2 slices containing 9 voxels each, so in total 18 voxels, with 7 parameters for the 2D Gauss in each voxel and 4 global free parameters for the threshold, it has to handle 130 parameters. With these conditions this fit has a runtime of about 45 min.

B.9. ^{37}Ar S1-cS2 voxel-fit results

The following table contains the results of the 2D fit using the skewed Gaussian function, including a threshold but with fixed parameters as given in Table 4.4. Additionally, the correction factors for the S1 are given. These values are used to calculate the photon and electron yield of ^{37}Ar. It is noticeable that the rotation angle Θ is very stable, varying only by one per mille across the TPC, whereas the skewness parameter varies by up to 50 %.

Slice	Voxel	S1	$cS2_b$	σ_{S1}	σ_{cS2}	Θ	α	$S1_{cor}$
0	0	10.416 ±0.062	1247.525 ±2.189	5.76 ±0.088	124.955 ±1.11	9.439 ±0.001	1.73 ±0.117	1.249
0	1	10.4 ±0.062	1247.364 ±2.152	5.682 ±0.095	125.873 ±1.075	9.438 ±0.001	1.566 ±0.123	1.262
0	2	10.373 ±0.061	1254.425 ±2.25	5.767 ±0.093	127.305 ±1.11	9.436 ±0.001	1.753 ±0.128	1.274
0	3	10.357 ±0.066	1256.907 ±2.492	6.298 ±0.088	130.442 ±1.249	9.439 ±0.001	2.431 ±0.163	1.292
0	4	10.245 ±0.063	1258.362 ±2.155	5.777 ±0.094	127.318 ±1.224	9.438 ±0.001	1.813 ±0.142	1.285
0	5	10.535 ±0.063	1251.886 ±2.258	5.677 ±0.096	127.829 ±1.131	9.437 ±0.001	1.57 ±0.117	1.263
0	6	10.461 ±0.065	1235.19 ±2.333	5.875 ±0.095	127.854 ±1.152	9.436 ±0.001	1.743 ±0.125	1.254
0	7	10.561 ±0.058	1237.198 ±2.259	5.937 ±0.086	127.427 ±1.128	9.438 ±0.001	2.089 ±0.136	1.247

(To be continued)

Slice	Voxel	S1	$cS2_b$	σ_{S1}	σ_{cS2}	Θ	α	$S1_{cor}$
0	8	10.581 ±0.057	1235.218 ±2.148	5.825 ±0.085	124.922 ±1.074	9.437 ±0.001	1.901 ±0.122	1.25
0	9	10.368 ±0.064	1244.691 ±2.588	5.864 ±0.094	135.996 ±1.285	9.437 ±0.001	1.953 ±0.144	1.262
0	10	10.382 ±0.06	1247.681 ±2.402	5.94 ±0.088	134.944 ±1.179	9.436 ±0.001	1.966 ±0.132	1.274
0	11	10.408 ±0.058	1242.427 ±2.403	5.856 ±0.088	131.941 ±1.166	9.434 ±0.001	2.027 ±0.135	1.278
0	12	10.191 ±0.062	1251.162 ±2.52	5.706 ±0.09	133.61 ±1.244	9.436 ±0.001	1.919 ±0.132	1.299
0	13	10.06 ±0.06	1234.111 ±2.347	5.858 ±0.086	134.432 ±1.145	9.436 ±0.001	1.921 ±0.133	1.298
0	14	10.045 ±0.07	1234.921 ±2.625	5.461 ±0.11	134.568 ±1.292	9.435 ±0.001	1.473 ±0.138	1.307
0	15	10.223 ±0.062	1247.3 ±2.513	5.87 ±0.088	138.491 ±1.239	9.436 ±0.001	1.934 ±0.13	1.3
0	16	10.078 ±0.074	1247.827 ±2.591	5.893 ±0.106	135.652 ±1.244	9.433 ±0.001	1.616 ±0.135	1.294
0	17	10.206 ±0.065	1248.42 ±2.491	5.826 ±0.091	134.725 ±1.228	9.436 ±0.001	1.726 ±0.124	1.268
0	18	10.568 ±0.062	1234.091 ±2.362	5.668 ±0.102	131.79 ±1.16	9.433 ±0.001	1.575 ±0.123	1.26
0	19	10.474 ±0.059	1224.83 ±2.381	5.801 ±0.088	133.797 ±1.173	9.435 ±0.001	1.861 ±0.121	1.253
0	20	10.439 ±0.065	1224.761 ±2.563	5.862 ±0.094	137.494 ±1.272	9.436 ±0.001	1.831 ±0.131	1.253
0	21	10.446 ±0.059	1223.766 ±2.305	5.841 ±0.092	135.284 ±1.131	9.435 ±0.001	1.79 ±0.132	1.24
0	22	10.599 ±0.056	1227.148 ±2.379	6.186 ±0.083	133.263 ±1.214	9.437 ±0.001	2.457 ±0.15	1.252
0	23	10.596 ±0.058	1227.586 ±2.276	6.015 ±0.087	132.943 ±1.109	9.435 ±0.001	1.972 ±0.128	1.251
0	24	10.438 ±0.058	1243.397 ±2.327	6.012 ±0.084	131.156 ±1.124	9.435 ±0.001	2.114 ±0.131	1.26
1	0	11.693 ±0.06	1282.416 ±2.492	6.167 ±0.094	140.694 ±1.253	9.435 ±0.001	1.892 ±0.116	1.136
1	1	11.567 ±0.059	1285.689 ±2.405	6.096 ±0.092	144.596 ±1.224	9.437 ±0.001	1.753 ±0.112	1.149
1	2	11.406 ±0.063	1284.755 ±2.529	6.018 ±0.104	146.75 ±1.272	9.436 ±0.001	1.569 ±0.119	1.159
1	3	11.437 ±0.066	1279.06 ±2.644	6.094 ±0.104	141.705 ±1.335	9.436 ±0.001	1.752 ±0.126	1.165

(To be continued)

Slice	Voxel	S1	$cS2_b$	σ_{S1}	σ_{cS2}	Θ	α	$S1_{cor}$
1	4	11.542 ±0.062	1280.797 ±2.415	6.073 ±0.097	142.725 ±1.227	9.436 ±0.001	1.708 ±0.112	1.154
1	5	11.567 ±0.061	1284.791 ±2.571	5.767 ±0.102	143.977 ±1.308	9.436 ±0.001	1.579 ±0.116	1.142
1	6	11.523 ±0.065	1275.956 ±2.545	6.366 ±0.103	141.473 ±1.261	9.435 ±0.001	1.847 ±0.13	1.135
1	7	11.553 ±0.064	1277.244 ±2.599	6.242 ±0.102	144.765 ±1.311	9.437 ±0.001	1.816 ±0.128	1.132
1	8	11.548 ±0.059	1280.822 ±2.409	6.226 ±0.088	144.496 ±1.221	9.436 ±0.001	1.932 ±0.11	1.139
1	9	11.532 ±0.063	1278.625 ±2.7	6.243 ±0.094	146.998 ±1.368	9.437 ±0.001	2.031 ±0.127	1.158
1	10	11.317 ±0.061	1271.839 ±2.549	5.979 ±0.101	147.575 ±1.277	9.435 ±0.001	1.648 ±0.121	1.171
1	11	11.176 ±0.064	1269.437 ±2.573	5.901 ±0.113	144.27 ±1.272	9.434 ±0.001	1.546 ±0.132	1.171
1	12	11.289 ±0.065	1273.421 ±2.75	6.006 ±0.103	153.648 ±1.381	9.434 ±0.001	1.611 ±0.117	1.171
1	13	11.138 ±0.064	1269.95 ±2.669	6.154 ±0.101	148.679 ±1.329	9.436 ±0.001	1.822 ±0.134	1.176
1	14	11.053 ±0.07	1257.946 ±2.922	5.986 ±0.107	149.269 ±1.464	9.437 ±0.001	1.722 ±0.133	1.186
1	15	11.342 ±0.062	1270.32 ±2.573	6.282 ±0.094	148.226 ±1.288	9.436 ±0.001	1.865 ±0.118	1.164
1	16	11.417 ±0.068	1290.056 ±3.045	6.164 ±0.103	150.507 ±1.554	9.437 ±0.001	2.115 ±0.152	1.164
1	17	11.469 ±0.063	1275.141 ±2.766	6.024 ±0.109	152.531 ±1.378	9.435 ±0.001	1.71 ±0.136	1.146
1	18	11.525 ±0.062	1272.477 ±2.712	6.173 ±0.098	151.671 ±1.361	9.435 ±0.001	1.832 ±0.12	1.14
1	19	11.462 ±0.062	1258.742 ±2.575	5.899 ±0.102	148.43 ±1.304	9.436 ±0.001	1.545 ±0.113	1.147
1	20	11.586 ±0.063	1244.485 ±2.667	5.944 ±0.108	151.787 ±1.339	9.433 ±0.001	1.527 ±0.116	1.143
1	21	11.544 ±0.058	1256.827 ±2.537	5.838 ±0.096	149.54 ±1.288	9.435 ±0.001	1.629 ±0.112	1.13
1	22	11.413 ±0.06	1255.44 ±2.63	5.841 ±0.102	151.845 ±1.322	9.434 ±0.001	1.554 ±0.113	1.141
1	23	11.618 ±0.057	1271.562 ±2.498	6.084 ±0.089	150.994 ±1.277	9.437 ±0.001	1.839 ±0.113	1.14
1	24	11.468 ±0.062	1275.202 ±2.581	6.068 ±0.104	149.196 ±1.272	9.435 ±0.001	1.654 ±0.126	1.15

(To be continued)

Slice	Voxel	S1	$cS2_b$	σ_{S1}	σ_{cS2}	Θ	α	$S1_{cor}$
2	0	12.826 ±0.061	1312.882 ±2.701	6.503 ±0.096	158.094 ±1.393	9.436 ±0.001	1.896 ±0.109	1.02
2	1	12.751 ±0.057	1305.994 ±2.535	6.429 ±0.096	155.236 ±1.287	9.436 ±0.001	1.895 ±0.113	1.038
2	2	12.54 ±0.06	1307.312 ±2.677	6.367 ±0.088	156.3 ±1.359	9.437 ±0.001	1.784 ±0.098	1.048
2	3	12.726 ±0.066	1296.964 ±2.74	6.205 ±0.116	154.615 ±1.404	9.434 ±0.001	1.436 ±0.106	1.043
2	4	12.697 ±0.062	1314.642 ±2.803	6.403 ±0.098	160.557 ±1.451	9.437 ±0.001	1.893 ±0.114	1.036
2	5	12.768 ±0.063	1305.46 ±2.764	6.413 ±0.101	158.508 ±1.423	9.436 ±0.001	1.754 ±0.108	1.024
2	6	12.822 ±0.068	1269.738 ±2.602	4.886 ±0.051	156.132 ±1.325	9.431 ±0.0	0.002 ±2.624	1.023
2	7	12.798 ±0.06	1286.892 ±2.685	6.522 ±0.101	160.202 ±1.358	9.434 ±0.001	1.8 ±0.109	1.023
2	8	12.706 ±0.058	1298.865 ±2.532	6.341 ±0.1	158.062 ±1.286	9.434 ±0.001	1.647 ±0.102	1.029
2	9	12.358 ±0.067	1298.984 ±2.956	6.613 ±0.104	158.149 ±1.501	9.436 ±0.001	2.038 ±0.132	1.059
2	10	12.397 ±0.062	1298.159 ±2.724	6.25 ±0.102	162.274 ±1.393	9.434 ±0.001	1.565 ±0.101	1.057
2	11	12.358 ±0.061	1299.129 ±2.835	6.412 ±0.096	164.963 ±1.449	9.436 ±0.001	1.897 ±0.114	1.063
2	12	12.421 ±0.065	1294.266 ±2.79	6.228 ±0.107	160.743 ±1.382	9.434 ±0.001	1.673 ±0.109	1.063
2	13	12.26 ±0.065	1290.3 ±2.923	5.939 ±0.111	160.742 ±1.442	9.434 ±0.001	1.406 ±0.11	1.061
2	14	12.321 ±0.07	1282.592 ±3.063	6.316 ±0.112	160.904 ±1.562	9.434 ±0.001	1.645 ±0.114	1.066
2	15	12.371 ±0.061	1287.199 ±2.73	6.278 ±0.096	161.12 ±1.412	9.436 ±0.001	1.747 ±0.107	1.059
2	16	12.553 ±0.07	1312.69 ±3.281	6.16 ±0.117	168.071 ±1.688	9.435 ±0.001	1.588 ±0.119	1.045
2	17	12.533 ±0.062	1299.952 ±2.878	6.164 ±0.103	164.698 ±1.476	9.435 ±0.001	1.673 ±0.109	1.039
2	18	12.689 ±0.064	1286.847 ±2.833	6.554 ±0.108	157.534 ±1.418	9.434 ±0.001	1.855 ±0.122	1.033
2	19	12.671 ±0.063	1284.093 ±2.822	6.646 ±0.095	163.509 ±1.466	9.436 ±0.001	1.985 ±0.109	1.035
2	20	12.685 ±0.064	1273.112 ±2.848	6.11 ±0.117	164.795 ±1.45	9.434 ±0.001	1.366 ±0.107	1.036

(To be continued)

Slice	Voxel	S1	$cS2_b$	σ_{S1}	σ_{cS2}	Θ	α	$S1_{cor}$
2	21	12.593 ±0.056	1286.793 ±2.737	6.524 ±0.093	164.089 ±1.368	9.436 ±0.001	1.933 ±0.112	1.028
2	22	12.607 ±0.063	1283.917 ±2.841	6.149 ±0.105	160.948 ±1.467	9.436 ±0.001	1.615 ±0.11	1.036
2	23	12.714 ±0.059	1288.37 ±2.681	6.262 ±0.095	163.63 ±1.381	9.435 ±0.001	1.68 ±0.098	1.04
2	24	12.742 ±0.056	1289.714 ±2.77	6.13 ±0.096	162.834 ±1.406	9.433 ±0.001	1.822 ±0.108	1.046
3	0	14.358 ±0.065	1332.352 ±2.892	6.8 ±0.101	166.587 ±1.522	9.437 ±0.001	1.886 ±0.101	0.913
3	1	13.991 ±0.061	1320.016 ±2.77	6.553 ±0.117	170.126 ±1.417	9.434 ±0.001	1.519 ±0.107	0.943
3	2	13.981 ±0.063	1316.408 ±2.821	6.657 ±0.109	169.552 ±1.451	9.434 ±0.001	1.627 ±0.099	0.95
3	3	13.996 ±0.072	1318.77 ±3.051	6.998 ±0.121	164.353 ±1.558	9.435 ±0.001	1.763 ±0.115	0.946
3	4	14.036 ±0.064	1326.834 ±2.851	6.638 ±0.112	170.061 ±1.474	9.435 ±0.001	1.59 ±0.104	0.938
3	5	14.099 ±0.064	1322.883 ±2.88	6.542 ±0.116	170.003 ±1.487	9.433 ±0.001	1.522 ±0.101	0.925
3	6	14.316 ±0.061	1320.984 ±2.846	6.564 ±0.106	172.583 ±1.474	9.434 ±0.001	1.666 ±0.098	0.919
3	7	14.251 ±0.061	1312.881 ±2.718	6.478 ±0.109	167.43 ±1.414	9.434 ±0.001	1.489 ±0.092	0.923
3	8	14.189 ±0.061	1321.773 ±2.667	6.582 ±0.102	166.211 ±1.393	9.436 ±0.001	1.6 ±0.092	0.933
3	9	13.788 ±0.064	1314.304 ±2.988	6.486 ±0.112	169.123 ±1.533	9.433 ±0.001	1.666 ±0.107	0.967
3	10	13.665 ±0.061	1317.963 ±2.879	6.676 ±0.107	176.755 ±1.472	9.434 ±0.001	1.687 ±0.106	0.972
3	11	13.713 ±0.06	1316.339 ±2.885	6.34 ±0.111	174.834 ±1.484	9.433 ±0.001	1.521 ±0.101	0.969
3	12	13.612 ±0.063	1310.655 ±2.968	6.214 ±0.122	172.402 ±1.519	9.433 ±0.001	1.414 ±0.11	0.975
3	13	13.365 ±0.069	1314.481 ±3.205	6.678 ±0.116	172.256 ±1.641	9.435 ±0.001	1.752 ±0.118	0.969
3	14	13.737 ±0.071	1306.245 ±3.407	6.636 ±0.116	177.737 ±1.764	9.435 ±0.001	1.771 ±0.115	0.976
3	15	13.624 ±0.061	1304.971 ±2.821	6.358 ±0.112	172.232 ±1.454	9.433 ±0.001	1.469 ±0.099	0.97
3	16	13.74 ±0.07	1321.943 ±3.409	6.217 ±0.128	179.197 ±1.767	9.433 ±0.001	1.426 ±0.112	0.957

(To be continued)

Slice	Voxel	S1	$cS2_b$	σ_{S1}	σ_{cS2}	Θ	α	$S1_{cor}$
3	17	13.829 ±0.066	1323.283 ±3.048	6.484 ±0.116	173.807 ±1.573	9.434 ±0.001	1.551 ±0.106	0.943
3	18	13.994 ±0.063	1310.893 ±2.981	6.622 ±0.114	172.85 ±1.526	9.434 ±0.001	1.68 ±0.11	0.936
3	19	14.099 ±0.062	1297.875 ±2.888	6.632 ±0.104	173.501 ±1.495	9.434 ±0.001	1.699 ±0.098	0.939
3	20	14.026 ±0.061	1292.416 ±2.869	6.613 ±0.109	174.734 ±1.471	9.434 ±0.001	1.655 ±0.103	0.939
3	21	14.145 ±0.063	1305.943 ±2.797	6.808 ±0.115	171.833 ±1.434	9.434 ±0.001	1.57 ±0.102	0.935
3	22	13.739 ±0.066	1314.09 ±3.089	6.478 ±0.114	179.005 ±1.601	9.435 ±0.001	1.506 ±0.104	0.936
3	23	14.025 ±0.059	1312.112 ±2.8	6.664 ±0.107	176.932 ±1.434	9.433 ±0.001	1.632 ±0.1	0.946
3	24	13.804 ±0.063	1316.101 ±2.987	6.707 ±0.106	175.049 ±1.533	9.435 ±0.001	1.804 ±0.109	0.955
4	0	15.935 ±0.068	1357.843 ±3.226	7.111 ±0.109	188.217 ±1.699	9.436 ±0.001	1.787 ±0.096	0.819
4	1	15.672 ±0.064	1349.437 ±2.929	7.222 ±0.112	181.204 ±1.514	9.434 ±0.001	1.74 ±0.097	0.867
4	2	15.468 ±0.068	1348.63 ±3.137	7.118 ±0.12	182.503 ±1.622	9.434 ±0.001	1.716 ±0.106	0.877
4	3	15.428 ±0.073	1346.735 ±3.426	6.946 ±0.126	182.113 ±1.783	9.435 ±0.001	1.695 ±0.111	0.869
4	4	15.553 ±0.068	1345.955 ±3.169	7.105 ±0.121	182.734 ±1.637	9.434 ±0.001	1.727 ±0.108	0.861
4	5	15.866 ±0.068	1355.977 ±3.206	6.927 ±0.123	186.629 ±1.676	9.435 ±0.001	1.549 ±0.102	0.839
4	6	16.149 ±0.068	1340.359 ±3.102	7.051 ±0.12	183.324 ±1.623	9.435 ±0.001	1.606 ±0.097	0.829
4	7	16.263 ±0.065	1331.099 ±3.033	6.925 ±0.125	187.879 ±1.585	9.433 ±0.001	1.449 ±0.095	0.833
4	8	15.891 ±0.063	1345.281 ±2.933	7.116 ±0.108	182.271 ±1.53	9.435 ±0.001	1.733 ±0.094	0.857
4	9	14.863 ±0.066	1343.931 ±3.403	6.814 ±0.11	191.915 ±1.769	9.434 ±0.001	1.835 ±0.106	0.909
4	10	14.933 ±0.058	1344.223 ±2.874	7.056 ±0.11	184.42 ±1.494	9.434 ±0.001	1.751 ±0.1	0.903
4	11	14.841 ±0.066	1344.502 ±3.183	6.861 ±0.117	186.011 ±1.648	9.435 ±0.001	1.695 ±0.109	0.914
4	12	14.731 ±0.066	1331.906 ±3.227	6.795 ±0.11	183.717 ±1.6	9.433 ±0.001	1.702 ±0.1	0.92

(To be continued)

Slice	Voxel	S1	$cS2_b$	σ_{S1}	σ_{cS2}	Θ	α	$S1_{cor}$
4	13	14.684 ±0.071	1326.333 ±3.487	6.771 ±0.132	186.805 ±1.794	9.432 ±0.001	1.587 ±0.114	0.91
4	14	14.79 ±0.073	1330.128 ±3.551	6.893 ±0.126	186.972 ±1.842	9.434 ±0.001	1.697 ±0.115	0.913
4	15	14.832 ±0.061	1322.738 ±3.158	6.917 ±0.107	188.1 ±1.559	9.433 ±0.001	1.756 ±0.101	0.902
4	16	15.113 ±0.155	1316.621 ±36.563	5.049 ±0.045	185.508 ±1.466	9.43 ±0.0	0.0 ±3.976	0.889
4	17	15.398 ±0.067	1337.182 ±3.351	7.055 ±0.118	190.534 ±1.722	9.433 ±0.001	1.777 ±0.106	0.868
4	18	15.603 ±0.068	1327.662 ±3.107	6.822 ±0.142	181.966 ±1.611	9.432 ±0.001	1.388 ±0.109	0.865
4	19	15.608 ±0.063	1316.656 ±2.975	6.787 ±0.119	185.822 ±1.549	9.433 ±0.001	1.459 ±0.095	0.861
4	20	15.558 ±0.061	1318.546 ±2.993	6.931 ±0.108	190.902 ±1.561	9.434 ±0.001	1.627 ±0.091	0.857
4	21	15.438 ±0.064	1331.84 ±3.093	7.105 ±0.106	191.236 ±1.616	9.435 ±0.001	1.765 ±0.095	0.859
4	22	15.463 ±0.064	1322.371 ±3.158	7.03 ±0.113	184.487 ±1.612	9.432 ±0.001	1.803 ±0.103	0.868
4	23	15.35 ±0.06	1327.894 ±2.915	6.79 ±0.108	185.359 ±1.509	9.433 ±0.001	1.624 ±0.093	0.88
4	24	14.885 ±0.063	1339.197 ±3.076	6.73 ±0.111	186.458 ±1.598	9.434 ±0.001	1.631 ±0.1	0.898
5	0	17.951 ±0.079	1381.923 ±3.995	7.519 ±0.136	202.545 ±2.068	9.434 ±0.001	1.907 ±0.118	0.74
5	1	16.629 ±0.073	1373.284 ±3.565	7.1 ±0.128	191.238 ±1.86	9.434 ±0.001	1.719 ±0.107	0.819
5	2	17.138 ±0.081	1371.31 ±3.863	7.35 ±0.141	193.576 ±2.019	9.434 ±0.001	1.734 ±0.115	0.809
5	3	17.302 ±0.087	1368.591 ±4.259	6.967 ±0.156	197.107 ±2.253	9.434 ±0.001	1.498 ±0.116	0.805
5	4	16.75 ±0.082	1370.829 ±3.964	7.32 ±0.137	194.466 ±2.071	9.434 ±0.001	1.8 ±0.116	0.818
5	5	17.645 ±0.081	1364.039 ±3.831	7.229 ±0.14	195.422 ±2.028	9.435 ±0.001	1.603 ±0.107	0.764
5	6	17.771 ±0.079	1365.396 ±3.899	7.129 ±0.144	197.901 ±2.04	9.434 ±0.001	1.648 ±0.117	0.74
5	7	17.85 ±0.075	1361.685 ±3.708	7.346 ±0.13	198.516 ±1.935	9.434 ±0.001	1.757 ±0.105	0.755
5	8	17.203 ±0.071	1361.638 ±3.575	7.18 ±0.124	194.138 ±1.85	9.433 ±0.001	1.812 ±0.106	0.801

(To be continued)

Slice	Voxel	S1	$cS2_b$	σ_{S1}	σ_{cS2}	Θ	α	$S1_{cor}$
5	9	15.615 ±0.073	1351.924 ±3.77	6.882 ±0.126	195.057 ±1.981	9.433 ±0.001	1.86 ±0.124	0.866
5	10	16.074 ±0.072	1358.041 ±3.649	6.873 ±0.123	200.0 ±1.927	9.434 ±0.001	1.566 ±0.097	0.838
5	11	15.603 ±0.075	1358.36 ±3.868	6.639 ±0.14	200.332 ±2.026	9.433 ±0.001	1.43 ±0.11	0.909
5	12	15.861 ±0.074	1349.167 ±3.87	7.094 ±0.126	197.127 ±1.99	9.432 ±0.001	1.849 ±0.112	0.915
5	13	15.562 ±0.081	1342.583 ±4.142	7.337 ±0.146	197.002 ±2.101	9.432 ±0.001	1.87 ±0.136	0.901
5	14	15.475 ±0.082	1346.897 ±4.129	6.531 ±0.168	196.248 ±2.142	9.432 ±0.001	1.301 ±0.128	0.882
5	15	15.374 ±0.071	1343.756 ±3.634	6.805 ±0.137	198.279 ±1.883	9.432 ±0.001	1.496 ±0.112	0.886
5	16	16.011 ±0.086	1361.896 ±4.437	7.249 ±0.153	201.869 ±2.28	9.432 ±0.001	1.763 ±0.132	0.857
5	17	16.528 ±0.079	1359.936 ±4.149	7.237 ±0.14	200.74 ±2.126	9.433 ±0.001	1.885 ±0.129	0.817
5	18	16.427 ±0.08	1349.52 ±4.174	7.114 ±0.135	206.38 ±2.187	9.433 ±0.001	1.718 ±0.112	0.822
5	19	17.157 ±0.076	1346.013 ±3.866	7.245 ±0.132	199.501 ±2.008	9.433 ±0.001	1.799 ±0.112	0.815
5	20	17.326 ±0.072	1320.601 ±3.758	7.275 ±0.133	201.604 ±1.925	9.431 ±0.001	1.781 ±0.112	0.796
5	21	16.67 ±0.078	1350.541 ±3.822	7.102 ±0.145	202.63 ±1.998	9.434 ±0.001	1.468 ±0.11	0.846
5	22	16.891 ±0.078	1342.17 ±3.963	7.265 ±0.136	199.695 ±2.057	9.433 ±0.001	1.789 ±0.116	0.833
5	23	16.761 ±0.073	1344.062 ±3.807	7.01 ±0.132	203.369 ±1.988	9.433 ±0.001	1.642 ±0.108	0.827
5	24	15.566 ±0.073	1360.508 ±3.936	6.938 ±0.123	205.018 ±2.048	9.433 ±0.001	1.772 ±0.109	0.883

Table B.2.: *Fit results of the 2D skew Gauss fit to the ^{37}Ar data. The TPC volume is divided into 6 slices in z, each of which is divided into 25 equally sized voxels. S1 and $cS2_b$ are the mean values for the position in S1-$cS2_b$ -space, with σ_{S1}/σ_{cS2} the corresponding standard deviation. Θ is the rotation angle with respect to the S1-$cS2_b$ -axes and α is the skewness in S1. The fit parameters for the threshold component are not listed as they are fixed for this fit. Additionally the correction factor for S1 is given by $S1_{cor}$.*

B.10. XENONnT data analysis

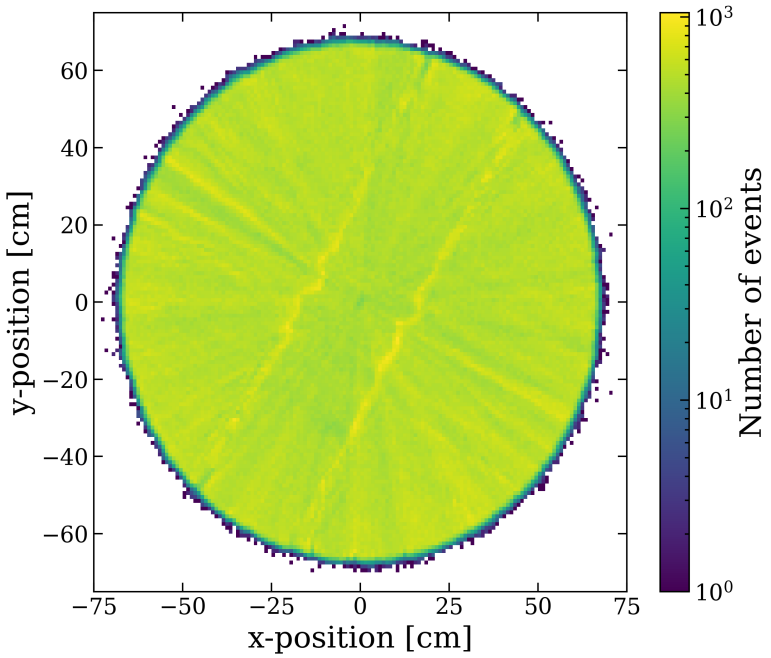

(a) *x-y distribution of ^{37}Ar data without wire cut.*

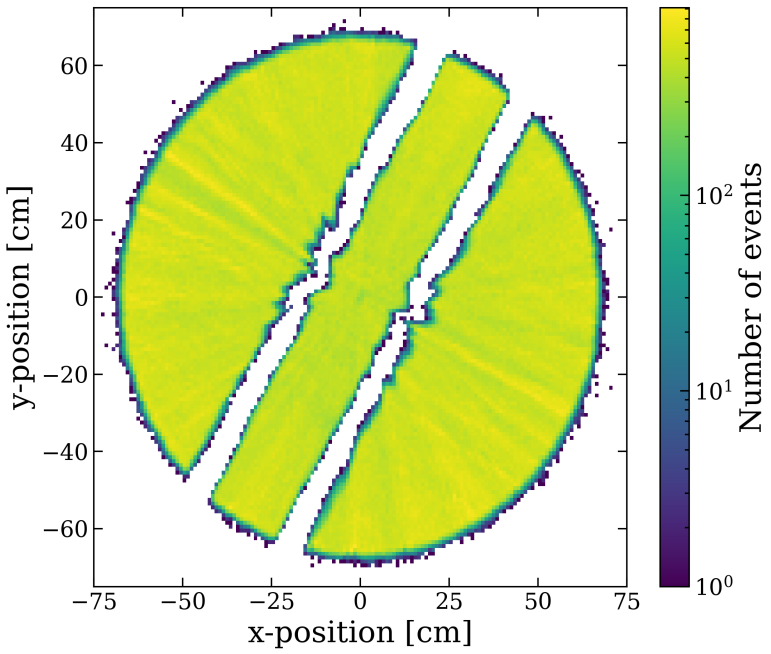

(b) *x-y distribution of ^{37}Ar data with wire cut.*

Figure B.29.: *Fig. B.29a shows the effect of the transverse gate wires on event distribution. Fig. B.29b shows the data after the wire cut is applied.*

Acronyms

AFT area-fraction-top

ALP axion like particle

AP afterpulse

APD avalanche photo diode

BBF Bayesian Band Fitting

BBN Big-Bang nucleosynthesis

CAD computer aided design

CES combined energy scale

CMB cosmic microwave background

DC dark count

DM dark matter

ER electronic recoil

FF fill-factor

IC intergrated circuit

LCE light collection efficiency

LED light emitting diode

LET linear energy transfer

LNGS Laboratori Nazionali del Gran Sasso

MACHO Massive Compact Halo Object

MCMC Marcov Chain Monte Carlo

MOND Modified Newtonian dynamics

MPPC Multi-Pixel Photon Counter

NEST Noble Element Simulation Technique

NIM Nuclear Instrumentation Modul

NR nuclear recoil

PAX Processor for Analyzing XENON

PBH Primordial Black Hole

PCB printed circuit board

PDE photon detection efficiency

PMT photo multiplier tubes

PTFE Polytetrafluoroethylene

QE quantum efficiency

ROI range of interest

SD spin-dependent

SI spin-independent

SiPM silicon photomultiplier

SM standard model

SR0 Science Run 0

SR1 Science Run 1

TeVeS tensor-vector-scalar

TPC time projection chamber

TPF Top Pattern Fit

VUV vacuum ultraviolet

WIMP weakly interacting massive particle

List of Figures

1.1. Galaxy rotation curves . . . 16
1.2. Cosmic Microwave Background by the Planck satellite . . . 18
1.3. Temperature Power Spectrum of the CMB . . . 19
1.4. Event rates for different detector materials . . . 24
1.5. Exclusion limits for spin-independent nuclear recoils achieved for multiple experiments . . . 25
1.6. Detection channels used by various direct DM detection experiments . 26

2.1. Charge and light yields in xenon . . . 34
2.2. Working principle of a time projection chamber . . . 35
2.3. Separation of ER and NR events by different S1-S2 ratios . . . 36
2.4. Schematic of the so-called *Doke* plot . . . 38
2.5. Schematic and working principle of a PMT . . . 39
2.6. Afterpulse timing for different contaminants in PMTs . . . 40
2.7. Simplified schematic of XENON1T gas system . . . 41
2.8. Working scheme of the XENON1T event builder . . . 44
2.9. Summary of signal correction . . . 46
2.10. Example plot of the XENON1T position correction . . . 47

3.1. Decay scheme of ^{37}Ar into ^{37}Cl . . . 50
3.2. Ampule filling system . . . 53
3.3. Prepared ampule blanket . . . 53
3.4. Dosing branch for XENON1T . . . 54
3.5. CAD drawing of the source container with ampule and guillotine mechanism . . . 55
3.6. Injection steps of ^{37}Ar into the XENON1T TPC . . . 59
3.7. ^{37}Ar and ^{83m}Kr event number decays after last injection and ^{83m}Kr source closing . . . 61
3.8. Event numbers during distillation of the ^{37}Ar from the XENON1T system 62

4.1. Effect of cuts on selected ^{37}Ar events . . . 71
4.2. Effect of cuts on background events . . . 72
4.3. Event rate during distillation after ^{37}Ar data selection and cut application 73
4.5. Example of exponential fit on $s2_{bottom}$ time slice . . . 74
4.4. Exponential distribution of the the ^{37}Ar $s2_{bottom}$ size in dependence of the drift time . . . 75
4.6. Exponential fit to extract the electron lifetime based on ^{37}Ar data . . 76

4.7. Exponential fit to extract the electron lifetime based on ^{83m}Kr data . 78
4.8. Comparison of the results from the ^{37}Ar and ^{83m}Kr fits 79
4.9. Comparison of the results from the ^{129m}Xe and ^{131m}Xe fits 80
4.10. Data selection in the high energy region for ^{222}Rn and ^{218}Po 81
4.11. Comparison of the results from the ^{218}Po and ^{222}Rn fits 82
4.12. Comparison of the electron lifetime results from the different isotopes 83
4.13. Simulated drift field in the XENON1T detector 84
4.14. Relative charge yield changes of different sources in varying drift fields 85
4.15. Relative charge yield changes of ^{37}Ar and ^{83m}Kr in varying drift fields 86
4.16. Comparison of the fit to ^{83m}Kr data before and after field correction . 88
4.17. Threshold selection of AP events in the time delay parameter 91
4.18. Threshold selection for ^{83m}Kr events in the time delay parameter . . . 92
4.19. ^{37}Ar drift time plot with the AP correction applied 93
4.21. x-y distribution of main S2 and corresponding first AP candidate . . 96
4.22. Population selection for advanced AP selection 97
4.23. x-y distribution of S2 and main AP population for ^{83m}Kr 98
4.24. Z-distribution comparison for the first AP candidates of ^{37}Ar and ^{83m}Kr 99
4.25. Direct comparison of two AP corrections 100
4.26. Comparison of the cS1-cS2 distribution for a single voxel for ^{83m}Kr and ^{37}Ar 101
4.27. Section map showing the subdivision of the x-y-plane 103
4.28. Comparison of cS1-cS2$_b$ signal shape between top and bottom of the TPC 104
4.29. Comparison of cS1-cS2$_b$ signal shape between top and bottom of the TPC with ^{37}Ar electron lifetime correction 105
4.30. Shape comparison between skewed Gaussian and standard un-skewed Gauss-distributions 105
4.31. S1 threshold modeling 107
4.32. Example of a S1 value overcompensation for free threshold parameters 109
4.33. Example of one voxel fit from the top of the TPC: contour and S1 projection 112
4.34. Doke plot with the light and charge gain factors of the XENON1T detector 113
4.35. ^{37}Ar energy peak reconstruction 115
4.36. Energy resolution of the XENON1T detector at 2.82 keV 116
4.37. Single electron S2 selection 118
4.38. Single Gaussian fits on data selected with modified selection criteria . 119
4.39. Summed Gaussian fit on all single electron data 120
4.40. Section map for the single electron S2 gain 121
4.41. Comparison of the effect of S2-only and S1-S2 data selection 124
4.42. S2-only best-fit model 126
4.43. Summary plot for the photon and electron yields for ^{37}Ar 128

4.44. Impact of the corrections learned from the ^{37}Ar calibration on the XENON1T low-energy excess . . . 131
4.45. Direct comparison of low-energy data from XENON1T and XENONnT 132

5.1. New dosing system of XENONnT . . . 137
5.2. Event rate development during XENONnT calibration . . . 139
5.3. ^{37}Ar and ^{83m}Kr data taken during XENONnT calibration . . . 141
5.4. Electron lifetime measurement for XENONnT . . . 142
5.5. Comparison of XENON1T and XENONnT ^{37}Ar data . . . 144

6.1. Semiconductor band structure . . . 148
6.2. P-N-junction in equilibrium and with an applied reversed bias voltage 149
6.3. SiPM structure . . . 150
6.4. Structure of a SiPM on the example of the KETEK sample . . . 151
6.5. Equivalent circuit of a single SiPM pixel and a full SiPM . . . 152
6.6. Example of a hit spectrum for a SiPM . . . 153
6.7. Example of nonlinearity in SiPM signals . . . 158

7.1. SiPMs tested in the setup . . . 161
7.2. CAD drawing of test setup . . . 162
7.3. Cabling and grounding scheme of SiPM test setup . . . 163
7.4. Cooling cycle of test setup during a run . . . 164
7.5. Cross section of the illumination cylinder . . . 165
7.6. Projection of the hole sequence of the illumination cylinder . . . 165
7.7. PMT noise on SiPM signals . . . 167
7.8. Gas recirculation system of the test setup . . . 169
7.9. Amplifier board schematic . . . 171
7.10. Layout and picture of the amplifier board . . . 172
7.11. Temperature stability of the amplifier board . . . 173
7.12. Amplifier box . . . 174
7.13. Readout chain for the SiPM and PMT signals . . . 175
7.14. Signal quality for the three tested SiPM models . . . 176
7.15. System configuration for LED triggered measurement . . . 177
7.16. Spectrum fit with multiple Gaussians . . . 178
7.17. Breakdown voltage estimation . . . 179
7.18. Bias voltage dependent gains . . . 180
7.19. Photon-count spectrum of the S13370 . . . 181
7.20. Correlated noise probabilities of the S13370 . . . 182
7.21. Readout chain for dark count rate measurement . . . 183
7.22. Dark count rates of the S13370 . . . 184

A.1. Comparison of uncorrected S1 shapes in different voxels of the TPC . 188
A.2. Comparison of the threshold shape for fits with free parameters . . . 189
A.3. Example voxel result of a global fit . . . 190

B.1. Phase diagram of xenon . . . 193
B.2. Decay curves of liquid xenon for different types of exciting particles . 194
B.3. Background event numbers before XENON1T ^{37}Ar calibration 195
B.4. 0.27 keV line of the ^{37}Ar decay in cS1-cS2 . . . 196
B.5. Ellipsoidal ^{37}Ar event selection for the rate calculation . . . 197
B.6. Electron lifetime fit of ^{129m}Xe . . . 198
B.7. Electron lifetime fit of ^{131m}Xe . . . 199
B.8. Electron lifetime fit of ^{218}Po . . . 200
B.9. Time slice fit of ^{218}Po . . . 200
B.10. Electron lifetime fit of ^{222}Rn . . . 201
B.11. Time slice fit of ^{222}Rn . . . 201
B.12. Electron lifetime fit of field corrected ^{37}Ar data . . . 202
B.13. Electron lifetime fit of field corrected ^{83m}Kr data . . . 202
B.14. Electron lifetime fit of field corrected ^{129m}Xe data . . . 203
B.15. Electron lifetime fit of field corrected ^{131m}Xe data . . . 203
B.16. Simple AP selection for ^{129m}Xe . . . 204
B.17. Simple AP selection for ^{131m}Xe . . . 204
B.18. Distribution of the second AP candidate of ^{37}Ar . . . 205
B.19. Distribution of the third AP candidate of ^{37}Ar . . . 205
B.20. 2D-Skew Gauss fit examples with free and with fixed threshold parameters 206
B.21. Example of a SiPM I-V curve . . . 207
B.22. Operational specifications of the Hamamatsu model S10943 MPPC . 208
B.23. Dimensional drawing of the Hamamatsu model S10943 MPPC . . . 209
B.24. Dimensional drawing of the Hamamatsu model S13770 MPPC . . . 209
B.25. Operational specifications of the Hamamatsu model S13370 MPPC . 210
B.26. Sensor arrangement in the SiPM test setup . . . 211
B.27. Copper-sheet shielding of the PMT . . . 212
B.28. Amplifier box components . . . 214
B.29. Transverse wire effect and wire cut effect . . . 225

List of Tables

2.1. Isotope composition of natural xenon 30
2.2. Volatilities of various noble gases 42

3.1. Half-lifes of isotopes created during irradiation of a fused quartz ampule 51
3.2. Table of all relevant argon isotopes with natural abundance 52
3.3. List of volumes of the dosing branch components 56
3.4. Event numbers for the ^{37}Ar injections in XENON1T 60
3.5. Results of quick distillation data analysis 62

4.1. List off cuts applied to the ^{37}Ar data 69
4.2. Summary table of the electron lifetimes determined with different isotopes 83
4.3. Summary table of the electron lifetimes before and after field correction 87
4.4. Table of the fit parameters used to describe the S1 threshold 107
4.5. TPC-mean $S1/\mathrm{cS2}_b$ fit results 110
4.6. Photon gain g1 and electron gain g2 of XENON1T 114
4.7. Light and charge yield of xenon for 2.82 keV (electronic recoil) at a drift field of 82 V/cm. 114
4.8. Table of selections applied to the single electron S2 population 118
4.9. List of values used to directly obtain the charge yield 122

5.1. Volumes and activities of the XENONnT dosing system 136
5.2. Table of injections during XENONnT calibration 138

7.1. Table of illumination cylinder hole dimensions 166

A.1. Table of threshold fit parameter results for different voxelisations . . . 191

B.1. Component values of the SiPM amplifier board 213
B.2. Table of voxel fit results 224

Bibliography

[1] G. Bertone, D. Hopper. *History of dark matter*, Rev. Mod. Phys. **90**, 45002 (2018). doi:10.1103/RevModPhys.90.045002.

[2] F. Zwicky. *Die Rotverschiebung von extragalaktischen Nebeln*, Helvetica Physica Acta, Vol.**6**, p. 110-127 (1933). https://ned.ipac.caltech.edu/level5/March17/Zwicky/paper.pdf.

[3] Yoshiaki Sofue, Vera Rubin. *Rotation Curves of Spiral Galaxies*, Ann.Rev.Astron.Astrophys. 39 (2001) 137-174. http://arxiv.org/abs/astro-ph/0010594v2.

[4] Prajwal R. Kafle, Sanjib Sharma et.al. *On the Shoulders of Giants: Properties of the Stellar Halo and the Milky Way Mass Distribution*, ApJ, 794, 59, 2014. arXiv:https://arxiv.org/abs/1408.1787v1. doi:10.1088/0004-637X/794/1/59.

[5] S. D. M. White, M. Davis, C. S. Frenk. *The size of clusters in a neutrino-dominated universe*, MNRAS, 209, 27P (1984). doi:10.1093/mnras/209.1.27P.

[6] Ralph A. Alpher, Robert Herman. *Evolution of the Universe*, Nature, **162**, 774-775 (1948). doi:10.1038/162680a0.

[7] A. A. Penzias, R. W. Wilson. *A Measurement of Excess Antenna Temperature at 4080 Mc/s* . Astrophysical Journal. **142**, 419-421. doi:10.1086/148307.

[8] Planck Collaboration, N. Aghanim et al. *Planck 2018 results. I. Overview and the cosmological legacy of Planck*. Astron.Astrophys. 614 (2020) A1. doi:10.1051/0004-6361/201833880.

[9] Planck Collaboration, N. Aghanim et al. *Planck 2018 results. VI. Cosmological parameters*. Astron.Astrophys. 614 (2020) A6. https://arxiv.org/abs/1807.06209. doi:10.1051/0004-6361/201833910.

[10] M. Schumann. *Direct detection of WIMP dark matter: concepts and status*, J. Phys. G: Nucl. Part. Phys., **46**: 103003 (2019). doi:10.1088/1361-6471/ab2ea5.

[11] L. Roszkowski. *Particle dark matter - A theorist's perspective*, Pramana **62**, 389 (2004). doi:10.1007/BF02705097.

[12] L. Roszkowski et al. *WIMP dark matter candidates and searches - current status and future prospects*, Rep. Prog. Phys. **81**, 066201 (2018). doi:10.1088/1361-6633/aab913.

[13] S. Weinberg. *A new light boson?*, Phys. Rev. Lett. **40**(4), 223-226 (1978). doi:10.1103/PhysRevLett.40.223.

[14] F. Wilczek. *Problem of strong P and T invariance in the presence of instantons*, Phys. Rev. Lett. **40**(5), 279-282 (1978). doi:10.1103/PhysRevLett.40.279.

[15] G. Bertone. *Particle Dark Matter: Observations, Models and Searches*, Cambridge University Press (2010). doi:10.1017/CBO9780511770739.

[16] K. Griest. *Galactic Microlensing as a Method of Detecting Massive Compact Halo Objects*, Astrophysical Journal **366**: 412 (1991). doi:10.1086/169575.

[17] T. D. Brandt. *Constraints on MACHO Dark Matter from compact stellar systems in ultra-faint dwarf galaxies*, ApJL, **824**: L31 (2016). doi:10.3847/2041-8205/824/2/L31.

[18] Y. Ali-Haïmoud, E. D. Kovetz, M. Kamionkowski. *Merger rate of primordial black-hole binaries*, Phys. Rev. D **96**, 123523 (2017). doi:10.1103/PhysRevD.96.123523.

[19] M. Milgram. *A modification of the Newtonian dynamics as a possible alternative to the hidden mass hypothesis*, Astrophysical Journal **270**: 365-370 (1983). doi:10.1086/161130.

[20] S. McGaugh. *The Baryonic Tully-Fisher Relation of Gas Rich Galaxies as a Test of LCDM and MOND*, Astrophysical Journal. **143**(2): 40 (2012). doi:10.1088/0004-6256/143/2/40.

[21] B. Famaey, S. McGaugh. *Modified Newtonian Dynamics (MOND): Observational Phenomenology and Relativistic Extensions*, Living Rev Relativ 15(**1**):10 (2012). doi:10.12942/lrr-2012-10.

[22] The KATRIN Collaboration. *Direct neutrino-mass measurement with sub-electronvolt sensitivity*, Nature Physics **18**, 160-166 (2022). doi:10.1038/s41567-021-01463-1.

[23] Felix Kahlhoefer. *Review of LHC Dark Matter Searches*, Int. J. Mod. Phys. A **32** 1730006 (2017). doi:10.1142/S0217751X1730006X.

[24] T. Marrodán Undagoitia, L. Rauch. *Dark matter direct-detection experiments*, J. Phys. G: Nucl. Part. Phys. **43** 013001 (2016). doi:10.1088/0954-3899/43/1/013001.

[25] L. E. Strigari. *Dark Matter in Dwarf Spheroidal Galaxies and Indirect Detection: A Review*, Rep. Prog. Phys. **81** 056901 (2018). doi:10.1088/1361-6633/aaae16.

[26] S. Sivertsson et al. *The local dark matter density from SDSS-SEGUE G-dwarfs*, Monthly Notices of the Royal Astronomical Society 478 **2**:1677-1693 (2018). doi:10.1093/mnras/sty977.

[27] M. C. Smith et al. *The RAVE survey: constraining the local Galactic escape speed*, Monthly Notices of the Royal Astronomical Society 379 **2**:755-772 (2007). doi:10.1111/j.1365-2966.2007.11964.x.

[28] Jodi Cooley. *Dark Matter direct detection of classical WIMPs*, SciPost Phys. Lect. Notes 55 (2022). doi:10.21468/SciPostPhysLectNotes.55.

[29] V. Chepel and H. Araújo. *Liquid noble gas detectors for low energy particle physics*, JINST **8**:R04001 (2013). doi:10.1088/1748-0221/8/04/R04001.

[30] E. Aprile et al. (XENON Collaboration). *Dark Matter Search Results from a One Ton-Year Exposure of XENON1T*, Phys. Rev. Lett. **121**, 111302 (2018). doi:10.1103/PhysRevLett.121.111302.

[31] SLAC. *Dark Limit Plotter*. https://supercdms.slac.stanford.edu/science-results/dark-matter-limit-plotter.

[32] R. Bernabei et al. *Final model independent result of DAMA/LIBRA-phase 1*, Eur. Phys. J. C **73** 2648 (2013). doi:10.1140/epjc/s10052-013-2648-7.

[33] E. Shields, J. Xu, F. Calaprice. *SABRE: A new NaI(Tl) dark matter direct detection experiment*, Phys. Procedia **61** 169 (2015). doi:10.1016/j.phpro.2014.12.028.

[34] G. Angloher, P. Carniti, L. Cassina et al. *The COSINUS project: perspectives of a NaI scintillating calorimeter for dark matter search*, Eur. Phys. J. C **76** 441 (2016). doi:10.1140/epjc/s10052-016-4278-3.

[35] I. Coarasa et al. *ANAIS - 112 three years data: a sensitive model independent negative test of the DAMA/LIBRA dark matter signal*, (2024). doi:10.48550/arXiv.2404.17348.

[36] P.-A. Amaudruz et al. (DEAP-3600 Collaboration). *Design and Construction of the DEAP-3600 Dark Matter Detector*, Astropart.Phys. **108**, 1-23 (2019). doi:10.1016/j.astropartphys.2018.09.006.

[37] P. Agnes, T. Alexander, A. Alton et al. *First results from the DarkSide-50 dark matter experiment at Laboratori Nazionali del Gran Sasso*, Physics Letters B, Volume **743**, 456-466 (2015). doi:10.1016/j.physletb.2015.03.012.

[38] C. E. Aalseth, F. Acerbi, P. Agnes et al. *DarkSide-20k: A 20 tonne two-phase LAr TPC for direct dark matter detection at LNGS*, Eur. Phys. J. Plus **133**, 131 (2018). doi:10.1140/epjp/i2018-11973-4.

[39] E. Aprile et al. (XENON Collaboration). *The XENON1T Dark Matter Experiment.*, Eur. Phys. J. C **77**: 881 (2017). doi:10.1140/epjc/s10052-017-5326-3.

[40] Laboratori Nazionali del Gran Sasso, (2023). https://www.lngs.infn.it/en/research.

[41] M. Antonello et al. *The SABRE project and the SABRE Proof-of-Principle*, Eur. Phys. J. C, **79**:363, (2019). https://arxiv.org/pdf/1806.09340.pdf.

[42] G. Angloher et al. *COSINUS: Cryogenic Calorimeters for the Direct Dark Matter Search with NaI Crystals*, J. Low Temp. Phys., **200**:428-436, (2020). doi:10.1007/s10909-020-02464-9.

[43] E. Aprile et al. *Constraining the Spin-Dependent WIMP-Nucleon Cross Sections with XENON1T*, Phys. Rev. Lett. **122**, 141301 (2019). doi:10.1103/PhysRevLett.122.141301.

[44] E. Aprile et al. *First observation of two-neutrino double electron capture in* ^{124}Xe *with XENON1T*, Nature 568, 532 (2019)). doi:10.1038/s41586-019-1124-4.

[45] E. Aprile, T. Doke. *Liquid Xenon Detectors for Particle Physics and Astrophysics*, Rev. Mod. Phys. **82**, 2053 (2010). doi:10.1103/RevModPhys.82.2053.

[46] C.E. Dahl. *The physics of background discrimination in liquid xenon, and first results from Xenon10 in the hunt for WIMP dark matter*, PhD thesis, 2009.

[47] M. Szydagis et.al. *NEST: A Comprehensive Model for Scintillation Yield in Liquid Xenon*, JINST **6**, P10002 (2011). doi:10.1088/1748-0221/6/10/P10002.

[48] R.L. Platzman. *Total ionization in gases by high-energy particles: An appraisal of our understanding*, The International Journal of Applied Radiation and Isotopes 10 (**2**):116-127, 1961. doi:10.1016/0020-708X(61)90108-9.

[49] J. Aalbers et. al. (LZ Collaboration). *Search for new physics in low-energy electron recoils from the first LZ exposure*, Phys. Rev. D **108**, 072006 (2023). https://arxiv.org/pdf/2307.15753.pdf.

[50] Yue Meng et. al. (PandaX-4T Collaboration). *Dark Matter Search Results from the PandaX-4T Commissioning Run*, Phys. Rev. Lett. **127**, 261802 (2021). https://arxiv.org/pdf/2107.13438.pdf.

[51] K.Thieme. L.Baudis, P.Sanchez-Lucas. *A measurement of the mean electronic excitation energy of liquid xenon*, Eur. Phys. J. C **81**: 1060 (2021). doi:10.1140/epjc/s10052-021-09834-x.

[52] G. Anton et. al. (EXO-200 Collaboration). *Measurement of the scintillation and ionization response of liquid xenon at MeV energies in the EXO-200 experiment*, Phys. Rev. C **101**, 065501 (2020). doi:10.1103/PhysRevC.101.065501.

[53] M. Scharff J. Lindhard, V. Nielsen and P.V. Thomsen. *Integral equations governing radiation effects*, Kgl. Danske Videnskab., Selskab. Mat. Fys. Medd. **33** (1963).

[54] J. Thomas and D.A. Imel. *Recombination of electron-ion pairs in liquid argon and liquid xenon*, Phys. Rev. A **36**, 614 (1987). doi:10.1103/PhysRevA.36.614.

[55] B. Lenardo, K. Kazkaz, A. Manalaysay, J. Mock, M. Szydagis, and M. Tripathi. *A Global Analysis of Light and Charge Yields in Liquid Xenon*, IEEE Transactions on Nuclear Science **62**, 3387 - 3396 (2015). doi:10.1109/TNS.2015.2481322.

[56] ESTAR. *Stopping Power and Range Tables for Electrons*, 2023. https://physics.nist.gov/cgi-bin/Star/e_table.pl.

[57] E. Aprile et al. (XENON Collaboration). *First Dark Matter Search Results from the XENON1T Experiment*, Phys. Rev. Lett. **119**, 181301 (2017). doi:10.1103/PhysRevLett.119.181301.

[58] E. Aprile et al. (XENON Collaboration). *XENON1T Dark Matter Data Analysis: Signal Reconstruction, Calibration and Event Selection.*, Phys. Rev. D **100**, 052014 (2019). doi:10.1103/PhysRevD.100.052014.

[59] E. Aprile et al. (XENON Collaboration). *First Dark Matter Search with Nuclear Recoils from the XENONnT Experiment*, Phys. Rev. Lett. **131**, 041003 (2023). doi:10.1103/PhysRevLett.131.041003.

[60] V. Álvarez et al. *NEXT-100 Technical Design Report (TDR): Executive Summary*, JINST **7**:T06001 (2012). doi:10.1088/1748-0221/7/06/T06001.

[61] P. Barrow et al. *Qualification tests of the R11410-21 photomultiplier tubes for the XENON1T detector*, JINST **12**:P01024 (2017). doi:10.1088/1748-0221/12/01/P01024.

[62] Melanie Scheibelhut. *Design and Commissioning of ReStoX for XENON1Tl*, Talk at DPG 2015. http://xenon.physik.uni-mainz.de/presentations/2015_DPG_scheibelhut_v6.pdf.

[63] Michael Murra. *Intrinsic background reduction by cryogenic distillation for the XENON1T dark matter experiment*, PhD thesis 2018.

[64] E. Aprile et al. (XENON Collaboration). *Removing krypton from xenon by cryogenic distillation to the ppq level*, Eur. Phys. J. C, **77**, (2017). doi:10.1140/epjc/s10052-017-4757-1.

[65] E. Aprile et al. (XENON Collaboration). *Application and modeling of an online distillation method to reduce krypton and argon in XENON1T*, Prog. Theor. Exp. Phys. **5** 2022, (2022). doi:10.1093/ptep/ptac074.

[66] Jelle Aalbers. *Dark Matter Search with XENON1T*, PhD thesis, 2018. https://pure.uva.nl/ws/files/25577409/Thesis.pdf.

[67] C. H. Faham et al. *Measurements of wavelength-dependent double photoelectron emission from single photons in VUV-sensitive photomultiplier tubes.*, JINST **10** P09010 (2015). doi:10.1088/1748-0221/10/09/P09010.

[68] E. Aprile et al. (XENON Collaboration). *XENON1T Dark Matter Data Analysis: Signal Background Models, and Statistical Inference*, Phys. Rev. D **99**, 112009 (2019). doi:10.1103/PhysRevD.99.112009.

[69] M.-M. Bé et. al. *Table of Radionuclides, Monographie BIPM-5, volume 7.*, Bureau International des Poids et Mesures, Pavillon de Breteuil, F-92310 Sèvres, France (2013).

[70] V. P. Chechev. *The evaluation of half-lives and other decay data used in nuclear astrophysics and cosmochronolog*, Phys. Atom. Nuclei, **74**, 1713-1717 (2011). doi:10.1134/S106377881111007X.

[71] M. Szydagis et.al. *Noble Element Simulation Technique*, (v2.3.6) (2022). https://zenodo.org/records/6448408#.Y01Zo0xBw-U.

[72] E. M. Boulton et al. *Calibration of a two-phase xenon time projection chamber with a ^{37}Ar source*, JINST, **12**, P08004 (2017). doi:10.1088/1748-0221/12/08/P08004.

[73] Alejandro Sonzogni. *National Nuclear Data Center v3.0*. https://www.nndc.bnl.gov/nudat3/.

[74] TRIGA Mainz. https://www.kernchemie.uni-mainz.de/reaktor/technische-daten/.

[75] Daniel Wenz. *Improving the calibration of MainzTPC using the isotope 37Ar*, Master thesis, 2018. http://xenon.physik.uni-mainz.de/mainzTheses/Master_Thesis_Daniel_Wenz_20180605.pdf.

[76] Christopher Hils. *Studie von internen Kalibrationsmethoden für Flüssig-Xenon-TPCs zur direkten Suche nach Dunkler Materie*, Diploma thesis, 2014. http://xenon.physik.uni-mainz.de/mainzTheses/Diplomarbeit_ChristopherHils.pdf.

[77] E. Aprile et al. (XENON Collaboration). *Excess Electronic Recoil Events in XENON1T.*, Phys. Rev. Lett. D **102**, 072004 (2020). doi:10.1103/PhysRevD.102.072004.

[78] G. J. Feldman and R. D. Cousins. *A Unified approach to the classical statistical analysis of small signals*, Phys. Rev. D **57**, 3873 (1998). doi:10.1103/PhysRevD.57.3873.

[79] Chart Industries. *2S132C-X GAS PUMP Operation Manual* .

[80] Natascha Rupp. Internal note: *Rn222 evolution before and after magnetic pump installation.*, 2018. https://xe1t-wiki.lngs.infn.it/doku.php?id=xenon:xenon1t:ratesrn222_after_pump.

[81] E. Aprile et al. (XENON Collaboration). *Rn222 emanation measurements for the XENON1T experiment*, Eur. Phys. J. C, **81**, 337 (2021). doi:10.1140/epjc/s10052-020-08777-z.

[82] Jelle Aalbers, Joey Howlett, Evan Shockley. Internal note: *S1/S2 detection efficiency for SR1*, 2018. https://xe1t-wiki.lngs.infn.it/doku.php?id=xenon:xenon1t:analysis:sciencerun1:daqtriggerpaxefficiency.

[83] Evan Shockley. Internal note: *Data Driven Pax Efficiency*, 2017. https://xe1t-wiki.lngs.infn.it/doku.php?id=xenon:shockley:datadriven_paxeff.

[84] CERN. https://indico.cern.ch/category/6015/attachments/192/631/Statistics_Fitting_II.pdf.

[85] Kaixuan Ni. *Analyzing the XENON1T Dark Matter Search Data*, 2018. Talk UCLA.

[86] Christopher Geis. *The XENON1T water Cherenkov muon veto system and commissioning of the XENON1T Dark Matter experiment*, PhD thesis, 2018. https://publications.ub.uni-mainz.de/theses/volltexte/2018/100002172/pdf/100002172.pdf.

[87] Jelle Aalbers. Internal note: *S2-only analysis for XENON1T SR0*, 2017. https://xe1t-wiki.lngs.infn.it/doku.php?id=xenon:xenon1t:aalbers:s2only_sr0.

[88] E. Aprile et al. (XENON Collaboration). *Energy resolution and linearity of XENON1T in the MeV energy range.*, Phys. Phys. J.C. (2020) **80**:785. doi:10.1140/epjc/s10052-020-8284-0.

[89] E. Aprile et al. (XENON Collaboration). *Search for Light Dark Matter in XENON10 Data.*, Phys. Rev. Lett. **107**, 051301 (2011). doi:10.1103/PhysRevLett.107.051301.

[90] E. Aprile et al. (XENON Collaboration). *Low-mass dark matter search using ionization signals in XENON100.*, Phys. Rev. Lett. D **95**, 059901 (2017). doi:10.1103/PhysRevD.94.092001.

[91] E. Aprile et al. (XENON Collaboration). *Light Dark Matter Search with Ionization Signals in XENON1T.*, Phys. Rev. Lett. **123**, 251801 (2019). doi:10.1103/PhysRevLett.123.251801.

[92] E. Aprile et al. (XENON Collaboration). *Low-energy Calibration of XENON1T with an Internal ^{37}Ar Source*, Eur. Phys. J. C, **83**, 542 (2023). doi:10.1140/epjc/s10052-023-11512-z.

[93] Emanuele Angelino. *Calibration, simulation and analysis of the low-energy region in XENON project for direct dark matter search*, PhD thesis, 2023.

[94] E. Aprile et al. (XENON Collaboration). *Emission of single and few electrons in XENON1T and limits on light dark matter.*, Phys. Rev. Lett. D **106**, 022001 (2022). doi:10.1103/PhysRevD.106.022001.

[95] D. S. Akerib et al. (LUX Collaboration). *Tritium calibration of the LUX dark matter experiment*, Phys. Rev. D **93**, 072009 (2016). doi:10.1103/PhysRevD.93.072009.

[96] L. Baudis et al. *The first dual-phase xenon TPC equipped with silicon photomultipliers and characterisation with ^{37}Ar*, Eur. Phys. J. C, **80**, 477 (2020). doi:10.1140/epjc/s10052-020-8031-6.

[97] D. S. Akerib et al. (LUX Collaboration). *Ultra-Low Energy Calibration of LUX Detector using ^{127}Xe Electron Capture*, Phys. Rev. D **96**, 112011 (2017). doi:10.1103/PhysRevD.96.112011.

[98] E. Aprile et al. (XENON Collaboration). *Signal Yields of keV Electronic Recoils and Their Discrimination from Nuclear Recoils in Liquid Xenon*, Phys. Rev. D **97**, 092007 (2018). doi:10.1103/PhysRevD.97.092007.

[99] R. D. Peccei and Helen R. Quinn. *CP Conservation in the Presence of Pseudoparticles.*, Phys. Rev. Lett. **38**, 1440 (1977). doi:10.1103/PhysRevLett.38.1440.

[100] J. Preskill, M. B. Wise, and F. Wilczek. *Cosmology of the invisible axion.*, Physics Letters B **120**, 127 (1983). doi:10.1016/0370-2693(83)90637-8.

[101] L. Abbott and P. Sikivie. *A cosmological bound on the invisible axion.*, Physics Letters B **120**, 133 (1983). doi:10.1016/0370-2693(83)90638-X.

[102] M. Dine and W. Fischler. *The not-so-harmless axion.*, Physics Letters B **120**, 137 (1983). doi:10.1016/0370-2693(83)90639-1.

[103] S. Moriyama. *Proposal to Search for a Monochromatic Component of Solar Axions Using* ^{57}*Fe.*, Phys. Rev. Lett. **75**, 3222 (1995). doi:10.1103/PhysRevLett.75.3222.

[104] K. Fujikawa and R. E. Shrock. *Magnetic Moment of a Massive Neutrino and Neutrino-Spin Rotation.*, Phys. Rev. Lett. **45**, 963 (1980). doi:10.1103/PhysRevLett.45.963.

[105] N. F. Bell, M. Gorchtein, M. J. Ramsey-Musolf, P. Vo gel, P. Wang. *Model independent bounds on magnetic moments of Majorana neutrinos*, Physics Letters B **642**, 337-383 (2006). doi:10.1016/j.physletb.2006.09.055.

[106] Evan Shockley. *Study of Excess Electronic Recoils Events in XENON1T* , PhD thesis 2020.

[107] E. Aprile et al. (XENON Collaboration). *Search for New Physics in Electronic Recoil Data from XENONnT*, Phys. Rev. Lett. **129**, 161805 (2022). doi:10.1103/PhysRevLett.129.161805.

[108] J. Howlett G. Plante, E. Aprile and Y. Zhang. *Liquid-phase purification for multi-tonne xenon detectors*, Eur. Phys. J. C, **82**, 860 (2022). https://arxiv.org/pdf/2205.07336.pdf. doi:10.1140/epjc/s10052-022-10832-w.

[109] C. Huhmann M. Murra, D. Schulte and C. Weinheimer. *Design, construction and commissioning of a high-flow radon removal system for XENONnT*, Eur. Phys. J. C, **82**, 1104 (2022). doi:10.1140/epjc/s10052-022-11001-9.

[110] E. Aprile et al. (XENON Collaboration). *Design and performance of the field cage for the XENONnT experiment*, Eur. Phys. J. C, **84**, 138 (2024). doi:10.1140/epjc/s10052-023-12296-y.

[111] E. Aprile et al. (XENON Collaboration). *The XENONnT dark matter experiment*, Eur. Phys. J. C, **84**, 784 (2024). doi:10.1140/epjc/s10052-024-12982-5.

[112] B. G. Streetman, S. K. Banerjee. *Solid State Electronic Devices (7th ed.)*. Pearson Education, 2016.

[113] N. Otte. *The Silicon Photomultiplier - A new device for High Energy Physics, Astroparticle Physics, Industrial and Medical Applications*, SNIC Symposium, Stanford, California, 3-6 April 2006.

[114] A. Ghassemi et al. *A technical guide to silicon photomultipliers (MPPC) - Section 1*, Online Resources - Technical Note. https://hub.hamamatsu.com/us/en/technical-notes/mppc-sipms/a-technical-guide-to-silicon-photomutlipliers-MPPC-Section-1.html.

[115] N. Dinu, A. Nagai, A. Para. *Breakdown voltage and triggering probability of SiPM from IV curves at different temperatures*, Nucl. Instrum. Methods A, **845**, 64-68 (2017). doi:10.1016/j.nima.2016.05.110.

[116] A. N. Otte, D. Garcia, T. Nguyen, D. Purushotham. *Characterization of three high efficiency and blue sensitive silicon photomultipliers*, Nucl. Instrum. Methods A, **846**, 106-125 (2017). https://arxiv.org/pdf/1606.05186.pdf. doi:10.1016/j.nima.2016.09.053.

[117] E. Sciatta et al. *Arrays of Geiger mode avalanche photodiodes*, IEEE Photonics Technology Letters **18** No.15, 1633-1635, 2006. doi:10.1109/LPT.2006.879576.

[118] R. H. Haitz. *Mechanisms Contributing to the Noise Pulse Rate of Avalanche Diodes*, J. Appl. Phys. **36**, 3123-3131 (1965). doi:10.1063/1.1702936.

[119] F. G. Dalla Betta. *Advances in Photodiodes*. IntechOpen, 2011. doi:10.5772/588.

[120] A. Ghassemi et al. *A technical guide to silicon photomultipliers (MPPC) - Section 4*, Online Resources - Technical Note. https://hub.hamamatsu.com/us/en/technical-notes/mppc-sipms/a-technical-guide-to-silicon-photomutlipliers-MPPC-Section-4.html.

[121] Ieki K. et al. *Large-area MPPC with enhanced VUV sensitivity for liquid xenon scintillation detector*, Nucl. Instrum. Methods Phys. Res. A, **925**, 148-155 (2019). doi:10.1016/j.nima.2019.02.010.

[122] Alexander Fieguth. *Distillation column for the XENON1T experiment*, J. Phys.: Conf. Ser. **718** 042020.

[123] Hamamatsu. *Preliminary data sheet for Photomultiplier tube R8520-06-AL*, Private communication.

[124] Ketek. *KETEK SiPM sample datasheet*, Private communication.

[125] CAEN S.p.A. *Technical Information Manual: Model A 1510 12 CH FLOATING HV BOARD*, 2014.

[126] Kaizuworks Corporation. *Data sheet: Model KN2104 12 CH PMT Amplifier*. http://www.kaizuworks.co.jp/__HPB_Recycled/PDF(ENGLISH)/KN2104.pdf.

[127] Avtech Electrosystems Ltd. *Instruction manual: Model AVI-V-HV1-C PULSE GENERATOR*. https://www.avtechpulse.com/archives/old-manuals/AVHtoAVL-3%20%202000/AVI-V-HV1,HV2,HV3(SCHROFFCHASSISandMODULE)/02_AVI-V-HV1-C.pdf.

[128] S. Vinogradov. *Analytical models of probability distribution and excess noise factor of Solid State Photomultiplier signals with crosstalk*, Nucl. Instrum. Methods Phys. Res. A, **695**, 247-251 (2012). doi:10.1016/j.nima.2011.11.086.

[129] Bastian Beskers. *Design and commissioning of a dual-phase xenon time-projection-chamber for studies of the scintillation pulse shape*, PhD thesis, 2017. doi:http://doi.org/10.25358/openscience-2674.

[130] Pierre Sissol. *MainzTPC: Detector Commissioning and Study of the Low-Energy Response of Electronic Recoils in Liquid Xenon for Dark Matter Applications*, PhD thesis, 2019. doi:http://doi.org/10.25358/openscience-2678.

[131] Hamamatsu. *VUV4 MPPC Product Flyer*, Online Resources. https://hamamatsu.su/files/uploads/pdf/3_mppc/s13370_vuv4-mppc_b_(1).pdf.